Measurement of Charms and Bottoms with Semi-leptonic Decay Modes in $p+p$ Collisions at $\sqrt{s} = 200$ GeV

Ryohji Akimoto

Center for Nuclear Study,
Graduate School of Science,
University of Tokyo

A Dissertation Submitted in Partial Fullfillment of
the Requirements for the Degree of Doctor of Science

Abstract

A heavy quark is an interesting probe to understand a parton behavior in the extremely hot and dense matter created by the relativistic heavy-ion collision. The heavy quarks are only produced in initial parton scattering in heavy-ion collisions due to their large masses. It means that the properties of the heavy quarks at the initial stage of the heavy-ion collisions can be well described by those of $p+p$ collisions. Therefore, the difference of the final states of the heavy quarks between the heavy-ion collisions and $p+p$ collisions represents modifications during passing through the matter. The heavy quarks are expected to take longer time to equilibrate with the matter than light quarks since the energy loss of the heavy quarks is smaller than that of light quarks due to dead cone effect. Due to the long relaxation time, a history of interactions between the matter and the heavy quarks, which are strongly related to the properties of the matter, can be preserved in their diffusion during passing through the matter.

Since the energy loss depends on quark mass, the comparison of modifications during traveling in the matter between charm and bottom can test descriptions of the interaction. A new approach has been developed to evaluate the fraction of the bottom contribution in the heavy quark electrons. The fraction is evaluated by using the distances of the closest approach to the beam collision vertex, called DCA. DCA distributions of the electrons from charm and bottom decays have significantly different widths due to the difference of their life-times. The fraction can be evaluated by using the difference of their widths. Tracking with a good position resolution is necessary around a beam collision point to achieve the measurement. A silicon tracking system called VTX has been installed in PHENIX experiment in 2011 to achieve the precise tracking.

The bottom fraction has been evaluated at PHENIX experiment by the new approach in $p+p$ collisions with $\sqrt{s} = 200$ GeV at $1.5 < p_T < 5$ GeV/c. The bottom fraction at $p_T < 2.5$ GeV/c is succeeded to be measured for the first time. The fraction at $p_T > 2.5$ GeV/c is consistent with other results, and thus it is confirmed that the evaluation by the new approach has been succeeded. The result can also provide a good test of perturbative QCD (pQCD) calculations. There is not a significant difference in differential cross sections of the electrons from charm and bottom decays between the predictions and measured results though center values of the predictions are ∼50% smaller than the measured results. The total cross section of the bottom production is also determined by extrapolating with FONLL calculations, and it is 3.41 ± 0.53 (stat) ± 2.14 (sys) μb. There is not a significant difference between the prediction and our result.

Contents

List of Figures

vii

x

List of Tables

Chapter 1

Introduction

1.1 Quark Gluon Plasma

Color confinement is one of the most interesting phenomena in the strong interaction. It is the phenomenon that a particle with a color charge can only exist in a color-singlet state, and a single quark is bound together into a color-singlet state, a meson or baryon. It is believed based on that a stable single quark has never been observed. Asymptotic freedom is supposed to be deeply related to the cause of color confinement. Asymptotic freedom is a feature of a non-abelian gauge theory. Quantum ChromoDynamics (QCD) is the theory of the strong interaction, and it is described by a non-abelian $SU(3)$ gauge theory. Unlike Quantum ElectroDynamics (QED), the gauge bosons can interact each other in QCD as a consequence of the non-abelian gauge theory. Due to the self-interaction of the gauge bosons, the running coupling constant of QCD decreases as the energy scale increases. This nature is called asymptotic freedom. The running coupling constant (α_s) can be expressed as a function of the momentum transfer (Q^2) as follows.

$$\alpha_s \sim \frac{12\pi}{(33 - 2N_f)\log{(Q^2/\Lambda_{QCD})}}, \tag{1.1}$$

where N_f is the number of quark flavors, $\Lambda_{QCD} \sim 0.2$ GeV is the QCD scale. The asymptotic freedom suggests a possibility that color confinement can be broken in an extremely high temperature or high density, i.e. a phase transition occurs from the confined state (ordered phase) to the deconfined state (disordered phase). The deconfined state is called Quark Gluon Plasma (QGP) [2].

Lattice QCD calculations, which is a numerical approach based on the first principal, predict that the phase transition occurs at a critical temperature, $T_c \simeq 170$ MeV or the transition energy density $\epsilon_c \simeq 1$ GeV/fm^3 [3, 4, 5]. Figure 1.1 shows the entropy density ($s = \epsilon + p$) over T^3 as a function of T/T_c calculated by the lattice QCD [6]. The entropy density increases rapidly around at $T_c \sim 170$ MeV due to the increase of the degree of freedom by the deconfinement.

High-energy heavy-ion collision is expected to be a powerful and unique tool to achieve very high temperature and density which are enough to create QGP [7, 8]. There have been many attempts to produce QGP experimentally from heavy-ion collisions. The experiments of heavy-ion collisions began at Bevalac at Lawrence Berkeley National Laboratory (LBNL) with ∼2A GeV and a fixed target in the middle of 1970's, then followed in Alternating Gradient Synchrotron (AGS) at Brookhaven National Laboratory (BNL) and in Super Proton Synchrotron (SPS) at European Laboratory for Particle Physics (CERN). Currently, heavy-ion collision experiments have been performed with Relativistic Heavy Ion Collider (RHIC) at BNL and Large Hadron Collider (LHC) at CERN. RHIC and LHC can collide heavy nuclei with the center-of-mass energy per nucleon pair up to 200 GeV and 2.76 TeV, respectively.

There are a lot of indications that a new state of matter is formed [9, 10, 11, 12]. Major experimental findings at early stage of RHIC experiments are a suppression of jets at heavy-ion collisions by comparing with $p+p$ collisions [9, 10], which indicates formation of high density matter, and a large azimuthal anisotropy in non-central heavy-ion collision, which can be successfully described by a relativistic hydrodynamics model [11, 12]. Studies of the properties of the matter by the experiments of heavy-ion collision have a difficulty due to the fact that the matter undergoes several stages during its space-time evolution, as is described in Sec. 2.1.1. Since observables are measured through measurements of particles after the space-time evolution, they are affected by integrated information of the interaction with the matter. Therefore, the studies of the properties are necessary to be carried out with multiple probes with different features.

1.2   Heavy Quark

Heavy quarks (charm and bottom) are only produced in initial parton scatterings due to their large masses, and their initial states can be understood well from the measurements of $p+p$ collisions. In addition, the momentum transfer to create the heavy quarks is much larger than Λ_{QCD} due to their large masses, and thus, it leads to $\alpha_s \sim 0.3$, which is enough small to apply perturbative QCD (pQCD) to calculate the production of the heavy quarks. Therefore, the measurements of charm and bottom productions in $p+p$ collisions can provide a good test of pQCD calculations.

The energy loss of the heavy quark is smaller than that of light quarks due to dead cone effect [13], and thus, the heavy quark is not expected to fully equilibrate with the matter, which is different from light quarks. The thermal relaxation time of the heavy quarks has been argued to be larger than that of light quarks by a factor of m_{HQ}/T [14], where m_{HQ} is a mass of heavy quarks and T is a typical temperature of the matter. Due to the long relaxation time, the heavy quarks serve as impurities in the thermalizing matter, and a history of interactions between the matter and the heavy quarks, which are strongly related to the properties of the matter, can be preserved in their diffusion during passing through the matter.
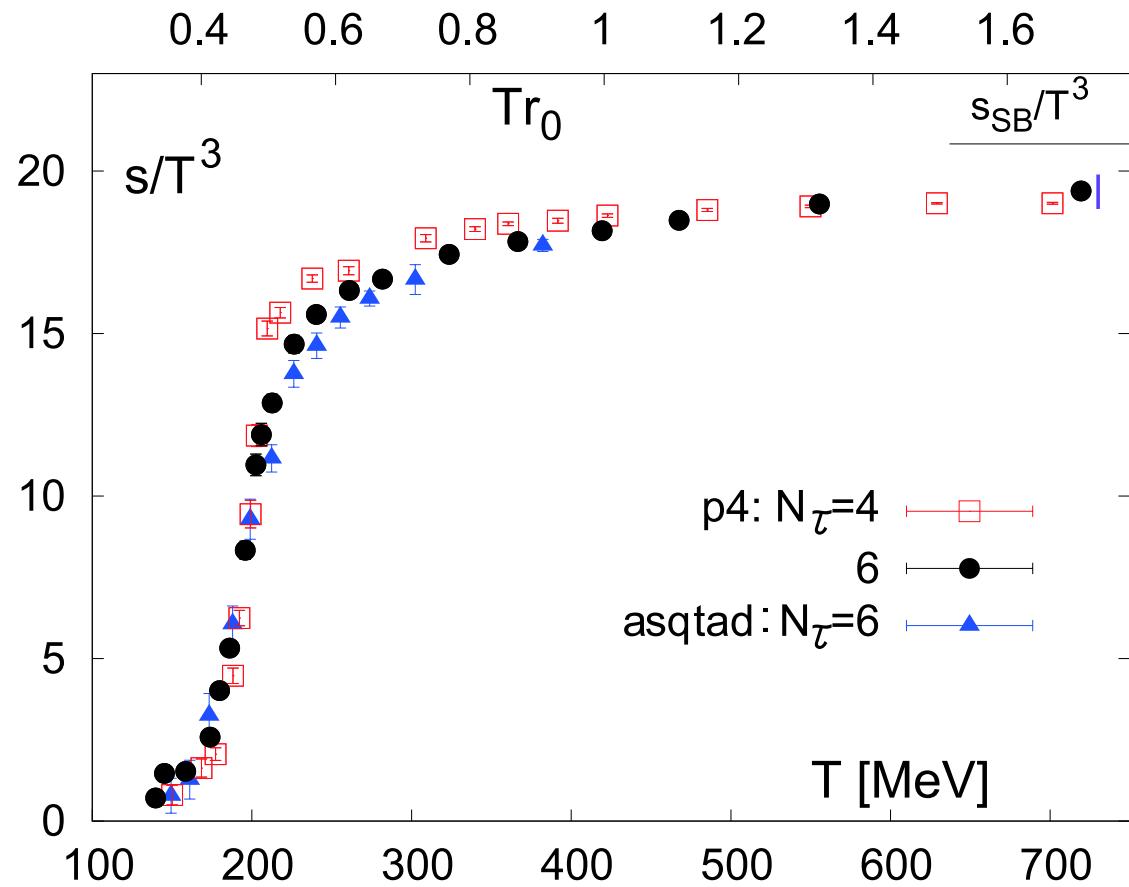
Figure 1.1: The entropy density $(s = \epsilon + p)$ over T^3 as a function of T/T_c calculated by the lattice QCD [6].

In order to extract the properties of the matter, understandings of the interaction between the heavy quarks and the matter are necessary. Since the energy loss depends on quark mass, the comparison of modifications during traveling in the matter between charm and bottom is expected to provide detail information about the interaction.There are results about charm and bottom measurement in $p+p$ collisions [15, 16]. However, the results are only for high-p_T region and the approaches employed to extract the results are hard to be employed for heavy-ion collisions due to a large background derived from a high multiplicity condition of heavy-ion collisions. The difficulty to employ the approaches in heavy-ion collisions is discussed in Sec. 2.3.

1.3   Distance of Closest Approach

The distance of the closest approach (DCA) to a beam collision vertex is utilized to extract charm and bottom signals in this thesis. Figure 1.2 illustrates a decay of a D meson ($D \rightarrow e + K + \nu$). A D meson is created by a beam collision, and proceeds and decays far from the collision point. An electron is ejected by the decay. DCA of the electron track is the distance between the track, which is represented as the red arrow in Fig. 1.2, and collision point. Without a magnetic field, the DCA can be written by $d \cdot \sin \theta$, where d is the distance between the decay point and the beam collision point, and θ is the angle difference between the tracks of D meson and electron. Therefore, DCA depends on the life-time of a mother particle and the q-value of a decay mode. Yields of charm and bottom can be evaluated by using the difference of their life-times. The analysis with the DCA is called "DCA approach". Details of the approach are written in Sec. 2.3 and chapter 4.

The DCA is calculated by interpolating from a detector hit point taking account of a bending in a magnetic field. The interpolation is peroformed by assuming a track path is a circle. The PHENIX detector complex has spectrometers which can measure momenta with good precision. However, the resolution of the interpolation is not good since the spectrometers locate far from the beam path (220 cm). A silicon tracking system called VTX has been installed for the DCA measurement in the PHENIX detector complex for the DCA measurement. The VTX enable to measure tracks around beam collision points with a good precision. Two panels of Fig. 1.3 illustrate the interpolation by using VTX hits. The VTX is a barrel detector with 4 barrels surrounding the beam path. The innermost barrel locates at 2.6 cm far from the beam path and its position is 14 μm and 152 μm for directions perpendicular and parallel to the beam path, respectively [17]. Details of the VTX is written in Sec. 3.2.8.

Here, the definition of the DCA used in this thesis is given. The DCA is calculated in 2-dimensional plane perpendicular to the beam path, i.e. a track is projected in the plane, and the DCA is the distance of the closest approach of the projected track to the beam collision point. The coordinate of the axis parallel to the beam path is
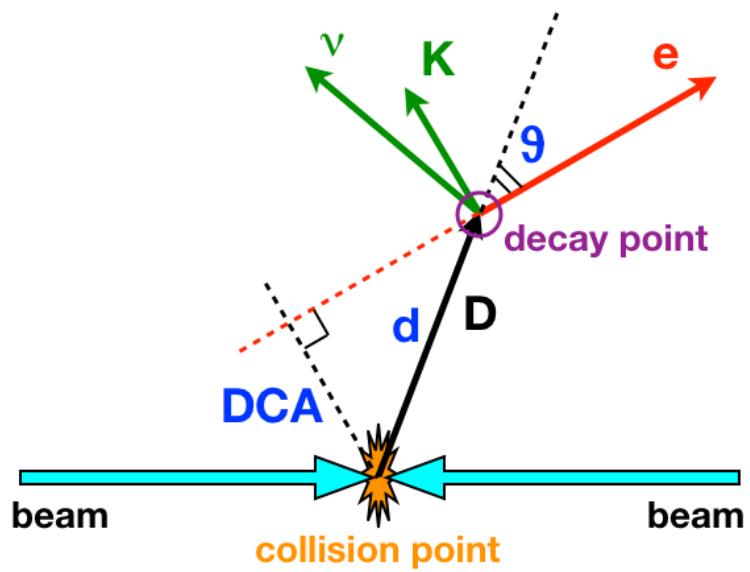
Figure 1.2: An illustration of a D meson decay $(D \rightarrow e + K + \nu)$.
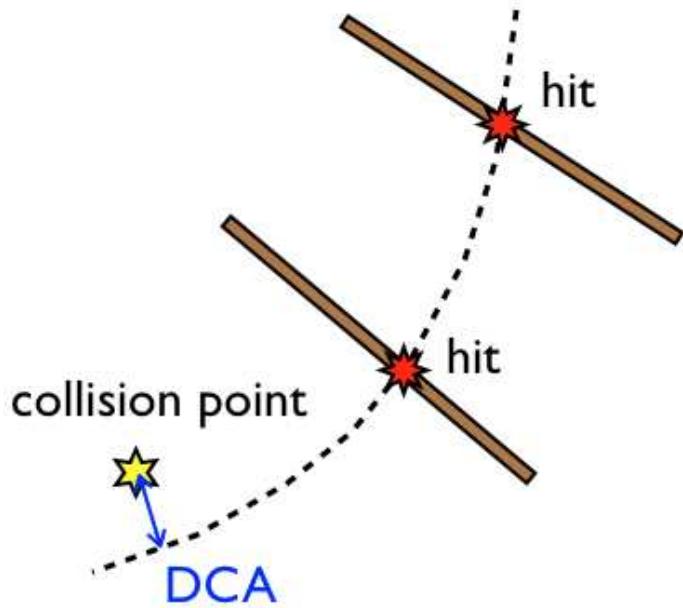
Figure 1.3: The interpolation for DCA calculation by using VTX hits.

ignored in the calculation of the DCA, and thus, the DCA calculated in 3-dimensional space is not exactly the same as the DCA used in this thesis. The sign of the DCA is defined by an alignement of the projected track and beam collision point. A track of a charged particle is rotated by a magnetic field. When the beam collision point is inside to rotation circle, its DCA is positive. Otherwise, it is negative. The left and right panels of Fig. 1.3 show tracks with positive and negative DCA, respectively.

1.4   Objective and Organization of Thesis

The fraction of electrons* from bottom decay in the electrons from charm or bottom decays in $p+p$ collisions with $\sqrt{s} = 200$ GeV is measured from the DCA approach in this thesis. By combining a published result of the cross section of the electrons from charm or bottom decays [18], the cross section of the electrons from charm decays and that of bottom decays are evaluated. The cross sections are important since they can provide information of initial condition of the heavy quarks in heavy-ion collisions and they are used as a reference for spectra of the heavy quark in heavy-ion collisions. In addition, the measurements of charm and bottom productions in $p+p$ collisions can provide a good test of pQCD calculations.

The organization of this thesis is as follows. In chapter 2, theoretical and experimental backgrounds are described. In chapter 3, the RHIC accelerator complex and the PHENIX detectors are described. In chapter 4, the analysis of the DCA approach to extract the fraction of electrons from bottom decay in the electrons from charm or bottom decays is explained. In chapter 5, the fraction of the bottom contribution, the differential invariant cross section of the electrons from charm and bottom decays, and the total cross section of bottom production are shown. In chapter 6, the interpretations of the results are discussed. Chapter 7 is the conclusion of this thesis.

---

*Electrons and positrons are simply called electrons in this thesis.

Chapter 2

Physics Background

In this chapter, theoretical and experimental backgrounds of our work are described. At first, the picture and description of high-energy heavy-ion collisions in Sec. 2.1. These are necessary to understand results of the heavy-ion collision experiments. In Sec. 2.2 and Sec. 2.3, theoretical descriptions and experimental results about heavy quarks are described. The electrons from heavy-quark decay have been measured in our work. Theoretical descriptions of the production, hadronization, and decay of heavy quarks are summarized in Sec. 2.2. Experimental results about heavy quarks in heavy-ion collisions and their theoretical interpritations are described in Sec. 2.3.

2.1 Relativistic Heavy Ion Collision

A relativistic heavy-ion collision is a unique tool to create an extremely hot and dense matter. Several collider experiments have been performed by using RHIC and LHC in order to study the QGP.

A heavy-ion collision experiment began at Bevalac at Lawrence Berkeley National Laboratory (LBNL) with $\sim 2A$ GeV and a fixed target in the middle of 1970's. Then experiments were carried out in Alternating Gradient Synchrotron (AGS) at Brookhaven National Laboratory (BNL) and in Super Proton Synchrotron (SPS) at European Laboratory for Particle Physics (CERN). Their beam energies were $14A$ GeV and $160A$ GeV, respectively. Currently, heavy-ion collision experiments have been performed with Relativistic Heavy Ion Collider (RHIC) at BNL and Large Hadron Collider (LHC) at CERN. RHIC and LHC can collide heavy nuclei with the center-of-mass energy per nucleon pair up to 200 GeV and 2.76 TeV, respectively.

2.1.1 Space-Time Evolution

The matter created by relativistic heavy-ion collisions undergoes a space-time evolution. The evolution of the matter is expected to be described based on the scenario proposed by J.D. Bjorken [19]. It is assumed that the space-time evolution depends on

only the proper time $\tau = \sqrt{t^2 - z^2}$ in the high energy limit in the scenario. Figure 2.1 shows a space-time picture of the evolution of the matter created in the heavy-ion collision with the longitudinal coordinate z and the time coordinate t. The space-time evolution can be separated into mainly the following four different phases separated by the dotted lines in Fig. 2.1:
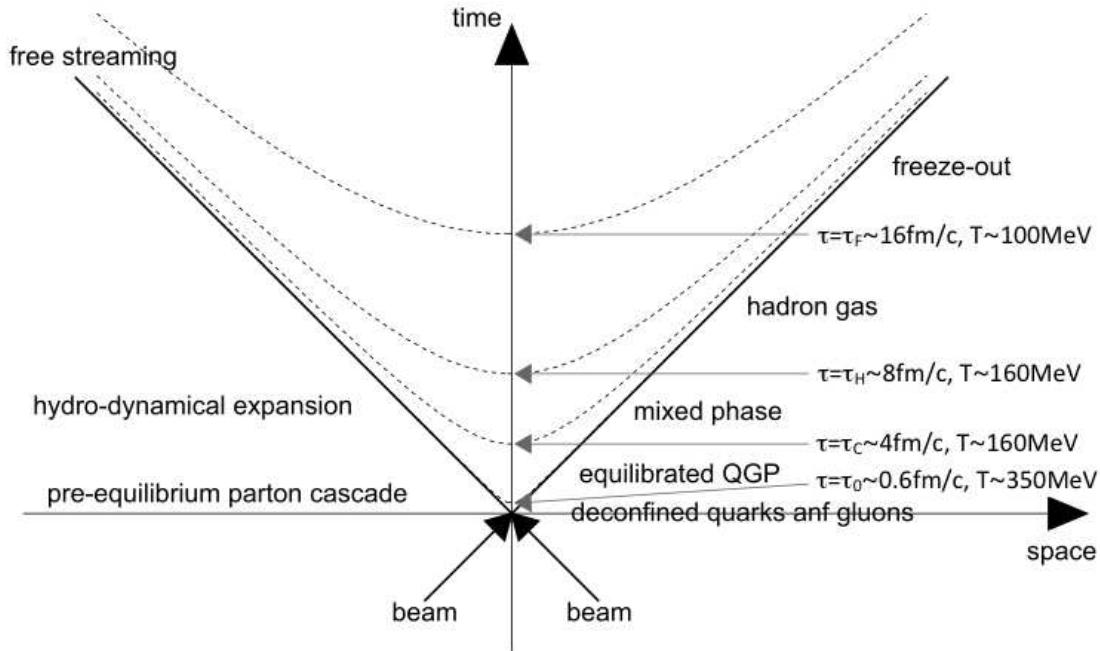
Figure 2.1: A space-time picture of evolution of the matter created in a heavy ion collision at RHIC. The proper times τ and temperatures T for different phases are expected from a hydrodynamical model [20]. The mixed phase would exist only if the transition is first order.

1. Pre-equilibrium ($\tau = 0 \sim \tau_0$)

   Two incoming nuclei collide each other and many parton collisions take place. Incoming partons lose their kinematic energy by the collisions, and a large amount of energy is deposited at a tiny colliding region. A lot of secondary particles are produced in the region. The secondary particles subsequently interact with each other and the system is led to a local equilibrium.

2. Deconfined partonic phase (QGP) in thermal equilibrium ($\tau = \tau_0 \sim \tau_C$)

   If the deposited energy is enough large to occur a phase transition, the QGP phase can be formed ($\tau = \tau_0$). The QGP is likely to evolve like a fluid, expands and cools down according to hydrodynamics.

8

3. Mixed phase between QGP and hadrons ($\tau = \tau_C \sim \tau_H$)

   When the system cools down to the transition temperature T_C, a phase transition is taken place from the QGP to a phase of ordinary hadronic matter. A hadronization starts, and the mixed phase consisting of the quarks, gluons, and hadrons is made.

4. Hadron gas ($\tau = \tau_H \sim \tau_F$)

   The system finishes hadronization. The produced hadrons keep interacting with each other until the system cools down to the kinematic freeze-out temperature T_F.

We never know where each of observed particles is generated. It leads our study to understand properties of QGP difficult since measured particles are affected by integrated information of the interaction with a matter at each of the stages. Therefore, it is important to study the properties with multiple probes with different features.

2.1.2   Collision Geometry

The collision geometry of the heavy-ion collisions play an important role in collision dynamics, and thus, important to interpret observed results. The participant-spectator picture is a simple geometrical picture characterizing the collision with the impact parameter, b, which is shown in Fig. 2.2. Figure 2.2 illustrates central (left) and peripheral collisions (right) of nuclei with radii R. The central (peripheral) collision is a collision with small b (large b). As shown in Fig. 2.3, incoming nuclei look like a thin pancake due to the Lorentz contraction. When $b > 2R$, where R represents the radius of the nuclei, the incoming nuclei interact mainly by the electromagnetic force. As b decreases, the nuclei geometrically overlap, then an effect by the strong interaction suddenly increases. When $b < 2R$, the nucleons in the nuclei are classified into two groups: the participant, which is in the overlapping region, and the spectator, which is not. Since the spectator keeps its longitudinal velocity and emerges at nearly zero degrees in the collisions, it is relatively easy to separate the spectator and participant experimentally. The relations between the impact parameter, centrality, the number of participants (N_{part}), and the number of binary collisions (N_{coll}) are obtained based on Glauber model [21, 22]. Figure 2.4 shows N_{part} and N_{coll} as a function of the impact parameter in Au+Au collision with $\sqrt{s_{NN}} = 200$ GeV calculated based on the Glauber model [23].

Particle Production

N_{coll} and N_{part} are important parameters for particle production in heavy-ion collision. Particle production in soft processes is expected to be proportional to N_{part}, and that in hard processes is expected to be proportional to N_{coll}. Figure 2.5 shows total multiplicity of charged particles at normalized by $\langle N_{part}/2 \rangle$ as a function of N_{part},
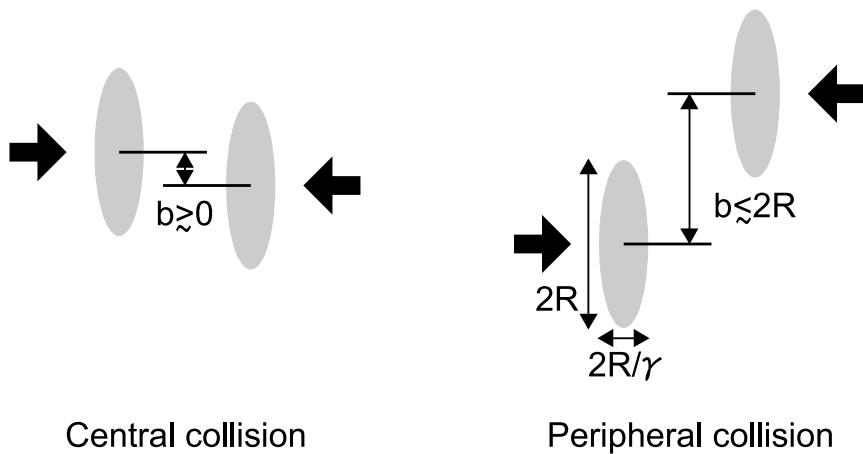
Figure 2.2: A cartoon of central (left) and peripheral (right) collisions of nuclei with radii R.
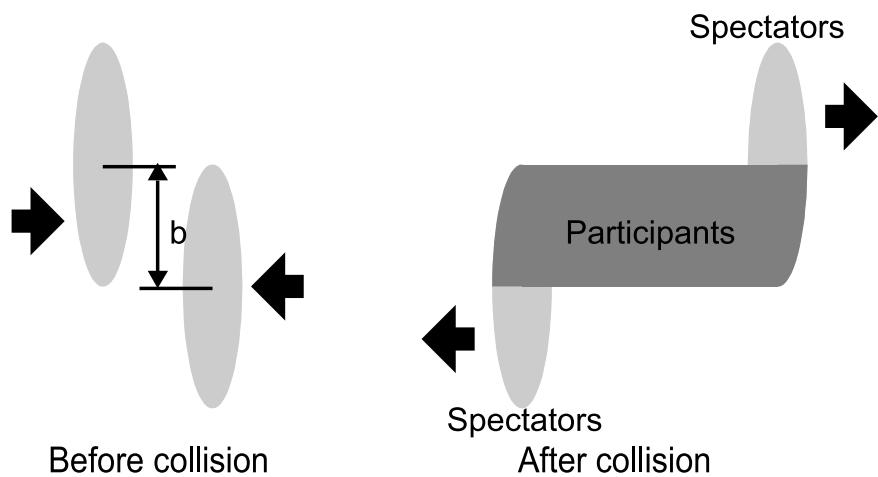
Figure 2.3: An illustration of the colliding nuclei before (left) and after (right) a collision in the participant-spectator picture.
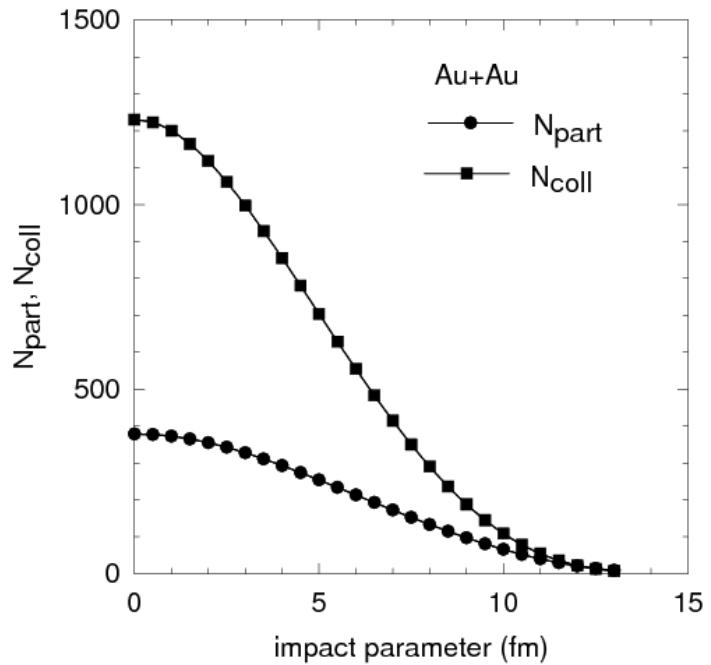
Figure 2.4: N_{part} and N_{coll} as a function of the impact parameter in Au+Au collision with $\sqrt{s_{NN}} = 200$ GeV calculated based on the Glauber model [23]. Inelastic nucleon+nucleon cross section (σ_{NN}) and nuclear charge density ($\rho(r)$) are assumed to be $\sigma_{NN} = 42$ mb and $\rho(r) = \rho_0(1 + \exp\frac{r-R}{a})^{-1}$, respectively, where $R = 6.38$ fm and $a = 0.535$ fm.

measured by PHOBOS experiment [24]. The normalized total multiplicity of charged particles, which is dominated by particles produced by soft processes, is constant, and thus the total multiplicity is scaled by N_{part}, from peripheral to central collisions. As is described in Sec. 2.2, heavy quarks are produced by hard processes, and integrated yield of electrons from heavy quark decays is proportional to N_{coll}. In order to quantify effects from the matter created by heavy-ion collisions on particle produced by hard processes, following nuclear modification factor (R_{AA}) is utilized:

$$R_{AA} = \frac{dN_{AA}/dp_T}{N_{coll} \cdot dN_{pp}/dp_T}. \tag{2.1}$$
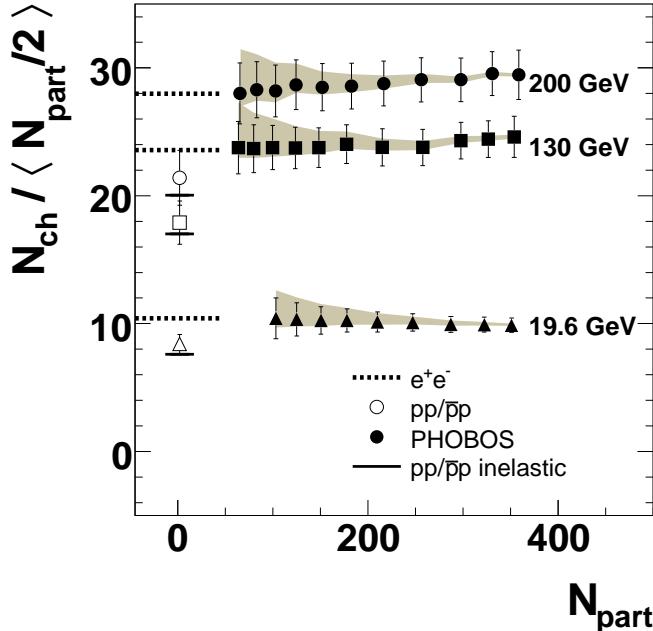
Figure 2.5: Total multiplicity of charged particles at normalized by $\langle N_{part}/2 \rangle$ as a function of N_{part} for $\sqrt{s_{NN}}$ = 19.6, 130, and 200 GeV, measured by PHOBOS experiment [24].

2.2   Heavy Quark

The heavy quarks are only produced in initial parton scattering in heavy-ion collisions due to their large masses. It means that the properties of the heavy quarks at the initial stage of the heavy-ion collisions can be described by those of $p+p$ collisions, and thus, the difference of the final states of the heavy quarks between the heavy-ion collisions and $p+p$ collisions represents modifications during passing through the matter.

12

Measurement of heavy quarks are performed with decay electrons. Heavy quark production, hadronization (fragmentation), and decay are described in following sections. Decay modes of heavy quarks with a lepton in decay products are called semi-leptonic decay modes. In this thesis, semi-leptonic decay modes with an electron in decay products are simply called semi-leptonic decay modes.

2.2.1 Heavy Quark Production

The energy scale for the production of heavy quarks $Q^2 \sim M^2_{c(b)}$ is much higher than Λ_{QCD}, and thus, the coupling constant α_s is ~ 0.3. It is small enough to apply the perturbative QCD (pQCD) calculation for the production of heavy quarks. The general perturbative calculation for the total cross section of quark-antiquark pair production by a parton scattering can be expressed by the following equation.

$$\sigma_{ij}(\hat{s}, M^2_Q, \mu^2_R) = \frac{\alpha^2_s(\mu^2_R)}{M^2_Q} \sum_{k=0}^{\inf} (4\pi\alpha_s(\mu^2_R))^k \sum_{l=0}^{k} f^{(k,l)}_{ij}(\eta) \left[\ln\left(\frac{\mu^2_R}{M^2_Q}\right) \right]^l, \qquad (2.2)$$

where μ^2_R is called renormalization scale, which is a order of the square of the quark mass, M^2_Q, and $\hat{s}$ is the center-of-mass energy of the parton scattering. The dimensionless parameter $\eta = \hat{s}/M^2_Q - 1$ reflects the phase space of the heavy quark pair production ($\sqrt{\hat{s}}$ should be at least $2M_Q$ to create aquark-antiquark pair). i and j are the indices of parton, and they correspond to q, $\bar{q}$, or g. $f^{(k,l)}_{i,j}$ is a dimensionless scaling function representing the amplitude of a partonic scattering diagram. k represents the order of the process diagram. $k=0$ corresponds to the Leading-Order (LO) and $k=1$ corresponds to the Next-Leading-Order (NLO). Figure 2.6 shows Feynman diagrams of LO and important NLO process. The total cross section for heavy quark production can be calculated in $p+p$ collisions with a parton distribution function (PDF) in protons, $\sigma_{ij}(\hat{s}, M^2_Q, \mu^2_R)$, as follows:

$$\sigma_{pp}(s, M^2_Q, \mu^2_R, \mu^2_F) = \sum_{i,j=q,\bar{q},g} \int_{4M^2_Q/s}^{1} d\tau \int_\tau \frac{dx_1}{x_1} F^p_i(x_1, \mu^2_F) F^p_j(\tau/x_i, \mu^2_F) \sigma_{ij}(\tau s, M^2_Q, \mu^2_R).$$

$$(2.3)$$

μ^2_F is a momentum transfer scale (factorization scale) of the PDF factorization. $F^p_i(x_1, \mu^2_F)$ is a PDF in term of a momentum fraction, x_1, and factorization scale. Eq. 2.3 have three free parameters, M^2_Q, μ^2_R and μ^2_F. The uncertainty of the perturbative calculation is usually determined by varying these parameters.

Fixed-Order plus Next-to-Leading-Log Calculation

Fixed-Order plus Next-to-Leading-Log (FONLL) calculation is the theory based on pQCD calculation about heavy quark production [25, 26]. FONLL can be compared

13
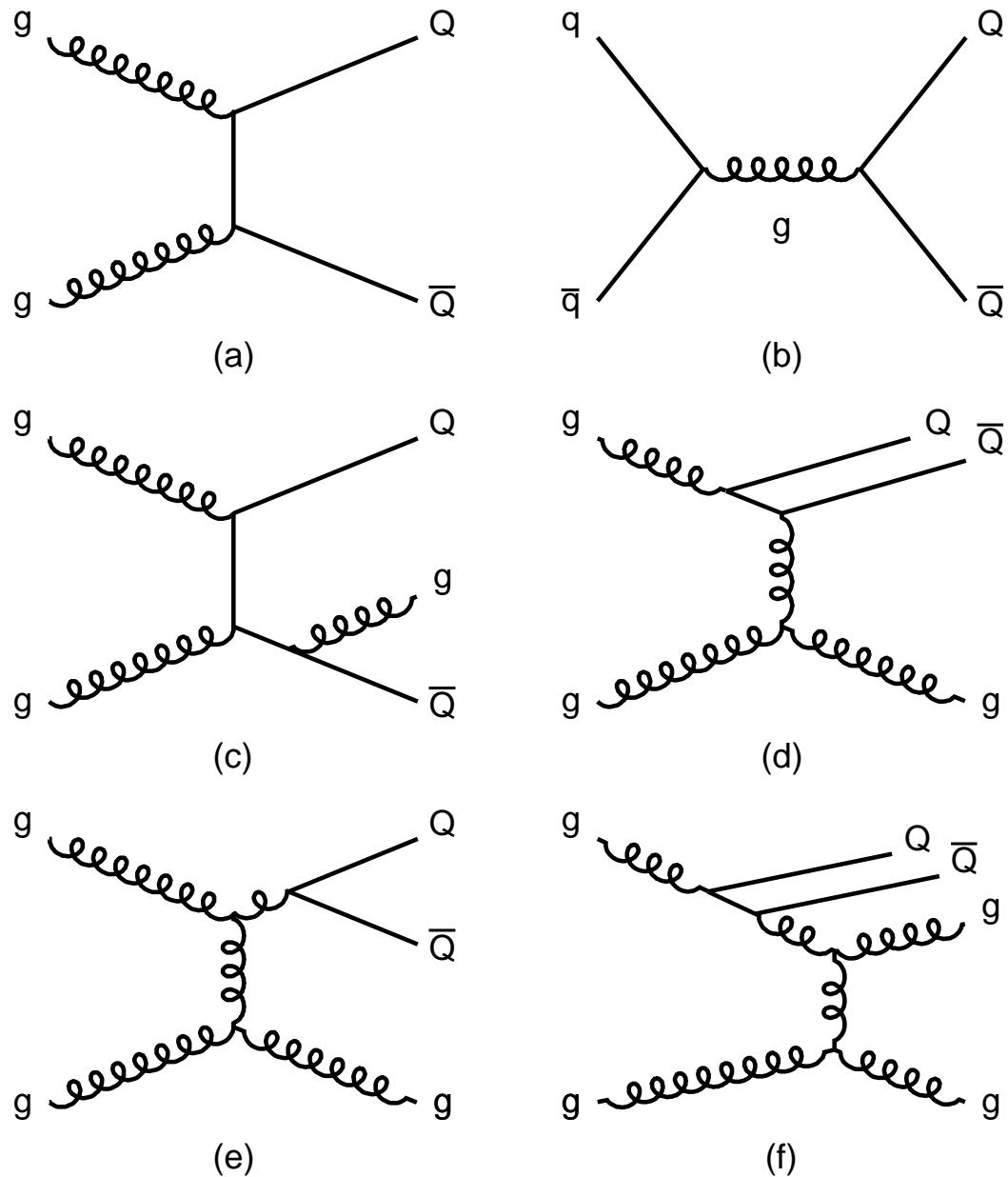
Figure 2.6: The leading order and important the next leading order Feynman diagrams. (a) gluon fusion. (b) quark-antiquark annihilation. (c) pair creation with gluon emission. (d) flavor excitation. (e) gluon splitting. (f) gluon splitting with excitation character.

directly with the experimental results. The differential invariant cross section of the heavy-quark hadrons can be written as follows:

$$E\frac{d^3\sigma^l}{dp^3} = E^{HQ}\frac{d^3\sigma^{HQ}}{dp^3} \otimes D(Q \to H_{HQ}),\qquad(2.4)$$

where the symbol $\otimes$ denotes a generic convolution, the leptonic decay spectrum term $f(H_{HQ} \to l)$ also implicitly accounts for the proper branching ratio and $D(Q \to H_{HQ})$ denotes fragmentation process. The distribution of heavy quarks, $E^{HQ}d^3\sigma^{HQ}/dp^3$ is evaluated at the Fixed-Order plus Next-to-Leading-Log (FONLL) level pQCD calculation. FONLL includes the full fixed-order NLO result (FO) and re-summation perturbative terms proportional to $\alpha_s^n(\log^k(p_T/m))$ to all orders with next-to-leading logarithmic (NLL) accuracy (i.e. $k = n,\ n-1$), where m is mass of heavy quark. The NLL terms take an important role to converge of the perturbative series for high p_T ($p_T > m$) region. Heavy quark fragmentation is implemented within the FONLL formalism that merges the FO + NLL calculations. The NLL formalism is used to extract the non-perturbative fragmentation effects from the experimental data in e^+e^- collisions using Mellin transforms [27]. Figure 2.7 shows the p_T distributions of B hadron measured in CDF with FONLL predictions in $p+\bar{p}$ collisions at $\sqrt{s} = 1.96$ TeV [28]. Figure 2.8 shows the differential cross sections of non-photonic electrons from heavy quark measured in RHIC with FONLL predictions in $p+p$ collisions at $\sqrt{s} = 200$ GeV. The red and blue points represents the cross sections reported from PHENIX and STAR experiments [15, 29]. The solid line represents the central value of the FONLL calculation, and the dash line represents its uncertainty. FONLL calculation provides a successful description for the experimental p_T distributions of heavy quark. However, there is large theoretical uncertainty for the absolute value of cross section at FONLL. For example, FONLL predicts the total cross section of charm, $\sigma_{c\bar{c}}$ to be 256^{+400}_{-146} μb and the total cross section of bottom, $\sigma_{b\bar{b}}$ to be $1.92^{+1.21}_{-0.78}$ μb in $p+p$ collisions a $\sqrt{s} = 200$ GeV.

2.2.2 Fragmentation

Heavy quarks created by parton scatterings pick up light quarks in order to create color singlet hadrons, which is called as fragmentation process. The differential cross section of heavy quark hadrons ($d\sigma^H/dp_T^H$) can be written as follows:

$$\frac{d\sigma^H}{dp_T^H} = \int d\hat{p}_T dz \frac{d\sigma_{HQ}}{d\hat{p}_T} D_{HQ}^H(z)\delta(p_T^H - z \cdot \hat{p}_T),\qquad(2.5)$$

where $\hat{p}_T$ is the transverse momentum of heavy quarks and p_T^H is the transverse momentum of heavy quark hadrons. $d\sigma^{HQ}/d\hat{p}_T$ is the differential cross section of heavy quarks, and z is the momentum fraction of the heavy quark carried by the hadron. $D_{HQ}^H(z)$ is called as fragmentation function and determines the the probability of

15
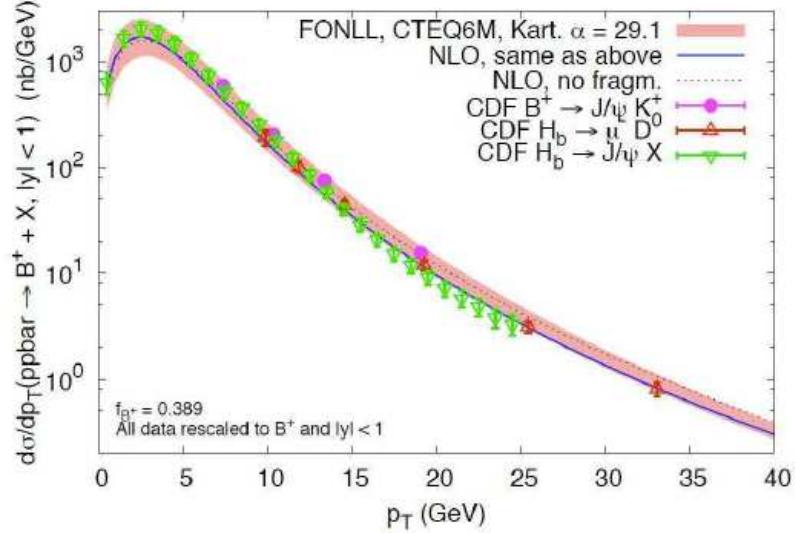
Figure 2.7: The p_T distributions of B hadron measured in CDF with FONLL predictions in $p+\bar{p}$ collisions at $\sqrt{s} = 1.96$ TeV.
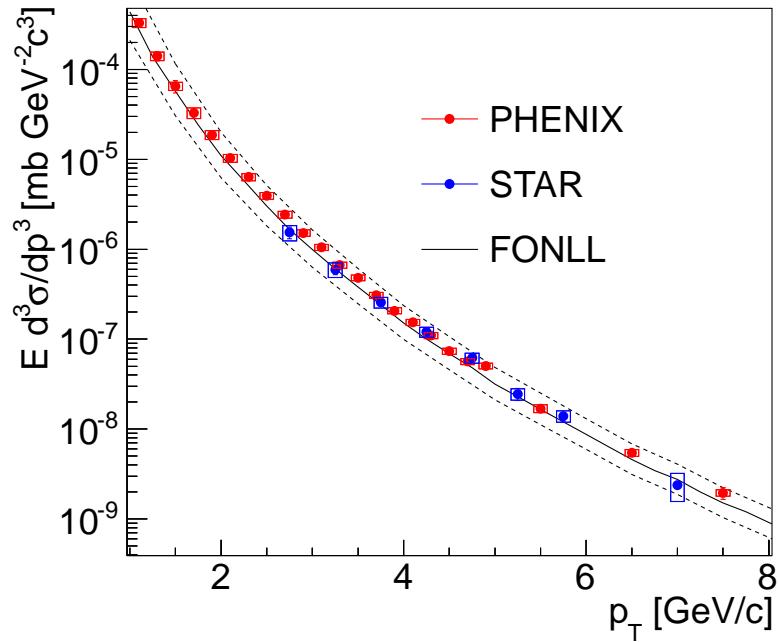
Figure 2.8: The differential cross sections of non-photonic electrons from heavy quark measured in RHIC with FONLL predictions in $p+p$ collisions at $\sqrt{s} = 200$ GeV. The red and blue points represents the cross sections reported from PHENIX and STAR experiments [15, 29]. The solid line represents the central value of the FONLL calculation, and the dash line represents its uncertainty.

16

producing hadron with given momentum fraction (z). The fragmentation function of heavy quarks should be much larger than that of a light hadron. In the limit of a very heavy quark, one expects that the fragmentation function for a heavy quark to go into any heavy hadron to be peaked near 1. The fragmentation function can be split into a perturbative part and an non-perturbative part. Non-perturbative effect in the calculation of the heavy quark fragmentation function is performed in practice by convolving the perturbative result with a phenomenological non-perturbative form. There are various parameterizations for the non-perturbative part which have free parameters. The free parameters in the non-perturbative parameterizations are determined by the experimental results in e^+e^- collisions based on the assumption that the fragmentation function is independent on how to be produced. In general, the parameters in the non-perturbative forms do not have any absolute meaning, since these depend on the order of the perturbative calculation in the fragmentation function. The most accurate approach to derive the fragmentation function is to use the Mellin transforms of the fragmentation function and obtain the momenta of this transform from the experimental data. The treatment of the fragmentation process discussed above is expected to be valid in $p+p$ collisions. In the case of heavy-ion collisions, the coalescence process becomes important in the fragmentation of heavy quark.

2.2.3   Semi-leptonic Decay

There are two merits in the measurement via decay electrons with PHENIX detector comparing to a full reconstruction of a hadronic decay with all decay products: one is a large branching ratio and the other is a good signal-to-noise (S/N) ratio. Total branching ratio of semi-leptonic modes are around 10% for both charm and bottom. Branching ratios of main semi-leptonic decay modes are summarized in Tab. 2.1. On the other hands, a specific mode of hadronic decay modes is small, especially for bottom. Branching ratios of hadronic decay modes of B meson is $\sim 10^{-4}$. A S/N ratio of electrons from heavy-quark decays is achieved ~ 1 at $p_T > 1.5$ GeV/c, as is described in Sec. 4.8.8. However, there is a disadvantage that measured electrons are sum of charm and bottom decays, and thus, an additional information is necessary to separate yields of charm and bottom decays. Contributions of charm and bottom decays are evaluated by using a DCA distribution in this thesis.

For processes where the momentum transfer is much less than the W boson mass, the amplitude of a semi-leptonic decay of a quark, Q, to another one, q ($Y_{Qq'} \rightarrow X_{qq'} + l + \nu$), can be given by

$$M(Y_{Qq'} \rightarrow X_{qq'} + l + \nu) = i\frac{G_F}{\sqrt{2}}V_{qQ}L^\mu H_\mu, \qquad (2.6)$$

where G_F is the Fermi constant of the weak interaction and V_{qQ} is an element of the Cabibbo-Kobayashi-Maskawa (CKM) matrix. L^μ is the leptonic current and H_μ is

the hadronic current. H_μ is difficult to calculate from first principles since it includes non-perturbative QCD effect. The hadronic current is usually parameterized with form factors.

Table 2.1: Branching ratios and q-values for main semi-leptonic decay channels of charm and bottom hadrons.

hadron	decay channel	branching ratio	q-value
D^+	$D^+ \to e^+ \overline{K}^0 \nu_e$	8.83±0.22%	1.37 GeV
	$D^+ \to e^+ \overline{K}^{*0} \nu_e$	3.68±0.21%	0.97 GeV
D^0	$D^0 \to e^+ K^- \nu_e$	3.55±0.05%	1.37 GeV
	$D^0 \to e^+ K^{*-} \nu_e$	2.17±0.16%	0.97 GeV
D_s	$D_s \to e^+ \phi \nu_e$	2.49±0.14%	0.97 GeV
	$D_s \to e^+ \eta \nu_e$	2.67±0.29%	1.42 GeV
	$D_s \to e^+ \eta' \nu_e$	0.99±0.23%	1.01 GeV
Λ_c	$\Lambda_c \to e^+ \Lambda \nu_e$	2.1±0.6%	1.17 GeV
B^+	$B^+ \to e^+ \overline{D}^0 \nu_e$	2.23±0.11%	3.41 GeV
	$B^+ \to e^+ \overline{D}^{*0} \nu_e$	5.68±0.19%	3.27 GeV
B^0	$B^0 \to e^+ D^- \nu_e$	2.17±0.12%	3.41 GeV
	$B^0 \to e^+ D^{*-} \nu_e$	5.01±0.12%	3.27 GeV
B_s	$B_s \to e^+ D_s \nu_e X$	7.9±2.3%	-
Λ_b	$\Lambda_b \to e^- \Lambda_c \overline{\nu}_e$	5.0+1.9%-1.4%	3.33 GeV
	$\Lambda_b \to e^- \Lambda_c \pi^+ \pi^- \overline{\nu}_e$	5.6±3.1%	3.05 GeV

2.3 Measurement of Heavy Quark

Measurements of heavy quarks have been carried out at several species of beam collision systems ($p+p$, $d+$A, and A+A) and RHIC and LHC [18, 30, 29, 31]. In this section, these results are described. In addition, understandings of interaction between heavy quarks and the matter created by heavy-ion collisions from the results are described.

2.3.1 Medium Modification

Medium modification of heavy quarks is studied by the measurement of the heavy quark electrons in A+A collisions. Figure 2.9 show R_{AA} for 0-10% central (most central) collisions and azimuthal anisotropy for 0-92% central collisions of the single electrons, and corresponding π^0 data at PHENIX [32, 10]. From the measurement, a

strong suppression at high p_T and a large azimuthal anisotropy have been observed in Au+Au collisions. It indicates that the heavy quarks as well as light quarks strongly interact with the matter created in A+A collisions. R_{AA} at high p_T is almost same level as π^0. However, the complete understanding of the parton behavior in the QGP, which is essential to extract QGP properties, is still a challenging task since the mechanism of the energy loss is different between light and heavy quarks, as is shown in Sec. 2.3.3.

Figure 2.10 shows R_{AA} of the heavy quark electrons for different p_T ranges as a function of the number of participant nucleons, N_{part} [18]. As is shown in Fig. 2.4, larger N_{part} means smaller impact parameter, i.e. more central collision. The green and blue circles are for the heavy quark electrons with $p_T > 0.3$ GeV/c and with $p_T > 3.0$ GeV/c, respectively. The red points are for π^0 with $p_T > 4.0$ GeV/c. For the integration interval $p_T > 0.3$ GeV/c containing more than a half of the heavy quark electrons, R_{AA} is consistent with unity for all N_{part}. It shows that the total yield is well scaled by N_{coll} for any collision size and supports the expectation that heavy quark is only produced in the initial hard scattering.

2.3.2   Initial Modification

There are known normal nuclear effects without a phase transition, which modify the yield and p_T distribution of produced particles such as Cronin effect [33] or nuclear shadowing [34]. They are called initial state effects. In order to extract the information of the matter created by heavy-ion collisions, these nuclear effects should be taken into account. At RHIC and LHC, d+A or p+A collision experiments has been performed to estimate the effects.

Initial nuclear modification of heavy quark production is studied by the measurement of the electrons from heavy quark hadrons in d+Au collisions at $\sqrt{s_{NN}} = 200$ GeV at PHENIX [30]. Figure 2.11 shows the nuclear modification factor of the electrons from heavy quark in d+Au collisions ($R_{d\mathrm{Au}}$) defined in Eq. 2.1. The measured $R_{d\mathrm{Au}}$ indicates the yield of the electrons from heavy quark is slightly enhanced in d+Au collisions for the measured p_T range, while it is almost consistent with unity due to large uncertainty. Therefore, it is hard to explain the suppression described in Sec. 2.3.1. The left and right panels of Fig. 2.12 shows the modifications of charm and bottom cross-sections, respectively, by the nuclear effects of the PDFs calculated using the EKS 98 nuclear weight functions [35] They shows that charm production is not modified and bottom production is slightly enhanced (anti-shadowing) by the PDF modification. Therefore, the slight enhancement of the measured $R_{d\mathrm{Au}}$ could be interpreted as the Cronin effect.
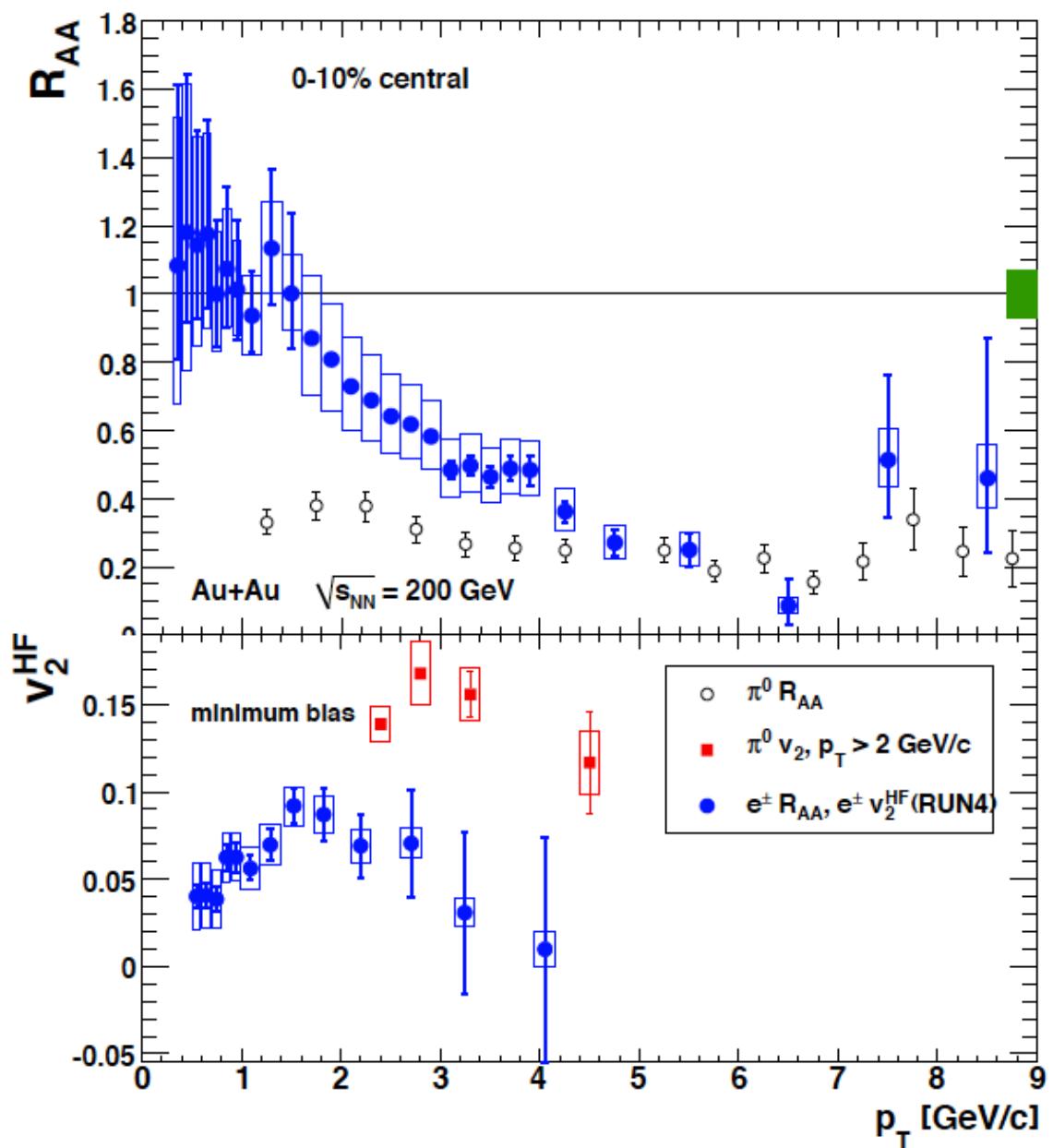
Figure 2.9: R_{AA} and azimuthal anisotropy of the heavy quark electrons.
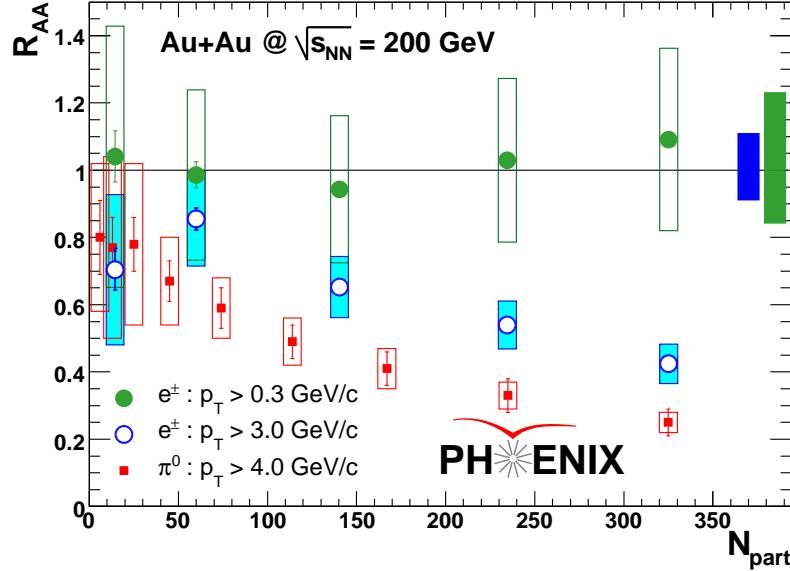
Figure 2.10: R_{AA} of the heavy quark electrons for different p_T ranges as a function of the number of participant nucleons, and that of π^0. The green and blue circles are for the heavy quark electrons with $p_T > 0.3$ GeV/c and with $p_T > 3.0$ GeV/c, respectively. The red points are for π^0 with $p_T > 4.0$ GeV/c.

2.3.3 Theoretical Description

The heavy quarks are only produced in initial parton scatterings due to their large masses, and their initial states can be understood well from the measurements of $p+p$ collisions. The heavy quark is not expected to fully equilibrate with the matter since the energy loss of the heavy quark is smaller than that of light quarks due to dead cone effect [13]. Soft gluon emission in forward direction of a heavy quark is suppressed. The distribution of the gluon radiation at forward direction ($\theta \sim 0$; θ is gluon radiation angle) is given by

$$dP_{HQ} = \frac{\alpha_s C_F}{\pi} \frac{d\omega}{\omega} \frac{\theta^2 d\theta^2}{(\theta^2 + \theta_0^2)^2}, \tag{2.7}$$

where C_F is the Casimir factor composed of color charge (4/3 for quarks), ω is emitted gluon energy, θ_0 is the heavy quark mass (m_{HQ}) divided by its energy (E_{HQ}), m_{HQ}/E_{HQ}. The distribution of a massless parton can be expressed by

$$dP_0 = \frac{\alpha_s C_F}{\pi} \frac{d\omega}{\omega} \frac{d\theta^2}{\theta^2}. \tag{2.8}$$

Therefore, the distribution of a heavy quarks is suppressed from that of a massless parton by a factor

$$dP_{HQ} = dP_0 \cdot \left(1 + \frac{\theta_0^2}{\theta^2}\right)^{-2}. \tag{2.9}$$

21
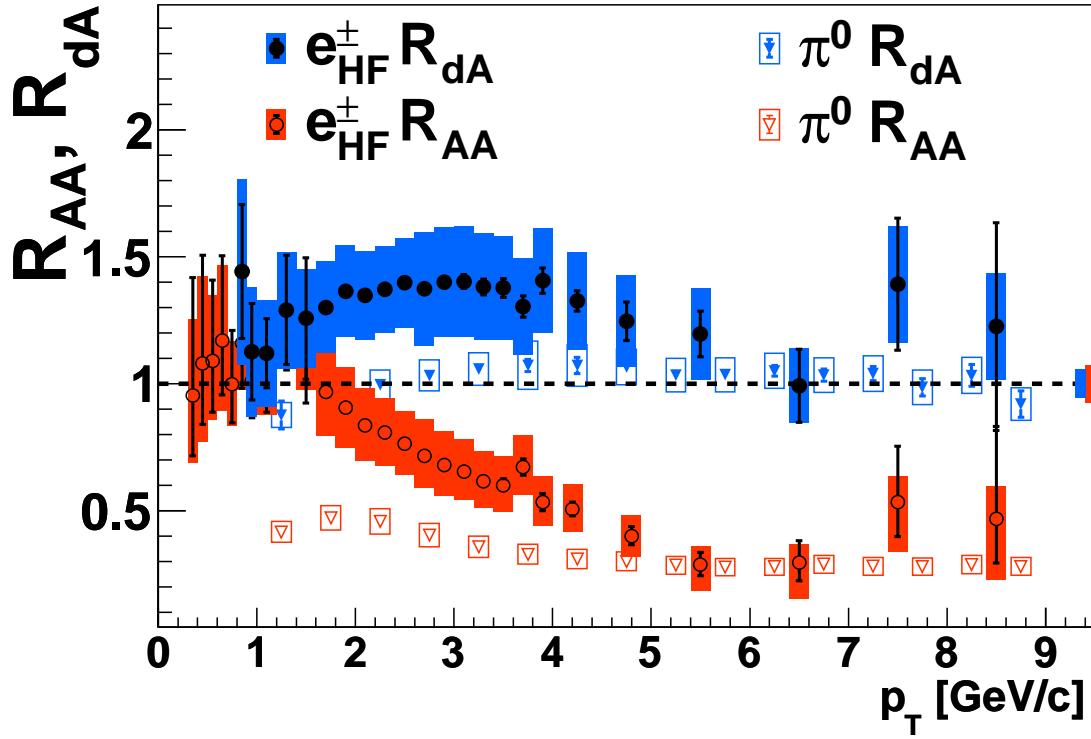
Figure 2.11: Nuclear modification factor of the heavy quark electrons for d+Au (blue) and Au+Au (red) collisions. The circles and the triangles represent those for the heavy quark electrons and π^0, respectively.
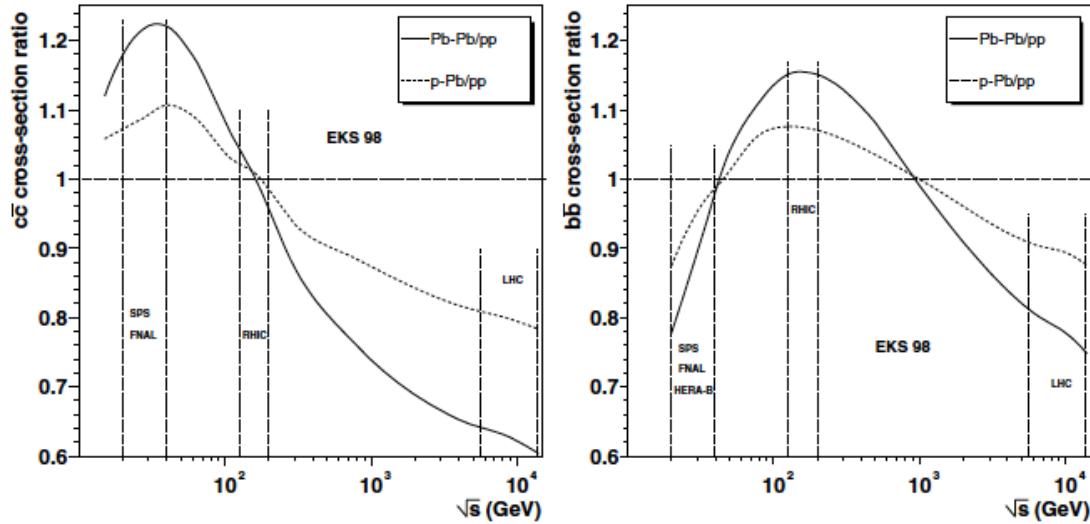
Figure 2.12: Modifications of charm (left) and bottom (right) cross-sections by the nuclear effects of the PDFs calculated using the EKS 98 nuclear weight functions.

Figure 2.13 shows a ratio of gluon emission spectra of charm and light quarks in a hot and dense QCD matter [13]. The solid and dashed lines represent the ratios for quark momenta $p_q = 10$ GeV and $p_q = 100$ GeV, respectively. $x = \omega/p_q$. As is shown in Fig. 2.13, the ratio is small, i.e. gluon emission is largely suppressed, when the emitted gluon energy is small ($x \sim 1$), while the ratio becomes 1 when the emitted gluon energy is extremely high ($x \sim 0$).
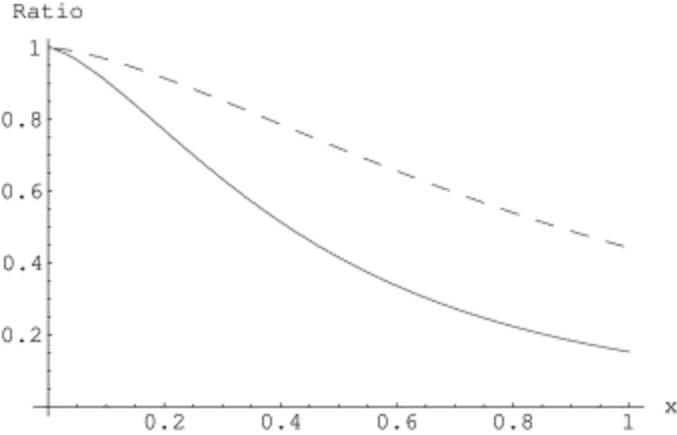
Figure 2.13: A ratio of gluon emission spectra of charm and light quarks [13]. The solid and dashed lines represent the ratios for quark momenta $p_q = 10$ GeV and $p_q = 100$ GeV, respectively. $x = \omega/p_q$, where ω is emitted gluon energy and p_q is a quark momentum.

The thermal relaxation time of the heavy quarks has been argued to be larger than that of light quarks by a factor of m_{HQ}/T due to small energy loss [14], where m_{HQ} is a mass of heavy quarks and T is a typical temperature of the matter. Therefore, the heavy quarks serve as impurities in the thermalizing matter, and a history of interactions between the matter and the heavy quarks can be preserved in their diffusion during passing through the matter. Several studies has been carried out to interpret the large suppression and large azimuthal anisotropy of heavy quarks with Fokker-Plank equation based on Boltzmann transport equation to treat nonequilibrium state. The Boltzmann equation for the phase-space density of heavy quarks ($f(t, \vec{x}, \vec{p})$) is

$$\left(\frac{\partial}{\partial t} + \frac{\vec{p}}{E} \cdot \vec{\nabla}_x + \vec{F} \cdot \vec{\nabla}_p \right) f(t, \vec{x}, \vec{p}) = C[f], \quad (2.10)$$

where $\vec{F}$ is the force on heavy quarks from the surrounding medium. $\vec{p}$ and E denote the momentum and energy of heavy quarks, respectively. $C[f]$ is the collision integral induced by scattering off particles in the surrounding medium. Here, $\vec{F}$ is assumed to be 0, and a uniform medium is assumed, then, the Boltzmann equation is integrated over the spatial coordinates to obtain an equation for the density function of the

heavy quark in momentum space, $f_{HQ}(t, \vec{p})$,

$$f_{HQ}(t, \vec{p}) \equiv \int d^3x f(t, \vec{x}, \vec{p}), \tag{2.11}$$

$$\frac{\partial f_{HQ}(t, \vec{p})}{\partial t} = C[f_{HQ}]. \tag{2.12}$$

$C[f_{HQ}]$ can be written as an integral over all momentum transfers, k,

$$C[f_{HQ}] = \int d^3k \left[w(p+k, k) f_{HQ}(p+k) - w(p, k) f_{HQ}(p) \right], \tag{2.13}$$

where $w(p, k)$ represents a transition rate for the momentum of a heavy quark from p to $p-k$. The two terms in the integral represent the scattering of the heavy quark into ("gain term") and out ("loss term") of the momentum state. Eq. 2.12 still constitutes a differential-integral equation for f_{HQ} which in general is difficult to be solved. Since the heavy-quark mass is much larger than the momentum transfer, which is typically around the temperature of the medium ($k \sim T$), it can be assumed that momentum of heavy quarks is much larger than the momentum transfer. Therefore, the transition rate in Eq. 2.13 can be expanded for small k,

$$w(p+k, k) f(p+k) \sim w(p, k) f(p) + k \cdot \frac{\partial}{\partial p} (w(p, k) f(p)) + \frac{1}{2} k_i k_j \frac{\partial^2}{\partial p_i \partial p_j} (w(p, k) f(p)), \tag{2.14}$$

then, Eq. 2.12 is approximated by the Fokker-Planck equation,

$$\frac{\partial f_{HQ}(t, \vec{p})}{\partial t} = \sum_i \frac{\partial}{\partial p_i} \left[A_i(p) f_{HQ}(t, \vec{p}) + \frac{\partial}{\partial p_j} (B_{ij}(p) f_{HQ}(t, \vec{p})) \right], \tag{2.15}$$

where the transport coefficients, A_i and B_{ij}, are given by

$$A_i(p) = \int d^3k \, w(p, k) k_i, \tag{2.16}$$

$$B_{ij}(p) = \frac{1}{2} \int d^3k \, w(p, k) k_i k_j. \tag{2.17}$$

A_i represents the average momentum change of the heavy quark per unit time and thus describes the friction in the medium. B_{ij} represents the average momentum broadening per unit time, i.e., the diffusion in momentum-space. A microscopic view can provide an input to the calculation of these transport coefficients. For example, elastic $Q + i \rightarrow Q + i$ scattering ($i = q, \bar{q}, g$), the transition rate, w, can be expressed via the quantum mechanical scattering amplitude, M,

$$w(p, k) = \int \frac{d_i d^3q}{16(2\pi)^9 \omega_p \omega_q \omega_{q+k} \omega_{p-k}} f_i(q) \overline{|M_{iQ}|^2} (2\pi)^4 \delta(\omega_p + \omega_q - \omega_{q+k} - \omega_{p-k}), \tag{2.18}$$

24

where d_i denotes the spin-color degeneracy of the parton, $f_i(q)$ is its phase-space density of partons in the medium, p and q ($p - k$ and $q + k$) are the initial (final) momenta of the heavy quark and the parton, respectively. All incoming and outgoing particles are on their mass shell, i.e., $\omega_p = \sqrt{m^2 + p^2}$ with their masses.

Properties of the medium are expected to affect to the diffusion of heavy quarks. For example, the ratio of shear viscosity (η) to entropy density (s) is related to the spatial diffusion of heavy quarks [36, 37]. η/s is an important property to represent a strength of coupling of the medium. It is indicated that the matter created by the heavy-ion collisions has a very small η/s and behaves as a nearly ideal fluid [38]. The relation between η/s and the spatial diffusion of heavy quarks has been discussed in strongly and weakly coupling regimes [36, 37]. In the strong-coupling regime, the relation has been discussed in a framework based on AdS/CFT correspondence. In the framework, η/s is expected to be related to

$$\eta/s \approx \frac{1}{2} D_s T, \qquad (2.19)$$

where D_s represents the spatial diffusion and T represents the temperature of the surrounding medium. In the weak-coupling regime, the relation has been discussed in an ultra-relativistic gas as follows:

$$\eta/s \approx \frac{1}{5} D_s T. \qquad (2.20)$$

The transport coefficients are evaluated by several approaches of interactions between heavy quarks and the medium including perturbative and non-perturbative QCD such as an interaction based on Ads/CFT correspondence, one taking into account resonances of heavy and light quarks, or lattice QCD calculation [39, 40, 41, 42, 43]. Figure 2.15 shows R_{AA} of electrons from heavy-quark decays in Au+Au with $\sqrt{s} = 200$ GeV [18], and theoretical estimations by several models [40, 41, 42]. The black and green points represent R_{AA} of collisions with 0-92% and 10-20% centralities, respectively. The magenta line corresponds to the model based on AdS/CFT correspondence [41]. The blue line corresponds to the model based on pQCD [40]. The red line corresponds to the model based on pQCD including resonance states of heavy and light quarks in scattering amplitude. [40]. The red and blue lines show theoretical predictions for collisions with 0-92% centrality, and the magenta line show that for collisions with 10-20% centrality. The black and green boxes on $R_{AA} = 1$ represents errors of N_{coll} for black (0-92%) and green (10-20%) points, respectively. It is hard to select the interaction models from the results of the heavy-quark electrons. It causes a large uncertainty of the spatial diffusion of heavy quarks, which related to η/s [36, 37, 44]. η/s values as a function of temperature of medium evaluated by several models are shown in Fig. 2.14 [36]. It is expected that the separation of charm and bottom are more informative to select them. Figure 2.16 shows R_{AA}s of electrons from charm and those from bottom for several interaction models. The

magenta line corresponds to the model based on AdS/CFT correspondence [41]. The blue line corresponds to the model based on pQCD [40]. The red line corresponds to the model based on pQCD including resonance states of heavy and light quarks in scattering amplitude. [40]. Solid and dashed lines represent R_{AA}s of electrons from charm and those from bottom, respectively. The red and blue lines show theoretical predictions for collisions with 0-92% centrality, and the magenta line show that for collisions with 10-20% centrality. Differences between each model are more clear than those in the results of electrons from heavy quarks without the separation.
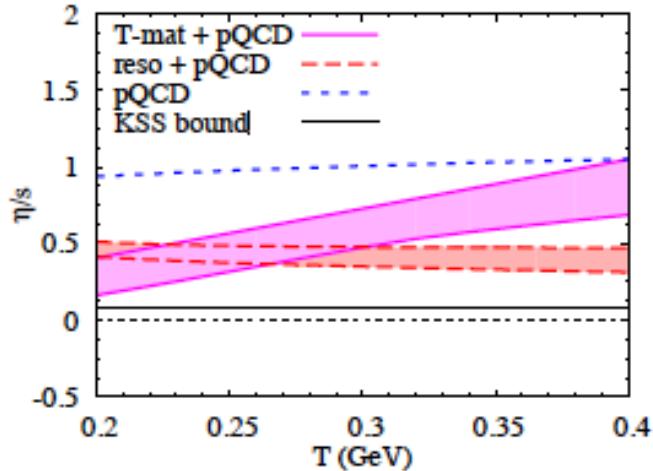
Figure 2.14: η/s values as a function of temperature of medium evaluated by several interaction models [36].

2.4   Separation of Charm and Bottom

2.4.1   Correlation of Decay Products

A fraction of bottom contribution in electrons from heavy-quark decays has been measured only for $p+p$ collisions [15, 16]. They utilized correlations of electrons and hadrons from heavy quark decays to extract charm and bottom signals. Figure 2.17 shows the results of the measurements. The triangles and stars represent the results reported from PHENIX and STAR experiments, respectively. The associated squares and bars represent systematic and statistical errors, respectively. The bottom signal has been successfully extracted in $p+p$ collisions.

   Although this approach is succeeded for $p+p$ collisions, it is hard to accomplish in A+A collisions due to a large combinatorial background due to a large amount of uncorrelated hadrons. The multiplicity of charged particles in $p+p$ collisions with $\sqrt{s} = 200$ GeV, $dN_{ch}^{pp}/d\eta|_{\eta=0} = d(N_{\pi^\pm} + N_{K^\pm} + N_{p^\pm})/d\eta|_{\eta=0} = 2.16 \pm 0.15$ [45],
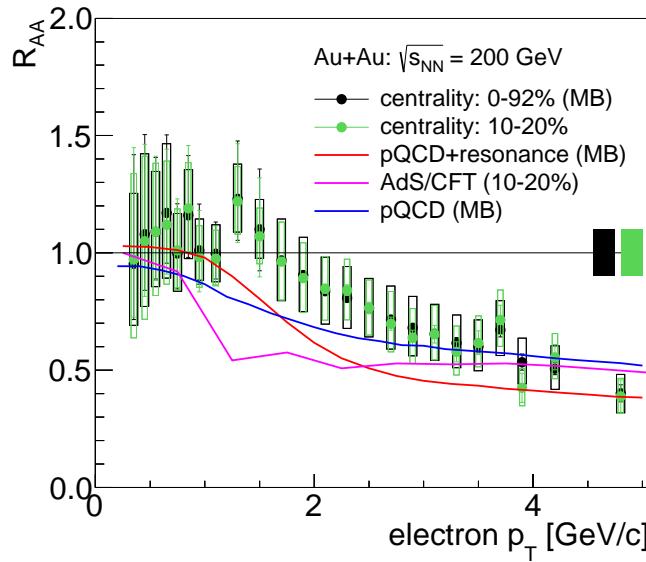
Figure 2.15: R_{AA} of electrons from heavy-quark decays in Au+Au with $\sqrt{s}$ = 200 GeV [18], and theoretical estimations by several models [40, 41, 42]. The black and green points represent R_{AA} of collisions with 0-92% and 10-20% centralities, respectively. The magenta line corresponds to the model based on AdS/CFT correspondence [41]. The blue line corresponds to the model based on pQCD [40]. The red line corresponds to the model based on pQCD including resonance states of heavy and light quarks in scattering amplitude. [40]. The red and blue lines show theoretical predictions for collisions with 0-92% centrality, and the magenta line show that for collisions with 10-20% centrality. The black and green boxes on R_{AA} = 1 represents errors of N_{coll} for black (0-92%) and green (10-20%) points, respectively.

Figure 2.16: R_{AA}s of electrons from charm and those from bottom for several interaction models [40, 41, 42]. The magenta line corresponds to the model based on AdS/CFT correspondence [41]. The blue line corresponds to the model based on pQCD [40]. The red line corresponds to the model based on pQCD including resonance states of heavy and light quarks in scattering amplitude. [40]. Solid and dashed lines represent R_{AA}s of electrons from charm and those from bottom, respectively. The red and blue lines show theoretical predictions for collisions with 0-92% centrality, and the magenta line show that for collisions with 10-20% centrality.

whereas, that in Au+Au collisions with $\sqrt{s_{NN}} = 200$ GeV, $dN_{ch}^{AA}/d\eta|_{\eta=0} = 242 \pm 14$ (687 $\pm$ 37) for centrality of 0-70% (0-5%) [46]. Therefore, the S/N ratio in Au+Au collisions is $\sim 1/100$ smaller than that in $p+p$ collisions due to increase of a combinatorial background, and thus, statistical errors in Au+Au collisions increase to 10 times larger than those in $p+p$ collisions. An alternative method is necessary to extract bottom signal in A+A collisions. The approach described in this thesis does not utilize a correlation, and is free from the combinatorial background. Therefore the approach is promising.
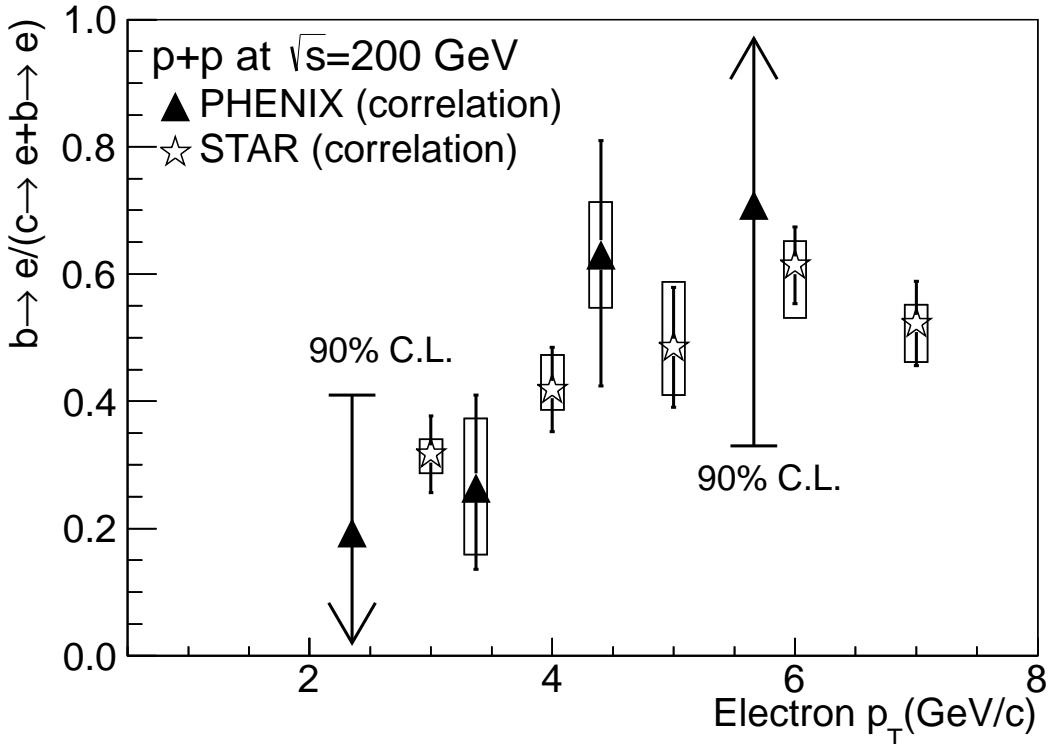
Figure 2.17: The fraction of the bottom contribution in the heavy quark electrons as a function of p_T. The triangles and stars represent the results reported from PHENIX and STAR experiments, respectively. The associated squares and bars represent systematic and statistical errors, respectively.

2.4.2 DCA Approach

Charm and bottom contributions in the electrons from heavy-quark decays are evaluated by using DCA distributions in this thesis. The DCA depends on the life-times of the heavy-quark hadrons and q-values of their decay modes. Since life-times and q-values of charm hadrons and bottom hadrons are largely different, widths of their DCA distributions are also different, and thus, contributions of the charm and bottom electrons in the measured DCA distribution can be evaluated. Figure 2.18 shows

RMS values of DCA distributions of electrons from charm and bottom decays as a function of electron p_T. The RMS values are calculated with a PYTHIA simulation. Details of simulation tuning is described in Sec. 4.7.2. The black and red points represent RMS values for charm and bottom decays, respectively.
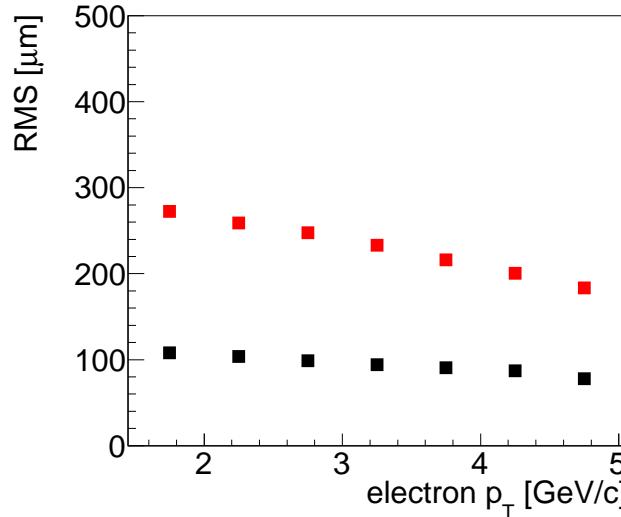
Figure 2.18: RMS values of DCA distributions of electrons from charm and bottom decays as a function of electron p_T. The black and red points represent RMS values for charm and bottom decays, respectively.

A large difference of the DCA distributions of the electrons from charm and bottom is mainly derived from the difference of their life-times. The heavy-quark hadrons are decayed by the weak interaction. Most of the difference of the life-times is due to elements of the CKM matrix. The life-times and q-values for the decay modes with electron in their decay products are summarized in Table 2.1 and 2.2. Figure 2.19 shows examples of D meson and B meson decay diagrams accompanying an electron. The decay width (Γ^{HQ}) can be written as

$$\Gamma^{HQ} = \frac{m_{HQ}}{4 \cdot (4\pi)^3} \int dx dy \theta(x + y - x_m)\theta(x_m - x - y + xy) \sum |M^{HQ}|^2, \qquad (2.21)$$

where, $x = 2E_e/m_{HQ}$ and $y = 2E_\nu/m_{HQ}$ are the rescaled energies of electron and neutrino in the heavy quark rest frame. $x_m = 1 - (m_q/m_{HQ})^2$ is kinematic limit to the energy transfer. As is shown in Eq. 2.6, the decay matrix elements are proportional to elements of the CKM matrix, and the corresponding elements for the charm and bottom decays are $|V_{cs}| = 0.97344 \pm 0.00016$ and $|V_{cb}| = 0.0412^{+0.0011}_{-0.0005}$, respectively [47].

Table 2.2: Life-times of charm and bottom hadrons.

Hadron	$c\tau$
$D^{\pm}$	311.8 μm
D^0	122.9 μm
D_s	149.9 μm
Λ_c	59.9 μm
$B^{\pm}$	491.1 μm
B^0	457.2 μm
B_s	441 μm
Λ_b	417 μm
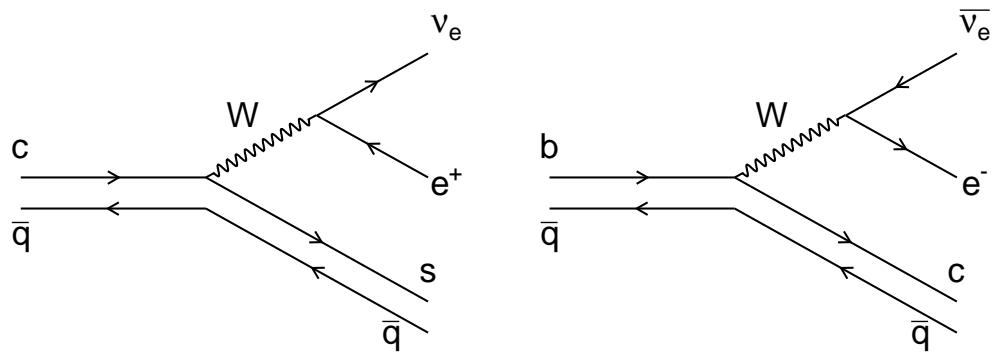
Figure 2.19: Examples of D meson (left) and B meson (right) decays.

Chapter 3

Experimental Setup

The experiment of $p+p$ collisions with $\sqrt{s}$ = 200 GeV has been performed by using RHIC and PHENIX detector, especially two central arm spectrometers. RHIC is a collider for $p+p$, $d+$A, and A+A collisions. Each of the spectrometers covers $|\eta| < 0.35$ in pseudo-rapidity and $\Delta\phi < \pi/2$ in azimuth in a nearly back-to-back configuration. In this chapter, the accelerator complex including RHIC and the details for the PHENIX detector are described.

In Sec. 3.1, the accelerator complex for $p+p$ collisions is described. In Sec. 3.2, an overview of PHENIX detector and the detectors used in this thesis are described. Details and usages in this thesis of the detectors are summarized in the beginning of Sec. 3.2. In Sec. 3.3, data acquisition system and triggers used for data collection are described.

3.1 Relativistic Heavy Ion Collider (RHIC)

Proton beams are accelerated and collided by the Relativistic Heavy Ion Collider (RHIC) at Brookhaven National Laboratory (BNL), which has been operated since 2000 [48]. Figure 3.1 shows the layout of the accelerator complex at BNL, which consists of the Tandem Van de Graaff accelerator, the proton linac, the booster synchrotron, the Alternating Gradient Synchrotron (AGS) and RHIC. The circumference of RHIC is 3834 m. RHIC can accelerate protons, deuterons, and several species of heavy ions (Cu, Au, U) at the maximum center-of-mass energy of 510 GeV in $p+p$ collisions and 200 GeV per nucleon in heavy ion collisions.

The proton beam is supplied by Linear Accelerator (LINAC) facility, which consists of Optically Pumped Polarized HIon Sources (OPPIS), a radiofrequency quadrupole (RFQ) pre-injector, and nine radio-frequency cavities. The LINAC can provide polarized or un-polarized proton beams. The LINAC is capable to produce up to 35 mA proton beam at the energy of 200 MeV. The beam intensity is 15×10^{11} proton/pulse at the ion source and 6×10^{11} at the end of LINAC. The beam is injected into the Booster Accelerator for further acceleration. The Booster Accelerator facility accepts
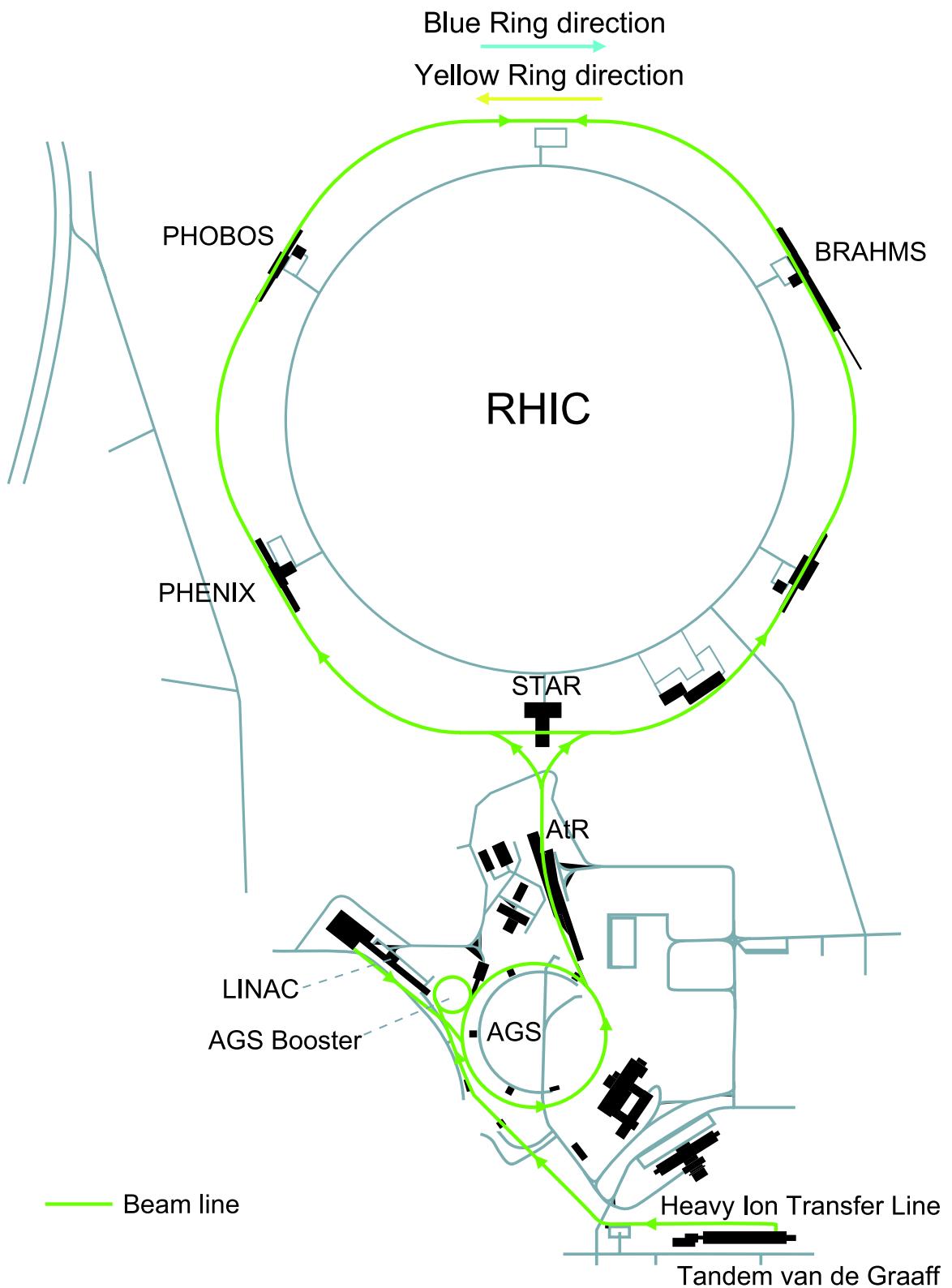
Figure 3.1: The accelerator complex including RHIC at BNL.

the beam from LINAC. It is utilized as a pre-accelerator, and the beam is acceler-
ated up to 1.5 GeV. The machine circumference is 200 m. The Alternating Gradient
Synchrotron (AGS) accepts the beam from Booster and is served as an injector for
the RHIC. The AGS has the circumference of 800 m. The AGS employs the concept
of the alternating gradient focusing, in which the field gradients of the accelerators
240 magnets are successively alternated inward and outward, permitting particles to
be propelled and focused in both the horizontal and vertical planes at the same time.
The beam is accelerated up to 24.3 GeV, and delivered to RHIC via AGS to RHIC
Line (ATRL). There are two rings in RHIC called Blue Ring (circulating clockwise)
and Yellow Ring (circulating counter-clockwise). Each of them has circumference of
3.83 km. The rings are kept to be the vacuum of 5×10^{-11} Torr. Each ring has 192
superconducting dipole magnets with the magnet field of 3.46 T. 12 common dipole
magnets, 492 quadrupole magnets, and 852 trim or corrector magnets are used. The
RHIC accepts heavy ion or proton beams from AGS and stores them. The designed
maximum luminosity is 2×10^{26} cm^{-2}sec^{-1} for Au beam and 2×10^{32}cm^{-2}sec^{-1} for
proton beam. Each bunch has the length of 5 ns and bunch-crossing rate is 9.4 MHz.
The major parameters achieved in $p+p$ collisions with $\sqrt{s}$ = 200 GeV at Year-2012
Run (Run12) are summarized in Table 3.1 [1]. The RHIC collides two beams head-on
using DX dipole magnet at six interaction regions. Four of the interaction regions are
equipped with the experiments, PHENIX, STAR, BRAHMS, and PHOBOS.

Table 3.1: Summary of the major design parameters of $p+p$ with $\sqrt{s}$=200 GeV collisions
at Year-2012 Run [1].

parameters	value
Bam energy	100 GeV
Luminosity (peak) [cm^{-2}sec^{-1}]	4.6×10^{31}
Luminosity (average) [cm^{-2}sec^{-1}]	3.3×10^{31}
Integrated luminosity (delivered to PHENIX) [pb^{-1}]	37.9
Number of bunches	109
Number of particles/bunch	1.6×10^{11}
Emittance (RMS) (μm)	$3.3 \rightarrow 4.2$
β^* (m)	0.85
Beam spot size (μm)	$115 \rightarrow 129$

3.2 PHENIX Detector Complex

In this section, the detector used in this thesis are described. As is written in Sec. 1.4,
charms and bottoms are measured with decay electrons and the ratio of electrons from
charm and bottom decays is measured from the DCA approach. In order to achieve
the measurement, electron identification and precise tracking around beam collision

point are necessary.

A ring imaging Cherenkov detector (RICH) [49], electromagnetic calorimeter (EM-Cal) [50], drift chamber (DC), and pad chambers (PC1, 2, 3) [51] are used for electron identification. Cherenkov photons are measured with RICH, and almost all hadrons can be rejected by requiring an emission of Cherenkov photons up to $p < 4.9$ GeV/c. In addition, requirements related to the ratio of deposited energy at EMCal and momentum measured by DC and PC, and shower shape in EMCal are used for the electron identification. Details of the electron identification is described in Sec. 4.3.

As is described in Sec. 1.3, a precise tracking around beam collision point for the measurement of the DCA is performed by using hits on VTX and reconstructed momentum by the central arms. The momentum is measured by DC and PC. VTX is also used to measure the beam collision point.

Beam-beam counters (BBCs), which are located at pseudo-rapidity $3.1 < |\eta| < 3.9$, measure the position of the collision vertex along the beam axis (z_{vertex}) at each collision and provide an event trigger, as is described in Sec. 3.3. RICH and EMCal are also used to provide a trigger for collecting data to enhance electron sample, as is described in Sec. 3.3.

The above detectors are briefly reviewed in following sections. The central arm contains other detectors such as the time of flight detector or the aerogel Cherenkov counter for hadron identification. They are not described in this section since they are not used in this analysis.

3.2.1 Detector Overview

Global Coordinate System

Figure 3.2 illustrates the definition of the PHENIX global coordinate system. The origin of the global coordinate system is set at the center of the interaction point along the center of the cylindrical beam pipe. The z-axis is defined as an axis along the center of the beam pipe and north is defined as the positive direction. The y-axis is the altitude relative to the origin, and the x-axis is defined to form a right handed coordinate system. The azimuthal angle ϕ is a counterclockwise angle with respect to the positive x direction and the polar angle θ is defined as an angle with respect to the positive z direction. The r direction is defined in the x-y plane as a distance from the beam axis. The pseudo-rapidity η is written as:

$$\eta = -\ln \tan\left(\frac{\theta}{2}\right). \tag{3.1}$$

Detector Overview

Figure 3.3 shows the layout of the PHENIX detector configuration in Run12. Both beam (top panel) and side (bottom panel) views are shown. The PHENIX detector
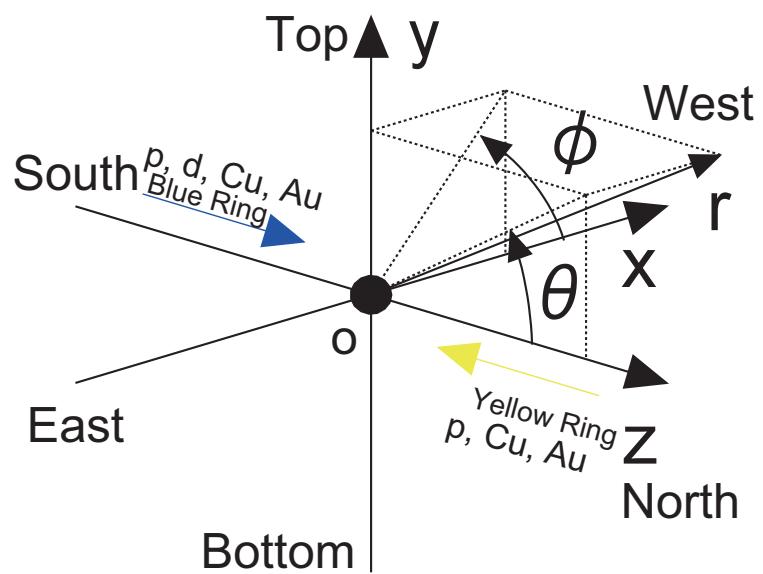
Figure 3.2: Definition of the global coordinate system used in the PHENIX experiment.

mainly consists of global detectors, central arms (East and West) and muon arms (North and South). The acceptance coverage and the feature of each detector is summarized briefly in Table 3.2. The beam pipe is made of Be, whose radius and

Table 3.2: Summary of the PHENIX detector complex.

Subsystems	$\Delta\eta$	$\Delta\phi$	Information
Central Magnet (CM)	±0.5	$360°$	Up to 1.15 T·m
Muon Magnet (MM)	$\pm1.1\text{-}2.5$	$360°$	0.72 T·m (for $\eta = \pm2$)
BBC	$\pm3.0\text{-}3.9$	$360°$	Event trigger, Collision vertex
VTX	±1.2	$140°\times2$	Tracking around collision vertex
Drift Chamber (DC)	±0.35	$90° \times 2$	$\Delta p/p = 1.0\%$ at $p = 1$ GeV/c
Pad Chamber (PC)	±0.35	$90° \times 2$	Tracking for non-bend direction
RICH	±0.35	$90° \times 2$	Electron identification
EMCal (PbSc)	±0.35	$90° \times 1.5$	4 sectors in West and 2 sectors in East
EMCal (PbGl)	±0.35	$45°$	2 sectors only in East
Muon Tracker	$\pm1.2\text{-}2.4$	$360°$	Tracking for muons
Muon identifier	$\pm1.2\text{-}2.4$	$360°$	Concrete absorbers plus chambers

thickness are 20 mm and 500 μm (which corresponds to 0.14% of radiation length), respectively.

3.2.2 Magnet

The three magnets, Central Magnet (CM), North Muon Magnet (MMN) and South Muon Magnet (MMS) [52] form the PHENIX magnet system. The magnetic field produced by the magnets is shown in Fig. 3.4. The PHENIX Central Magnet (CM) realizes an axial field positioned at $z = \pm0.45$ m covering the pseudo-rapidity range of $|\eta| < 0.35$. The momenta of charged particles are determined using the magnetic bending by the CM. The CM is energized by two, inner and outer, concentric coils, which can be operated separately. In Run12, the same polarity operation (++ configuration) was selected. Figure 3.5 shows the field strength created by the CM as a function of the distance from the beam axis. The squares correspond to the field configuration of Run12. The field strength is 0.9 T around the beam axis (X = 0), then it decreases and then residucal field at the DC is small.

3.2.3 Beam-Beam Counter

The Beam-Beam Counter (BBC) is designed to measure a charged particle multiplicity, a timing of the collision, and z coordinate of the collision vertex. The BBC is also utilized as the trigger for beam collision events. The BBC consists of two
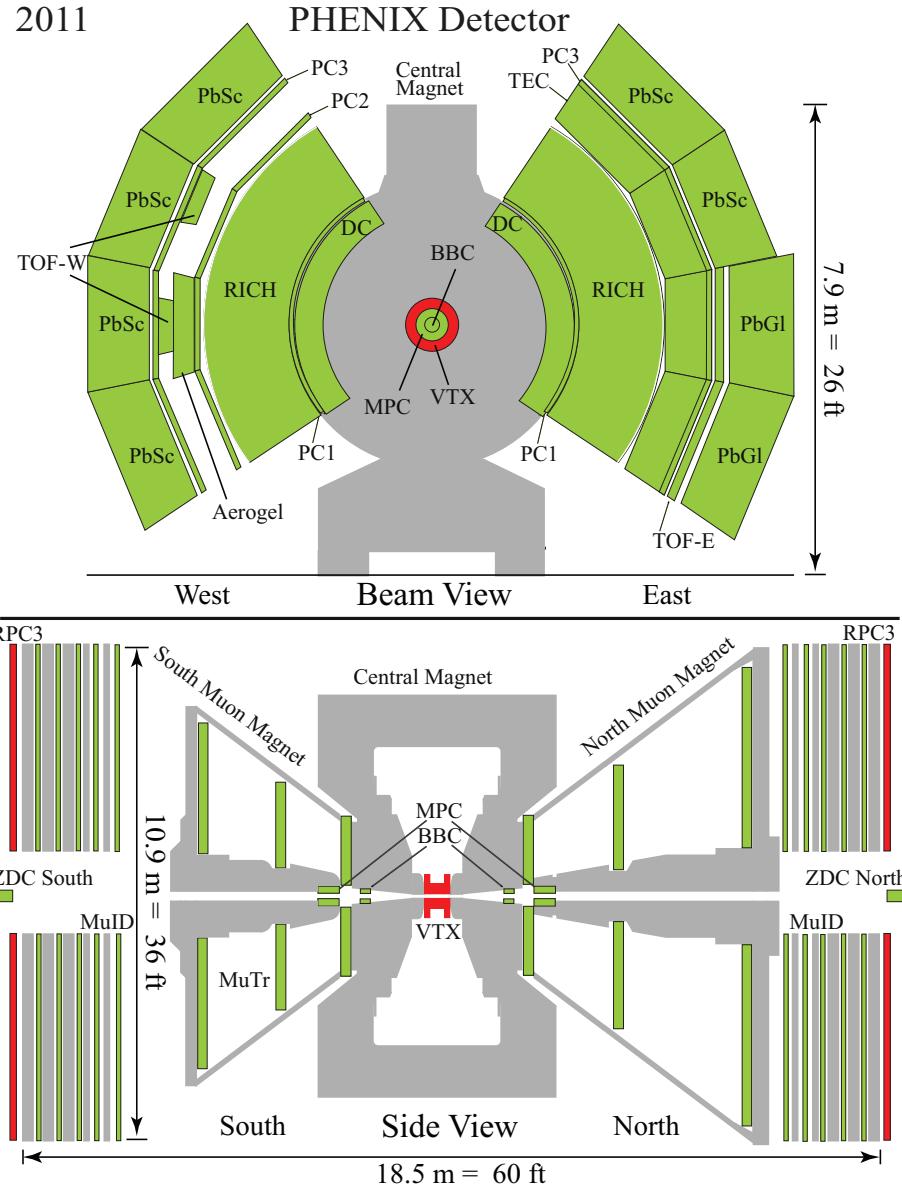
Figure 3.3: Layout of the PHENIX detector configuration in the Run12. Beam view (top panel): Inner detectors, two Central Arms and Central Magnet are shown. Side view (bottom panel): Inner detectors, two Muon Arms, Central Magnet and Muon Magnets are shown.
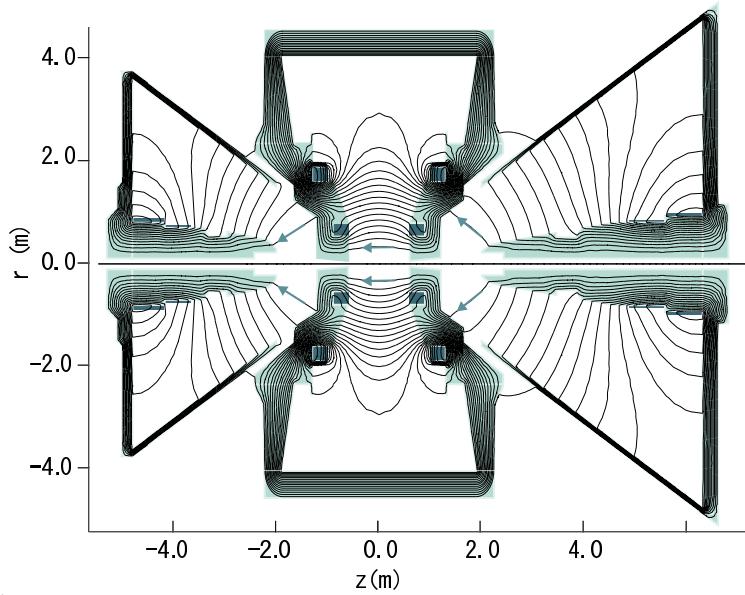
Figure 3.4: The field lines of th central magnet and muon magnets shown ona vertical cutaway drawing of the PHENIX magnets. The beams travel along the $r = 0$-axis in this figure and collide at $r = z = 0$. Arrows indicate the field direction.
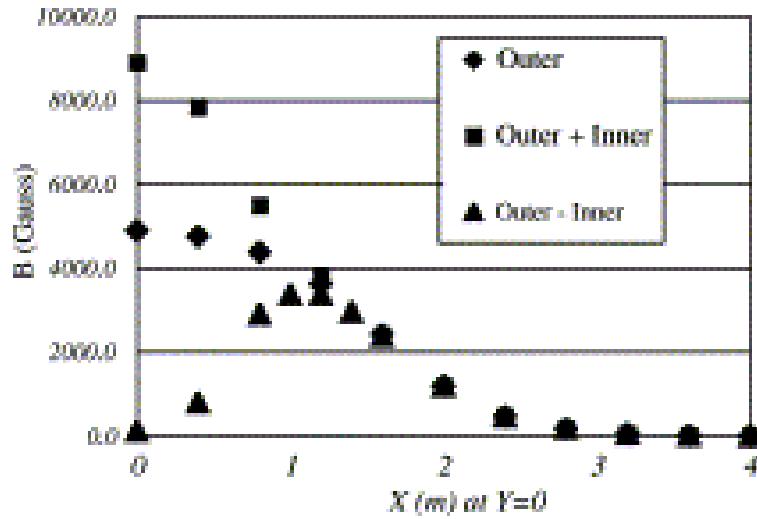
Figure 3.5: The field strength created by the CM with $++$ (squares) and $+-$ (triangles) field configuration as a function of the distance from the beam axis.

arrays of Cherenkov counters which are located at 144 cm away from the interaction point in the north and south side separately, and its pseudo-rapidity coverage is $3.0 < |\eta| < 3.9$. Each array also consists of 64 modules of 1-inch diameter mesh-dynode phototubes (Hamamatsu R6178) equipped with 30 mm-quartz Cherenkov radiators on their heads. Pictures in Fig. 3.6 show (a) a single BBC module, (b) a BBC array comprising 64 single modules and (c) the BBC mounted on the PHENIX detector.
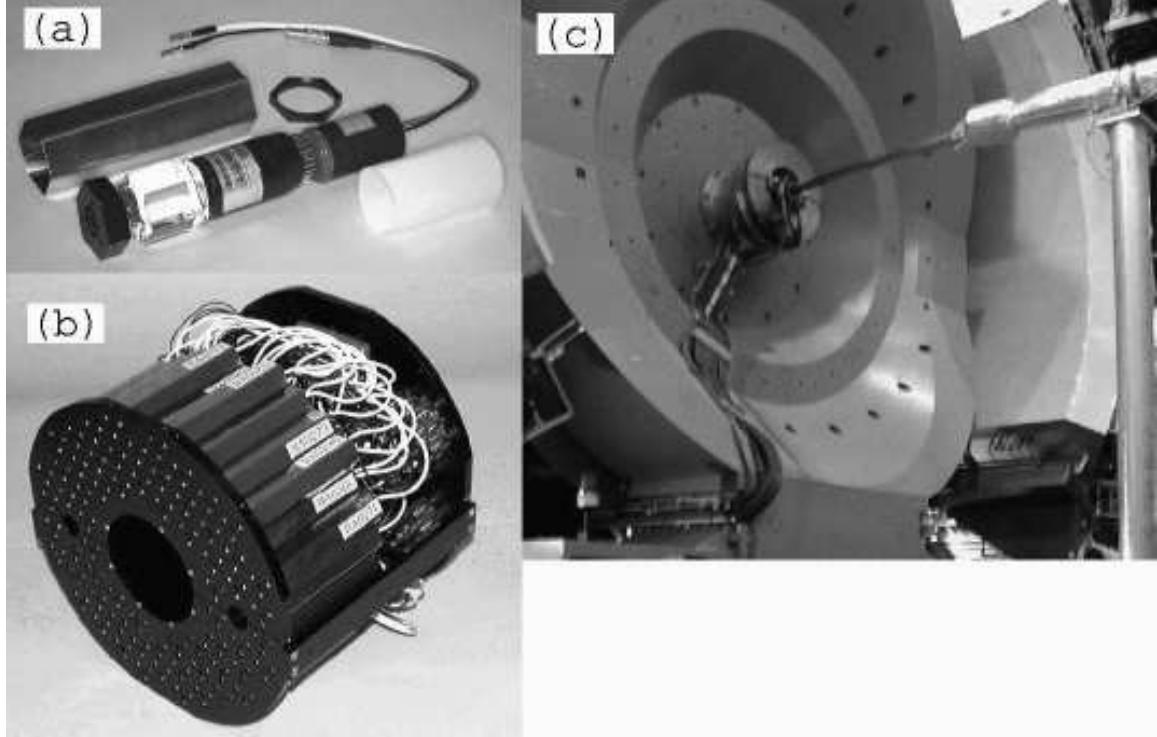
Figure 3.6: Pictures of the BBC. (a) A single BBC module consisting of a 1-inch diameter mesh-dynode phototube equipped with a 30 mm-quartz Cherenkov radiator. (b) A BBC array comprising 64 single modules. (c) The BBC mounted on the PHENIX detector.

The collision time (T_0) and the collision vertex (z_{vertex}) are calculated using the average of the arrival times (T_s for the south array and T_n for the north array) of the fast leading charged particles from a beam collision into the BBC arrays as follows:

$$T_0 = \frac{T_n + T_s}{2} - \frac{|z_{BBC}|}{c} + t_{\text{offset}}, \tag{3.2}$$

$$z_{vertex} = \frac{c \cdot (T_1 - T_2)}{2} + z_{\text{offset}}, \tag{3.3}$$

where z_{BBC} is the BBC located position at 144 cm from the interaction point and $t_{\text{offset}}, z_{\text{offset}}$ are the time and z-position offsets intrinsically introduced by devices. The z-vertex resolution is ~ 2.0 cm in $p+p$ collisions.

3.2.4 Drift Chamber

The drift chamber (DC) is utilized to measure charged particle trajectories in the r-ϕ plane and to determine their momenta with a good resolution. The DC system consists of two independent gas volumes located in the west and east arms. The gas volumes are filled with a gas mixture of 50% argon and 50% ethane. The DC locates at $r = 2.02 \sim 2.46$ m in each of the arms and covers ± 90 cm along the z direction as an active area. Each DC is located in a high residual magnetic field region up to 0.06 T at maximum. The DC is constructed with a cylindrical titanium frame as shown in Fig. 3.7. The frame is divided in 20 sectors which covers 4.5° in ϕ. In each sector, six types of wire modules: X1, U1, V1, X2, U2, V2 are stacked radially as shown in Fig. 3.8. Each wire module contains twenty sensing (anode) planes (twelve X, four U and four V wire planes) and four cathode planes forming cells with a 20-25 mm drift space in the ϕ direction. The sensing (S) wires are separated by potential (P) wires, and surrounded by gate (G) and back (B) wires. The G wires limit the track sample length to roughly 3 mm and terminated unwanted drift lines. They minimize the time speed of drifting electrons from a single track and thereby decreases the pulse width. The B wires have a rather low potential and terminate most of the drift lines from their side. They eliminate left-right ambiguity and decrease the signal rate per electronics channel by a factor of two.

The X1 and X2 wire cells run in parallel to the beam axis to precisely measure tracks in the r-ϕ plane. The U and V wire cells, which are used for pattern recognition, are located behind the X wire cell. The U and V wires have stereo angles of about 6° relative to the X wires and measure the z coordinate of the track. The stereo angle is set to minimize track ambiguities by matching the z coordinate of the pad chamber. Each sensing wire is separated into two halves at the center to satisfy the requirement of efficient track recognition for up to 500 tracks in the whole PHENIX fiducial volume, and signals are independently extracted.

With the 50%-Argon and 50%-Ethane gas mixture, the stable drift velocity plateau at 53 mm/μs is achieved for the field gradation from 800 V·cm to 1.4 kV·cm. The maximum drift time in a cell is approximately 470 ns.

3.2.5 Pad Chamber

The pad chamber (PC) is used to determine three dimensional spatial positions. The spatial position information from the PC is important for momentum determination in the z-direction (p_z). The PC is a multi-wire proportional chamber with a cathode readout and forms three separate layers (PC1, PC2, PC3) as shown in Fig. 3.9. The PC1 is the innermost chamber locating at $r = 2.47 \sim 2.52$ m in radial distance from the interaction point, *i.e.* the region between DC and the ring imaging Cherenkov detector (RICH) in both east and west arms. The PC2 layer exists only in the west arm and is placed behind the RICH at $r = 4.15 \sim 4.21$ m. The PC3 is located in front of the electromagnetic calorimeter (EMCal) and occupies the region between
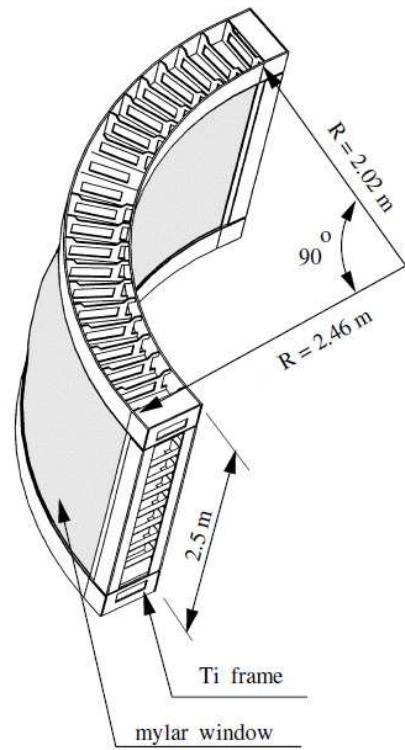
Figure 3.7: A frame of the drift chamber.
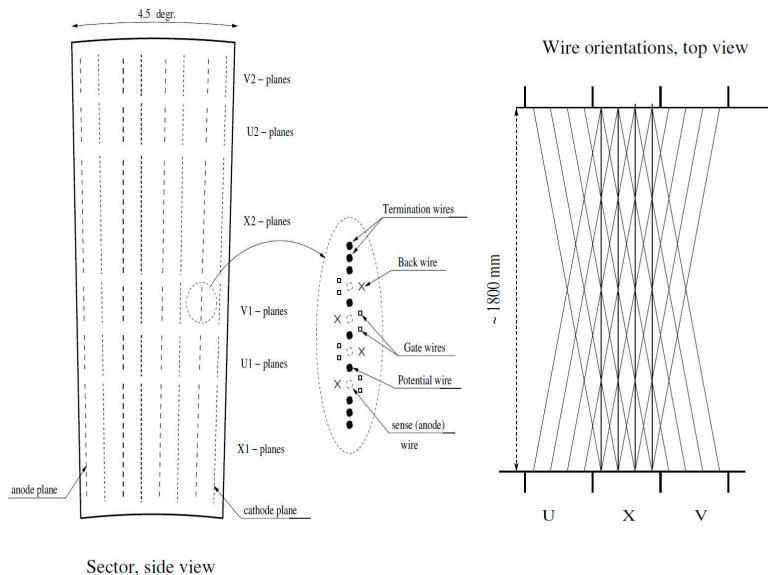
Figure 3.8: The layout of wire positions in a sector. (Left) Side view of the wire position layout together with an enlarged view inside the anode plane. (Right) Top view of the stereo wire orientation.

43

$r = 4.91 \sim 4.98$ m. The PC1 is essential for determination of the three dimensional momentum by providing the z coordinate at the exit of the DC. The information from the DC and PC gives the straight line particle trajectories outside the magnetic field. The PC2 and PC3 are needed to resolve ambiguities in outer detectors where about 30% of particles striking the EMCal are produced by either secondary interaction or decays outside the aperture of the DC and PC1.
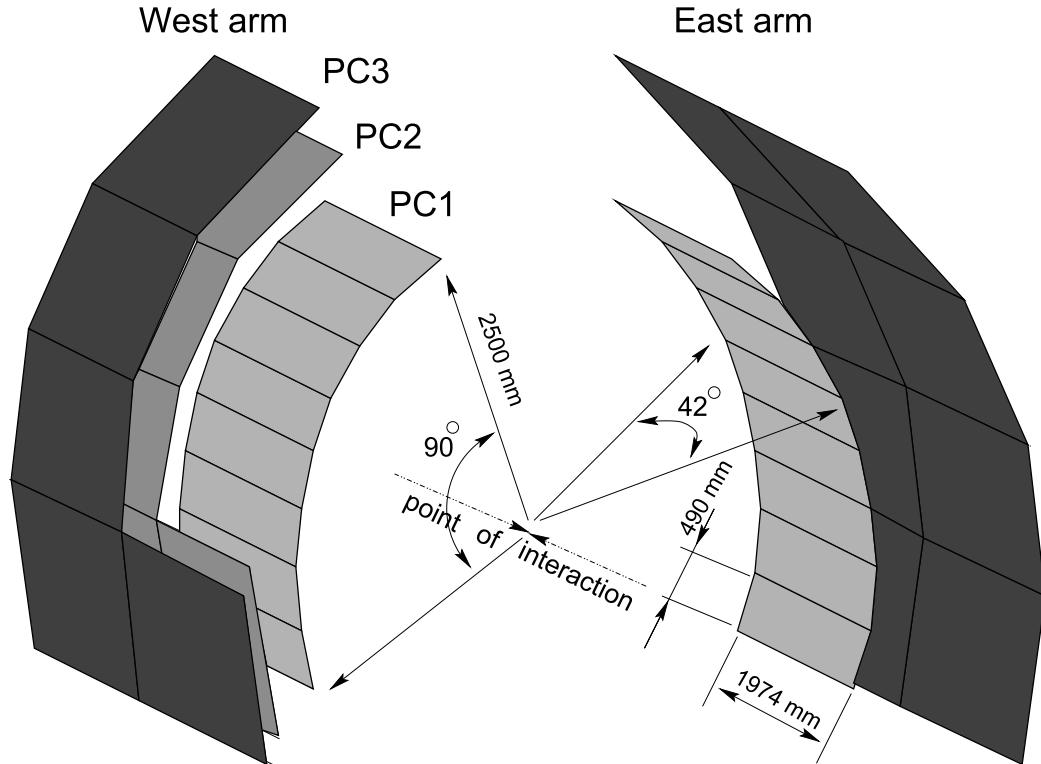
Figure 3.9: A schematic view of the PCs (PC1, PC2, PC3). Some sectors of PC2 and PC3 in the west arm are removed for clarity of the picture.

Each detector consists of a cathode panel and a signal plane of anode and field wires. One cathode is finely segmented into an array of pixels as shown in Fig. 3.10. A gas mixture of 50% argon and 50% ethene is filled in the PC at atmospheric pressure. The performance of the PCs are summarized in Table 3.3.

Table 3.3: Performance of pad chambers in Year-2002 and a cosmic ray test.

	PC1	PC2	PC3
Pad size ($\phi \times z$ mm^2)	8.4×8.4	13.6×14.4	16.0×16.7
Single hit resolution in z (mm)	1.7	3.1	3.6
Efficiency	≥99%	≥99%	≥99%

44
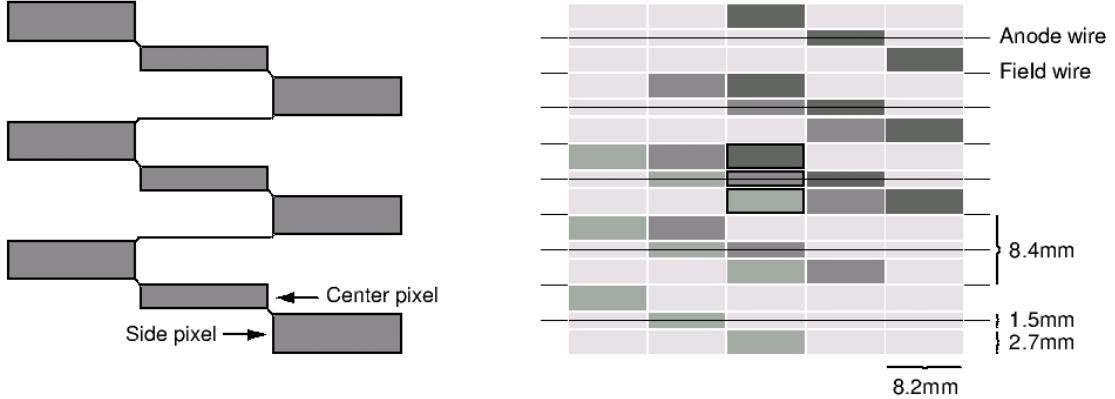
Figure 3.10: The pad and pixel geometry of the PC. A cell defined by three pixels is indicated at the center of the right figure.

3.2.6 Ring Imaging Cherenkov Detector

The ring imaging Cherenkov detector (RICH) [49] is the primary device to identify electrons. RICH is placed in both of the arms ar $r = 2.5 \sim 4.1$ m, covering $70° \leq \theta \leq 110°$ and $90°$ per arm in the azimuth. Figure 3.11 shows a cross-sectional view of RICH. RICH has a 40 m^3-volume aluminium vessel with an entrance window of 8.9 m^2, and an exit window of 21.6 m^2, which are made of 125 μm-thick aluminized Kapton foils in each arm. In the gas vessel, two arrays of 24 aluminium-evaporated mirror panels are mounted on the graphite-epoxy mirror support, and they are located symmetrically with respect to $z = 0$. The mirror panel substrates have a ~ 4.01 m-radius curvature. The Cherenkov light emitted from a charged particle is reflected by the spherical mirrors, and the reflected light is focused on two arrays of 1280 Hamamatsu H3171S UV phototubes with a cathode diameter of 25 mm. Each phototube array is located on either side of the RICH entrance window. The phototubes are fitted with 2 inch diameter Winston cones and have magnetic shields which allow to operate at up to the magnetic field of 0.01 T. Their UV glass windows absorb photons with a wavelength of below 200 nm. The phototube has a bi-alkaline photocathode and a linear focus 10 stage dynode. The maximum quantum efficiency is 27% ($> 19\%$ at $\lambda = 300$ nm and $> 5\%$ at $\lambda = 200$ nm). The typical dark current is 10 nA and the typical operation is 1.5 kV with a gain of 10^7.

Figure 3.12 shows a schematic view of RICH cut along the beam axis. The gas vessel is filled with CO_2 used as a radiator. Charged particles emit Cherenkov photons when they move faster than the speed of light over the refractive index of CO_2, 1.000410 at 20 °C and 1 atm [47]. A charged particle with $\beta\gamma > 35$ emits Cherenkov photons. The corresponding momentum thresholds for electrons and pions are 18 MeV/c and 4.9 GeV/c, respectively. The emitted photons are reflected and focused by the spherical mirror on the phototube array plane.
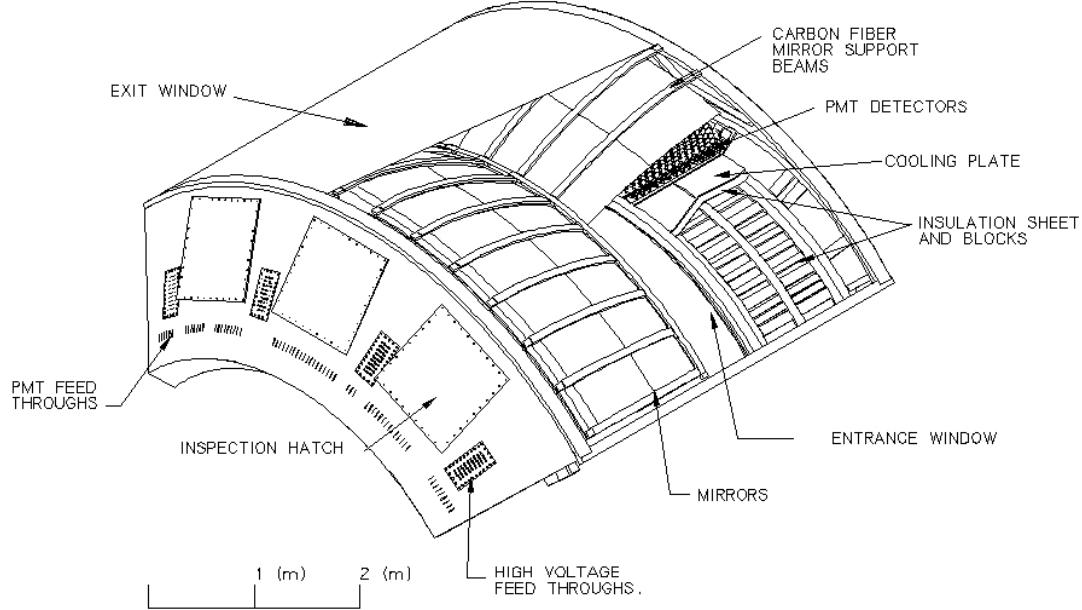
Figure 3.11: A cutaway view of RICH.

The RICH Front-End Electronics (FEE) processes the phototube signals at each bunch crossing (9.4 MHz) and transmits digitized data to the PHENIX data acquisition system on the trigger signal supplied by the PHENIX global trigger system (~ 25 kHz) [53]. The acceptable charge range is from 0 to 10 photoelectrons, which corresponds to the input charge from 0 to 160 pC preceded by the preamplifier. The charge resolution is $\sim 1/10$ photoelectron and the timing resolution is ~ 240 ps. Both of the charge and timing outputs are stored in Analog Memory Unit (AMU) clocked at the RHIC bunch crossing frequency. The analog data stored in the AMU are digitized only after the receipt of an acceptance from the PHENIX global trigger system.

3.2.7 Electromagnetic Calorimeter

The electromagnetic calorimeter (EMCal) is used to measure the energy and spatial position of electrons and photons produced in beam collisions. It covers the full central spectrometer acceptance of $70° \leq \theta \leq 110°$ and $90°$ in the azimuth. The EMCal in the west arm has four sectors of a lead scintillator sampling calorimeter (PbSc) and the one in the east arm has two sectors of a PbSc and two sectors of a lead glass Cherenkov calorimeter (PbGl). The pseudo-rapidity coverage is $|\eta| < 0.35$ for both PbSc and PbGl. The azimuthal coverage is $6 \times \pi/4$ for PbSc and $2 \times \pi/4$ for PbGl. The basic parameters of the EMCal are summarized in Table 3.4.

46
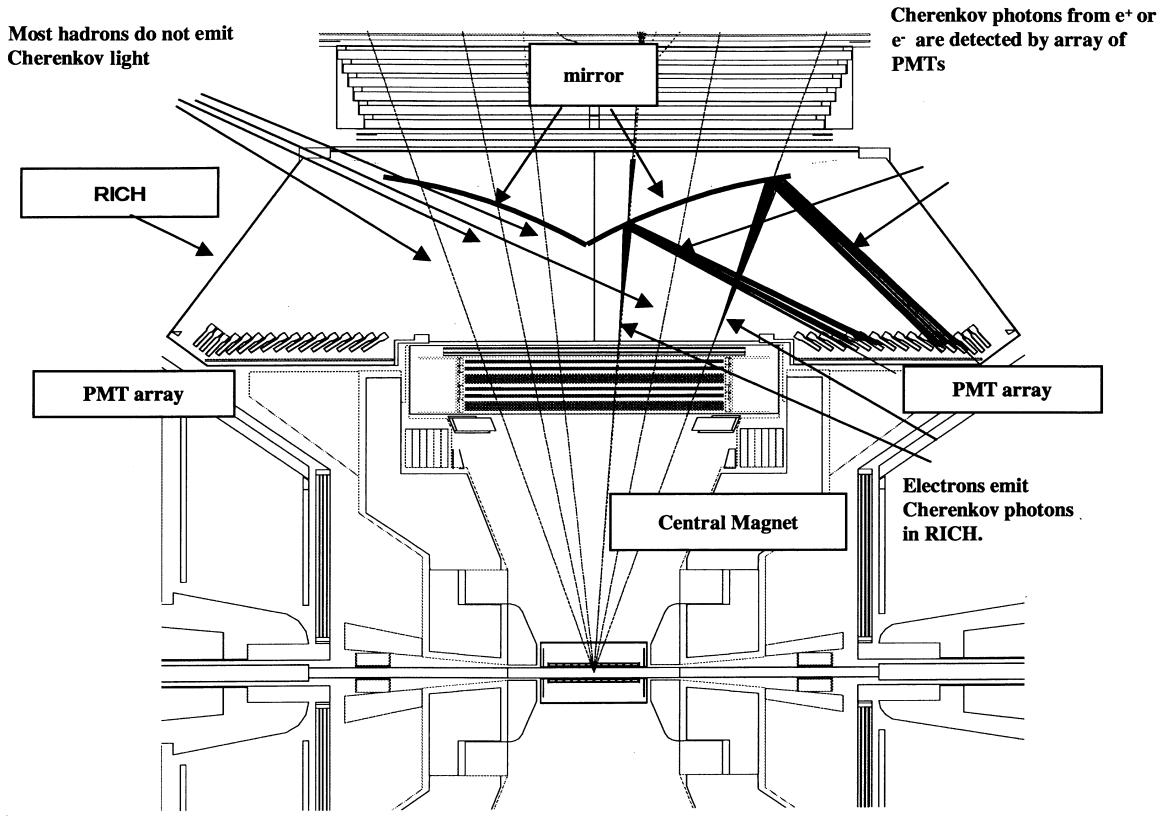
Figure 3.12: A schematic view of RICH cut along the beam axis.

Table 3.4: Summary of the basic parameters of the EMCal

	PbSc	PbGl
Type	Scintilator + Lead	Cherencov
Radiation length (X_0)	21 mm	29 mm
Interaction length	441 mm	380 mm
Moliere radius	30 mm	37 mm
Depth	375 mm (18 X_0)	400 mm (14 X_0)
Cross section of a channel	55.35×55.35 mm^2	40×40 mm^2
$\Delta\eta$ of a channel	11 mrad	8 mrad
$\Delta\phi$ of a channel	11 mrad	8 mrad

Lead Scintillator Calorimeter

The lead scintillator calorimeter (PbSc) is a shashlik type sampling calorimeter consisting of 15552 towers. Each PbSc tower contains 66 sampling cells consisting of alternating tiles of Pb and scintillator. These cells are optically connected by 36 longitudinally penetrating wavelength shifting fibers for light connection. 30 mm FEU115M phototubes are equipped at the back of the towers. Optically isolated four towers are mechanically grouped together into a single structural entity called a module as shown in Fig. 3.13. 36 modules are attached to a backbone and held together by welded stainless steel skins on the outside to form a rigid structure called a supermodule. 18 supermodules make one sector, a 2×4 m^2 plane with its own rigid steel frame. The energy resolution of PbSc from tests with electron beams is given by:

$$\frac{\sigma_E}{E} = \frac{8.1\%}{E\ (\text{GeV})} \oplus 2.1\%. \tag{3.4}$$
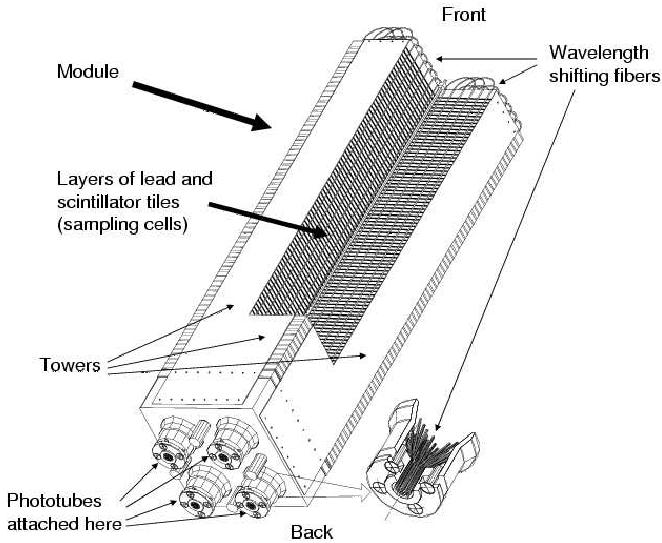
Figure 3.13: Interior view of a lead scintillator calorimeter module showing a stack of scintillator and lead plates, wavelength shifting fiber readout and leaky fiber inserted in the central hole. Its active depth is 375 mm (18 radiation length) and lateral segmentation size is 55.35×55.35 mm^2.

Lead Glass Calorimeter

The lead glass calorimeter (PbGl) array comprises 9216 towers. The Cherenkov photons emitted by electrons in electromagnetic showers are read out by FEU84 photo-

tube in the back end. The towers are individually wrapped with aluminized myler and shrink tube and 24 towers are glued together with a carbon fiber and an epoxy resin to form a selfsupporting supermodule as shown in Fig. 3.14. Each PbGl sector
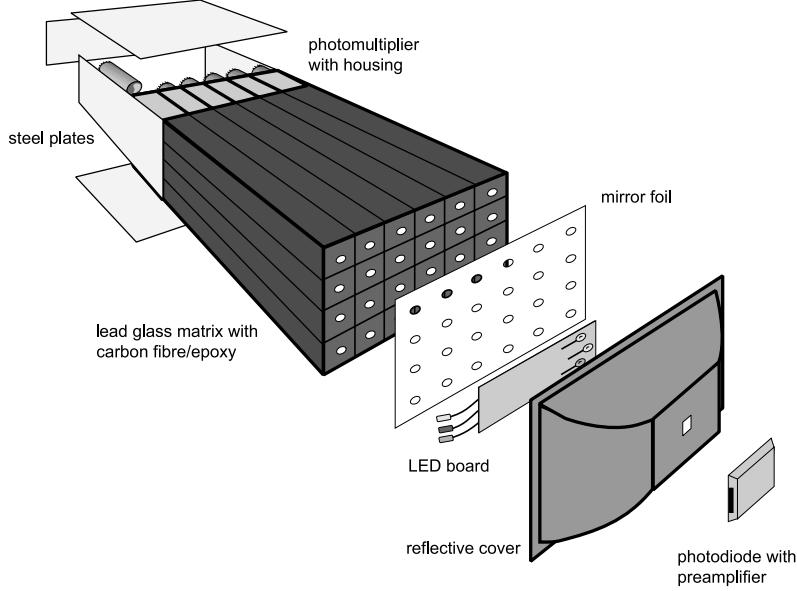
Figure 3.14: Exploded view of a lead glass calorimeter supermodule.

comprises 192 supermodules (16 supermodule wide by 12 supermodule high). The energy resolution of PbGl from the tests with electron beams is given by:

$$\frac{\sigma_E}{E} = \frac{5.9\%}{E \text{ (GeV)}} \oplus 0.8\%. \tag{3.5}$$

3.2.8 Silicon Vertex Tracker

The silicon vertex tracker (VTX) is utilized to measure tracks of charged particles around the beam collision vertex for the DCA measurement and to determine the beam collision vertex. Since the other trackers such as the DC or the PC locate far from the vertex, they can not achieve enough DCA resolution for the DCA approach. The VTX is required to be operated in high multiplicity environment $(dN_{ch}/d\eta|_{\eta=0} = 687 \pm 0.7 \text{ (stat.)} \pm 37 \text{ (syst.)}$ in central Au+Au collisions [46]). The requirements for the VTX are as follows:

- The DCA resolution is required to be less than 150 μm, which is driven by the difference of lifetime and q-value of D and B mesons.

- In order to avoid merging hit clusters, occupancy should be less than 1 % for readout pixels.

49

The VTX is a silicon tracking system consisting of two arms. Each of the arms has a multi-barrel structure with 4 barrels. Each barrel is called B0, B1, B2, and B3 from inner to outer barrels. They are located at $r = 2.6 \sim 17$ cm surrounding the beam axis. The pseudo-rapidity and the azimuthal coverages are ± 1.2 and $140° \times 2$ per arm, respectively. Figure 3.15 shows a picture of the VTX and Fig. 3.16 shows a cross-sectional view of the VTX. The VTX consists of two silicon detectors: One is a silicon pixel detector (VTXP) and the other is a silicon detector with a strip-pixel hybrid readout called a silicon stripixel detector (VTXS). The inner two barrels consist of the VTXP and the outer two barrels consists of the VTXS. Figure 3.17 and 3.18 show pictures of VTXP and VTXS module, respectively. B0 and B1 consist of 10 and 20 of modules, and B2 and B3 consist of 16 and 24 modules respectively. The basic parameters are summarized in Table 3.5. Average hit cluster sizes of the VTXP and VTXS are around 1.6 (1.0) and 1.3 (1.3), respectively, in azimuthal (z) direction. The occupancies summarized in Table 3.5 are calculated by assuming that hit cluster size is 1. Even when the realistic cluster sizes are taken into account in the occupancy calculation, the requirement, $< 1\%$, is achieved. The VTX is operated at a dark and low temperature environment, less than $10°$C, to decrease the thermal noise and the leakage current. In order to prevent a dew condensation, the VTX is installed in a gas seal and filled with dry nitrogen to keep dry. Details of the VTXP and the VTXS are described below.

Table 3.5: Major design parameters for the pixel detector. The maximum of the occupancies are evaluated with the multiplicity of central Au+Au collision with $\sqrt{s_{NN}} = 200$ GeV.

Barrel	0	1	2	3
Radius from beam axis	2.6 cm	5.1 cm	11.8 cm	16.7 cm
Pixel size	50 μm (ϕ) $\times$ 425 μm (z)		80 μm (ϕ) $\times$ 1000 μm (z)	
Radiation length	1.28%		5.43%	
Occupancy	0.53%	0.16%	4.5% (X) 4.7% (U) 0.2% ($X \times U$)	2.5% (X) 2.7% (U) 0.07% ($X \times U$)

Silicon Pixel Detector

The silicon sensor for the VTXP has $p^+ - n$ structure whose thickness is 200 μm. ALICE1LHCB chip [54] is employed as the readout chip. The chip was originally developed for the silicon pixel detector for the ALICE experiment and the ring imaging cherenkov detector for the LHCb experiment. One module is made of 16 of the chips. The data from 8 chips are read out in parallel. 1 chip has 32×256 readout pixels. The cooling is performed by flowing a hydrofluoroether inside the tube attached at the back of the module. The tube is fabricated by a curbon fiber to keep the radiation length of the module as small as possible. The surface of the tube is coated to be an
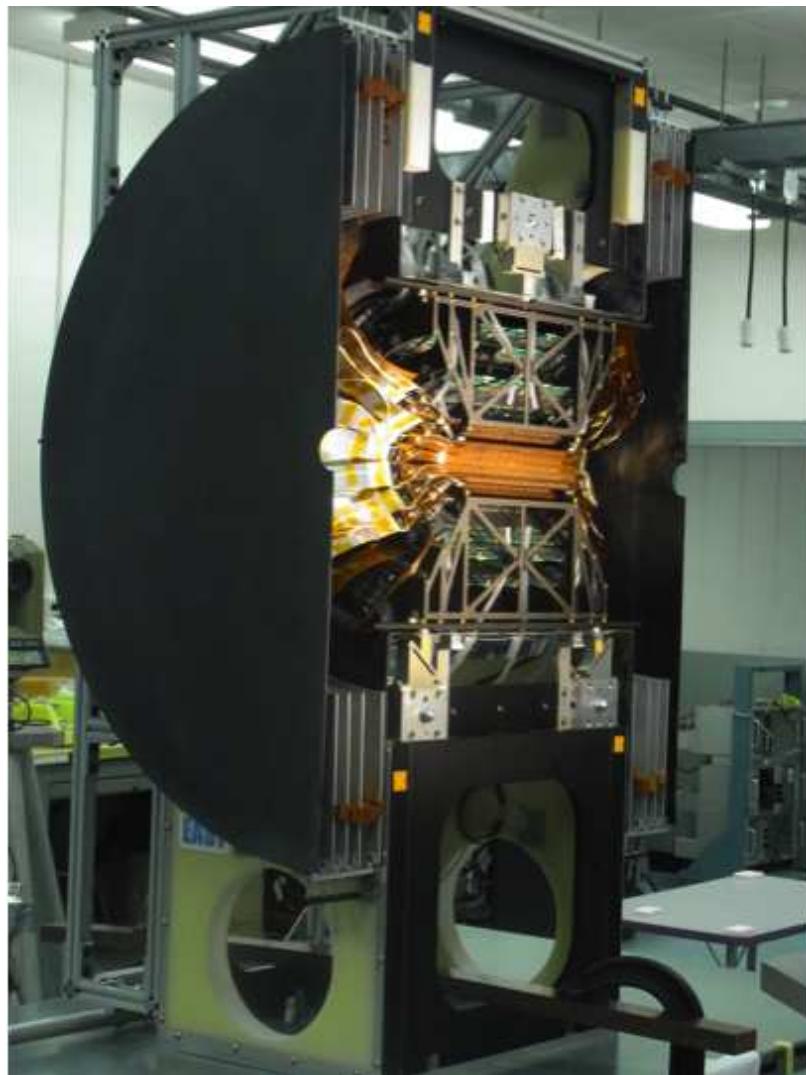
Figure 3.15: An Overview of a VTX arm.
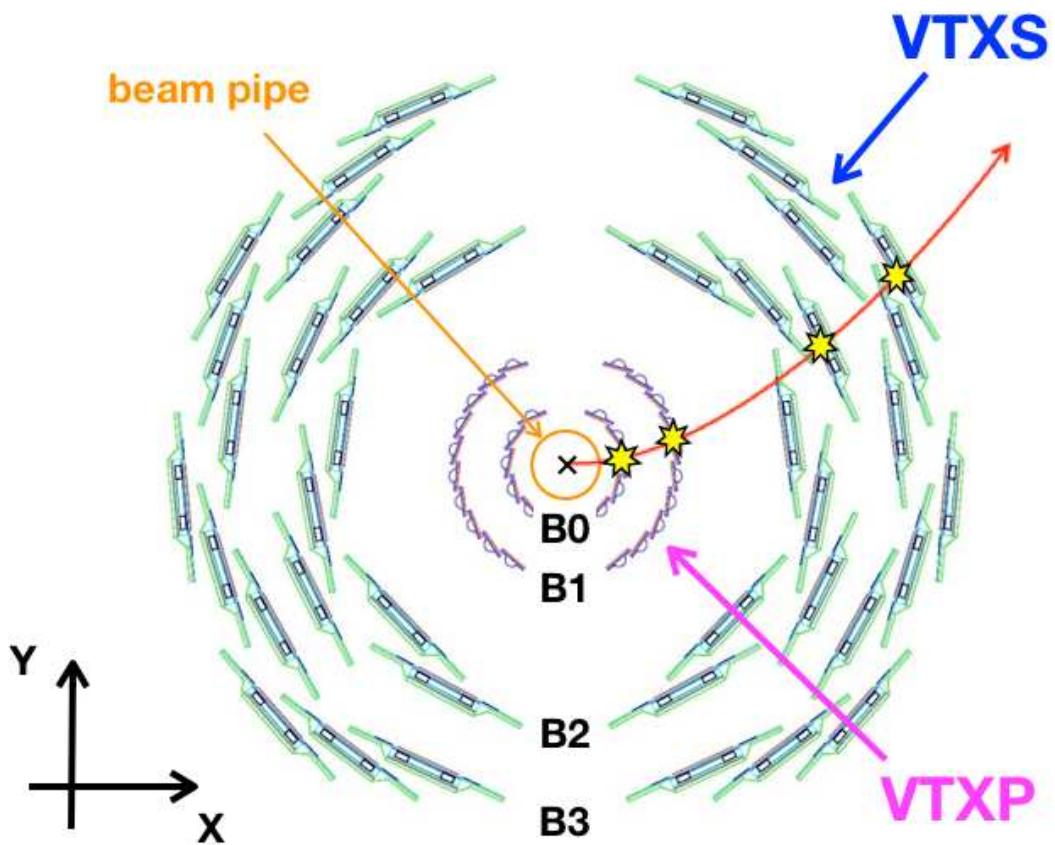
Figure 3.16: A cross-sectional view of VTX and beam pipe. The cross inside the beam pipe represents beam collision vertex. A charged track is ejected from the vertex, which is represented by the red arrow, and 4 hits are created on all the barrels, which are represented by yellow stars.

Figure 3.17: A picture of a VTXP module.
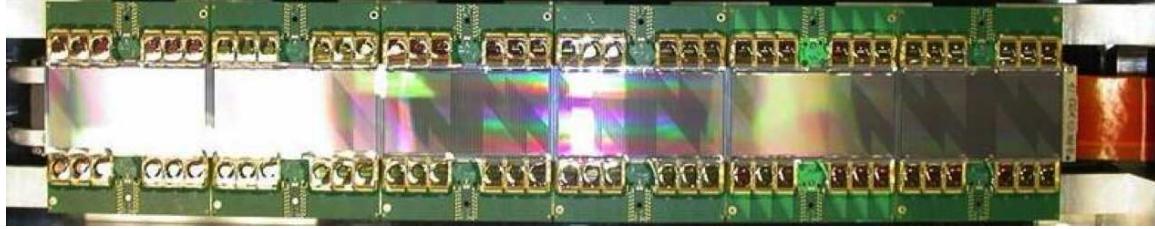
Figure 3.18: A picture of a VTXS module.

insulator. The tube is charged up by flowing the coolant. In order to prevent sparks, the fiber inside the tube, which is an electrical conductive material, is connected to the electrical ground and flow charges. The chip outputs binary hit information, and it is transfered to a FEM through a readout bus attached on the module. The chip and the bus are connected by wire bondings. The wires are encapsulated by a glue to avoid breaking the wires by a resonance which happens for an operation in a magnetic field. When a signal is transfered from the chip to the bus, a charge is flow inside the wire. When the wire is located at a magnetic field, it is kicked by the field and vibrates. If the event rate which corresponds to the frequency of the charge flow inside the wire, matches the vibration, a resonance happens, and thus, the wires are hardly damaged. The glue with the coefficient of thermal expansion near that of the sensor is selected as the encapsulator. The position resolution was evaluated by beam test using 120 GeV proton beam and it is 14 μm and 152 μm for the azimuthal and the beam directions, respectively [17]. A discriminator equiped on each readout pixel digitize a deposited energy. The typical threshold value of the discriminator corresponds to ~20% of the charge deposite of the minimum ionizing particle (MPV). A hit reconstruction efficiecy is more than 99% in a GEANT simulation with single electron tracks.

A schmatic of the circuitry of the readout chip for one pixel is shown in Fig 3.19. The chip consists of the analog and digital parts. The deposited charge at the sensor is collected by the input pad, and the collected charge is fed into a pre-amplifier followed by a shaper stage with a peaking time of 25 ns. Both of the blocks are differential, one input carrying the detector signal and the other tied to a clean reference. The pre-amplifier is a charge pre-amplifier with a feedback capacitor of 15 fF. It takes at most 200 ns to release the integrated charge. It is enough fast since nominal collision rate of $p+p$ with $\sqrt{s} = 200$ GeV is 300 kHz. The shaper differential output is fed into a discriminator and the analog signal is transformed to a digital signal. Timing resolution of the discriminator is ~25 ns. A uniform threshold was used for each of the chips though the threshold can be adjusted pixel by pixel. The output of the discriminator can be masked pixel by pixel and very hot pixels were masked during the data taking. The output of the discriminator is fed into the digital part. The digital part is operated sychronizing with the clock of the beam bunch, 9.4 MHz. The output of the discriminator is delayed at a delay unit, then taken a coincidence with a trigger which given externally. The delay unit is a counter and two units are

53

equiped for a pixel. When the signals whose charge is larger than the threshold of the discriminator arrive at the unit, the counting starts. If another signal arrives when two counters are occupied, the counter which start counting first is reset, and starts counting again. If the signal matches to the trigger, it is stored at a FIFO, then transfered to the FEM.
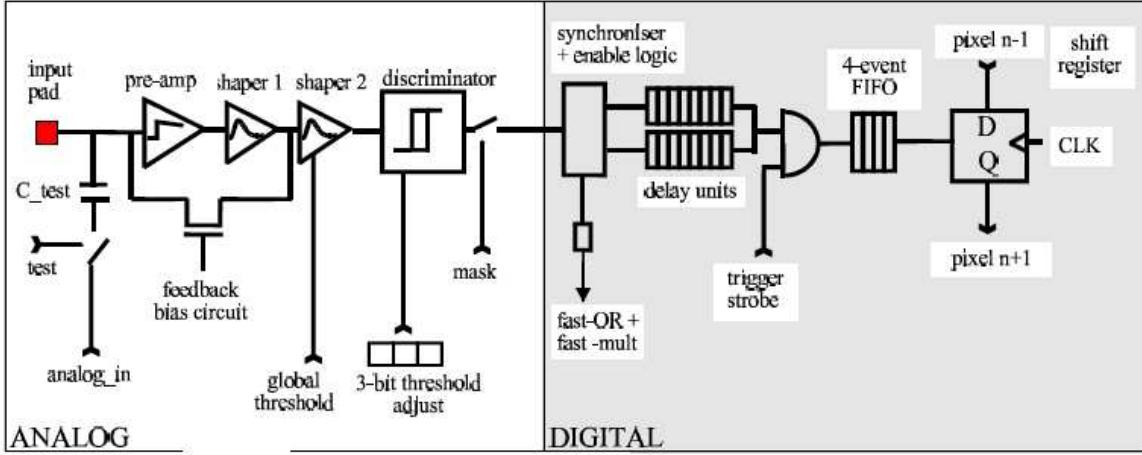
Figure 3.19: A schmatic of the circuitry of ALICE1LHCB chip.

Silicon Stripixel Detector

The silicon sensor for the VTXS is $p^+ - n - n^+$ structure whose thickness is 625 μm. SVX4 chip [55] is employed as a readout chip, which originally was developed in Fermilab. The chip outputs an 8-bit ADC information. A readout pixel is made of two spiral-shaped electrodes, which is illustrated in Fig.3.20 [56]. The blue spiral is connected to left and right spirals and make up of a X strip, and the red spiral is connected to upper-left and lower-right spirals and make up of a U strip. The position resolution which was evaluated at the same beam test as the pixel detector is 23 μm for the azimuthal direction [57]. In order to cancel a common noise between neighboring channels, a offset correction was performed by subtracting the average of neighboring 8 ADCs at event by event. Conceptual designs of the cooling and encapsulation are the same as those of VTXP. The S/N ratio was defined as the ratio of the peak of cluster ADC associated to tracks, to the standard deviation of pedestal (σ_0), which is around 5.3. Figure 3.21 shows distribution of ADC values. The peak is around 51 and therefore the S/N ratio is ~10. Only the ADC information with more than $3\sigma_0$ was stored. A hit reconstruction efficiency is ~85%, which was evaluated in a GEANT simulation with single electron tracks.

SVX4 chip employs a dead-timeless system. The chip consists of a pre-amplifier, a pipeline buffer, and an 8-bit ADC. The pre-amplifier is a charge pre-amplifier with a feedback capacitor of 220 fF. The output of the pre-amplifier is fed into the analog
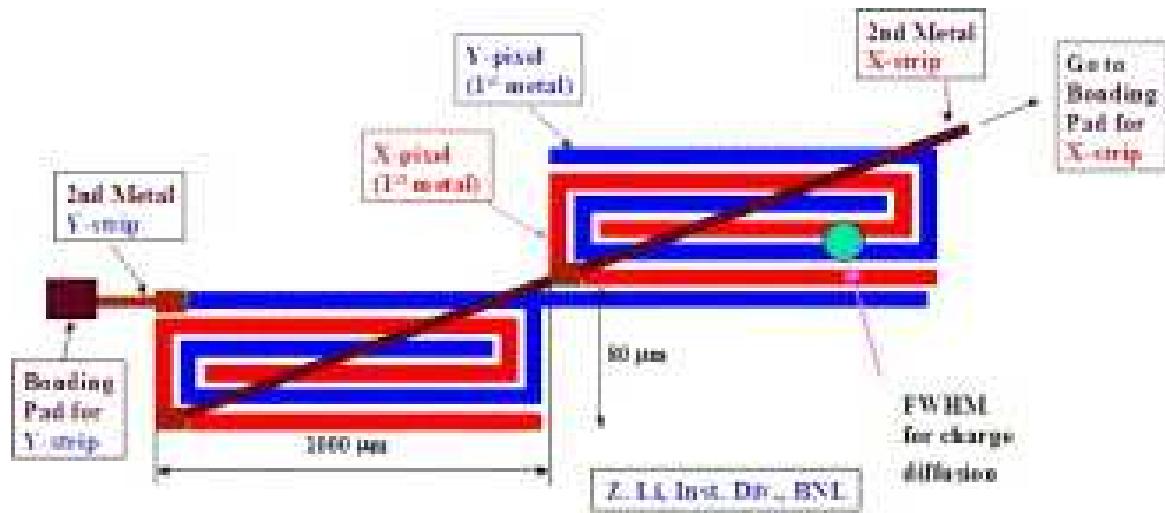
Figure 3.20: A schmatic view of a spiral-shape readout.
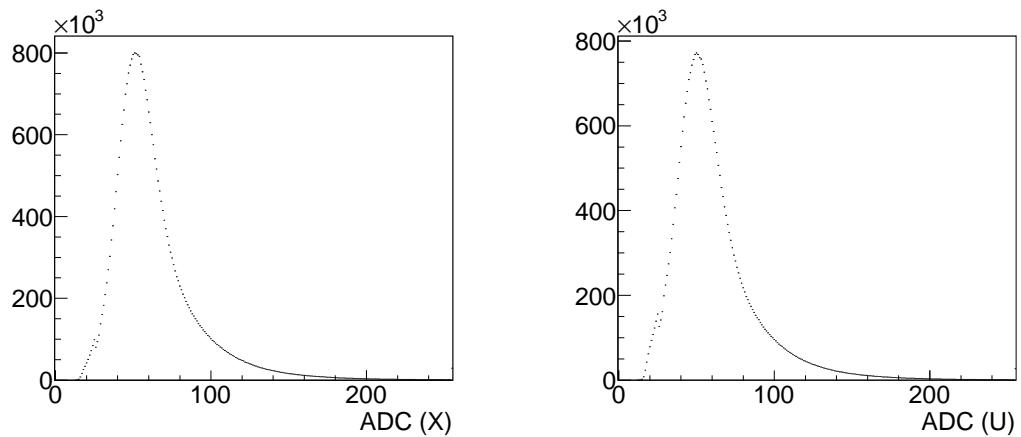
Figure 3.21: ADC distribution of X and U strips of VTX-stripixel detector.

pipeline. There are 46 pipelines for each pixels. The pipeline operates by sequentially sampling the output of the pre-amplifier on one of 46 storage capacitors. The pre-amplifier and the pipeline is conneted through a capacitor. Therefore, the charge stored at the feedback capacitor is not distorbed by the samplings. At each of the beam clocks, the sampling capacitor is switched to the next capacitor. Before the switching, the charge stored at the next capacitor is reset by a switch. The charge integrated by the feedback capacitor is reset by another switch. The switch is turned on at the abort gap of the beam clock. One of the sampling capacitor is selected by a trigger, and the charge stored at the selected capacitor is read out after a digitization.

3.3   Data Acquisition

The data aquisition system of the PHENIX experiment and triggers for a data sampling are summarized in this section. The Level-1 trigger (LVL1) is designed to select interesting events with a sufficient rejection of uninterested events by reducing the data logging rate up to 400 MB/s, which is the maximum to be handled by the PHENIX data acquisition system [58]. The LVL1 trigger is a parallel, pipelined and deadtimeless system.

3.3.1   Trigger

The RHIC beam bunches cross each other in 9.4 MHz frequency at the PHENIX interaction region and the total data volume from PHENIX detectors for an event is $\sim$45 kB in p+p 200 GeV collisions. In order to collect interesting events efficiently, the LVL1 trigger for the data selection is necessary at a online level. In this thesis, the data collected with the minimum-bias trigger (MB trigger) and EMCal-RICH trigger for electron (electron trigger) were analyzed and details are described below.

MB Trigger

The MB trigger is created with the BBC signals. When at least one hit exist on both of the north and south BBC modules, the MB trigger is issued. A nominal raw rate of the MB trigger is 300 kHz in p+p 200 GeV collisions. Therefore the rate of the collected data size is much beyond the maximum logging rate, 400 MB/s. The data collected by the MB trigger were scaled down, and only about 1/1000 of the triggered events were recorded. The data collected with the MB trigger is called MB data in this thesis. Another trigger is generated by requiring that z coordinate of the collision vertex reconstructed by the BBC is in $\pm$15 cm in addition to the MB trigger. The trigger is called MB-narrow trigger.

Electron Trigger

The electron trigger is created by the EMCal and the RICH signals. Acceptance coverages of the EMCal and the RICH are divided into 16 trigger segments. Each segment consists of 9 trigger tiles for PbSc and 16 tiles for PbGl and RICH. Each trigger tile consists of 144 EMCal towers and 20 RICH phototubes. Deposited energies are summed for neighboring 2×2 EMCal towers in a tile. The summations are performed for non-overlapping combinations. If one of the sums in a EMCal tile exceeds threshold value, 600 MeV, the EMCal tile is fired. A RICH tile is fired if the sum of analog signals of all the channels at the tile exceeds a threshold. When a RICH hit tile and a EMCal hit tile are found along the same trajectory, the electron trigger is issued, as shown in Fig. 3.22. The trigger efficiency of the electron trigger as a function of electron p_T turns on from $p_T \sim 0.5$ GeV/c and becomes flat at $p_T > 1.5$ GeV/c, as is described in Sec. 4.7.3. In this analysis, the events collected by requiring both the electron trigger and the MB-narrow trigger were analyzed. A nominal raw rate of the event is 600 Hz, and more than 95%of the triggered data were successfully recorded.
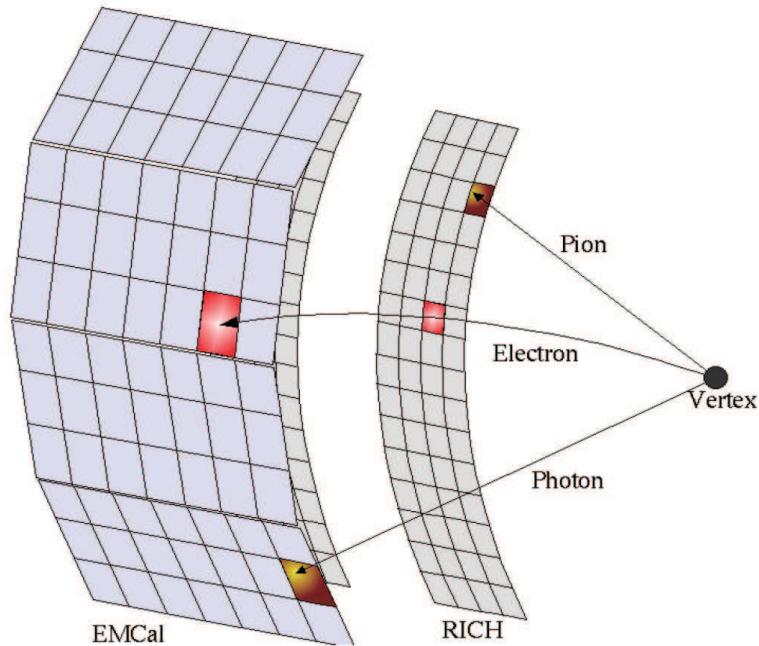
Figure 3.22: The principal scheme of the electron trigger.

3.3.2   Data Acquisition System

The PHENIX data acquisition (DAQ) system processes the signals from detector subsystems, produces the trigger decision, and stores the triggered data [58]. The

typical data logging rate of $p+p$ collisions is 5 kHz. The schematic flow diagram of the data acquisition system is shown in Fig. 3.23.

Overall control of the DAQ is provided by the Master Timing Module (MTM), the Granule Timing Module (GTM) and the Global Level-1 Trigger System (GL1). The MTM receives 9.4 MHz RHIC clock and delivers it to the GTM and GL1. The GTM delivers the clock, the control commands (Mode bits), an event accept signal to the Front End Module (FEM) of each detector. The GTM equips a fine delay tuning of the clock with ~ 50 ps step in order to compensate the timing difference among the FEMs. The GL1 produces the first LVL1 trigger decision combining LVL1 signals from detector components.

The FEM of each detector is designed to convert the analog response of the detector into the digitized signal. The LVL1 trigger signals are simultaneously generated. The generation of the global decision, whether an event should be taken or not, takes ~ 30 bunch crossings. While the GL1 system is making a decision, the event data are stored in the FEM. After receiving the accept signal, each FEM starts to digitize the data.

The data collection from each FEM is performed by a Data Collection Module (DCM) via an optical fiber cable. The DCMs provide data buffering, zero suppression, error checking and data formatting. The DCMs send the compressed data to the Event Builder (EvB).

The EvB is the system which consists of 39 Sub Event Buffers (SEBs), an Asynchronous Transfer Mode (ATM) switch and 52 Assembly Trigger Processors (ATPs). The SEBs are the front end of the EvB and communicate with each granule and transfer the data from granules to the ATP via the ATM, where event assembly is performed. The combined data is stored to the disk with the maximum logging rate of 400 MB/s. In addition, a part of the data is used for online monitoring.
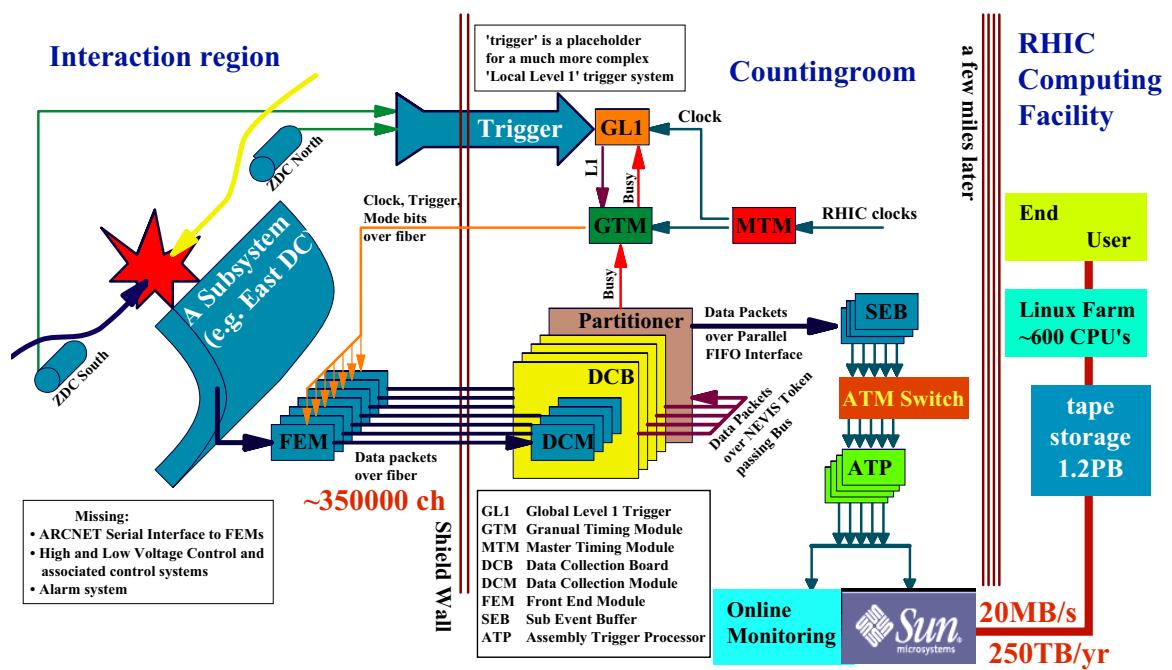
Figure 3.23: The schematic flow diagram of the data acquisition system.

Interaction region

ZDC North

ZDC South

A Subsystem (e.g. East DC)

FEM

~350000 ch

Data packets over fiber

Clock, Trigger, Mode bits over fiber

Missing:
• ARCNET Serial Interface to FEMs
• High and Low Voltage Control and associated control systems
• Alarm system

Shield Wall

'trigger' is a placeholder for a much more complex 'Local Level 1' trigger system

Trigger

GL1

Clock

L1

Busy

GTM

MTM

RHIC clocks

Busy

Partitioner

DCB

DCM

Data Packets over Parallel FIFO Interface

Data Packets over NEVIS Token passing Bus

Countingroom

SEB

ATM Switch

ATP

Online Monitoring

Sun microsystems

GL1   Global Level 1 Trigger
GTM   Granual Timing Module
MTM   Master Timing Module
DCB   Data Collection Board
DCM   Data Collection Module
FEM   Front End Module
SEB   Sub Event Buffer
ATP   Assembly Trigger Processor

a few miles later

RHIC Computing Facility

End User

Linux Farm ~600 CPU's

tape storage 1.2PB

20MB/s
250TB/yr

59

Chapter 4

Data Analysis

This chapter describes the data analysis to measure the invariant cross section of the electrons from charm and bottom decays in $p+p$ collisions at $\sqrt{s} = 200$ GeV. In this thesis, the electrons from charms or bottoms are called "heavy-quark electrons", and the electrons from charms and from bottoms are called charm electrons and bottom electrons, respectively.

The cross section of the charm and bottom electrons can be expressed as follows:

$$E\frac{d^3\sigma}{dp^3}\Big|_{c\to e} = E\frac{d^3\sigma}{dp^3}\Big|_{c+b\to e} \times \frac{N_e(p)|_{c\to e}}{N_e(p)|_{c+b\to e}}, \tag{4.1}$$

$$E\frac{d^3\sigma}{dp^3}\Big|_{b\to e} = E\frac{d^3\sigma}{dp^3}\Big|_{c+b\to e} \times \frac{N_e(p)|_{b\to e}}{N_e(p)|_{c+b\to e}}, \tag{4.2}$$

where $E\frac{d^3\sigma}{dp^3}|_{c\to e}$, $E\frac{d^3\sigma}{dp^3}|_{b\to e}$, and $E\frac{d^3\sigma}{dp^3}|_{c+b\to e}$ are the cross sections of the charm, bottom, and heavy-quark electrons, respectively, and $N_e(p)|_{c\to e}$, $N_e(p)|_{b\to e}$, and $N_e(p)|_{c+b\to e}$ are the numbers of the charm, bottom, and heavy-quark electrons, respectively, as a function of electron momentum, p.

The cross section of the heavy-quark electrons ($E\frac{d^3\sigma}{dp^3}|_{c+b\to e}$) in $p+p$ collisions have already been reported [15, 29]. The result reported from PHENIX experiment [15] is utilized in this thesis. The fraction of the bottom contribution in the heavy-quark electrons (f_b), which is the second terms in Eq. 4.2, $N_e|_{b\to e}/N_e|_{c+b\to e}$ ($= 1 - N_e|_{c\to e}/N_e|_{c+b\to e}$), is evaluated in this thesis by the DCA approach. An overview of the DCA approach and brief explanations about following sections in this chapter are given at Sec. 4.1.

In this analysis, the data collected by requiring both the electron trigger and the MB-narrow trigger and by requiring MB trigger are analyzed. The former is simply called "data", and the latter is called "MB data" in this chapter. The integrated luminosity of the data after the event selection in Sec. 4.5 is 2.2 pb^{-1}.

4.1 Overview of Data Analysis

The basic idea of the analysis is to evaluate the yields of the charm and bottom electrons statistically by decomposing the DCA distribution of the inclusive electrons. The decomposition is performed by utilizing width differences of DCA distributions of electrons from charm, bottom, and background components, such as electrons from Dalitz decay of neutral pseudo-scalar mesons or from photon conversions.

The procedure of the decomposition is as follows:

1. Electrons are measured.

2. DCA distribution of the inclusive electrons is measured.

3. Yield ratios of all electron sources in the inclusive electrons are evaluated based on previously measured results. The yield ratios of the charm and bottom electrons cannot be separated here. They are handled in being combined as the heavy-quark electrons, and the yield ratio of the heavy-quark electrons is evaluated by using a previously measured result [15]. This step is described in Sec. 4.8.

4. Templates of DCA distributions of all electrons sources are evaluated by using simulations. This step is described in Sec. 4.9.

5. The DCA distribution of the inclusive electrons is fitted by using the yield ratios (Step 3) and the templates (Step 4).

The fraction of the bottom electrons in the heavy-quark electrons, f_b, is the only free parameter for the fitting at Step 5. Uncertainties of the yield ratios and the templates, which are evaluated at Step 3 and 4 are transferred into systematic errors of f_b by repeating the fitting. Each of the items which are taken into account for the systematic error evaluation is changed within its uncertainty, then the fitting is performed and f_b is evaluated. A difference of f_b before and after the change is assigned as systematic error. The DCA distribution of the data is stored in a histogram. The fitting is performed by the binned maximum likelihood method assuming that an entry at each bin of the histogram has a Poisson distribution. This analysis is carried out for the electron p_T ranges of 1.5-2.0, 2.0-2.5, 2.5-3.0, 3.0-4.0, and 4.0-5.0 GeV/c, independently. Each of them is called an analysis p_T bin in this thesis.

Brief descriptions about following sections are as follows: In Sec. 4.2, the track reconstruction by the central arms, which is called CNT, is described. The electron identification is performed with the CNTs. CNTs are also utilized for a track reconstruction with VTX which is used for DCA calculation. Momentum determination is also described in this section, which is used for the interpolation of DCA calculation. In Sec. 4.3, determinations of analysis variables used for the electron identification are described. In Sec. 4.4, track reconstructions with VTX, DCA calculation, and the

measurement of the beam collision point are described. Event and track selections are described in Sec. 4.4, and selection of good runs are described in Sec. 4.6. A stability of DCA distribution is also described in Sec. 4.6. A simulation study is important to evaluate the yield ratio and DCA template. Tunings of simulations are described in Sec. 4.7. The evaluations of the yield ratios and DCA templates, which correspond to Step 3 and 4, are described in Sec. 4.8 and Sec. 4.9, respectively. The evaluation of systematic error for f_b is described in Sec. 4.10.

4.2 Track Reconstruction with Central Arm

The track reconstruction technique in the PHENIX central arm is described in Ref. [59], and a brief description is given in this section.

The left and right panels in Fig. 4.1 show schematic views of a trajectory of a charged particle passing from the collision vertex to the DC in the x-y and r-z planes.
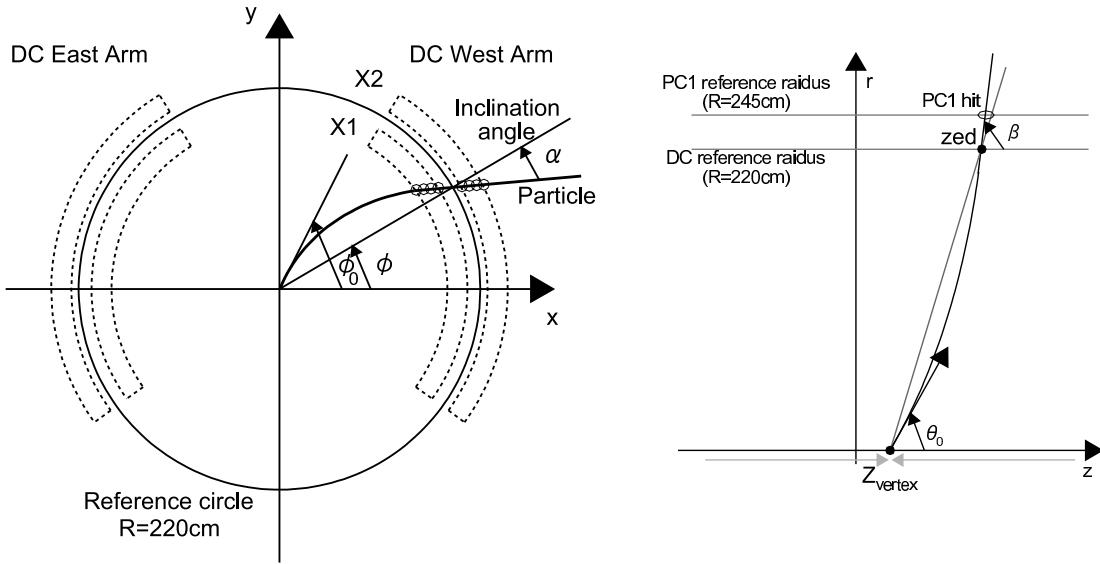
Figure 4.1: Schematic views of a trajectory of a charged particle from the collision vertex to the DC in the x-y (left) and r-z (right) planes. The Hough transform parameters, ϕ_0, ϕ, α are illustrated.

The variables to determine the trajectory and momentum are as follows:

- α: The angle between the projection of the trajectory in the x-y plane and the radial direction at the DC reference radius of $r = 220$ cm.

- ϕ: The azimuthal angle of the intersection at the DC reference radius of $r = 220$ cm.

63

- β: The polar angle of the intersection at the DC reference radius of $r = 220$ cm.

- zed: The z coordinate of the intersection at the DC reference radius of $r = 220$ cm.

- p_T: The reconstructed transverse momentum.

- θ_0: The reconstructed polar angle of the initial direction.

- ϕ_0: The reconstructed azimuthal angle of the initial direction.

- z_{vertex}: z coordinate of the beam collision vertex.

4.2.1 Track Reconstruction Technique
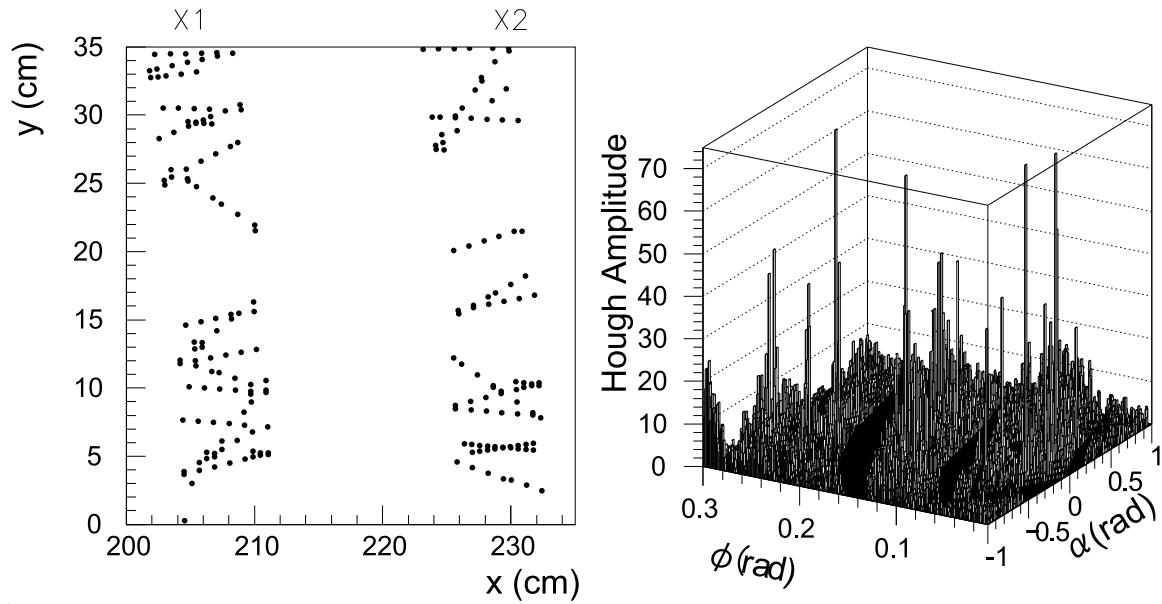
Figure 4.2: The Hough transformation of the DC hits in the x-y plane to the feature space of α and ϕ. The left panel shows simulated hits for a small physical region of the DC, and the right panel shows the feature space for this region. Tracks appear as peaks in the feature space.

A trajectory is uniquely determined by the four variables, p_T, θ_0, ϕ_0 and z_{vertex}. They are reconstructed from the following variables, α, ϕ, zed and z_{vertex}. The track reconstruction starts from finding hits in X1 and X2 wires of the DC. α and ϕ are determined from X1 and/or X2 hit positions by the Hough transformation with an assumption that trajectories are straight in the DC. Figure 4.2 shows an example of the Hough transformation in a part of the DC hits and the amplitude in a feature space. The following procedures are performed for the track reconstruction.

1. Find hits in X1 and X2 wires.

2. Calculate α and ϕ for possible hit pairs and a track reconstruction in x-y plane is performed by finding a peak in α-ϕ space.

3. Track reconstruction in z direction is preformed by using z_{vertex}, PC1 hits, and hits in the UV wires.

3-1. It is first attempted by integrated information from PC1 reconstructed clusters. If there is an unique PC1 hit, zed is calculated by using the PC1 hit and z_{vertex}.

3-2. If there are multiple PC1 hits, zed is calculated with UV hits.

Then, each reconstructed track is associated with hit information of outer detectors (PC2, PC3, EMCal and RICH). The residual magnetic field was not taken into account and the track was assumed to be a straight line at the association with the outer detectors.

Track Quality

A quality of a reconstructed track is defined by using hit information of X and UV wires in the DC and the associated PC1 hit. The track quality is implemented as the 6-bit variable, quality, for each track. Table 4.1 shows the bit definition of quality.

Table 4.1: The bit definition of quality.

	bit	decimal	description
LSB	0	1	X1 hit is used
	1	2	X2 hit is used
	2	4	UV hit is found
	3	8	UV hit is unique (No hit sharing)
	4	16	PC1 hit is found
MSB	5	32	PC1 hit is unique (No hit sharing)

4.2.2 Momentum Determination

An accurate analytical expression for a momentum of a charged particle is difficult due to a small non-uniformity of the magnetic field along a track. Thus, the non-linear grid interpolation technique [60] was employed to determine the initial kinematic parameters of charged particles traveling the magnetic field. A four-dimensional field integral grid was constructed within the entire radial extent of the CNT for the momentum determination based on the DC hits. The variables in the field integral grid ware z_{vertex}, θ_0, the total momentum p and the radius r at which the field integral $f(p, r, \theta_0, z_{vertex})$ was calculated. The field integral grid was generated by explicitly

swimming particles through the measured magnetic field map and numerically integrating to obtain $f(p, r, \theta_0, z_{vertex})$ for each grid point.

p_T (GeV/c) and α (rad) have the following relation:

$$p_T \simeq \frac{K}{\alpha}, \tag{4.3}$$

where $K \simeq 0.10$ GeV/c is the effective field integral expressed as:

$$K = \frac{e}{R} \int lBdl, \tag{4.4}$$

where e is the elementary charge in the hybrid unit ($e = 0.2998$ GeV/c T^{-1} m^{-1}) and R is the DC reference radius, 220 cm. An iterative procedure is used to determine the initial kinematic parameters of the reconstructed tracks with the initial assumption of Eq. 4.3. The momentum resolution depends on both the intrinsic angular resolution of the DC and the multiple scattering of a charged particle as it travels to the DC due to intervening materials. As a result, the p_T resolution is about 1.5% for tracks with $p_T = 1$ GeV/c and the reconstruction efficiency is larger than 99% for a single track. Figure 4.3 shows the p_T resolution of electrons as a function of p_T evaluated by an single-track simulation.
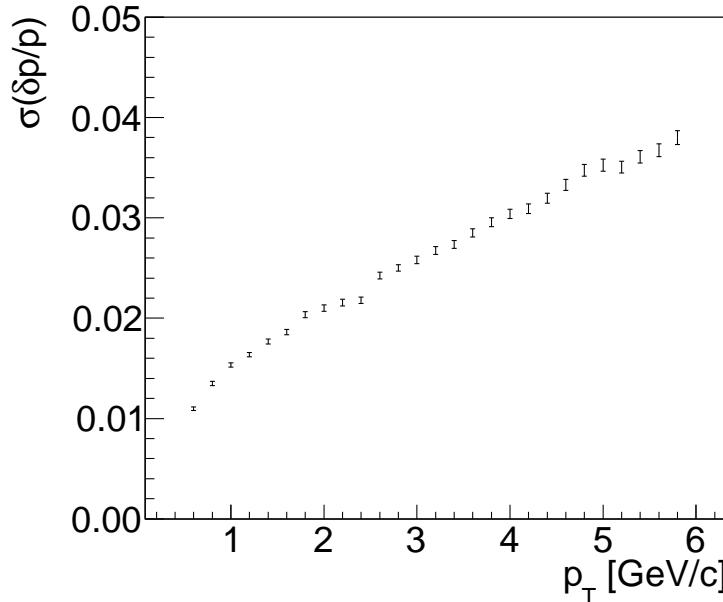
Figure 4.3: p_T resolution of electrons as a function of p_T evaluated by an single-track simulation.

The reconstructed track is extrapolated to outer detectors, PC, RICH, and EMCal to obtain the projected positions on the detectors. The projected position is used to search associated hit on the detector.

4.2.3 Analysis Variable

The global and track variables utilized in this thesis are summarized in Table 4.2.

Table 4.2: Summary of the global and track variables used in this thesis.

Variables	Descriptions
bbcz	z coordinate of the collision vertex measured by the BBC.
mom	Total momentum of a CNT.
the0	Initial polar angle of a CNT at the vertex.
phi0	Initial azimuthal angle of a CNT at the vertex.
dcphi	azimuthal angle where the CNT crosses the DC reference radius.
zed	z coordinate where the CNT crosses the DC reference radius.
quality	Quality of a CNT.

4.3 Electron Identification

Electron identification is carried out by RICH and EMCal, and the method is described in this section. Criteria to select electron candidates and the efficiency of the selection are summarized in Sec. 4.5.1. The variables utilized for electron identification are listed in Table. 4.3.

Table 4.3: Summary of the variables for electron identification.

Variables	Descriptions
RICH	
n0	The number of fired phototubes in the nominal ring area ($3.4 \leq r \leq 8.4$ cm)
n1	The number of fired phototubes in the larger ring area ($r \leq 11.0$ cm)
npe0	The number of photo-electrons detected in the nominal ring area
disp	Displacement between the track projection point on the RICH phototube plane and the point reconstructed from the associated fired phototubes
chi2	Ring shape parameter
EMCal	
ecore	The EMCal shower core energy (GeV)
emcsdphi_e	The difference between the track projection and the EMCal cluster position in the ϕ direction at the EMCal surface normalized to a σ
emcsdz_e	The difference between the track projection and the EMCal cluster position in the z direction at the EMCal surface normalized to a σ
prob	The probability for a shower being a electro-magnetic shower evaluated from shower shape in the EMCal.

4.3.1 Electron Identification with RICH

Track projections are reflected on the RICH mirrors and to the RICH phototube plane. Then, fired phototubes around the projection points are associated with tracks. Figure 4.4 shows a schematic view of the definition of variables used for determination of the RICH variables. The variable r_{cor}^i is the distance between the center of the phototube i and the projection vector.
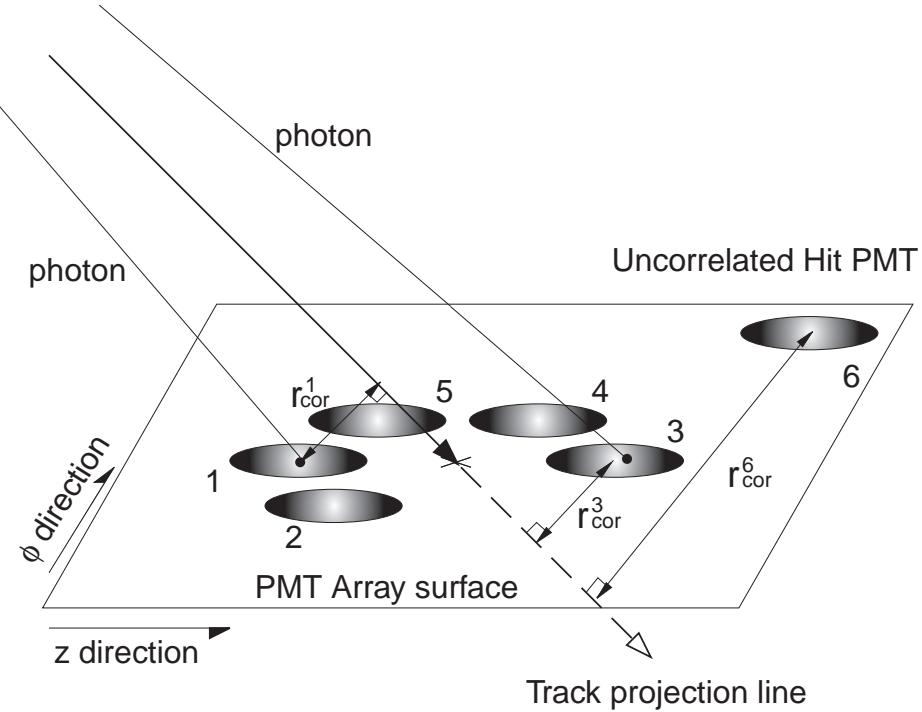
Figure 4.4: A schematic view of the definition of variables used for determination of the RICH variables. A track projection, five associated fired phototubes and one uncorrelated fired phototube are shown as an example. The distance between the center of the fired phototubes 1, 3, 6 and the track projection vector are represented as r_{cor}^1, r_{cor}^3 and r_{cor}^6, respectively.

Ring Association: n0, n1, npe0, disp

RICH variables, n0 and n1, are defined as:

$$n0 \equiv \text{the number of fired phototubes in } 3.4 \leq r_{cor}^i \leq 8.4 \text{ cm,} \qquad (4.5)$$

$$n1 \equiv \text{the number of fired phototubes in } r_{cor}^i \leq 11.0 \text{ cm,,} \qquad (4.6)$$

where the fired phototube is defined to have larger than 0.2 photo-electrons. The left panel of Fig. 4.5 shows the r_{cor} distribution. $< r_{cor} >$ of 5.9 cm is ideal ring radius. The shaded area shows the r_{cor} range of 5.9±2.5 cm corresponding ±1σ region.

68

A variable, npe0, is the sum of the number of photo-electrons, $N_{p.e.}(i)$, of the fired phototubes in $3.4 \leq r_{cor}^i \leq 8.4$ cm and $r_{cor}^i \leq 11.0$ cm.

$$\text{npe0} \equiv \sum_{3.4 \leq r_{cor}^i \leq 8.4 \text{ cm}} N_{p.e.}(i). \tag{4.7}$$

$N_{p.e.}$ is defined by using ADC values of pedestal (ADC_0) and one photo-electron peak ($ADC_{1p.e.}$) as follows:

$$N_{p.e.} = \frac{ADC - ADC_0}{ADC_{1p.e.} - ADC_0}. \tag{4.8}$$

The right panel of Fig. 4.5 shows the distribution of $N_{p.e.}$ for the hits associated to charged tracks. A peak locating at $N_{p.e.} \sim 1$ corresponds to the one photo-electron peak.
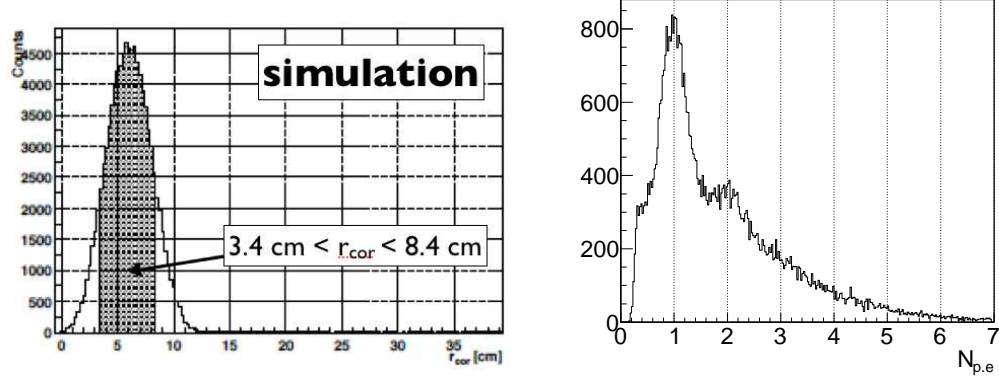
Figure 4.5: Left: r_{cor} distribution. The shaded area shows the r_{cor} range of 5.9±2.5 cm corresponding ±1σ region.
Right: $N_{p.e.}$ distribution. A peak locating at $N_{p.e.} \sim 1$ corresponds to the one photo-electron peak.

The position of the ring center, R_{center}, is calculated from the weighted average of the positions of fired phototubes, R_i,

$$R_{center} \equiv \frac{\displaystyle\sum_{3.4 < r_{cor}^i < 8.4 \text{ cm}} N_{p.e.}(i) \cdot R_i}{\text{npe0}}. \tag{4.9}$$

The displacement of R_{center} from the projection line is defined as disp.

Ring Shape: chi2/npe0

The variable, chi2/npe0, which represents an observed ring shape, is the weighted average of deviations of the fired phototubes from the ideal ring radius, $r_0 = 5.9$ cm.

69

The weight is the number of photo-electrons of each phototube,

$$\mathsf{chi2/npe0} \equiv \frac{\displaystyle\sum_{3.4 \le r^i_{cor} \le 8.4 \ \mathrm{cm}} N_{p.e.}(i) \cdot (r^i_{cor} - r_0)^2}{\mathsf{npe0}}. \tag{4.10}$$

4.3.2 Electron Identification with EMCal

The EMCal measures deposited energy and hit positions of charged particles and photons. The EMCal has eight sectors, W0-W3 (from bottom to top in the west arm) and E0-E3 (from bottom to top in the east arm). E0 and E1 are PbGl and the others are PbSc. Energy calibration of each EMCal tower is performed using the π^0 peak mass reconstructed from two photons.

Hit Position Association: $\mathsf{emcsdz\_e}, \mathsf{emcsdphi\_e}$

Distances between the projection point of a CNT on the surface of the EMCal ($\mathsf{pemcz}, \mathsf{pemcphi}$) and the hit position (the center of the electromagnetic shower: $\mathsf{emcz}, \mathsf{emcphi}$) are expressed by emcdz and $\mathsf{emcdphi}$ in the azimuthal and z directions, respectively.

$$\mathsf{emcdz} = \mathsf{emcz} - \mathsf{pemcz}, \tag{4.11}$$
$$\mathsf{emcdphi} = \mathsf{emcphi} - \mathsf{pemcphi}. \tag{4.12}$$

Variables, $\mathsf{emcdz}, \mathsf{emcdphi}$ depend on total momentum, momentum direction, electric charge of electrons/positrons, and the EMCal sector. Since their widths have a typical momentum dependence, they are normalized to the standard normal distribution with the mean of 0 and the σ of 1 for a convenience of the analysis. Normalized variables, $\mathsf{emcsdz\_e}, \mathsf{emcsdphi\_e}$, are written as:

$$\mathsf{emcsdz\_e} = \frac{\mathsf{emcdz} - \langle \mathsf{emcdz} \rangle}{\sigma_{\mathsf{emcdz(p)}}} \tag{4.13}$$

$$\mathsf{emcsdphi\_e} = \frac{\mathsf{emcdphi} - \langle \mathsf{emcdphi} \rangle}{\sigma_{\mathsf{emcdphi(p)}}}. \tag{4.14}$$

Energy-Momentum Matching: dep

Since both of PbSc and PbGl have enough depths for electrons to deposit all their energies, a ratio of the energy measured by the EMCal, E, to total momentum measured by the DC, p, distributes around 1. On the other hand, the depths are not enough to stop charged hadrons comparing to their nuclear interaction lengths. Therefore, E/p can be used to improve the electron identification capability. An corrected E/p, dep,

by the mean and width of E/p distribution of an electron sample is utilized in this analysis.

$$\mathsf{dep} = \frac{E/p - \langle E/p \rangle}{\sigma_{E/p}}, \tag{4.15}$$

where $\langle E/p \rangle$ and $\sigma_{E/p}$ represent the mean and sigma, respectively.

Probability for Shower Shape Matching: prob

In order to improve the purity of electron signals, information of the shower shape of the EMCal is utilized. The following valuable is calculated:

$$\chi^2 = \sum_i \frac{(E_i - \overline{E_i})^2}{\sigma_i^2}, \tag{4.16}$$

where E_i is the energy measured at i-th tower of the EMCal, $\overline{E_i}$ is the expected energy for an electro-magnetic particle from total measured energy, and σ_i is the standard deviation for E_i. Both $\overline{E_i}$ and σ_i are obtained from the data of an electron beam test. prob is defined as the probability for a shower being an EM shower, which is obtained by converting χ^2 to the probability.

4.4 Track Reconstruction with VTX

Tracks reconstructed with the VTX are utilized to measure the DCA. Both a precise tracking and the reconstruction of the beam collision vertex are necessary for the DCA measurement. The VTX has been utilized for both of them. The track reconstruction and the measurement of the DCA and the collision vertex are described in this section.

Two methods of track reconstructions are performed with the VTX. One is a reconstruction using only the VTX, which is called VTX stand-alone tracking. The other is a reconstruction using both the VTX and the central arm, which is called CNT-VTX tracking. The tracks reconstructed by the VTX stand-alone tracking (stand-alone tracks) are utilized to reconstruct the collision vertex since the acceptance of the VTX is wider than that of the central arm. The tracks reconstructed by the CNT-VTX tracking (CNT-VTX tracks) are utilized to calculate the DCA since the p_T resolution is better than that of the stand-alone tracks.

Clustered hits are used for these trackings. Any neighboring hit readout pixels or strips are bound into a cluster, and there is not a limitation in its cluster size. The position of a cluster on the VTXP is the average of the positions of readout pixels. The position of a cluster on the VTXS is the average of the positions of readout pixels weighted with respect to their ADC values. A cluster is called a hit in this thesis.

Valuables utilized for this analysis related to CNT-VTX tracks are listed in Table 4.4.

Table 4.4: Summary of the variables related to CNT-VTX tracks.

Variables	Descriptions
nvtxhit	The number of associated hits.
nvtxhit0	The number of associated hits on B0.
vtxchi2ndf	χ^2/NDF of a track fitting (see Sec. 4.4.3)

4.4.1   VTX Stand-alone Tracking

The procedure of the stand-alone tracking has three steps, a rough calculation of the collision vertex, finding track candidates, and selection of a track candidate. The rough calculation of the collision vertex in z direction (vtxz0) is performed as follows:

1. Two hits on different barrels are paired.

2. A linear projection is performed with the pair toward the center of the beam spot (beam center) and its closest approach to the beam center is calculated. The measurement of the beam center is described in Sec. 4.4.4.

3. z coordinates of the closest approaches are calculated.

4. The distribution of the z coordinates has a single peak structure and its mean around the peak is calculated. Only the pairs whose closest approaches are less than 1 cm from the beam center are utilized.

At Step 1, the pairs are searched with B0 and B1 when the number of the hits on B0 is larger than 30, go to Step 2. Then, when at least one pair with the closest approach of less than 1 cm, is found, go to Step 3. If not, go back to Step 1 and the pairs are searched with B2 and B3. If the number of the hits on B2 is larger than 30, and if at least one pair with the closest approach of less than 1 cm, is found, go to Step 3. Otherwise, the rough calculation is given up and bbcz is used. The resolution of the reconstructed collision vertex in z direction is around 1 mm in the $p + p$ collisions.
  The algorithm to find track candidates is as follows:

1. Linear projection is performed using vtxz0 and a hit on B0 toward the other barrels.

2. If a hit is found on a barrel inside a search window around the projection point, the hit is associated and a link is created. The hit search is repeated toward an outer barrel by an helix projection. Another projection toward an outer barrel is also performed without the found hit in order to avoid a disturb by a fake hit.

The axis of the helix at the Step 2 is parallel to z direction. The rotation diameter is calculated by fitting the hits in the link and the collision vertex by a circle in x-y plane.

Since the strength of the magnetic field is almost uniform where the VTX is installed, 0.9 T, the helix is a good approximation. The track candidates reconstructed by the algorithm are required that they has hit on B0 and more than 2 associated hits in total.

A track candidate is selected among candidates sharing an identical hit on B0. The candidates with the largest number of associated hits are selected at first. If there are more than one candidates which have the largest number of associated hits, the candidate with the least chi-square which is described in Sec. 4.4.3, is selected.

4.4.2 CNT-VTX Tracking

The algorithm of the CNT-VTX tracking is almost same as that of the stand-alone tracking except for two points. One is the method of the helix projection. A CNT is used as a seed, and the rotation diameter of the helix projection was calculated by p_T of the CNT. The other is the selection of a track candidate. In the CNT-VTX tracking, a track candidate is selected among candidates sharing an identical CNT. If there is not a candidate with more than two associated hits, the candidate with the least chi-square/NDF is selected. Otherwise, the candidate with the least chi-square/NDF is selected among the candidates with more than two associated hits. The CNT-VTX tracking algorithm requires that the number of associated hits is larger than 1.

4.4.3 Track Fitting

A track reconstructed by the stand-alone tracking or the CNT-VTX tracking is fitted by a multi-helices, shown in Fig. 4.6 and Fig. 4.7, in order to minimize the chi-square described as follows:

$$\chi_s^2 = \sum_{0 \leq i \leq n-1} \left(\frac{\Delta \phi_i^2}{\sigma_{\phi,i}^2} + \frac{\Delta z_i^2}{\sigma_{z,i}^2} \right) + \sum_{1 \leq j \leq n-2} \left(\frac{\Delta \theta_{xy,j}^2}{\sigma_{\theta_{xy},j}^2} + \frac{\Delta \theta_{rz,j}^2}{\sigma_{\theta_{rz},j}^2} \right), \tag{4.17}$$

$$\chi_c^2 = \sum_{0 \leq i \leq n-1} \left(\frac{\Delta \phi_i^2}{\sigma_{\phi,i}^2} + \frac{\Delta z_i^2}{\sigma_{z,i}^2} \right)$$

$$+ \sum_{1 \leq j \leq n-2} \left(\frac{\Delta \theta_{xy,j}^2}{\sigma_{\theta_{xy},j}^2} + \frac{\Delta \theta_{rz,j}^2}{\sigma_{\theta_{rz},j}^2} \right) + \frac{\Delta \theta_{xy,n-1}^2}{\sigma_{\theta_{xy},n-1}^2 + \sigma_{\mathsf{phi0}}^2} + \frac{\Delta \theta_{rz,n-1}^2}{\sigma_{\theta_{rz},n-1}^2 + \sigma_{\mathsf{the0}}^2}, \tag{4.18}$$

where

- χ_s^2 (χ_c^2): the chi-square for the stand-alone (CNT-VTX) tracking.

- $\Delta \phi_i$ (Δz_i): the difference of the hit position and the optimized position in azimuthal (z) direction.

73

- $\Delta\theta_{xy,i}$ ($\Delta\theta_{rz,i}$): the angle difference of the incoming and the outgoing helices in x-y (r-z) plane.

All the indices, i, correspond to indices of the associated hits. The counting begins from the innermost hit, i.e. 0th (($n-1$)-th) hit is the innermost (outermost) hit. Following σ values are used in simulations:

- $\sigma_{\phi,i}$ and $\sigma_{z,i}$: the readout pixel size divided by $\sqrt{12}$.

- $\sigma_{\theta_{xy},i}$ and $\sigma_{\theta_{rz},i}$: the RMS of the Gaussian approximation of the multiple Coulomb scattering divided by $\sqrt{2}$. The radiation length is averaged in each module and corrected by a path length in modules of each track.

- σ_{phi0} and σ_{the0}: 1 mrad and 7 mrad are used for σ_{phi0} and σ_{the0}, respectively. These values correspond to the resolution of the azimuthal and polar angles of a track outside of the VTX, respectively. They also corresponds to $\mathsf{phi0}$ and $\mathsf{the0}$ without installing the VTX. The resolution for σ_{phi0} is calculated from the position resolutions of X1 and X2 of the DC and the distance between X1 and X2 plane. The resolution for σ_{the0} is calculated from the resolution of z coordinate measured by the PC1 and the resolution of bbcz.

In order to take into account mis-alignment of the VTX modules, different σ values are used for the data in order for the chi-square distributions to be the same. A comparison of the distributions between the data and simulation is described in Sec. 4.7.1.

The NDF values of the chi-squares are as follow:

$$NDF_s = 2 \cdot N_{hit} - 5, \tag{4.19}$$
$$NDF_c = 2 \cdot N_{hit} - 2, \tag{4.20}$$

where NDF_s (NDF_c) is the NDF for the stand-alone (CNT-VTX) tracking and N_{hit} is the number of associated hits. The difference between NDF_s and NDF_c is three since there are two additional terms in the chi-square and the rotation diameters of the helices are fixed at the CNT-VTX tracking.

4.4.4 Beam Collision Vertex

The beam collision vertex is reconstructed for each collision with the stand-alone tracks. The procedure is as follows:

1. Each of the tracks is projected to the beam center, and the position and the momentum vector at the closest approach are calculated.

2. Each is approximated by a line at its closest approach with the momentum vector.
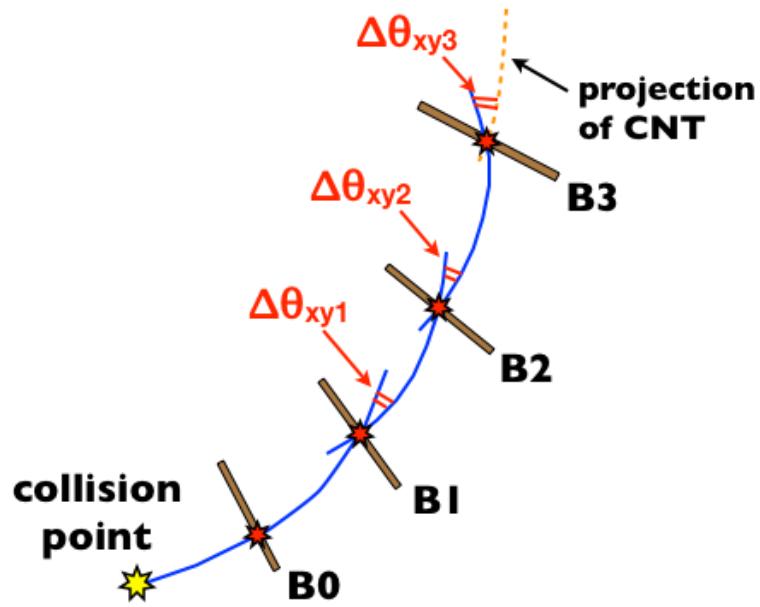
Figure 4.6: An illustration of a tracking with the VTX in x-y plane.
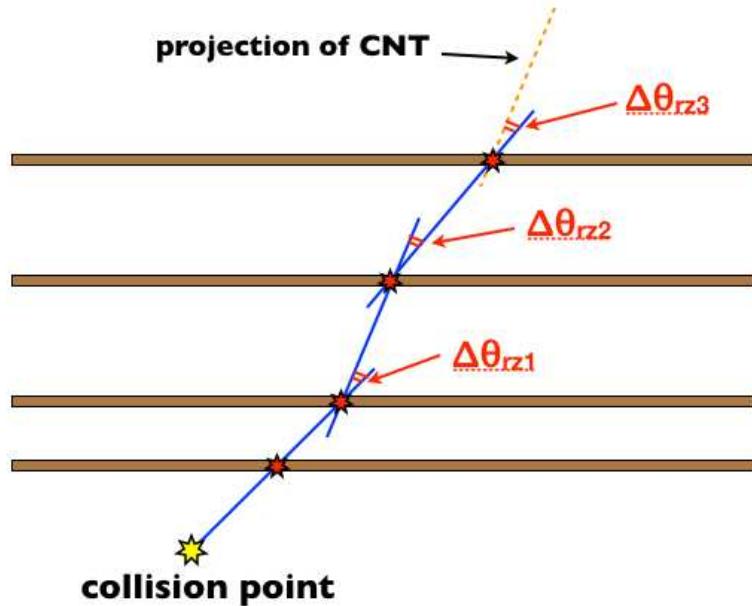
Figure 4.7: An illustration of a tracking with the VTX in r-z plane.

3. the collision vertex, (v_x, v_y), is calculated so that the χ^2 defined below is minimum:

$$\chi^2_{col} = \sum_i \frac{(a_{x,i} - v_x)^2 + (a_{y,i} - v_y)^2}{w_i^2}, \tag{4.21}$$

$$w_i = \sqrt{1 + 1/p_{Ti}^2}, \tag{4.22}$$

where $a_{x,i}$ $(a_{y,i})$ is the x coordinate (y coordinate) of the closest approach of i-th track.

4. go back to Step 1 by replacing the beam center to the collision vertex calculated at Step 3.

The collision vertex is calculated at the Step 3 by solving following equations:

$$\frac{\partial \chi^2_{col}}{\partial v_x} = 0, \tag{4.23}$$

$$\frac{\partial \chi^2_{col}}{\partial v_y} = 0. \tag{4.24}$$

The weight, w_i, corresponds to the normalized and approximated DCA resolution in x-y plane. The DCA resolution can be approximately described by terms from position resolution of associated hits (σ) and multiple Coulomb scattering (M) as follows:

$$\sigma_{DCA} = \sqrt{\sigma^2 + (M/p)^2} \tag{4.25}$$

$$\simeq \sigma \cdot \sqrt{1 + (r/p_T)^2}, \tag{4.26}$$

In the equations, p is approximated by p_T and β is approximated by 1. The ratio of σ and M, r, is almost 1, which is evaluated from the readout pixel size of the inner two barrels and the material of the innermost barrel of the VTX. The magnitude of the resolution, σ, is meaningless when the partial differential equations, Eq. 4.23 and 4.24, are solved, therefore, the following value is used as the weight:

$$w_i = \sqrt{1 + 1/p_{T,i}^2} \tag{4.27}$$

The iterations are stopped when the difference from the vertex calculated at the previous iteration is less than 10 μm.

Beam Center Calibration

The beam center is calibrated by the distribution of the collision vertices. The changing of the beam center is small during a data taking, which is called a run, therefore

the calibration is performed for each run. The beam center in x-y plane of a run is calculated by fitting the distribution of the collision vertices of high multiplicity collisions of the run with a Gaussian. Figure 4.8 shows the distribution of the collision vertices of high multiplicity collisions of a run. The black and red lines show the distribution and fitting result. The distribution is simulated by creating $p+p$ collision with a PYTHIA simulation. The blue line shows the distribution in the simulation. Not only the main peak but tails are successfully reproduced by the simulation. Figure 4.9 shows the beam center position as a function of run number. The left and right panels represents x and y coordinates of the beam center, respectively.
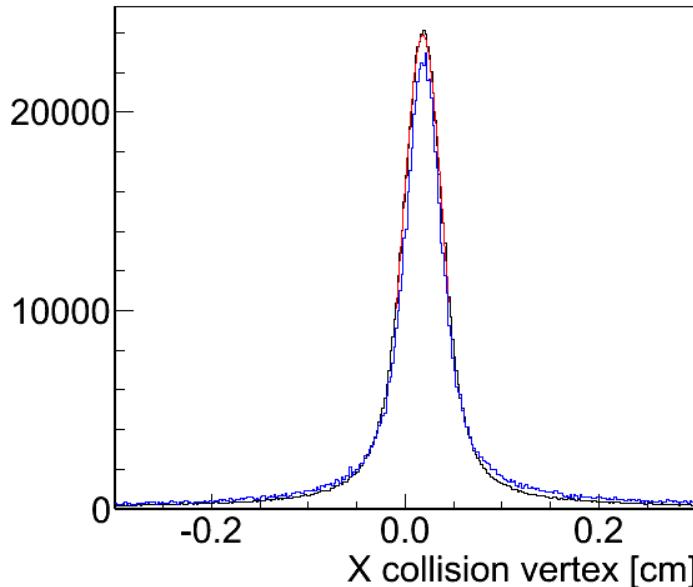
Figure 4.8: A distribution of the collision vertices of high multiplicity collisions of a run. The black and red lines show the distribution and fitting result by a Gaussian. The distribution is simulated by creating $p+p$ collision with a PYTHIA simulation. The blue line shows the distribution in the simulation.

4.4.5 DCA Measurement

In order to measure the DCA of a track, both its path and the collision vertex of the collision are necessary. The measurement of the collision vertex for each collision with a good precision is difficult in the $p+p$ collisions since the number of reconstructed tracks is small, typically $1 \sim 3$. Therefore, the beam center, not collision vertex, is used to measure the DCA. This means that the DCA resolution is limited by the beam size. This is only for the analysis of $p+p$ collisions and better resolution can be achieved in A+A collisions.
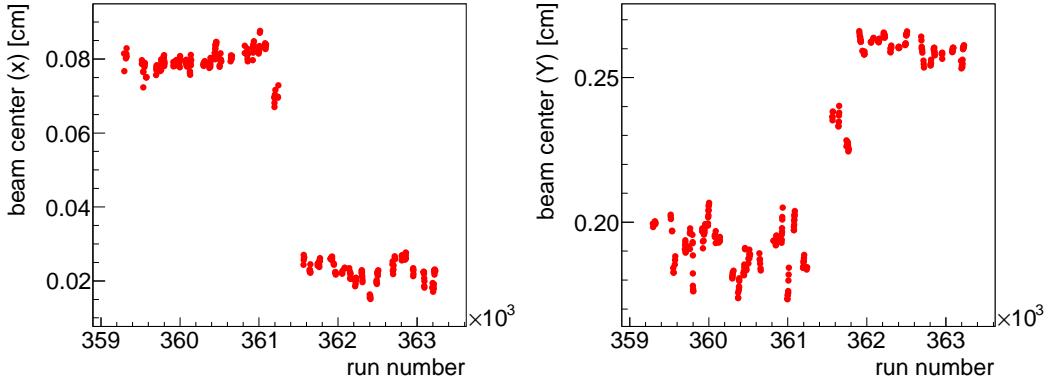
Figure 4.9: The beam center position as a function of run number. The left and right panels represents x and y coordinates of the beam center, respectively.

At first, the DCA is calculated only in x-y plane. The DCA is calculated with the outgoing vector and the optimized position of the innermost associated hit which are calculated by the track fitting, described in Sec 4.4.3. An circle extrapolation is performed from the optimized position with the diameter calculated with p_T and the strength of the magnetic field, 0.9 T. Then, the closest approach of the circle to the beam center is calculated. The sign is defined as follows:

- If the collision vertex is located inside of the circle, the sign is positive.

- Otherwise, the sign is negative.

Then, the DCA$_z$ is calculated as follows:

$$DCA_z = z_0 - |d\phi| \cdot \frac{p_z R}{p_T} - \mathsf{bbcz},\qquad(4.28)$$

where, z_0 is z coordinate of the innermost hit, $d\phi$ is the angle of the rotation during a traveling from the closest approach to the innermost hit, and R is the rotation diameter of the circle extrapolation. Only the DCA in x-y plane is used, and DCA_z is not used in this analysis.

Figure 4.10 shows the DCA resolution of electrons as a function of p_T evaluated by a single-track simulation. In the simulation, DCA with respect to the track generated point is calculated, and the contribution of the beam size is not included in the resolution. The DCA resolution at $p_T = 1$ GeV/c is $\sim$60 μm, then decreases to $\sim$20 μm at $p_T = 5$ GeV/c, which corresponds to the position resolution of the VTXP in azimuthal direction times $\sqrt{2}$. The DCA resolution of hadrons is evaluated with data by fitting a peak of the DCA distribution with a Gaussian, and it is compared with a simulation including the contribution of the beam size. Details of the comparison is presented at Sec. 4.9.1. The resolution of the data is $\sim$140 μm at $p_T = 1$ GeV/c and gradually improved up to $\sim$130 μm at $p_T = 5$ GeV/c, and it is successfully reproduced by the simulation.
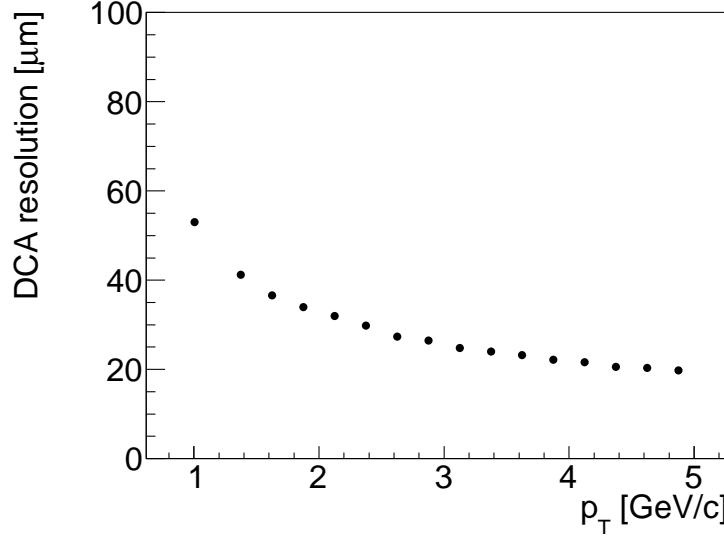
Figure 4.10: The DCA resolution of electrons as a function of p_T evaluated by a single-track simulation. In the simulation, DCA with respect to the track generated point is calculated, and the contribution of the beam size is not included in the resolution.

4.4.6 Detector Alignment

In order to achieve to measure DCA with a good precision, a calibration of geometrical positions of the VTX modules are essential. The geometrical positions are aligned with respect to the central arms. The CNT-VTX tracks measured in the data with the normal magnetic field condition (B = 0.9 T) are used for the alignment. The procedure of the alignment is as follows:

1. CNT-VTX tracks are reconstructed.

2. Residuals between an associated hit position and projection position in azimuthal and z directions are calculated, and a distribution of the residual is created for each modules for each direction. The projection position is calculated with p_T, phi0, and the0.

3. Each module are shifted by keeping its radial coordinate.

4. Step 1-3 are repeated until the shifts of the modules are converged.

In order to align the modules more precisely in x-y plane, their radial coordinates are tuned. The radial coordinate is tuned with the residual distribution as a function of the azimuth of associated hits. A misalignment of the radial coordinate causes an approximately linear correlation between the residual and the azimuth. A misalignment of the tilting angle of the module in x-y plane also causes another linear

correlation. However, it is difficult to distinguish when only taking care of x-y plane, and thus, a shift of radial coordinate is carried out to cancel the dependence. The left and right panel of Fig. 4.11 show the residuals at B0 of azimuthal and z directions, respectively, as a function of phi0, which demonstrate the residuals of each modules. Although there still exists a misalignment, enough DCA resolution has been achieved as is discussed at Sec. 4.4.5 and 4.9.1.
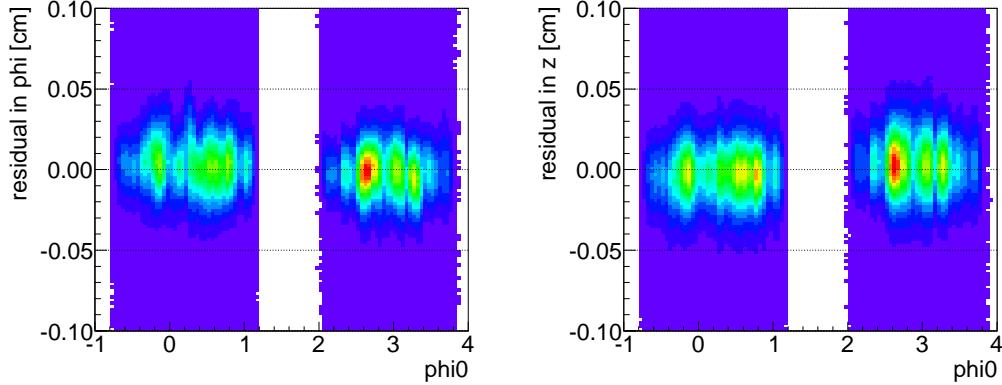
Figure 4.11: Residuals between an associated hit position and projection position at B0 in azimuthal (left) and z (right) directions as a function of phi0.

4.5   Event and Track Selection

4.5.1   Event and Track Selection

Following cuts are applied to select events and tracks in this analysis:

- Event selection

    - $|\mathsf{bbcz}| \leq 8$ cm

- Track selection

    - $\mathsf{quality} \geq 17$
    - $|\mathsf{zed}| \leq 75$
    - $\mathsf{nvtxhit} \geq 3$
    - $\mathsf{nvtxhit0} \geq 1$
    - $\mathsf{vtxchi2ndf} \leq 3$

- Electron candidate selection

- n0 $\geq$ 1
- disp $\leq$ 8 cm
- chi2/npe0 $\leq$ 25 cm^2
- dep $\geq$ -2
- prob $\geq$ 0.01
- $\sqrt{\mathsf{emcsdz\_e}^2 + \mathsf{emcsdphi\_e}^2} \leq 4$

- Hadron selection

  - n1 $= 0$

A set of the cuts about the track selection is called "good track cut" and about the electron candidate selection is called "e-ID cut" in this analysis. A hadron sample is utilized for some studies. The charged tracks selected by the good track cut and the hadron selection are called hadrons in this analysis.

The left and right panel of Fig. 4.12 show the efficiencies for the e-ID cut and hadron selection of electrons and charged pions, respectively, which are evaluated by a single-track simulations. The solid black circles represent the efficiencies for the e-ID cut. The efficiencies of electrons and charged pions are around 90% and $< 0.01\%$ at $1 < p_T < 5$ GeV/c, respectively. The open red and blue circles represent the efficiencies for the cut sets about RICH ($\mathsf{n0, disp, chi2/npe0}$) and EMCal ($\mathsf{dep, prob}$), respectively. The black open circles represent the efficiency for the hadron selection. The efficiencies of electrons and charged pions are around 2.5% and 100% at $1 < p_T < 4$ GeV/c, respectively. The red points of charged pions start increasing and black points start decreasing above 4 GeV/c since charged pions start radiating Cherenkov photons. In these simulations, hadron contamination in the electron candidates is negligibly small, especially at $p_T < 4$ GeV/c. However, a contribution of random associations of hits on the RICH is not negligible. Total hadron contamination in the inclusive electron is $\sim$1% at $p_T < 4$ GeV/c and increases to $\sim$2.3% at $p_T < 5$ GeV/c. The evaluation of the contribution is described at Sec. 4.8.6.

4.5.2   Isolation Cut

In addition to the cuts listed above, an isolation cut is performed to increase the fraction of the heavy-quark electrons in inclusive electrons. It is required in the isolation cut that there is not a hit around any associated VTX hit. Since the opening angle of an electron and a positron from a light neutral meson or a photon conversion is small these electrons create hits closely on the VTX. The decays from light neutral mesons and photon conversions are main background source, the isolation cut can significantly increase the fraction. In addition, due to small opening angle, the alignment of the hits created by the electron and positron are mainly decided by the magnetic field. For example, if the opening angle is exactly 0, azimuthal angle of
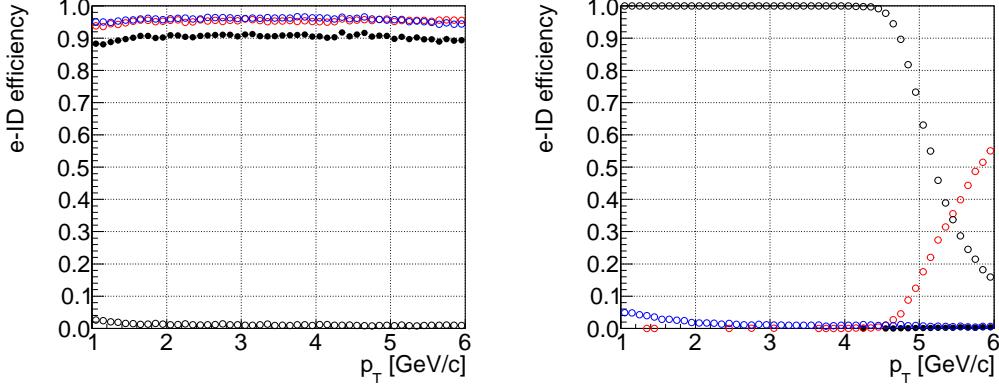
Figure 4.12: The efficiencies for the e-ID cut and hadron selection of electrons (left) and charged pions (right) evaluated by a single-track simulations. The solid black circles represent the efficiencies for the e-ID cut. The efficiencies of electrons and charged pions are around 90% and $< 0.01\%$ at $1 < p_T < 5$ GeV/c, respectively. The open red and blue circles represent the efficiencies for the cut sets about RICH ($\mathsf{n0, disp, chi2/npe0}$) and EMCal ($\mathsf{dep, prob}$), respectively. The black open circles represent the efficiency for the hadron selection. The efficiencies of electrons and charged pions are around 2.5% and 100% at $1 < p_T < 4$ GeV/c, respectively.

the hit created by the electron is always smaller than that created by the positron in the magnetic field of this experimental setup. On the other hand, the opening angles of the daughters of the heavy quarks are large due to large q-values, and thus, the fraction of the heavy-quark electrons rejected by the isolation cut is small. Following valuables are utilized for the cut:

$$\mathsf{cdphi} = c(\phi_{ass} - \phi_{near})[rad], \tag{4.29}$$

$$\mathsf{dz} = z_{ass} - z_{near}[cm], \tag{4.30}$$

$$\mathsf{dr} = \sqrt{(x_{ass} - x_{near})^2 + (y_{ass} - y_{near})^2}[cm], \tag{4.31}$$

where c is the charge of the track, ϕ_{ass} and ϕ_{near} are the positions in the azimuthal direction of an associated hit and a hit close to it, respectively, and $(x_{ass}, y_{ass}, z_{ass})$ and $(x_{near}, y_{near}, z_{near})$ are 3D position of an associated hit and a hit close to it, respectively. The left panel of Fig. 4.13 shows cdphi distributions of the electrons from π^0 decays (red) and charm electrons (blue) with $1.0 < p_T < 1.25$ GeV/c in a single-track simulation. The entries are normalized by the number of electron tracks. Hits located close to the electron tracks of π^0 decays much larger than that of charm electrons, and the cdphi of the electrons from π^0 decays distributes asymmetric. The cdphi of the inclusive electrons in the data also distributes asymmetric, which is shown in the right panel of Fig. 4.13. More detail comparison between the data and simulation is presented in Sec. 4.8.8. In this analysis, only hits close to less than ± 0.5 cm in the azimuthal direction and ± 3 cm in the z direction from projection

points of CNTs are utilized for this cut. Table 4.5 shows the cut parameters about the isolation cut. In order to take account of the asymmetric distributions, asymmetric cut parameter sets are employed. Since there are overlap regions between modules in the azimuthal direction, it requires that two hits are displaced more than twice of the readout pixel size or on the same modules.
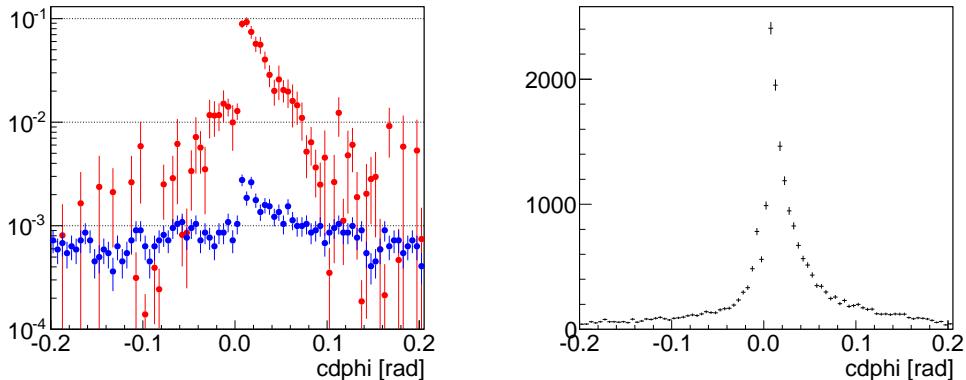
Figure 4.13: Left: `cdphi` distributions of the electrons from π^0 decays (red) and charm electrons (blue) $1.0 < p_T < 1.25$ GeV/c in a single-track simulation. Right: the distribution of the inclusive electrons in the data.

Table 4.5: Requirements of rejection by the isolation cut.

barrel	requirement
B0	-0.05<cdphi<0.2 ∩ |dz| <0.3 ∩ (dr>0.01 ∪ |dz| >0.085 ∪ (on same module))
B1	-0.02<cdphi<0.1 ∩ |dz| <0.3 ∩ (dr>0.01 ∪ |dz| >0.085 ∪ (on same module))
B2	-0.03<cdphi<0.045 ∩ |dz| <0.5 ∩ (dr>0.016 ∪ |dz| >0.2 ∪ (on same module))
B3	-0.03<cdphi<0.03 ∩ |dz| <0.5 ∩ (dr>0.016 ∪ |dz| >0.2 ∪ (on same module))

Around 80% of the conversion electrons and the electrons from π^0 decays are rejected by the isolation cut, whereas only 10% of the charm and bottom electrons are rejected, shown in Sec. 4.8.7. By using the cut, the fraction of the heavy-quark electrons in the inclusive electrons increases up to more than 50% at $p_T > 1$ GeV/c. The efficiency of the isolation cut and the fraction in the inclusive electrons of each electron source are described in Sec. 4.8.7 and 4.8.8.

4.6 Run Selection and Performance Stability

4.6.1 Run Selection

In this analysis, the beam center is utilized to calculate the DCA. Therefore, the beam center position should be measured precisely. However, the beam centers for

some runs were failed to measure. As is explained at Sec. 4.4.4, the beam center is calculated with the collision vertices reconstructed by the stand-alone tracks, but only 1/3 of events can succeed to measure the vertex. Therefore, when the number of events in a run is small, the beam center can not be measured with a good precision. Figure 4.14 shows widths of the distributions of the reconstructed collision vertices. The width is calculated by fitting the distribution with a Gaussian around the peak of the distribution. Only runs whose widths in the x and y directions are less than 300 μm are defined as good runs and the others are not used in this analysis.
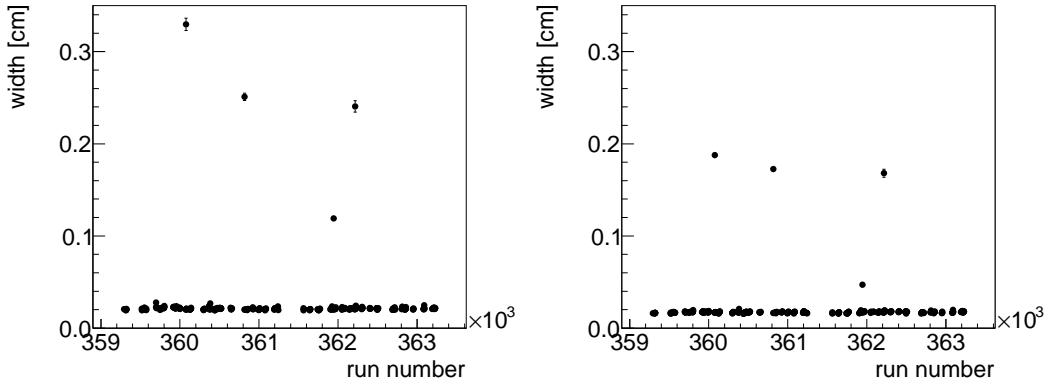
Figure 4.14: Widths of the distribution of the reconstructed collision vertices in x (left) and y (right) directions.

4.6.2 Performance Stability

A DCA distribution and a survival fraction after the isolation cut for each of the good runs are checked. The DCA distribution in the data is necessary to be understand well in order to simulate the distributions of all electron sources. The survival fraction in the data is also necessary to be understand well since it affects yield of each electron source after the isolation cut. Therefore, a run which has a strange DCA distribution or a strange survival fraction can disturb the final result. Figure 4.16 shows mean values and widths of the DCA distribution of charged tracks with $p_T > 1$ GeV/c. The mean and width were calculated by fitting the DCA distribution with a Gaussian. The mean should be independent of runs, and all the good runs satisfies following:

$$|m(run) - \overline{m}| < 3\sigma_m(run) + 5 \; [\mu\mathrm{m}], \qquad (4.32)$$

where $m(run)$ and $\sigma_m(run)$ are the mean and the fitting error for the mean of a run, and $\overline{m}$ is the mean of $m(run)$ calculated by fitting with a constant. $\overline{m}$ is -17 μm. The mean is shifted from 0 since the reconstructed p_T of a CNT is smaller than the p_T around the collision vertex due to energy loss at the VTX. Figure 4.15 illustrates a reconstructed path and a actual path. Due to the energy loss, a bending

84

of the reconstructed path becomes larger than that of the actual path, and thus, the collision vertex tends to be outside of a circle of the reconstructed path, which means the DCA tends to be smaller than the actual DCA. Since the resolution of the DCA
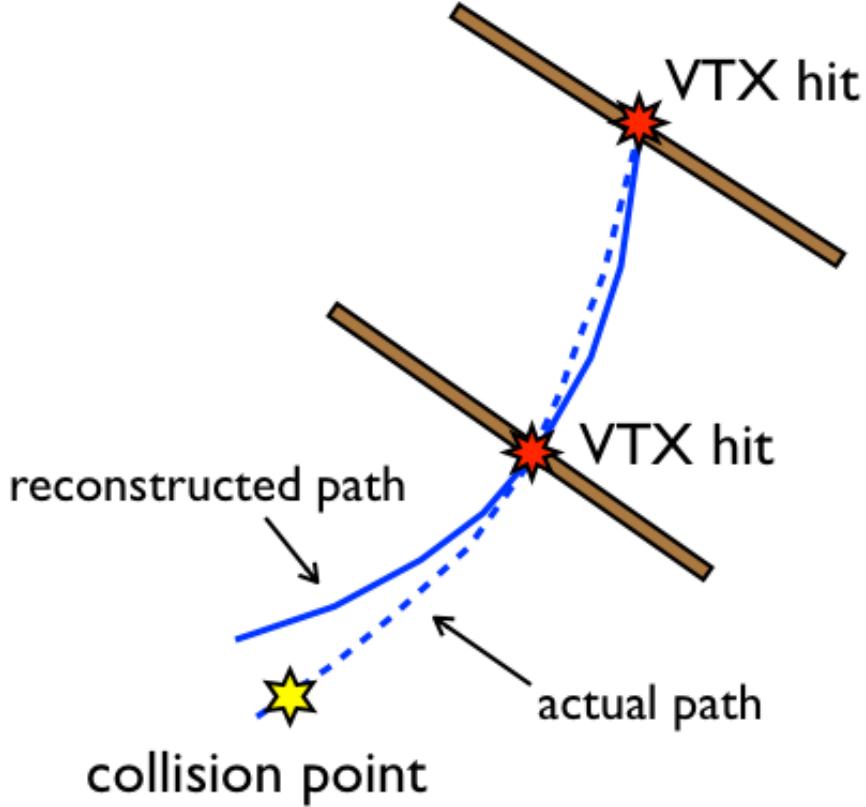
Figure 4.15: An illustration of a reconstructed path and an actual path.

distribution is 130-140 μm, an effect of the deviation, 5 μm, is very small.

The widths slightly have a dependence on runs. Figure 4.17 shows the distribution of the widths. The red line is a fitting result by a Gaussian and 1 σ of the Gaussian is around 8 μm. The beam size changed from 120 μm to 130 μm during a beam fill. The variation of the widths can almost be explained by the variation of the beam size.

The ratio of the entries at a tail and peak regions of hadron DCA distribution is also checked. The ratio is very important for this analysis. The tail region is defined as $|DCA| > 800$ μm and the peak region is defined as $|DCA| < 500$ μm. The left panel in Fig. 4.18 shows the ratio of each run. Associated error bars correspond to statistical errors. The errors are calculated by assuming both the entries distribute independent normal distributions. The ratios are fitted by a constant and the fitting result is defined as a center value. The right panel in Fig. 4.18 shows a distribution
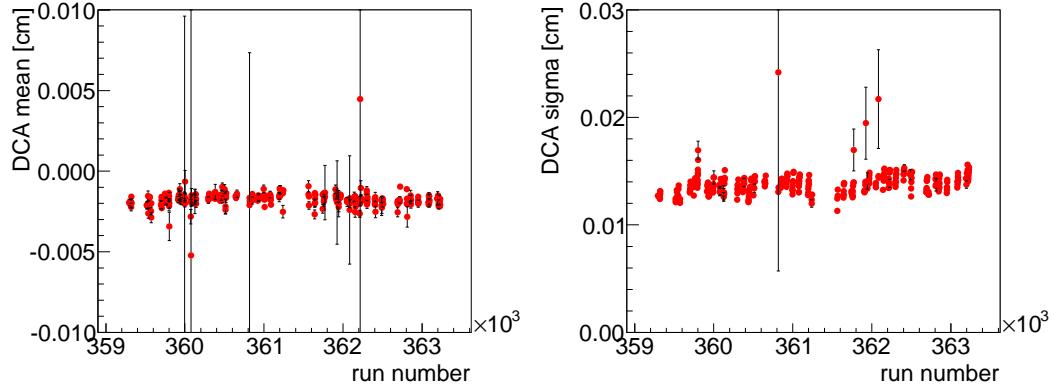
Figure 4.16: Means (left) and widths (right) of DCA distributions of charged tracks for good runs.

of differences between the ratios and the center value normalized by their statistical errors. All of the normalized differences are within ± 3.

The survival fraction of charged tracks with $p_T > 1\,\mathrm{GeV}/c$ after the isolation cut is calculated for each run. The left panel in Fig. 4.19 shows the fraction of each run. Associated error bars correspond to statistical errors. The errors are calculated by assuming the distribution of the fraction is a binomial distribution. The fractions are fitted by a constant and the fitting result is defined as a center value. The right panel in Fig. 4.19 shows a distribution of differences between the fractions and the center value normalized by their statistical errors. Almost all of the normalized differences are within ± 3.

4.6.3 DCA Distribution of Inclusive Electron

Figure 4.20 shows DCA distributions of inclusive electrons and hadrons for $p_T > 1.5\,\mathrm{GeV}/c$. The red and black lines show the distributions of electrons and hadrons. Mean and width values are different between the distributions. When the distributions are fitted by Gaussians, and their mean and width values are defined as the mean and RMS values of the Gaussians, the mean and width of electrons are -29.6 $\pm$ 1.5 μm and 149.4 $\pm$1.3 μm and those of hadrons are -12.2 $\pm$ 0.1μm and 135.1 $\pm$ 0.1 μm. The difference of the mean values is derived from a difference of energy losses at VTX between electrons and pions, which is main component of hadrons. Since the main component of the inclusive electrons is the charm electrons, whereas, the main component of the inclusive hadrons is pions which are produced by beam collisions or decays of short-life hadrons, such as ρ or ω. Therefore, the width of the inclusive electrons is larger than that of the inclusive hadrons.

The left panel of Fig. 4.21 shows DCA distributions of electrons and positrons for $p_T > 1.5\,\mathrm{GeV}/c$. The blue and red lines show the distributions of electrons and

86
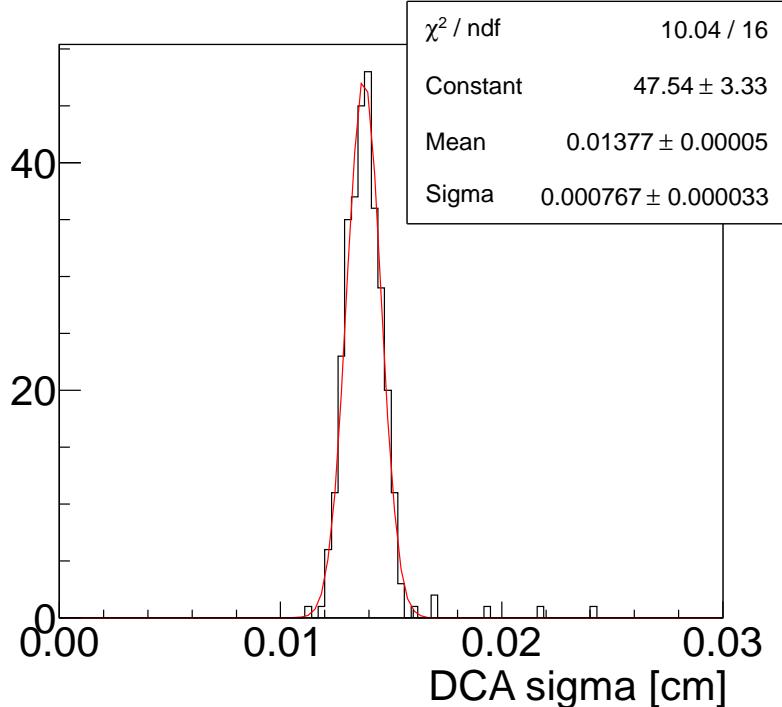
Figure 4.17: Distribution of widths of DCA distributions of runs.

positrons. The right panel of Fig. 4.21 shows a ratio of the DCA distributions as a function of DCA. The ratio is fitted by a constant and the red line in the panel shows the result. χ^2/NDF is good and the ratio is well approximated by a constant. Therefore, there is not a clear difference between DCA distributions of electrons and positrons, and they can be handled together. The fitting result is not 1 since reconstruction efficiencies, especially detector acceptance, are different.

4.7   Simulation Tuning

Simulation tunings are important since results of simulation studies have important roles in this analysis. In this section, the tuning about a detector response and a creation of the heavy-quark electrons by a simulation are summarized.

4.7.1   Detector Response

In order to reproduce a detector response, a GEANT3-based simulator, called PISA [61], is utilized. All of the materials in the experimental setup are installed, and dead and unstable regions of the detectors are masked in the PISA simulation. A single-track simulation with the PISA simulation is performed to check a detector response is
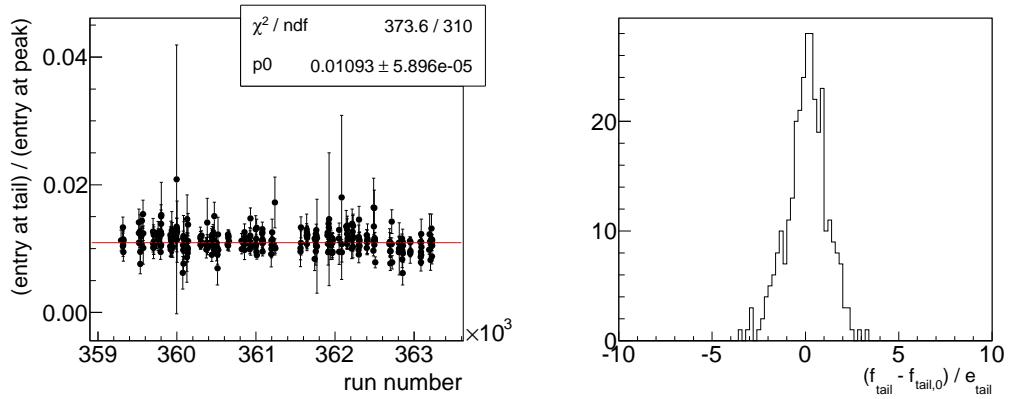
Figure 4.18: Left : Ratios of entries at a tail and peak of a DCA distribution of each run. Right : A distribution of the ratios normalized by their statistical errors.
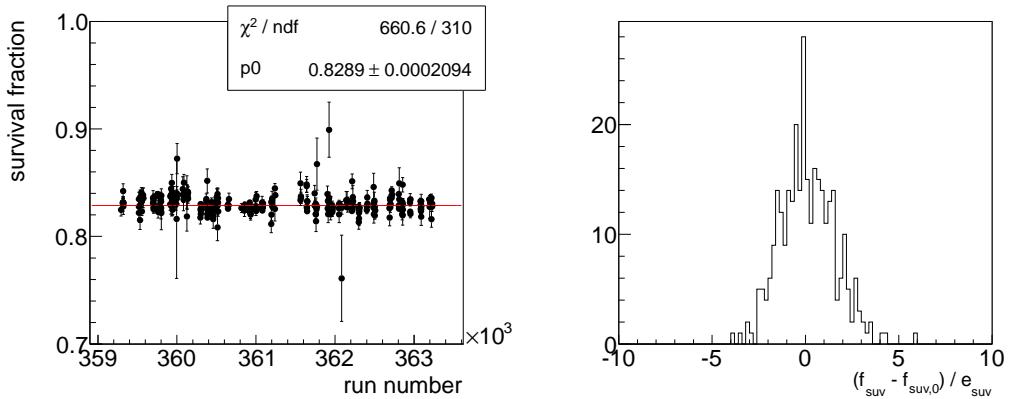
Figure 4.19: Left : A survival fraction after the isolation cut of each run. Right : a distribution of the fractions normalized by their statistical errors.

88
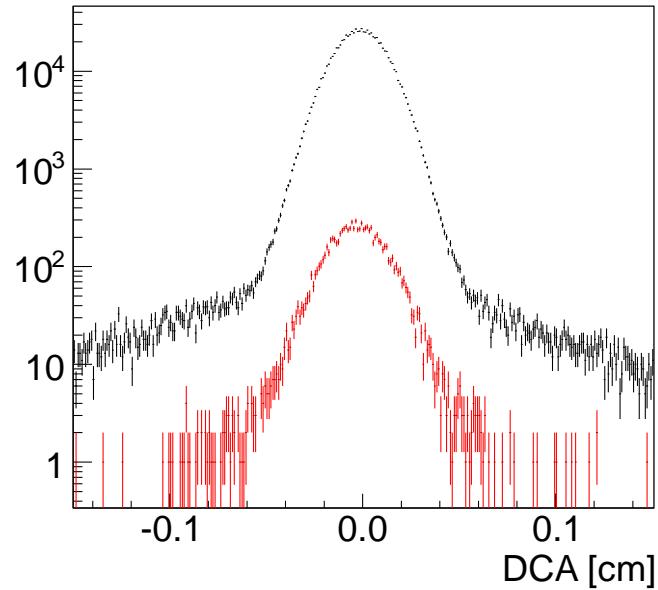
Figure 4.20: DCA distributions of inclusive electrons and hadrons for $p_T > 1.5$ GeV/c. The red and black lines show the distributions of electrons and hadrons.
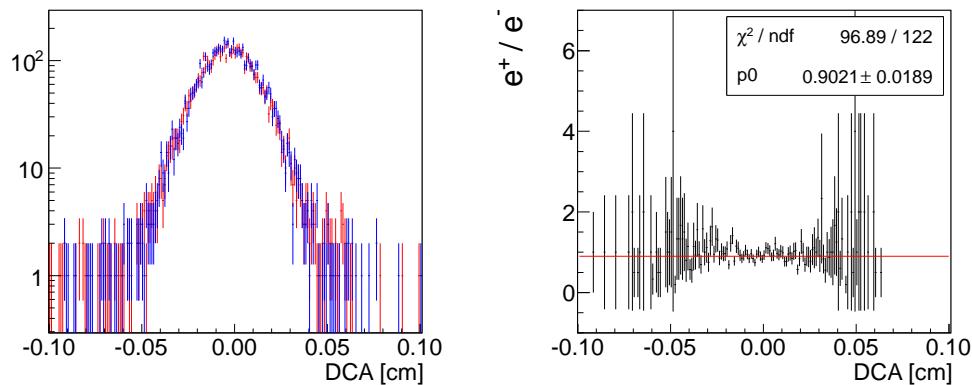
Figure 4.21: Left: DCA distributions of electrons and positrons for $p_T > 1.5$ GeV/c The blue and red lines show the distributions of electrons and positrons. Right: a ratio of the DCA distributions as a function of DCA.

surely reproduced. The responses are checked with the MB data. The responses of the detectors at the central arm are checked with electrons and the response of the VTX is checked with charged pions. The reason why charged pions are used is that statistics of electrons in the MB data after requiring an association of VTX hits is very small. Kinematical conditions of a sample of electrons and charged pions in the simulation are as follows:

- Transverse momentum: $0 < p_T < 7$ GeV/c (flat)

- Pseudo-rapidity: $|\eta| < 0.5$ (flat)

- Azimuthal angle: $0 < \phi < 2\pi$ (flat)

- Collision vertex (x, y): (0.08343cm, 0.2019cm) + a Gaussian distribution with $\sigma = 100$ μm

- Collision vertex (z): $|z - vertex| < 20$ cm (flat)

The electrons and charged pions are weighted according to their p_T and z coordinate of the collision vertex so that their distributions reproduce those in the data. The left and right panels in Fig. 4.22 show p_T distributions of the electrons and charged pions, respectively. The red histogram represents the weighted count of tracks in the simulation and the black histogram represents the raw count of tracks in the data. The red histograms reproduce the black histograms at $1 < p_T < 5$ GeV/c.
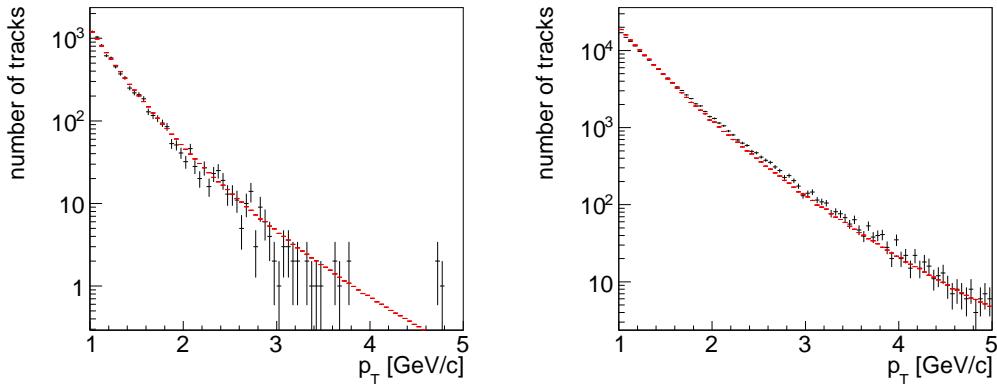
Figure 4.22: p_T distributions of the electrons (left) and charged pions (right) in a single-track simulation and the MB data. The red histogram represents the weighted count of tracks in the simulation and the black histogram represents the raw count of tracks in the data.

Analysis Variables

Figure 4.23 shows the distributions of the analysis variables related to the e-ID cut in the data and simulation. The black and red points represent the distributions of the data and simulation, respectively. The distribution of a variable is created by tracks with the e-ID cut and the good track cut without cuts related to the VTX and the cut related to itself, i.e. when $n0$ distribution is created, all cuts except for either $n0$ cut or the cuts related to the VTX are applied. The total weighted counts of the distributions are scaled to be the same as the total entries of the data. Although there are small differences between the distributions of the data and simulation, their impacts on the track selection is small.
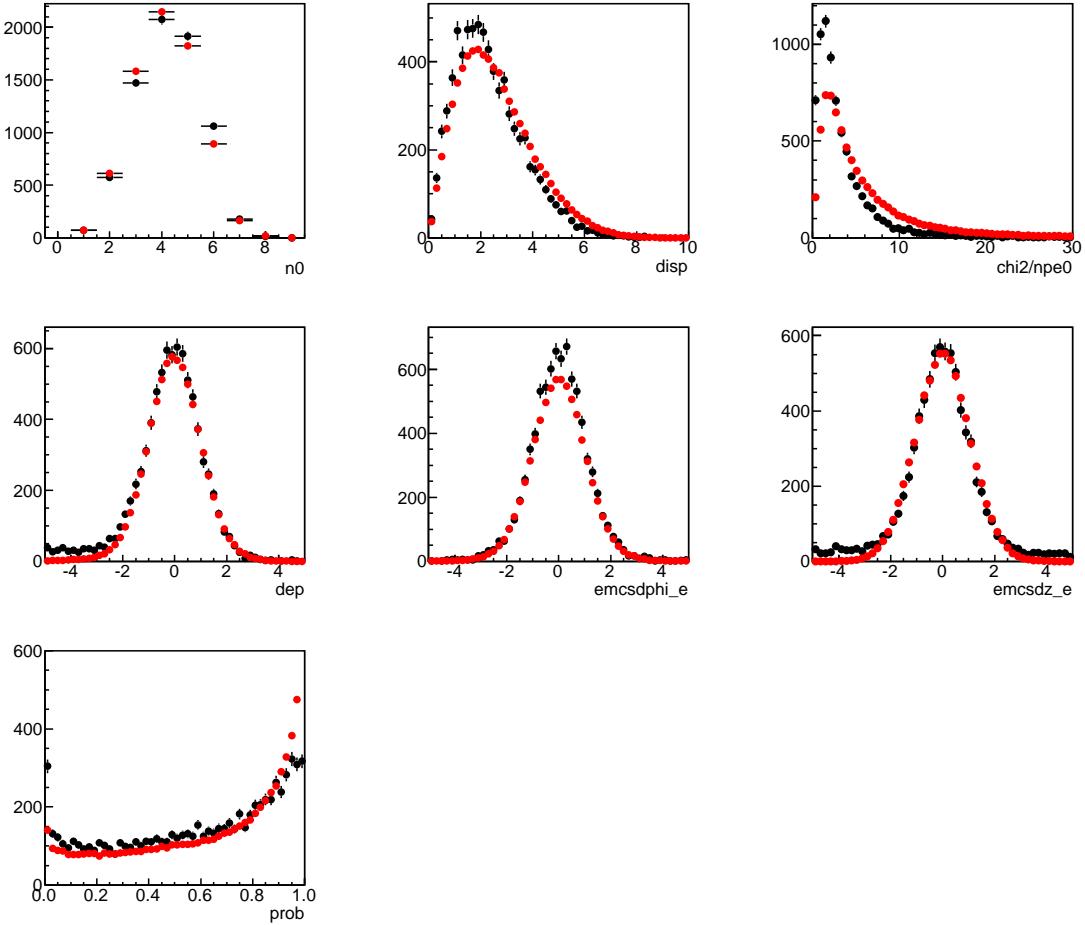
Figure 4.23: Distributions of the analysis variables related to the e-ID cut in the data and the simulation. The red and the black points represent the distributions of analysis variables for e-ID cut of the data and the simulation, respectively. The distribution of a variable is created by tracks with the e-ID cut and the good track cut without cuts related to the VTX and the cut related to itself.

χ_c^2 in Eq. 4.18 can be decomposed into three terms, χ_ϕ, χ_z, and χ_{ang}, as follows:

$$\chi_c^2 = \chi_\phi^2 + \chi_z^2 + \chi_{ang}^2, \tag{4.33}$$

$$\chi_\phi^2 = \sum_{0 \le i \le n-1} \frac{\Delta\phi_i^2}{\sigma_{\phi,i}^2}, \tag{4.34}$$

$$\chi_z^2 = \sum_{0 \le i \le n-1} \frac{\Delta z_i^2}{\sigma_{z,i}^2}, \tag{4.35}$$

$$\chi_{ang}^2 = \sum_{1 \le i \le n-2} \left(\frac{\Delta\theta_{xy,j}^2}{\sigma_{\theta_{xy},j}^2} + \frac{\Delta\theta_{rz,j}^2}{\sigma_{\theta_{rz},j}^2} \right) + \frac{\Delta\theta_{xy,n-1}^2}{\sigma_{\theta_{xy},n-1}^2 + \sigma_{\mathsf{phi0}}^2} + \frac{\Delta\theta_{rz,n-1}^2}{\sigma_{\theta_{rz},n-1}^2 + \sigma_{\mathsf{the0}}^2}. \tag{4.36}$$

Figure 4.24 and 4.25 show distributions of χ_c, χ_ϕ, χ_z, and χ_{ang} for CNT-VTX tracks with 3 associated hits and 4 associated hits, respectively. The black and red points represent the distributions of the data and simulation, respectively. The total weighted counts of the distributions of the simulation are scaled to be the total entries of the data. Different σ values in Eq. 4.34, 4.35, and 4.36 are utilized for the calculation for the data and simulation in order for these distributions to be the same.

Detector Acceptance

In order to reproduce a detector acceptance, a fiducial cut is applied in the simulation. All of the runs are divided into 8 groups and a different fiducial cut is applied for each of them. The fiducial cuts reproduce the dead area of a part of the runs, and these runs are called "stable runs". However, several runs have additional dead area, and these runs are called "unstable runs". In this analysis, both the stable and unstable runs are analyzed. The left panel of Fig. 4.26 shows the DCA distributions of the inclusive electrons with $p_T > 1$ GeV/c. The red and blue histograms represent the DCA distributions in all and the unstable runs, respectively. The right panel in Fig. 4.26 shows a ratio of the numbers of electrons of the unstable runs and all the runs as a function of DCA. The red line represents a result of a fitting by a constant. The constant fitting well matches the ratio, which means that a dependence on the DCA is small. The survival fraction for each electron sources may be affected. The effect is evaluated in Sec. 4.8.7.

Figure 4.27 and 4.28 show distributions of dcphi and zed of electrons with $p_T > 0.5$ GeV/c, respectively. The black and red points represent the distributions in the data of the stable runs of a run group and in the simulation, respectively. The comparisons are performed with all the track selection except for the cuts related to the VTX. The distributions of the simulation are scaled so that the number of CNTs in the simulation is the same as that in the data. The distributions are successfully reproduced by the simulation. Hit distributions of the VTX were compared between those in the data of the stable runs and simulation. Since the number of electrons is small,
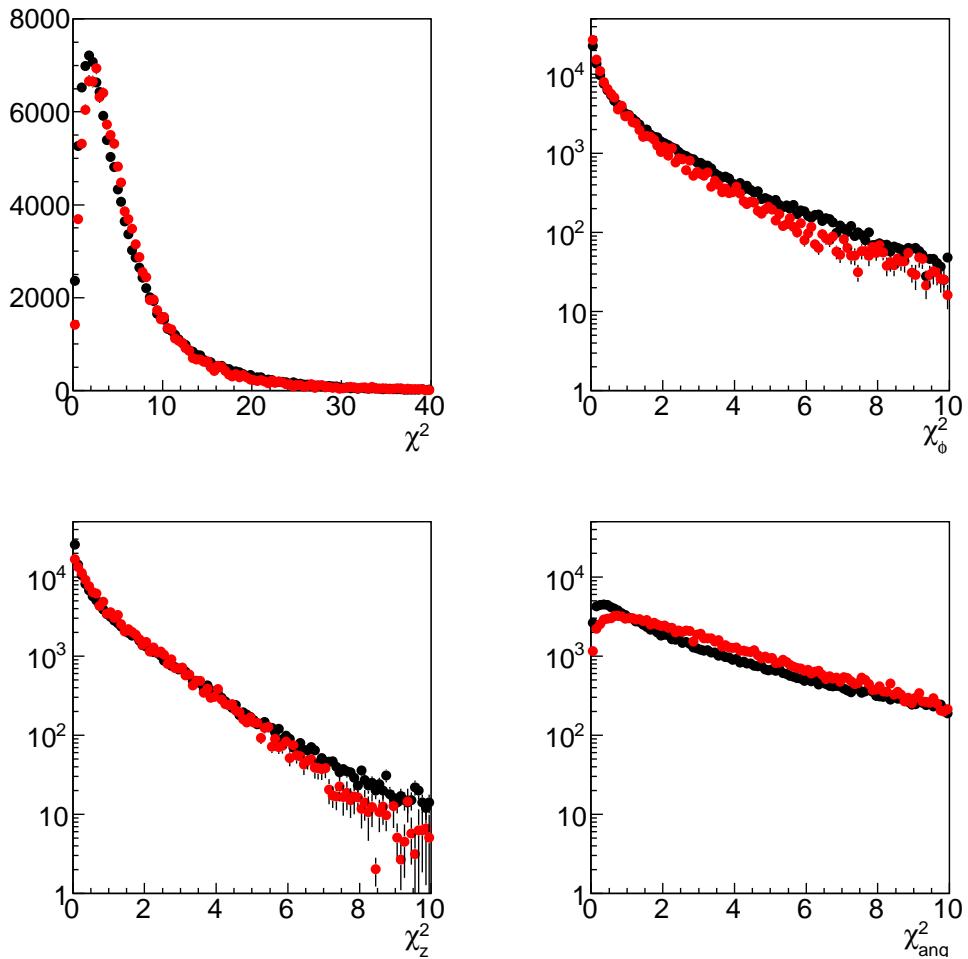
Figure 4.24: Distributions of chi-square components for CNT-VTX tracks with 3 associated hits in the data (black) and simulation (red). The top left, top right, bottom left, and bottom right panels show the distributions of total chi-square, χ^2_ϕ, χ^2_z, and χ^2_{ang}, respectively.
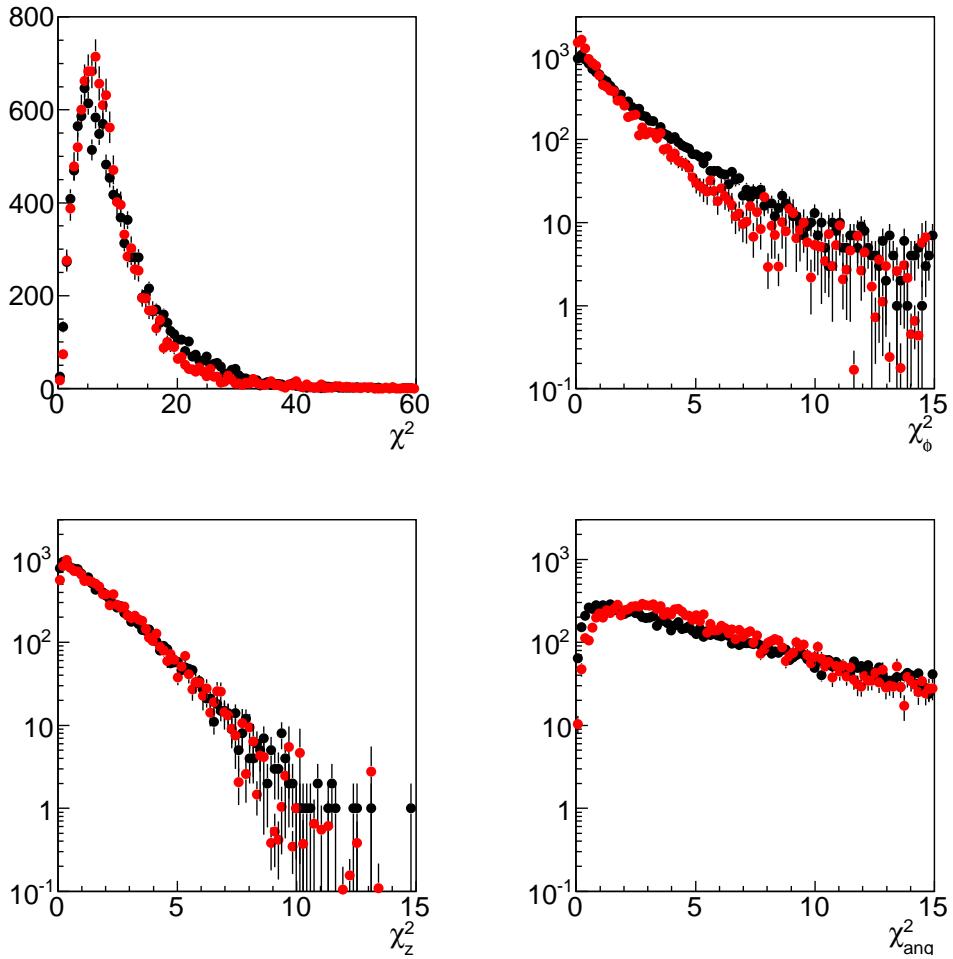
Figure 4.25: Distributions of chi-square components for CNT-VTX tracks with 4 associated hits in the data (black) and simulation (red). The top left, top right, bottom left, and bottom right panels show the distributions of total chi-square, χ^2_ϕ, χ^2_z, and χ^2_{ang}, respectively.
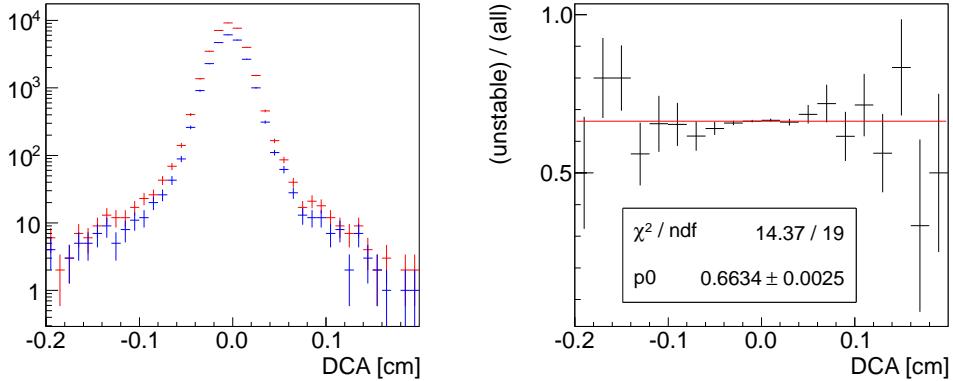
Figure 4.26: Left: the DCA distributions of the inclusive electrons in all (red) and the unstable runs (blue).
Right: a ratio of the number of electrons of the unstable runs over that of all the runs as a function of DCA. The red line represents a result of a fitting by a constant. The constant fitting well matches the ratio, which means that a dependence on the DCA is small.

the comparison is performed with all charged particles in the data and charged pions in the simulation. Figure 4.29 and 4.30 show hit distributions of the VTX in the azimuthal direction and the z direction, respectively, of the data for the stable runs of a run group and simulation. p_Ts of the tracks are larger than 1 GeV/c. The top-left, top-right, bottom-left, and bottom-right panels show the hit distributions at B0, B1, B2, and B3, respectively. The distributions of the simulation are scaled so that the number of CNTs in the simulation is the same as that in the data. The comparisons are performed with all the track selection except for the e-ID cut. The distributions are successfully reproduced by the simulation. The distributions of the other run groups are also reproduced by the simulation at the same level. The fiducial cut of the run group with the largest data (Gr7) was applied in PISA simulations. In addition, two more fiducial cuts are applied to evaluate an uncertainty derived from differences of the acceptance in simulation studies. The cut with relatively large (Gr2) and small (Gr3) dead area in the VTX are utilized.

4.7.2 Creation of Heavy Quark

The DCA distribution and the survival fraction for the charm and bottom electrons are evaluated by a simulation with PYTHIA code [62]. The PYTHIA is a well-known event generator for $p+p$ collisions. Parameters in the PYTHIA are tuned to reproduce previous results of heavy quark production measured by several experiments [63, 15]. Since all the charm or bottom hadrons are handled inclusively, the production ratios of the hadrons (D^+/D^0, B^+/B^0 etc) are important parameters. However, the ratios of experimental results are not reproduced by the PYTHIA with the default setup,
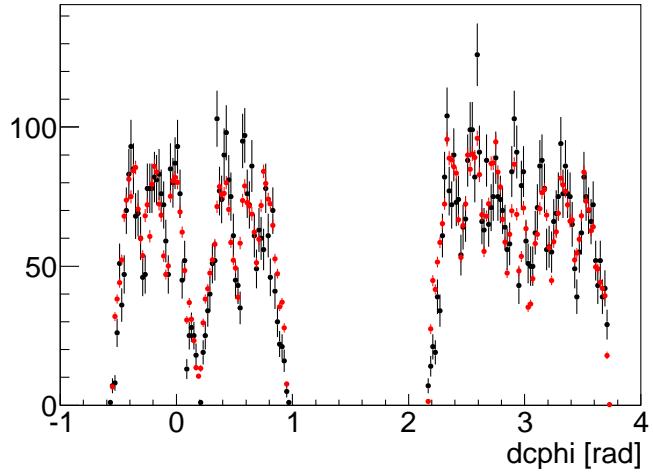
Figure 4.27: Distributions of dcphi of electrons with $p_T < 0.5$ GeV/c in the data of the stable runs of a run group and in the simulation. The black and red points represent the distributions of the data and simulation, respectively. The distributions of the simulation are scaled so that the number of CNTs in the simulation is the same as that in the data.
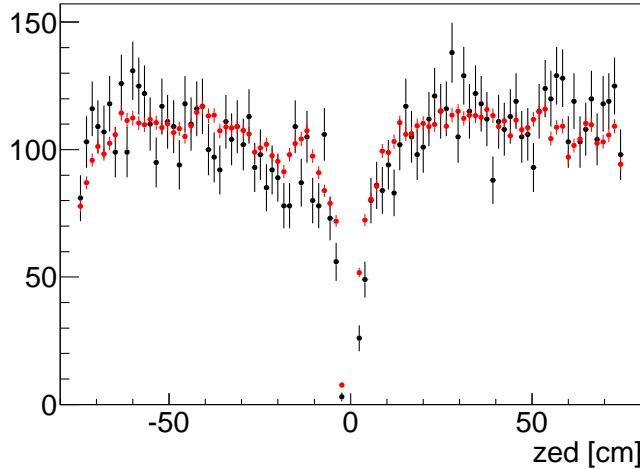
Figure 4.28: Distributions of zed of electrons with $p_T < 0.5$ GeV/c in the data of the stable runs of a run group and in the simulation. The black and red points represent the distributions of the data and simulation, respectively. The distributions of the simulation are scaled so that the number of CNTs in the simulation is the same as that in the data.
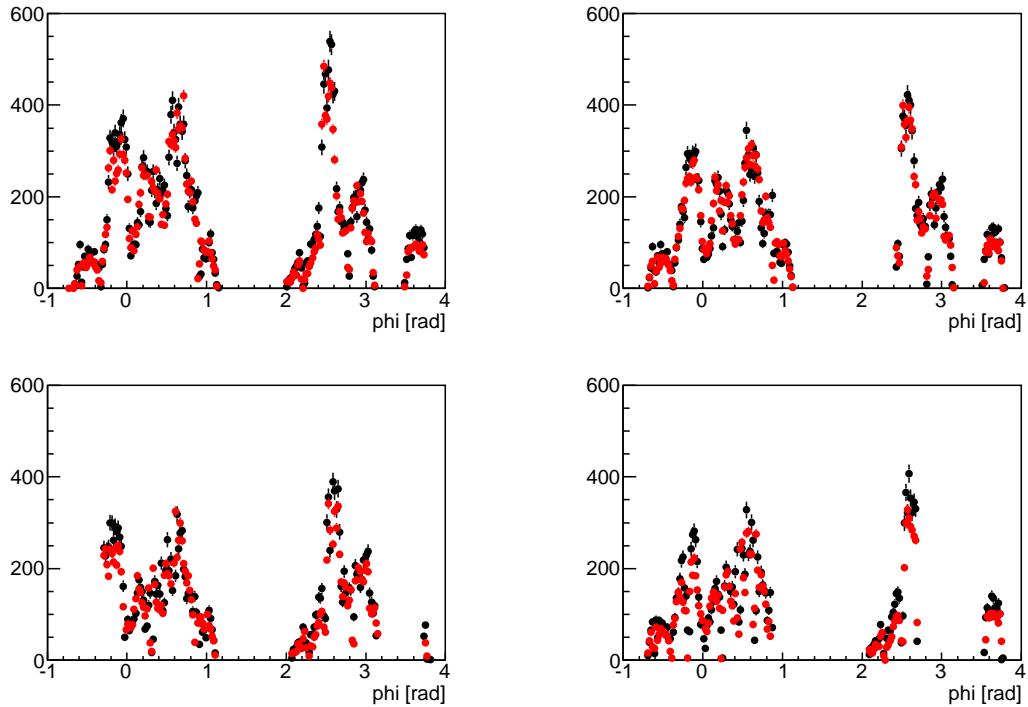
Figure 4.29: Hit distributions of the VTX in the azimuthal direction of the data for the stable runs of a run group and in the simulation. The top-left, top-right, bottom-left, and bottom-right panels show the hit distributions at B0, B1, B2, and B3, respectively. The black and red points represent the distributions of the data and simulation, respectively. The distributions of the simulation are scaled so that the number of CNTs in the simulation is the same as that in the data.
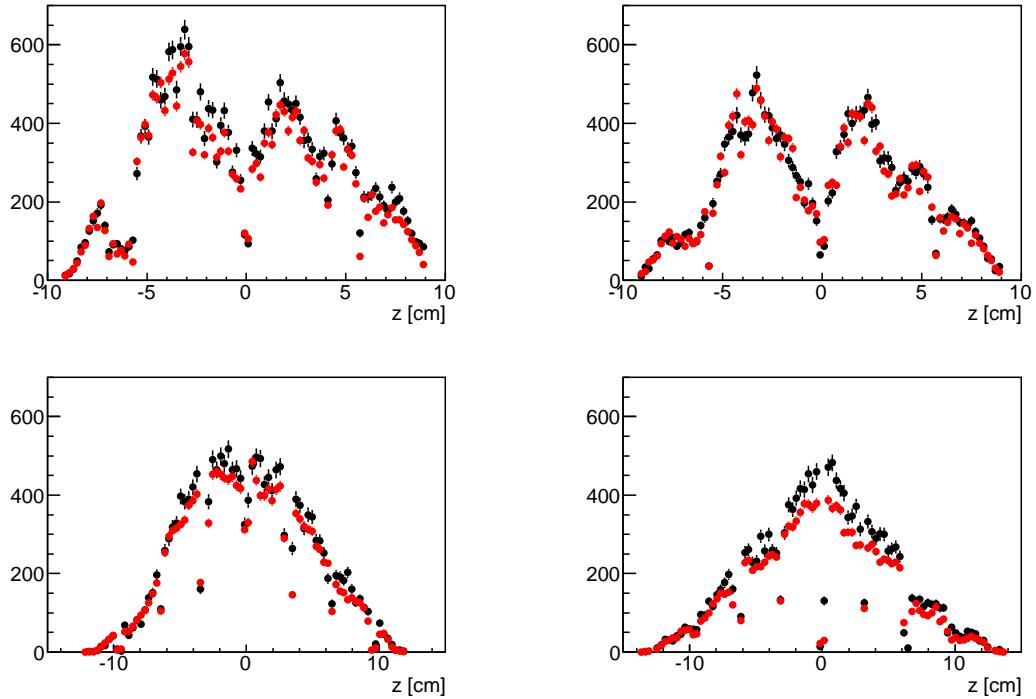
Figure 4.30: Hit distributions of the VTX in the z direction of the data for the stable runs of a run group and in the simulation. The top-left, top-right, bottom-left, and bottom-right panels show the hit distributions at B0, B1, B2, and B3, respectively. The black and red points represent the distributions of the data and simulation, respectively. The distributions of the simulation are scaled so that the number of CNTs in the simulation is the same as that in the data.

which is a well-known problem [64, 65, 66, 67, 68]. The ratios are also tuned according to experimental results. Since a dependence of the ratios on collision systems is not significant, the results measured with the several systems are averaged. Tuning parameters of PYTHIA are summarized at Table 4.6, and the ratios after the tuning are summarized in Table 4.7.

Table 4.6: A set of PYTHIA parameters used in this analysis.

parameter name	value	
charm mass	1.23 GeV	
bottom mass	4.17 GeV	
k_T	1.5 GeV	
k factor	2.5	
PARJ(13)	0.63 (charm)	0.75 (bottom)
PARJ(2)	0.20 (charm)	0.29 (bottom)
PARJ(1)	0.15 (charm)	0.34 (bottom)
MSTP(82)	4	
PARP(81)	1.9	
PARP(82)	2.0	
PARP(83)	0.5	
PARP(84)	0.4	
PARP(85)	0.9	
PARP(86)	0.95	
PARP(89)	1800	
PARP(90)	0.25	
PARP(67)	4.0	

Table 4.7: Ratios of charm and bottom hadrons in PYTHIA.

	data	PYTHIA (tuned)	PYTHIA (default)
D^+/D^0	0.400 ± 0.017	0.403	0.75
D_s/D^0	0.141 ± 0.009	0.141	0.30
Λ_c/D^0	0.191 ± 0.017	0.197	0.10
B^+/B^0	1.054 ± 0.075	1.004	0.75
B_s/B^0	0.267 ± 0.026	0.288	0.30
Λ_b/B^0	0.577 ± 0.290	0.643	0.10

The DCA distribution and survival fraction after the isolation cut are evaluated with the simulation. In order to evaluate uncertainties of them from uncertainties of the simulation, following items are changed in the evaluations:

- quark mass

99

- charm : 1.23 GeV → 1.4 GeV
- bottom : 4.17 GeV → 4.6 GeV

- hadron fractions

  - D^+/D^0 : ±0.05
  - D_s/D^0 : ±0.05
  - Λ_c/D^0 : ±0.1
  - B^+/B^0 : ±0.1
  - B_s/B^0 : ±0.1
  - Λ^b/B^0 : ±0.5

- p_T distributions of charm and bottom quark

p_T distributions are modified by applying weights according to quark p_T. The weights are decided so that the p_T distributions of charm and bottom can fit those derived from the FONLL calculation [26]. Distributions doubly weighted by the weigh are also utilized to evaluate the uncertainty. Figure 4.31 shows the p_T distributions of the heavy quarks in the PYTHIA and those after weighting.
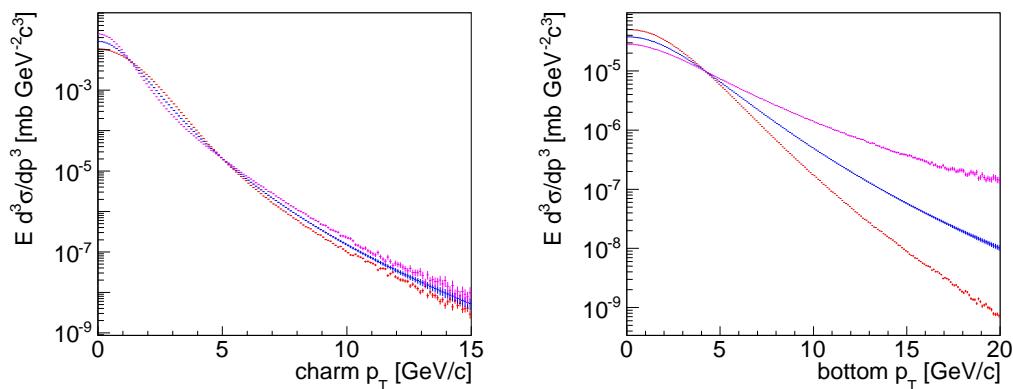
Figure 4.31: The invariant cross sections of charm (left) and bottom (right) in a simulation. The red, blue, and magenta lines represent the slope of the PYTHIA simulation, the single-weighted, and the double-weighted spectra. The single weighted spectrum equals to that of the FONLL calculation [26].

4.7.3   Trigger Efficiency

The data collected with the electron trigger is analyzed for this analysis. The measured p_T distribution is modified by the efficiency of the electron trigger. The modified

distribution is simulated by applying the efficiency as a weight. The efficiency is evaluated with the MB data. The efficiency is calculated by taking a ratio of the number of electron candidates which fire the electron trigger and that of all the electron candidates. The efficiency is evaluated for each of the EMCal sectors. Figure 4.32 shows the trigger efficiencies as a function of p_T. The left and right panels show the efficiency of a sector of PbSc and PbGl, respectively. The red lines represent curves of fitting functions. There is a small difference between two since the thresholds for the EMCal signals are different. Even at a high p_T, the efficiencies does not reach to 1. This can be explained by dead area of trigger modules.
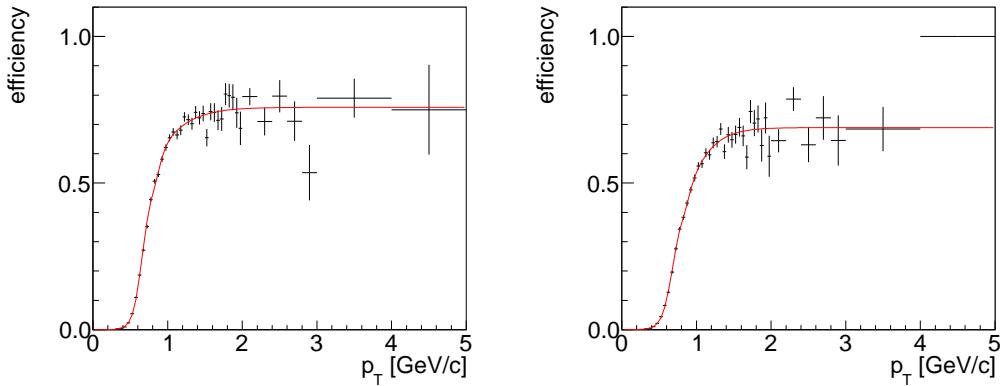
Figure 4.32: The trigger efficiencies of PbSc (left) and PbGl (right) as a function of p_T. The red lines represent curves of fitting functions.

The efficiency of the electron reconstruction also modifies the measured p_T distribution. The slope of the efficiency as a function of p_T is evaluated and the absolute value of the efficiency is not evaluated in this analysis. Since yield ratios of electrons from all sources are used in this analysis and absolute yields are not used. The modification is also simulated by applying the reconstruction efficiency as a weight. Details are described in Sec. 4.8.8.

4.8 Electron Yield

Yield ratios of all electron sources in the inclusive electrons are evaluated in this section. The inclusive electrons consist of following components:

- non-photonic electrons: the heavy-quark electrons and electrons from kaon decay (K_{e3} electrons).

- photonic electrons: electrons from Dalitz decays of neutral pseudo-scalar mesons (π^0, η, and η'), decays of light vector mesons (ρ, ω, ϕ, J/ψ, and ψ'), and electrons from photon conversions (conversion electrons).

- heavy quarkonia: electrons from decays of heavy quarkonia (J/ψ, ψ', and Υ).

- hadron contamination: hadrons identified as electrons mistakenly.

The main background sources at low p_T region are the electrons from π^0 decay and conversion electrons. At high p_T region, the contribution of heavy quarkonia, such as J/ψ, increases due to their large masses. After applying the isolation cut, the contribution of heavy quarkonia is the largest background at high p_T region.

4.8.1 Decay from Heavy Quark

The yield of heavy-quark electrons is evaluated with the previously published result from PHENIX experiment [15]. Since the statistics of electrons in the result is much larger than the data used in this analysis, a more precise measurement has been achieved in the result. The cross section is parameterized by a modified Hagedorn function as follows:

$$E\frac{d^3\sigma}{dp^3} = c(\exp^{-a\cdot p_T - b\cdot p_T^2} + p_T/p_0)^{-n}, \tag{4.37}$$

where a, b, c, p_0, and n are fitting parameters, and p_T is p_T of the electron. The left panel in Fig. 4.33 shows the invariant cross section of the heavy-quark electrons and the function, and the right panel shows deviations of the measured cross section from the function. The function successfully reproduces the cross section at p_T range used in this analysis ($1 < p_T < 5$ GeV/c). The yield for each of the analysis bins is calculated from the function.
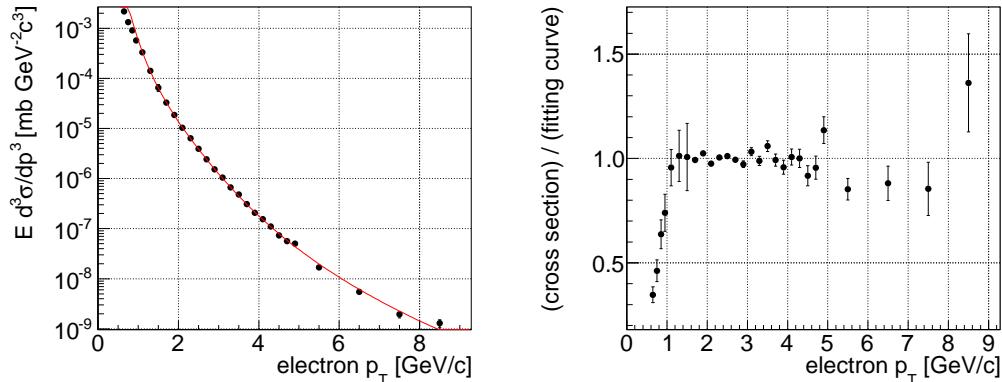
Figure 4.33: Left: The invariant cross section of the heavy-quark electrons. Right: Deviations from a modified Hagedorn function.

Statistical error

One or more points in the published result correspond to each of the analysis bins. The statistical error relative to the central value is calculated with the error of the

lowest p_T point in the analysis bin range. The error is corrected with the widths of the analysis bin, w_{ana}, and the published result, w_{pub}, as follows:

$$\sigma_{ana} = \sigma_{pub} \cdot \sqrt{\frac{w_{pub}}{w_{ana}}}, \tag{4.38}$$

where σ_{ana} and σ_{pub} represent the relative errors for this analysis and for the published result, respectively.

Systematic error

Since the systematic errors of the published result correlate between the analysis bins, the errors are evaluated by a different method from that employed for the statistical errors. The parameterization of the cross section is repeated by shifting $\pm 1\sigma$ of systematic errors, and calculated yields. Differences of yields between with and without the shift are assigned as systematic errors. Since the the differences for $+1\sigma$ shift and -1σ shift are almost symmetric, the average of them is assigned.

A quadratic sum of the statistical error and the systematic error is assigned as the total error. Figure 4.34 shows the total error, statistical error, and systematic error of each of the analysis p_T bins. The red solid, dashed-dotted, and dashed lines represent the total error, statistical error, and systematic error, respectively.

4.8.2   Decay from Light Mesons

Neutral Pion

The most important background source is π^0 decays. Not only electrons from π^0 Dalitz decays but also photons from π^0 decays create large amount of background, especially at low p_T region. p_T spectrum of electrons from π^0 Dalitz decay is evaluated by a Monte-Carlo simulation of particle decays based on measured p_T spectrum of π^0 [69]. The spectrum of π^0 is parameterized by a modified Hagedorn function. Figure 4.35 shows a measured cross section of π^0 and the fitting curve. Since the statistical errors are negligibly small comparing to the systematic errors, only the systematic errors are taken into account. The modified Hagedorn parameterization is repeated by shifting $\pm 1\sigma$ of systematic errors and differences of yields between with and without shift are assigned as a systematic error. The uncertainty is around 10% almost independent on p_T.

Other Light Mesons

p_T spectra of other light mesons, η, and η', ρ, ω, and ϕ, are derived from the pion spectrum assuming m_T scaling, i.e. the same modified Hagedorn parametrization is utilized only replacing p_T to $m_T = \sqrt{p_T^2 + m_h^2 - m_{\pi^0}^2}$, where m_h and m_{π^0} are
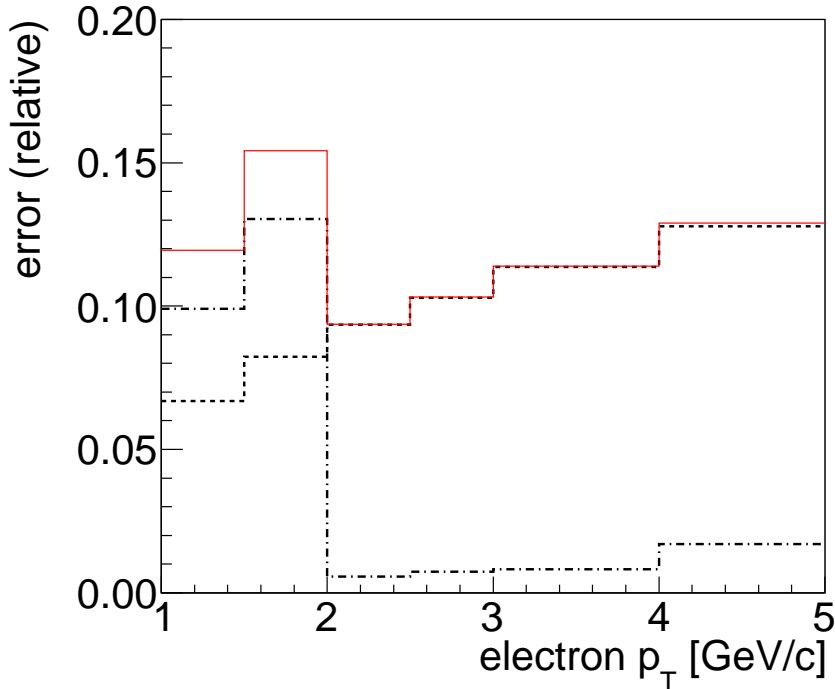
Figure 4.34: The total error (red solid line), statistical error (dashed-dotted line), and systematic error (dashed line) of the yield of the heavy quark electrons.

masses of a hadron and π^0. Normalization factors are changed from that of π^0 as follows:

- $\eta/\pi^0 = 0.51 \pm 0.01$ [70],

- $\eta'/\pi^0 = 0.26 \pm 0.02$ [71],

- $\rho/\pi^0 = 1.00 \pm 0.30$ [72],

- $\omega/\pi^0 = 0.81 \pm 0.09$ [73],

- $\phi/\pi^0 = 0.22 \pm 0.01$ [71],

The normalization factors are evaluated by ratios of mesons and π^0 at high p_T where $m_T \sim p_T$ (5 GeV/c is used). The systematic errors are calculated from the ratios in addition to the uncertainty of the π^0 spectrum.

4.8.3 Photon Conversion

Photon Source

There are two sources of photons. One is a decay of hadrons and the other is a direct radiation. The yield of conversion electrons of photons from hadron decays
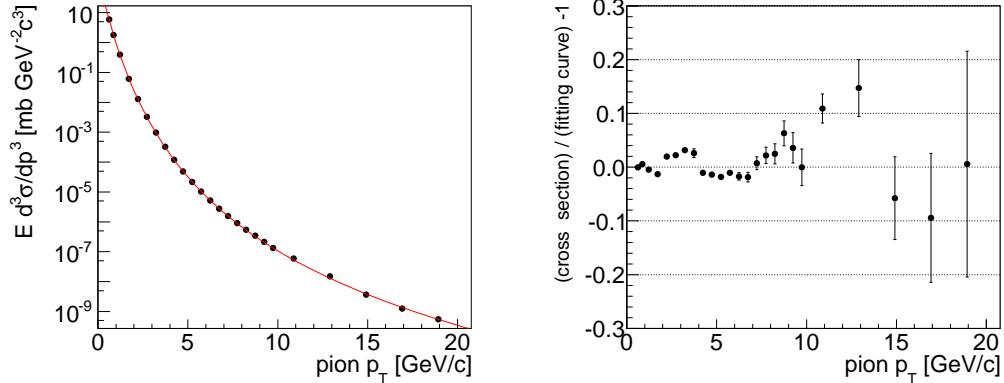
Figure 4.35: Left : The invariant cross section of π^0 and a fitting curve of modified Hagedorn function.
Right : Deviations of the invariant cross section from the fitting curve.

is evaluated based on the electrons from hadron Dalitz decays. Figure 4.36 shows the ratio of conversion electrons and electrons from π^0 Dalitz decay as a function of electron p_T which is evaluated by a π^0 single-track simulation with the PISA simulation. The red line shows a result of fitting by a constant. The ratio is flat and a dependence on the p_T is small.

A contribution from the direct radiation has two process. One is real photons produced in initial hard scattering processes, i.e. direct real photons convert to electron pairs in material in the experimental setup. The other is direct virtual photons. Every source of real photons also accompanies virtual photons. In the case of the π^0, these two sources correspond to the $\gamma\gamma$ decay and Dalitz decay, which is also called an internal conversion. Similarly, direct real photon production is accompanied by direct virtual photon production, i.e. the emission of e^+e pairs. The spectrum of the real direct photon has been measured by PHENIX experiment [74], and the spectrum is parametrized. The corresponding conversion electron spectrum is added to the conversion electrons. The ratio of virtual direct photons to real direct photons depends on p_T because the phase space for dielectron emission increases with increasing p_T. The same effect is seen in the Dalitz decays of light neutral mesons, i.e. the branching ratio of Dalitz decay relative to two photon decay increases as the mass of the hadron increases. Consequently, the ratio of virtual and real direct photon emission increases with p_T or, to be more precise, with a logarithmic dependence. Such dependence is implemented based on the theory. The systematic error of the direct photon measurement is directly propagated to the electron spectrum.

Evaluation of Material

The contribution of the conversion electrons largely depends on the material of the experimental setup. Photon conversions mainly occur at the beam pipe and B0 of the

105
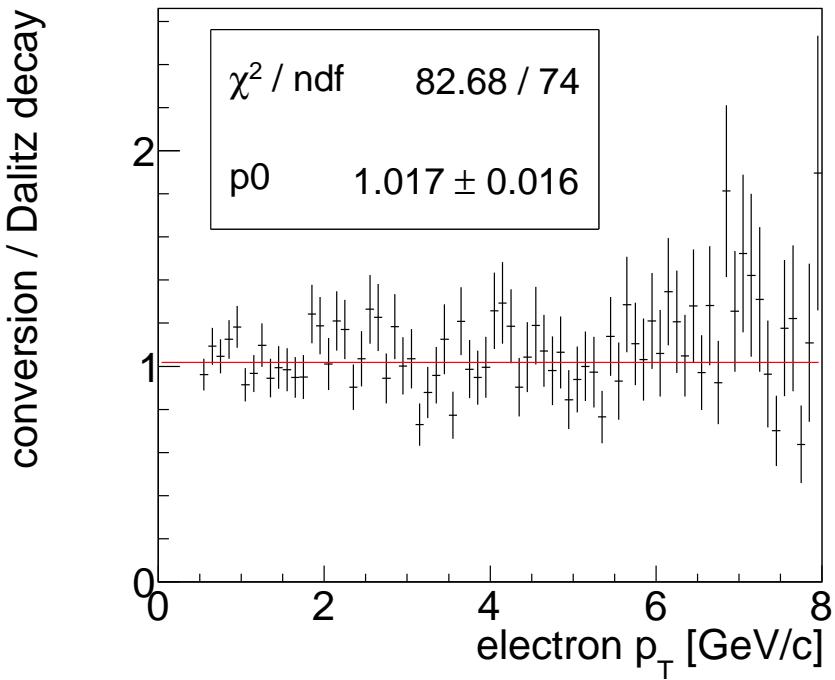
Figure 4.36: The ratio of conversion electrons and electrons from π^0 Dalitz decay as a function of electron p_T evaluated by a π^0 single-track simulation. The red line shows a result of fitting by a constant.

VTX for the electrons which passed the analysis cuts. Since the conversion occurred inside the silicon sensor of the VTX, the contribution depends on not only the amount of the material but also the depth of the sensor where the electrons converted inside the sensor can be detected.

The ratio of pairs of conversion electrons (conversion pairs) and those of electrons from hadron decays (decay pairs) is evaluated by using two distributions related to electron pairs. One is the distribution of the invariant mass of the electron pairs, and the other is the angle between the pair plane and the magnetic field, called ϕ_V, which

is calculated as follows:

$$\vec{u} = \frac{\overrightarrow{p_{e+}} + \overrightarrow{p_{e-}}}{|\overrightarrow{p_{e+}} + \overrightarrow{p_{e-}}|}, \tag{4.39}$$

$$\vec{v} = \frac{\overrightarrow{p_{e+}} \times \overrightarrow{p_{e-}}}{|\overrightarrow{p_{e+}} \times \overrightarrow{p_{e-}}|}, \tag{4.40}$$

$$\vec{w} = \vec{u} \times \vec{v}, \tag{4.41}$$

$$\overrightarrow{e_z} = (0, 0, 1), \tag{4.42}$$

$$\vec{a} = \frac{\overrightarrow{u} \times \overrightarrow{e_z}}{|\overrightarrow{u} \times \overrightarrow{e_z}|}, \tag{4.43}$$

$$\phi_V = cos^{-1}(\vec{w} \cdot \vec{a}). \tag{4.44}$$

The distributions of the conversion pairs and the decay pairs have different features. [75] The pair-mass distribution of the conversion pairs has a peak at $\sim$20 MeV though the actual pair-mass is $\sim$0 MeV. The pair mass of off-vertex tracks is reconstructed to slightly different value from the actual value due to the algorithm of p_T reconstruction of CNTs. In the algorithm, a track is assumed to come from the collision vertex, and thus, p_T of an off-vertex track is reconstructed to a different value, which depends on the created point of the pair. This is the reason why the pair-mass distribution of the conversion pairs has the peak at $\neq 0$ though the actual pair mass is almost 0. The peak corresponds to the conversion at the beam pipe, which locates at $r = 2.0$ cm, and B0, which locates at $r = 2.5$ cm. The ϕ_V distribution of the conversion pairs has a peak at $\phi_V = 0$ due to small opening angles of the pairs. On the other hand, the pair-mass distribution of the decay pairs has a peak around 10 MeV, and the ϕ_V distribution is flat.

The evaluation is performed with a π^0 single-track simulation. Almost 80% of photons and the decay pairs are from π^0 decays. and the pair-mass distribution where the mass is less than 0.1 GeV, and the ϕ_V distribution are well reproduced by scaling those of π^0 decays. The second largest source is decays from η meson, and the contribution is $\sim$15%. Since the ratio of branching ratios between $\eta \rightarrow e^+e^-\gamma$ and $\eta \rightarrow 2\gamma$, 1.780, is slightly different from that of π^0, 1.188, the result evaluated with the π^0 simulation is corrected with the difference. The remaining 5% was included in a systematic error. The distributions of the pair mass and ϕ_V are made for the conversion and decay pairs by the simulation. The normalization of the distributions are performed with respect to the branching ratios of $\pi^0 \rightarrow 2\gamma$ and $\pi^0 \rightarrow e^+e^-\gamma$. Then, two distributions of the data are fitted with two parameters, a and r, at the same time as follows:

$$\phi_V(data) = a \cdot (\phi_V(C) + r \cdot \phi_V(D)), \tag{4.45}$$

$$M_{ee}(data) = a \cdot (M_{ee}(C) + r \cdot M_{ee}(D)), \tag{4.46}$$

where $\phi_V(data)$ and $M_{ee}(data)$ are the distributions of ϕ_V and pair mass in data, respectively, $\phi_V(C)$ and $M_{ee}(C)$ are those of the pairs from photon conversions and

$\phi_V(D)$ and $M_{ee}(D)$ are from the Dalitz decays. The fitting is performed where the pair mass is less than 0.1 GeV. If all of the pairs are from π^0 decays and the conversion pairs are simulated exactly, r should be 1. The fitting result is shown in Fig. 4.37. The black histogram represents the distributions of the data. The blue, magenta, and red histograms represent the conversion pairs, decay pairs, and sum of them in the simulation. The ratio, r, evaluated by the fitting was 1.091 ± 0.067 and χ^2/NDF was 3.40. The ratio of the number of decay pairs and the conversion pairs from π^0 decays is 1.188 and that from π^0 and η decays is $(1.188 \times 0.8 + 1.780 \times 0.15)/0.95 = 1.281$. Therefore, r should be multiplied by $1.188/1.281$, and corrected from 1.091 ± 0.067 to 1.012 ± 0.062. Finally, the yield of the conversion electrons in simulations are corrected by $1/1.012$ and the error of $\sqrt{0.062^2 + 0.05^2}$ is assigned as a systematic error for the correction factor.
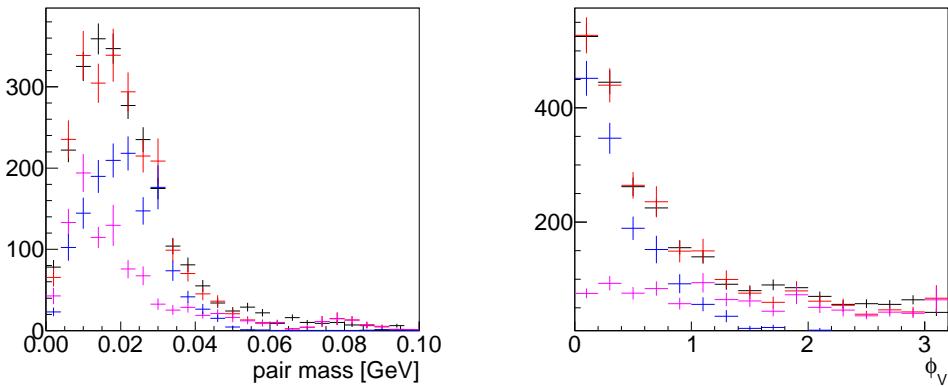
Figure 4.37: The pair-mass (left) and ϕ_V (right) distributions of e^+-e^- pairs. The black histogram represents the distributions of the data. The blue, magenta, and red histograms represent the distributions of conversion pairs, the decay pairs, and sum of them in the simulation. The histograms of the conversion pairs and the decay pairs are scaled with fitting results.

4.8.4 Heavy Quarkonium

The background from decay of J/ψ is important especially at $p_T > 3$ GeV/c. Since a large fraction of photonic electrons are rejected by the isolation cut, the background from J/ψ is the largest background at the p_T region. p_T spectra of charmonia, J/ψ and ψ', have been reported by PHENIX experiment [76, 77]. They are also represented by assuming m_T scaling but with a different parameterization of a modified Hagedorn function. Figure 4.38 shows a measured cross section of J/ψ and the fitting curve. The fitting curve reproduces the measured result very well. The systematic error is evaluated by the same method as of neutral pion. The error is around 12% almost independent on p_T.
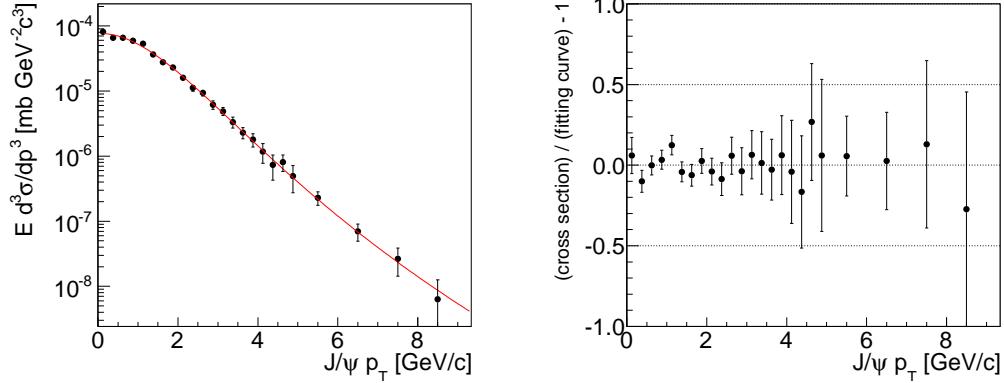
Figure 4.38: Left : The invariant cross section of J/ψ and a fitting curve of modified Hagedorn function.
Right : Deviations of the invariant cross section from the fitting curve.

The contribution of Υ is evaluated by using a preliminary result of PHENIX [78]. From the result, total cross section of Υ(1S+2S+3S) at $|y| < 0.35$ is $(122^{+43}_{-42})/\mathrm{BR}_{ee}$ pb, where BR_{ee} is the branching ratio of $\Upsilon \rightarrow \mathrm{e}^+\mathrm{e}^-$. Although the total cross section is around 1/100 comparing to that of J/ψ, the contribution of Υ increases as p_T increases due to its large mass, and it becomes $\sim$1/10 at $p_T = 5$ GeV/c. Since p_T spectrum is unknown, m_T scaling was also assumed and assigned twice error as large as the error on the result. The ratio of Υ(1S), Υ(2S), and Υ(3S) is also unknown, but since masses and branching ratios of $\Upsilon \rightarrow \mathrm{e}^+\mathrm{e}^-$ are almost same, all are assumed to be Υ(1S).

4.8.5 K_{e3}

Although p_T spectra of kaons are measured like other hadrons, an additional study is necessary for the evaluation of the K_{e3} contribution since efficiency of electrons from K_{e3} is different from others due to their long life. The contribution is estimated from the yield of the electrons from K_{e3} which created inside B0. The yield is evaluated with the PYTHIA simulation with the default setup, and weighted with respect to the p_T of kaons to reproduce the measured p_T spectra [71]. Since the statistics of the electrons from K_L^0 is very small, its yield is estimated from the yields of charged kaons as follow:

$$N_L = \frac{N_+ + N_-}{2} \frac{BR_L/c\tau_L}{BR_\pm/c\tau_\pm}, \tag{4.47}$$

where N_L, N_+, and N_- represent the yields for K_L^0, K^+, and K^- decays, respectively, and BR_L ($BR_\pm$) and $c\tau_L$ ($c\tau_\pm$) represent the branching ratios of K_{e3} decays and the life-time of K_L^0 ($K^\pm$), respectively. The electrons from $K^\pm$ may be reconstructed by associating a hit on the B0 created by the mother $K^\pm$. Therefore, 100% of systematic

109

error was assigned for the yield of $K^{\pm}$ decays as well as the uncertainty of the measured cross section of kaons.

4.8.6 Hadron Contamination

The contribution of the hadron contamination is evaluated by using the distribution of dep, which is explained at Sec. 4.3.2. The dep distribution has a Gaussian-like peak around 1, which is composed by electrons, and a exponential-like tail, which is composed by hadrons and decays from long-life particles such as kaons. For the evaluation of the absolute normalization of hadron component, prob, which is explained at Sec. 4.3.2, is utilized. The idea is to use prob cut is to enrich the hadron contamination. The prob $>$ 0.01 cut has about 50% hadron efficiency for p_T $>$ 1 GeV/c and 99% efficiency to electrons. Therefore, the hadron contamination is increased by a factor of 100 if reverse prob cut (prob $<$ 0.01) is applied. Then we can look at the dep distribution to see much enhanced hadron contamination.

The procedure is the following: Two dep distributions are prepared for both of hadron and electron candidates. One is the dep distributions with prob $<$ 0.01 (rejected sample), and the other is the distribution with prob $>$ 0.01 (accepted sample). The accepted samples of electrons and hadrons are named E_{OK} and H_{OK}, and the rejected samples of electrons and hadrons are named E_{NG} and H_{NG}, respectively. The electron candidates are selected by the good track cut and the e-ID cut except for dep and prob. Then, the distribution of H_{NG} is scaled by f_h and the distribution of E_{OK} by f_e, so that sum of these two distribution reproduces the distribution of E_{NG},

$$E_{NG} \sim f_e \cdot E_{OK} + f_h \cdot H_{NG}. \tag{4.48}$$

f_h corresponds to the probability that a hadron is mis-identified as an electron without prob, and f_e corresponds to the probability that an electron is rejected by the prob cut. The absolute normalization, f_{h0}, is the probability of the mis-identification with prob. Since the difference between H_{NG} and H_{OK} corresponds to that between f_h and f_{h0}, the hadron contamination in the accepted electron candidate can be determined as $(f_h \cdot H_{OK})/E_{OK}$.

f_h and f_e are evaluated by fitting with the distributions of E_{NG}, E_{OK}, and H_{NG}. The fitting is performed for $-3 <$ dep < 5. Left panel in the Fig. 4.39 shows the fitting result of E_{NG} for $1.5 < p_T < 2.0$ GeV/c. The black histogram represents the dep distribution of E_{NG}. The blue, green, and red histograms represent the dep distributions of E_{OK} scaled by f_e, H_{NG} scaled by f_h, and the sum of them. Left panel in the Fig. 4.39 shows the dep distribution of E_{OK} for $1.5 < p_T < 2.0$ GeV/c. The blue histogram represents the dep distribution of E_{OK}, and the magenta histogram represents the dep distribution of H_{OK} scaled by f_h. The dep distribution of E_{NG} is successfully reproduced by the scaled E_{OK} and H_{NG} distributions. The fitting results are summarized in Table 4.8.
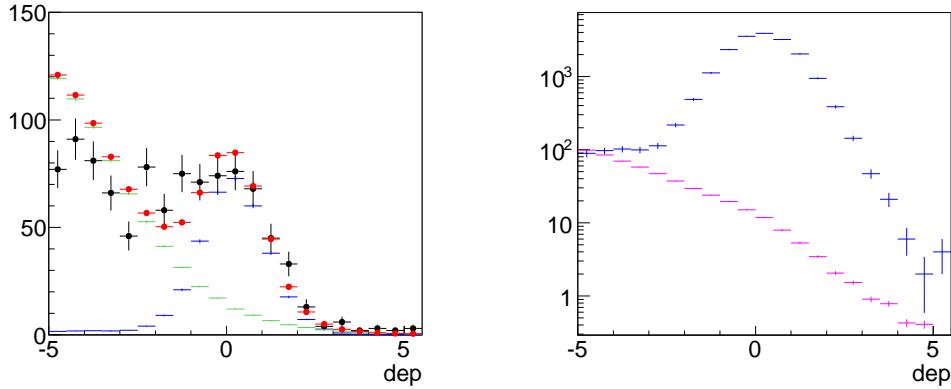
Figure 4.39: The distributions of dep for $1.5 < p_T < 2.0$ GeV/c. Left panel shows a non-scaled distribution for electrons (black) rejected by prob, and scaled distributions of rejected hadrons (green) and accepted electrons (blue). The red histogram represents the sum of the blue and green histograms. Right panel shows a non-scaled distribution for accepted electrons (blue) and a scaled distribution for accepted hadrons (magenta).

Table 4.8: Estimated hadron contamination in inclusive electrons.

p_T range	f_h	f_e	hadron contamination (%)	χ^2/NDF
1.0-1.5 GeV/c	0.0079 ± 0.0003	0.0136 ± 0.0006	1.12 ± 0.04	4.00
1.5-2.0 GeV/c	0.0065 ± 0.0005	0.0186 ± 0.0012	0.68 ± 0.05	2.49
2.0-2.5 GeV/c	0.0105 ± 0.0012	0.0156 ± 0.0022	1.04 ± 0.12	1.16
2.5-3.0 GeV/c	0.0063 ± 0.0016	0.0187 ± 0.0039	0.61 ± 0.16	1.46
3.0-4.0 GeV/c	0.0090 ± 0.0027	0.0136 ± 0.0046	0.86 ± 0.26	0.73
4.0-5.0 GeV/c	0.0246 ± 0.0109	0.0340 ± 0.0179	2.34 ± 1.04	0.97

111

4.8.7 Isolation Cut

A hit located close to associated hits of a track can be categorized into two. One is a hit created by correlated particles which created in the same decay chain of the track. An electron and a positron are created by a π^0 Dalitz decay. They create hits very closely, therefore they are rejected by the cut. The other is a hit created by uncorrelated particles. Particles created by a jet fragmentation is included in the latter. The survival fraction, ϵ^{iso}, can be expressed by a correlated term, ϵ^{corr}, and an uncorrelated term, ϵ^r, as follows:

$$
\begin{aligned}
\epsilon^{iso} &= \epsilon^{corr} \times \epsilon^r \\
&= (1 - \overline{\epsilon^{corr}}) \times (1 - \overline{\epsilon^r}),
\end{aligned}
\tag{4.49}
$$

where $\overline{\epsilon^{corr}}$ and $\overline{\epsilon^r}$ are the rejection fraction by correlated hits and by uncorrelated hits, respectively. ϵ^r is independent from sources of electrons, and all dependent terms are included in ϵ^{corr}. ϵ^r is approximated by ϵ^{iso} of hadron tracks. More detail discussion about ϵ^r is presented at Sec. 4.8.8.

ϵ^{corr} is evaluated by the PISA simulation with single mother hadrons. The numbers of all electrons and survival electrons after the cut are counted for each of the analysis p_T bins, and the ratio of them is considered as ϵ^{corr}. In order to simulate the decay chains of heavy quarks realistically, the heavy quark electrons are created by the PYTHIA, and all particles created from the same charm or bottom quarks are utilized to evaluate ϵ^{corr}. In order to evaluate a systematic error derived from an uncertainty of the detector acceptance, the evaluation is performed with three different fiducial cuts, Gr2, Gr3, and Gr7, and the results are combined as follows:

$$
\epsilon^{corr}(p_T) = \frac{\displaystyle\sum_i \left(\epsilon_i^{corr}(p_T)/\sigma_i^{corr}(p_T)^2 \right)}{\displaystyle\sum_i 1/\sigma_i^{corr}(p_T)^2},
\tag{4.50}
$$

$$
\sigma^{corr}(p_T) = \sqrt{\frac{1}{\displaystyle\sum_i 1/\sigma_i^{corr}(p_T)^2} + \sum_i \left(\epsilon_i^{corr}(p_T) - \epsilon^{corr}(p_T) \right)^2/2},
\tag{4.51}
$$

where index i corresponds to each of the fiducial cuts, ϵ_i^{corr} and σ_i^{corr} represent the fraction and the error of the fraction, respectively, evaluated with i-th fiducial cut. σ_i^{corr} is the statistical error of ϵ_i^{corr}. ϵ^{corr} and σ^{corr} represent the combined fraction and the error of the fraction. Variations of three are included in σ^{corr} by unbiased estimation of a standard deviation, which corresponds to the second term. Figure 4.40 shows ϵ^{corr} of each of the electron sources. A confirmation of ϵ^{corr} is also discussed at Sec. 4.8.8.
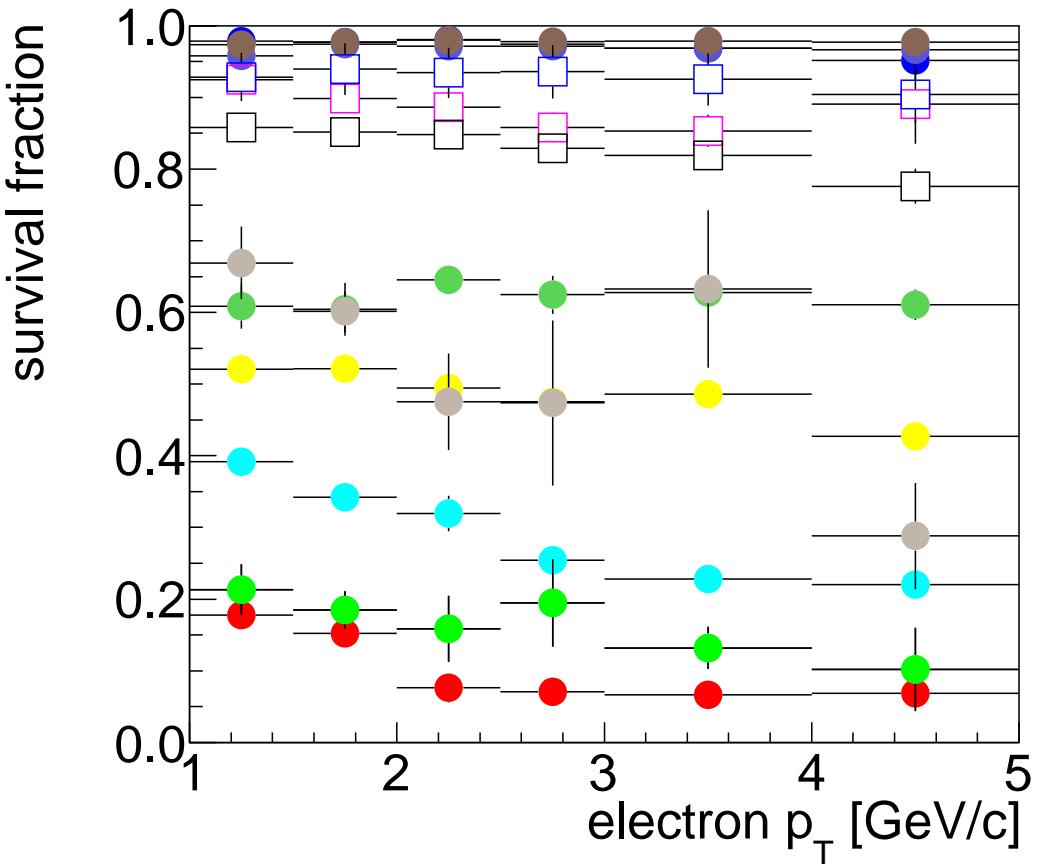
Figure 4.40: Survival fractions of electrons from π^0 Dalitz decay (red circles), η Dalitz decay (cyan circles), η' (yellow circles), ρ (blue circles), ω (dark green circles), ϕ (purple circles), kaon (silver circles), heavy quarkonia (brown circles), conversion electrons (light green circles), hadrons (open black squares), charm electrons (open blue squares), and bottom electrons (open magenta squares).

Correction of Isolation Cut Efficiency

The bottom fraction evaluated by the fitting corresponds following:

$$f_m = \frac{N^m_{b \to e}}{N^m_{c \to e} + N^m_{b \to e}} = \frac{\epsilon_b^{iso} N^0_{b \to e}}{\epsilon_c^{iso} N^0_{c \to e} + \epsilon_b^{iso} N^0_{b \to e}}, \tag{4.52}$$

where f_m represents the measured bottom fraction, $N^m_{c \to e}$ and $N^m_{b \to e}$ represent the numbers of measured electrons from charm and bottom decays, respectively, $N^0_{c \to e}$ and $N^0_{b \to e}$ represent those of created electrons from charm and bottom decays, respectively, and ϵ_c^{iso} and ϵ_b^{iso} represent efficiencies for the isolation cut of charm and bottom, respectively. Since the reconstruction efficiencies of the charm and the bottom electrons except for the isolation cut should be the same, ϵ^{iso} is enough to correct N^m. As is shown in Eq. 4.52, the measured bottom fraction is modified by ϵ^{iso} from the original bottom fraction. Following correction is performed for f_m:

$$f_0 = \frac{N^0_{b \to e}}{N^0_{c \to e} + N^0_{b \to e}} = \frac{f_m}{r^{iso} - r^{iso} f_m + f_m}, \tag{4.53}$$

where f_0 represents the original bottom fraction and $r^{iso} = \epsilon_b^{iso}/\epsilon_c^{iso} = \epsilon_b^{corr}/\epsilon_c^{corr}$. The error of f_0 derived from the fitting error of f_m is assigned as a statistical error, and from the error of r^{iso} is assigned as a systematic error.

4.8.8 Yield Ratio

Figure 4.42 shows the invariant cross sections of all electron sources. In this analysis, not absolute normalizations of the cross sections but yield ratios are important. The yield ratios before and after the isolation cut are calculated as follows:

$$R_i^0 = \frac{Y_i^0}{\sum\limits_{j \in all\ sources} Y_j^0}, \tag{4.54}$$

$$R_i^v = \frac{\epsilon_i^{iso} \cdot Y_i^0}{\sum\limits_{j \in all\ sources} \epsilon_j^{iso} \cdot Y_j^0} = \frac{\epsilon_i^{corr} \cdot Y_i^0}{\sum\limits_{j \in all\ sources} \epsilon_j^{corr} \cdot Y_j^0}, \tag{4.55}$$

where

- R_i^0: the yield ratio of i-th source before the isolation cut,

- R_i^v: the yield ratio of i-th source after the isolation cut,

- Y_i^0: the electron yield of i-th source before the isolation cut.

114

As is mentioned in Sec. 4.1, the yield ratios of the charm and bottom electrons are not separated here, and are handled in being combined as the heavy-quark electrons. The yield ratios of charm and bottom electrons are necessary to obtain ϵ^{corr} of heavy-quark electrons. The mean of those of charm and bottom electrons is utilized as that of heavy quark electrons, and an error is assigned to cover the errors of both charm and bottom electrons. When the ratios are calculated, a weight which corresponds to the reconstruction efficiency is applied to Y_i^0. Although the absolute value of the efficiency does not evaluated in this analysis, its dependence on p_T is evaluated with the sum of Y_i^0 and the measured p_T distribution of the inclusive electrons. The ratio of them represents not the absolute value but the dependence on p_T of the reconstruction efficiency. Figure 4.41 shows the measured p_T distribution of the inclusive electrons over the sum of Y_i^0. The p_T distribution is normalized by the number of the inclusive electrons for $p_T > 1$ GeV/c. The sum of Y_i^0 is not corrected by integrated luminosity. The ratio increases at $1 < p_T < 2$ GeV/c and is flat at $p_T > 2$ GeV/c. Figure 4.43
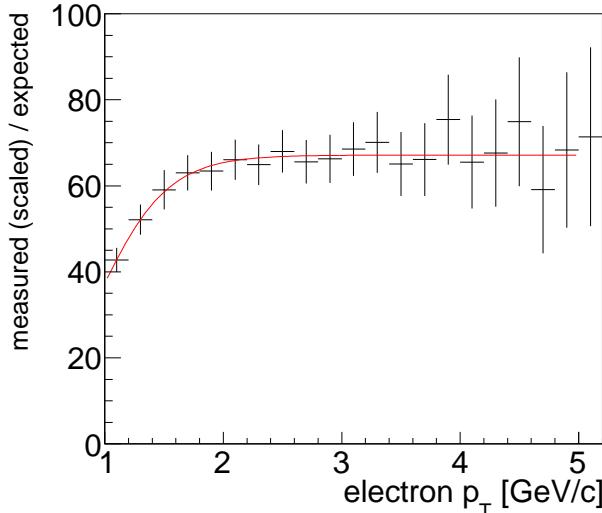
Figure 4.41: A relative reconstruction efficiency of electrons as a function of p_T. The efficiency is the measured p_T slope of the inclusive electrons over the sum of Y_i^0. The p_T distribution is normalized by the number of the inclusive electrons with $p_T > 1$ GeV/c. The sum of Y_i^0 is not corrected by integrated luminosity.

and Fig. 4.44 show the yield ratios before and after the isolation cut. Before the isolation cut is applied, photonic electrons are the largest background, but decays from heavy quarkonia become the largest at $p_T > 2.5$ GeV/c.

In order to check a consistency of the yield ratios and survival fraction, the hit distributions located close to associated hits to electron tracks are compared between the data and simulation. The hit distribution of the simulation is created by combining the distributions of all electron sources with respect to the yield ratios, shown
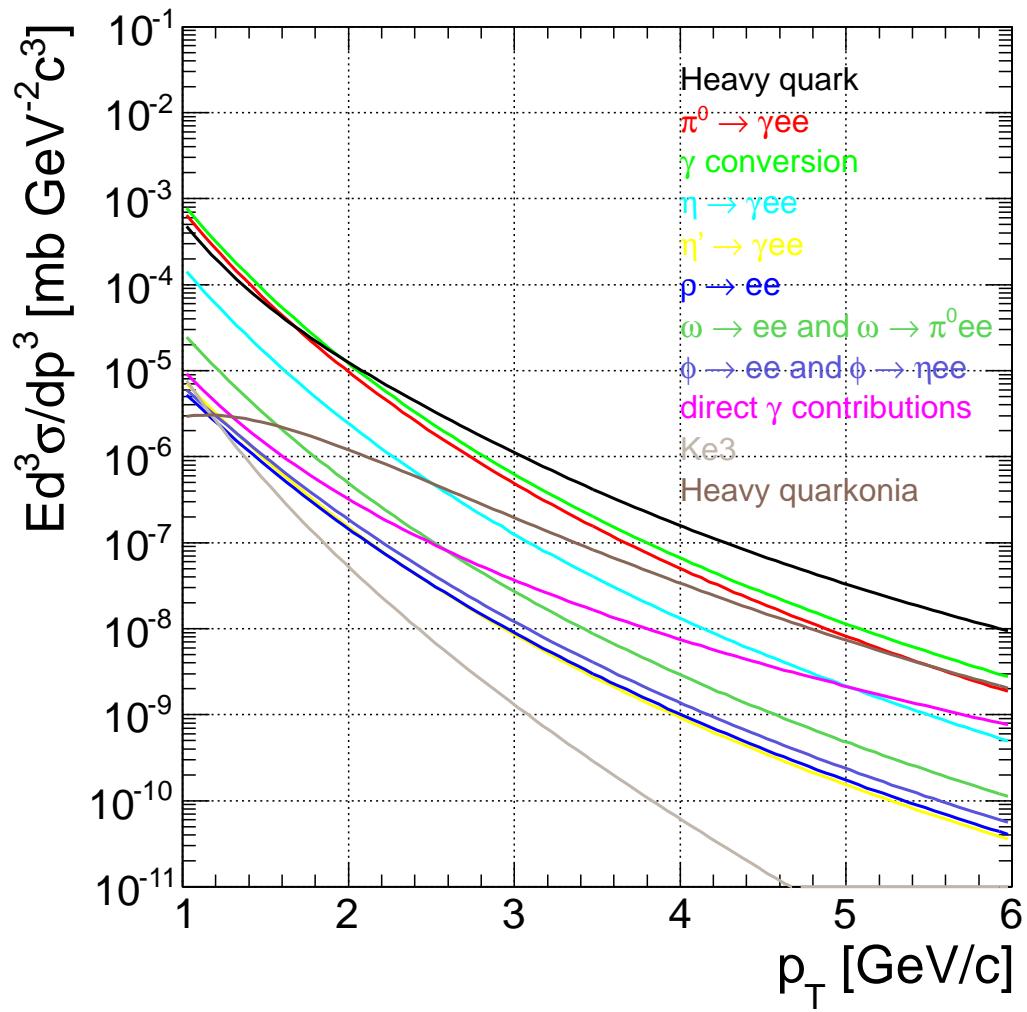
Figure 4.42: The invariant cross sections of electrons from π^0 Dalitz decay (red), η Dalitz decay (cyan), η' (yellow), ρ (blue), ω (dark green), ϕ (purple), direct virtual photon (magenta), kaon (silver), heavy quarkonia (brown), and heavy quark electrons (black), and conversion electrons (light green).
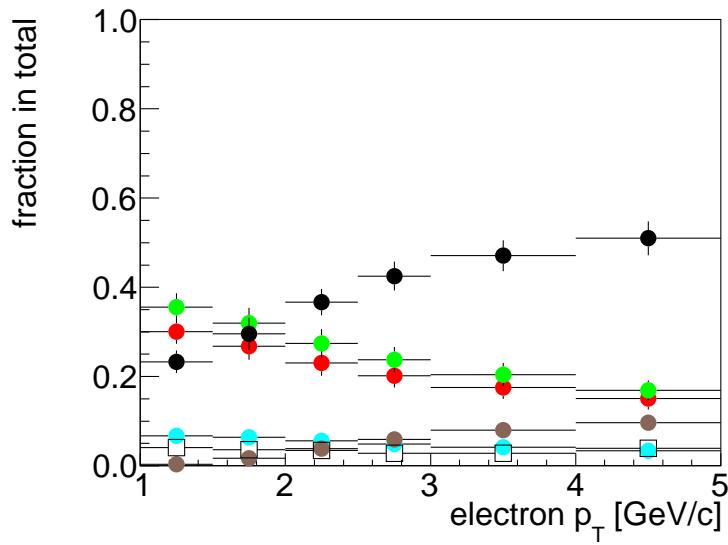
Figure 4.43: Yield ratios before the isolation cut of electrons from π^0 Dalitz decay (red), η Dalitz decay (cyan), heavy quarkonia (brown), heavy-quark electrons (black), conversion electrons (green), and the others (open black squares).
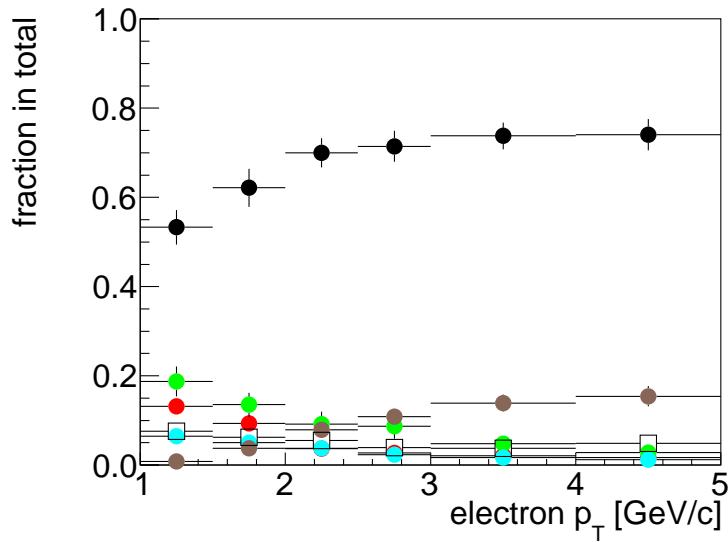
Figure 4.44: Yield ratios after the isolation cut of electrons from π^0 Dalitz decay (red), η Dalitz decay (cyan), heavy quarkonia (brown), heavy-quark electrons (black), conversion electrons (green), and the others (open black squares).

in Fig. 4.43. Figure 4.45 shows the hit distributions. The red represents the inclusive electrons of the data. The blue and magenta represent the electrons from π^0, conversion electrons in the simulation, respectively. The green and black represent the uncorrelated hits and the sum of electrons from all the sources, respectively. The distribution of the uncorrelated hits is the hit distribution of hadrons. The hit distributions are successfully reproduced by the simulation at any p_T range. The main contribution for the hit distribution of B0 is the electrons from π^0, and that of B1 is conversion electrons. Therefore, yields of the conversion electrons and the electrons from π^0 decays are successfully evaluated by the simulation. The contribution of conversion electrons is small in B0 though that of B1 is large. This is because hits created by a conversion pair are reconstructed into a hit cluster, not into two, since the conversion point is too close to B0. The negative side of cdphi distributions are mainly reproduced by the distributions of the uncorrelated hits for any p_T ranges though main contributors are different at each range, i.e. the main contributors at $1 < p_T < 2$ GeV/c are the conversion electrons and the electrons from π^0 decays, and that at $3 < p_T < 4$ GeV/c is the heavy quark electrons. It suggests that the uncorrelated term, ϵ^r, does not depend on sources of electrons and can be well approximated by the survival fraction of hadrons.

Another consistency check is performed by comparing the yields of the inclusive electrons of the data and the simulation after the isolation cut. This comparison also provide a good test of the yield and survival fraction of each electron source. The yield of the inclusive electrons of the simulation is calculated as follows:

$$Y_s^v = \sum_{i \in all\ sources} \epsilon_i^{iso} \cdot Y_i^0 \tag{4.56}$$

$$= \sum_{i \in all\ sources} \epsilon_i^{corr} \epsilon^r \cdot R_i^0\ Y_d^0, \tag{4.57}$$

where

- Y_s^v: the yield of the inclusive electrons in the simulation after the isolation cut,

- Y_i^0: the yield of i-th source before the isolation cut,

- Y_d^0: the yield of the inclusive electrons in the data before the isolation cut,

- R_i^0: the yield ratio of i-th source before the isolation cut, shown in Fig. 4.43.

The survival fraction of hadrons is utilized as ϵ^r. Figure 4.46 shows the yields of the inclusive electrons of the data and the simulation. The crosses and the open circles represent the yield of the data and the simulation, respectively. The black, the red, the green, and the brown circles represent the yields of heavy-quark electrons, conversion electrons, the electrons from π^0 decays, and form heavy quarkonia, respectively. The yields are almost consistent each other. It also support that the yield and survival fraction of each electron source are successfully evaluated by the simulations.

118
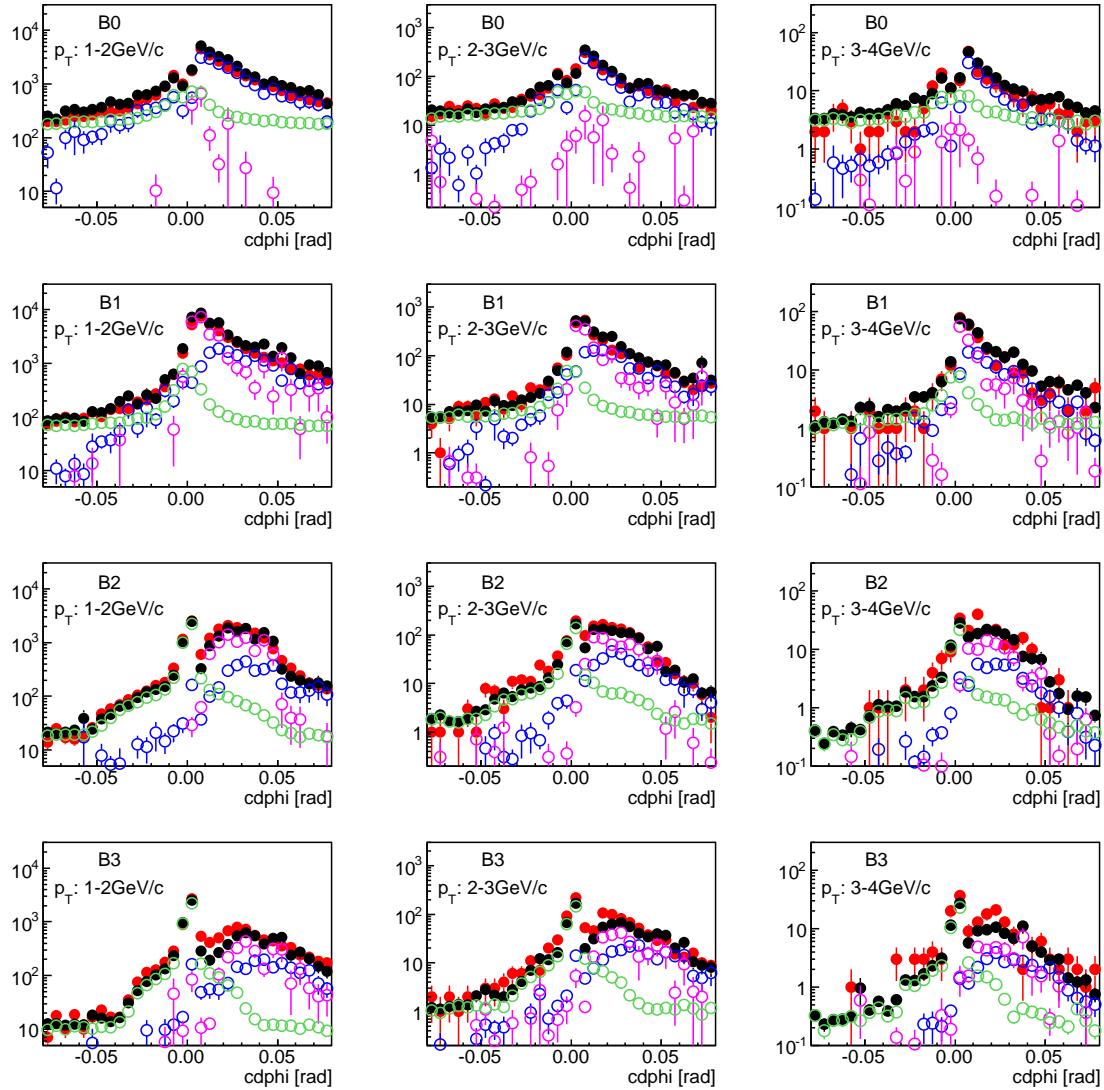
Figure 4.45: Hit distributions located close to associated hits to electron tracks. The red represents the distributions of the inclusive electrons of the data. The blue, the magenta, the green, and the black represent the distributions of the simulation of the electrons from π^0, conversion electrons, the uncorrelated hits, and the sum of electrons from all the sources.
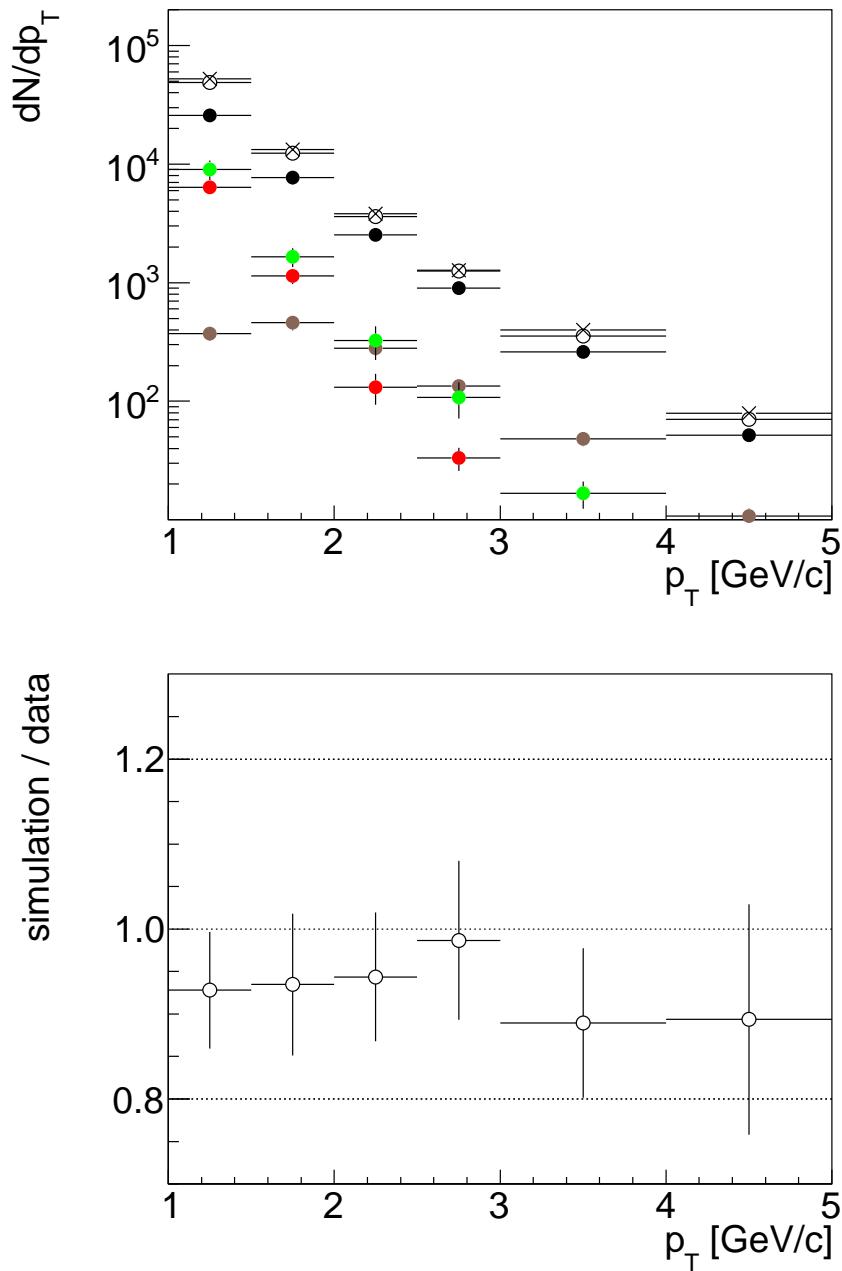
Figure 4.46: Yields of the inclusive electrons of the data and the simulation after the isolation cut. The crosses and the open circles represent the yield of the data and the simulation, respectively. The black, the red, the green, and the brown circles represent the yields of heavy-quark electrons, conversion electrons, the electrons from π^0 decays, and form heavy quarkonia, respectively.

4.9   DCA Distribution Evaluation

DCA distribution of each electron source is evaluated by simulations and data. Details of the evaluation is summarized in this section. Before describing the results of the simulation, a comparison of mean and width of DCA distributions of the data and simulation is described. It is demonstrated from the comparison that the simulation surely can be utilized to evaluate the distributions.

DCA distribution of each electron source can be categorized as follows:

- decays from short-life hadrons: light mesons, virtual direct photon, and heavy quarkonia,

- decays from long-life hadrons: charm, bottom, and kaon,

- conversion electrons,

- hadron contamination.

The DCA distribution of electrons from short-life hadrons should be approximated by that of single electron tracks created at the collision vertex. The DCA distribution of electrons from long-life hadrons and that of conversion electrons can not be approximated by that of single electron tracks since created points of the electrons are far from the collision vertex. Therefore, they are necessary to be evaluated respectively. The DCA distribution of the hadron contamination is evaluated by the distribution of hadrons.

4.9.1   DCA Distribution

The first step of simulating a DCA distribution is to evaluate the mean and the RMS of the DCA distribution of primary tracks. Those for hadrons can be evaluated with a peak of the DCA distribution of the inclusive hadrons since a large part of the inclusive hadrons after applying the good track cut are composed by pion, kaon, and proton created very close to the collision vertex. On the other hand, those for electrons can not be evaluated with the DCA distribution of the inclusive electrons since more than a half of the inclusive electrons are composed by decays from charms and bottoms. However, a comparison of the hadron DCA distribution between the data and the simulation can provide differences between the data and simulation, which can also applicable for the electron DCA distribution.

The DCA resolution is evaluated by fitting the DCA distribution by a Gaussian. The DCA resolution consists of two components: One is an intrinsic DCA resolution of tracks and other is the beam size. If the collision vertex is perfectly known, the DCA resolution should be equal to the former. The former can be approximated by a quadratic sum of a constant term and a term dumping with $1/p_T$. The constant term is due to the position resolution of a VTX hit and the other term is due to multiple

Coulomb scatterings. The beam size is independent on a property of a track, and thus, it can be expressed by a constant. Constant terms exist both of the two components, but its value is mainly decided by the beam size since the beam size is much larger than the position resolution. The DCA resolution as a function of p_T is fitted by $\sqrt{(a/p_T)^2 + b^2}$, where a and b are fitting parameters. Following results were obtained from the fitting:

$$a = 63.8 \pm 0.07 \ [\text{GeV} \cdot \mu\text{m}], \tag{4.58}$$

$$b = 128.3 \pm 0.02 \ [\mu\text{m}], \tag{4.59}$$

The DCA resolution is simulated by the PISA simulation of $\pi^\pm$ single track. Starting points of the $\pi^\pm$ is smeared in the track reconstruction with Gaussian random values with $\sigma = 130 \ \mu\text{m}$, i.e. the track is reconstructed with different collision vertex from the starting point, and the DCA is calculated with respect to the collision vertex. Figure. 4.47 shows the resolutions evaluated with the data and the simulation. Solid and open circles represent the resolutions of the data and the simulation, respectively, as a function of p_T. The red line represents the fitting result. The result of the simulation reproduces that of the data by smearing the starting point, and the difference of the resolutions between the data and simulation is $\pm 5 \ \mu\text{m}$. The difference is taken into account in systematic error, described in Sec. 4.10. This same smearing can be applicable for electron tracks, and the DCA resolution of electrons can be simulated by the smearing.

The mean of the DCA distribution is tuned so that a combination of simulated DCA distributions of all sources reproduces the DCA distribution of the inclusive electrons in the data. Figure 4.48 shows the mean of the DCA distribution of the inclusive electrons as a function of p_T. The mean values are calculated by fitting the peak of the DCA distributions by a Gaussian. The solid and open circles represent the mean of the data and the simulation, respectively. f_b in the simulation is optimized by the fitting. The mean values in the simulation successfully reproduces those in the data.

4.9.2   Decay of Short-life Hadrons

DCA distributions of the electrons from short-life hadrons are simulated by the PISA simulation with single electron tracks created at the collision vertex. From the simulation study, the distributions consist of a peak at DCA$\sim$0 and a tail with large DCA. The peak mainly consists of tracks reconstructed with the hits created by itself, and the tail consists of tracks reconstructed with the hits created by another particle. Details about the tail is described later in Sec. 4.9.6. The peak is approximated by a Gaussian which is evaluated by fitting a DCA distribution of electrons in a single-track simulation.
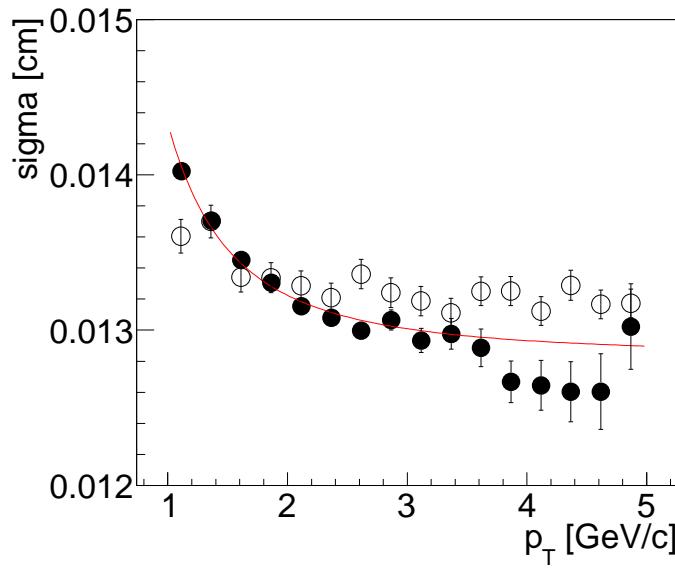
Figure 4.47: The width of DCA distribution of hadrons as a function of p_T. Solid and open circles represent the resolutions of the data and the simulation, respectively. The red line represents the fitting result.
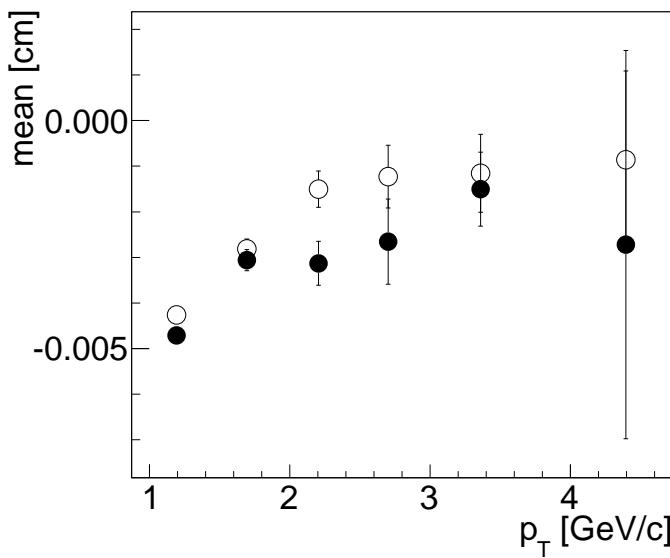
Figure 4.48: The mean of the DCA distribution of the inclusive electrons as a function of p_T. The solid and open circles represent the mean of the data and the simulation, respectively. The mean is evaluated by fitting the peak of the DCA distribution by a Gaussian. The bottom fractions in the simulation were optimized by the fitting.

123

4.9.3 Decay of Long-life Hadrons

In this analysis, a large DCA region where the ratio of charm and bottom electrons becomes almost same is important. However, in order to evaluate the shapes of the DCA distributions of charm and bottom electrons precisely by the PISA simulation, large statistics are necessary. Therefore, it is difficult. DCA distributions of electrons from decays of long-life hadrons, charm, bottom, and kaon, are evaluated by a Gaussian convolution of their DCA distributions created by the PYTHIA instead of utilizing results of the PISA simulation. The same RMS and shift of mean value are utilized for the convolution for all of them. Figure 4.49 and Fig. 4.50 show the distributions of charm electrons and bottom electrons with $1 < p_T < 2$ GeV/c, respectively. The left panels show the distributions evaluated by the convolution represented by the red lines, and by the PISA simulation represented by the black lines. The right panels show differences between them. All the distributions are scaled so that their integrals are 1. The distributions evaluated by the convolution successfully reproduce that evaluated by the PISA simulation, and uncertainties of the shapes evaluated by the convolution are much smaller than those by the PISA simulation.
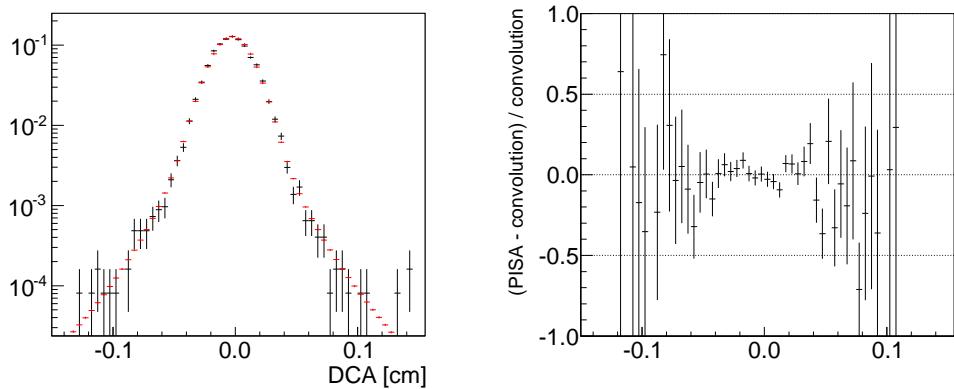
Figure 4.49: The DCA distributions of charm electrons with $1 < p_T < 2$ GeV/c evaluated by a Gaussian convolution represented and by the PISA simulation (left), and their difference (right). The red and black lines represent the distributions evaluated by the convolution and by the PISA simulation, respectively. All the distributions are scaled so that their integrals are 1.

4.9.4 Photon Conversion

The mean of the DCA distribution of conversion electrons is shifted to negative side more than others. Figure 4.51 illustrates a reconstruction of a conversion electrons. A photon projected from the collision point converts on a material and conversion electrons are ejected almost vertically from the material since the pair mass of the electrons is ~ 0. Therefore, the collision point tends to be outside of the bending
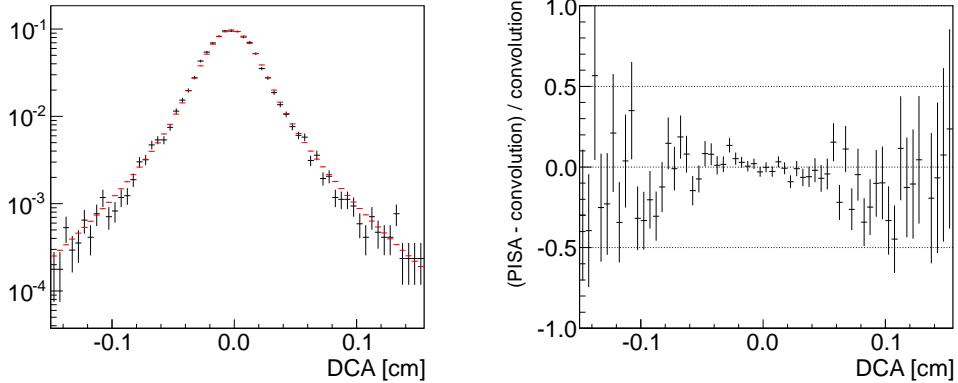
Figure 4.50: The DCA distributions of bottom electrons with $1 < p_T < 2$ GeV/c evaluated by a Gaussian convolution represented and by the PISA simulation (left), and their difference (right). The red and black lines represent the distributions evaluated by the convolution and by the PISA simulation, respectively. All the distributions are scaled so that their integrals are 1.

circles of the electron tracks as is illustrated in Fig. 4.51, and thus, the DCA values tend to be negative. This suggests that the RMS is also different from others.

The mean and RMS are evaluated by using the DCA distribution of electrons rejected by the isolation cut. A large part of the rejected electrons composed by the conversion electrons and the electrons from π^0 decays. The electrons from π^0 decays mainly have close hits on the B0. On the other hand, a large part of the conversion electrons do not have a close hit but have the hits on outer barrels, as is shown in Fig. 4.45. Therefore, a large part of the electrons which do not have a close hit on the B0 but have hit on outer barrels is the conversion electron. These electrons are utilized to evaluate the DCA distribution of the conversion electrons. Other contributions than the conversion electron are necessary to be subtracted. Here, the electrons which have close hits on the B0 are called B0 tracks, and those which do not have a close hit on the B0 but have hit on outer barrels are called $\overline{B0}$ tracks. It is assumed that B0 and $\overline{B0}$ tracks are composed only by the electrons from π^0 decays (π^0 component), conversion electrons (conversion component), and electrons rejected by hits created by uncorrelated tracks (uncorrelated component), and that B0 tracks are composed only by the conversion and the uncorrelated components and $\overline{B0}$ tracks composed by the three components. The fractions of B0 and $\overline{B0}$ tracks in total, N^{B0}/N_{all} and $N^{\overline{\mathrm{B0}}}/N_{all}$, can be expressed under the above assumptions as
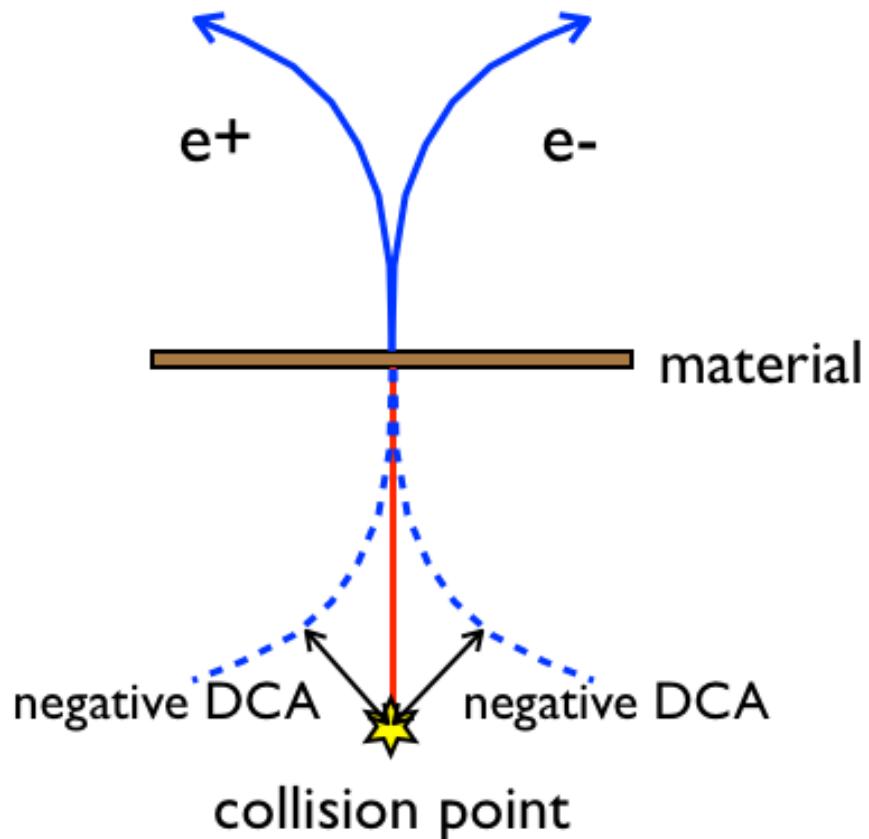
Figure 4.51: An illustration of a reconstruction of conversion electrons. A photon (red line) projected from the collision point converts on a material and conversion electrons are ejected (solid blue lines) almost vertically from the material. The dashed blue lines represent reconstructed paths of the electrons. The collision point tends to be outside of the bending circles of the electron tracks, and thus, the DCA values tend to be negative.

follow:

$$N^{\text{B0}}/N_{all} = (N_p^{\text{B0}} + N_u^{\text{B0}})/N_{all}$$
$$= \epsilon_p^{\text{B0}} R_p^0 + \epsilon_u^{\text{B0}}, \tag{4.60}$$
$$N^{\overline{\text{B0}}}/N_{all} = (N_c^{\overline{\text{B0}}} + N_p^{\overline{\text{B0}}} + N_u^{\overline{\text{B0}}})/N_{all}$$
$$= \epsilon_c^{\overline{\text{B0}}} R_c^0 + \epsilon_p^{\overline{\text{B0}}} R_p^0 + \epsilon_u^{\overline{\text{B0}}}, \tag{4.61}$$

where the subscripts, c, p, and u, represent the conversion, π^0, and uncorrelated components, respectively. ϵ^{B0} and $\epsilon^{\overline{\text{B0}}}$ represent the rejection fractions for B0 and $\overline{\text{B0}}$ tracks, respectively. ϵ_c^{B0} is assumed to be 0, as is assumed above. R_i^0 is defined at Eq. 4.54. ϵ_u^{B0} and $\epsilon_u^{\overline{\text{B0}}}$ are evaluated from hadrons. R_c^0 and R_p^0 are evaluated at Sec. 4.8.8. $\epsilon_c^{\overline{\text{B0}}}$ and $\epsilon_p^{\text{B0}} + \epsilon_p^{\overline{\text{B0}}}$ should be equal to 1-ϵ_c^{corr} and 1-ϵ_p^{corr} at Eq.4.49, respectively. In order to check the consistency between this estimation and the data, $\epsilon_p^{corr} R_p^0$ evaluated by this estimation is compared with that in Fig. 4.40. The results are summarized in Table. 4.9. They are consistent for any p_T range. Other compo-

Table 4.9: A consistency between this estimation and the data with $\epsilon_p^{corr} R_p^0$

p_T range	$\epsilon_p^{corr} R_p^0$	$1 - (N^{\text{B0}}/N_{all} - \epsilon_u^{\text{B0}}) - (N^{\overline{\text{B0}}}/N_{all} - \epsilon_c^{\overline{\text{B0}}} R_c^0 - \epsilon_u^{\overline{\text{B0}}})$
1.0-1.5 GeV/c	0.247 ± 0.022	0.202 ± 0.028
1.5-2.0 GeV/c	0.227 ± 0.026	0.188 ± 0.030
2.0-2.5 GeV/c	0.213 ± 0.027	0.181 ± 0.031
2.5-3.0 GeV/c	0.187 ± 0.024	0.183 ± 0.029
3.0-4.0 GeV/c	0.164 ± 0.024	0.114 ± 0.026
4.0-5.0 GeV/c	0.141 ± 0.023	0.073 ± 0.034

nents than the conversion are subtracted from $\overline{\text{B0}}$ tracks with Eq. 4.60 and Eq. 4.61. The distribution is fitted by a Gaussian and the mean and RMS are evaluated as a function of p_T. The left panel of Fig. 4.52 shows the DCA distribution related to the subtraction. The red histogram represents the distribution of $\overline{\text{B0}}$ tracks with $1 < p_T < 1.5$ GeV/c. The blue and green histograms represent those of the π^0 and uncorrelated components. The blue histogram is created as follows:

$$N_p^{\overline{\text{B0}}} = \frac{\epsilon_p^{\overline{\text{B0}}}}{\epsilon_p^{\text{B0}}} N_p^{\text{B0}} = \frac{\epsilon_p^{\overline{\text{B0}}}}{\epsilon_p^{\text{B0}}} (N^{\text{B0}} - \epsilon_u^{\text{B0}} N_{all}), \tag{4.62}$$

$$\frac{\epsilon_p^{\overline{\text{B0}}}}{\epsilon_p^{\text{B0}}} = \frac{N^{\overline{\text{B0}}} - N_c^{\overline{\text{B0}}} - \epsilon_u^{\overline{\text{B0}}} N_{all}}{N^{\text{B0}} - \epsilon_u^{\text{B0}} N_{all}}. \tag{4.63}$$

$\epsilon_u^{\text{B0}} N_{all}$ is evaluated with the DCA distribution of the inclusive electrons scaled by ϵ_u^{B0}, subtracted from the DCA distribution of the B0 tracks. Then, the subtracted distribution is scaled by $\epsilon_p^{\overline{\text{B0}}} / \epsilon_p^{\text{B0}}$. The green histogram is created with the DCA

distribution of the inclusive electrons scaled by $\epsilon_u^{\overline{\text{B0}}}$. The black histogram represents the conversion component, which is created by subtracting the blue and green histograms from the red histogram. The right panel of Fig. 4.52 shows the conversion component fitted by a Gaussian, which is represented by the red line. The left and right panels of Fig. 4.53 show the mean and RMS as a function of p_T represented as the solid circles. The mean and RMS are also evaluated by the PISA simulation, and its results are shown in the panels as open circles. The results of the data and the simulation are consistent. Since the mean and RMS of a large p_T region have a large uncertainty due to small statistics, they are approximated by functions. The fitting results are as follows:

$$\text{mean} : (-118.8 \pm 7.9)/p_T \ \mu\text{m}, \tag{4.64}$$

$$\text{RMS} : \sqrt{((90.9 \pm 5.0)/p_T)^2 + 130^2} \ \mu\text{m}. \tag{4.65}$$

A systematic error derived from the fitting errors is evaluated below at Sec. 4.10.
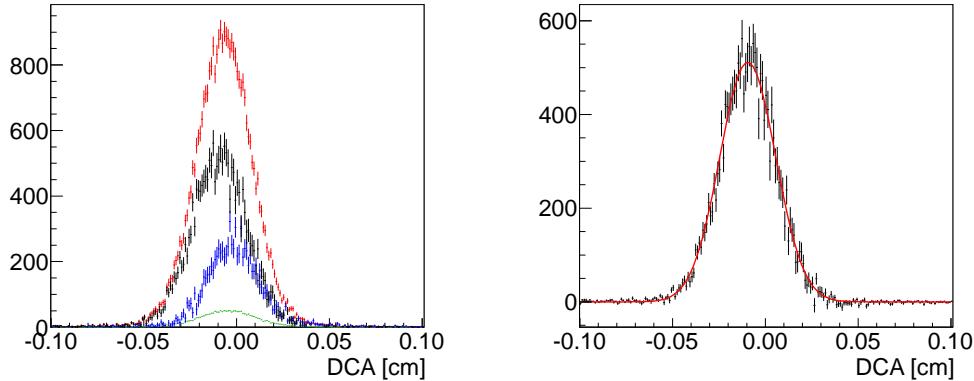
Figure 4.52: Left: The DCA distribution related to the subtraction. The red histogram represents the distribution of $\overline{\text{B0}}$ tracks with $1 < p_T < 1.5$ GeV/c. The blue, green, and black histograms represent those of the π^0, uncorrelated, and conversion components, respectively. The black histogram is created by subtracting the blue and green from the red.
Right: The DCA distribution of the conversion component fitted by a Gaussian. The black line represents the conversion component and the red line represents the Gaussian.

4.9.5 Hadron Contamination

The DCA distribution of hadrons is utilized as that of the hadron contamination. The dep cut is applied to select the hadrons in addition to the standard hadron selection. The efficiency for the dep cut for protons is different from those for pions and kaons due to the large mass of protons. Therefore, the compositions of pions, kaons, and
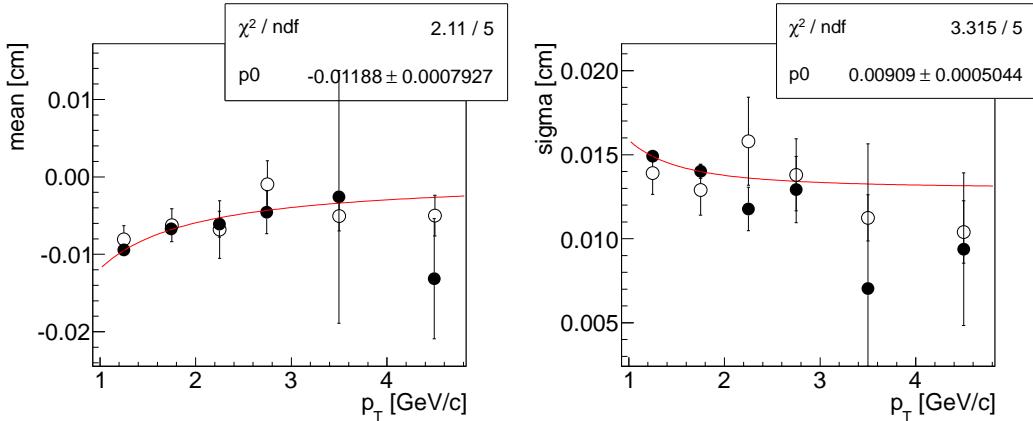
Figure 4.53: The mean (left) and RMS (right) of the DCA distribution of the conversion electrons as a function of p_T. The solid and open circles represent those of the data and PISA simulation. The red lines represent fitting functions.

protons in the inclusive hadrons are modified by the dep cut. The compositions of the hadrons with small DCA can be different from those of the hadron with large DCA since the former depends on the production mechanism of hadrons and the latter depends on yields of long-life hadrons, such as K_S^0 and Λ. Therefore, the DCA distribution can be modified by the dep cut. Figure 4.54 shows the DCA distributions of hadrons with $p_T > 1$ GeV/c. The black and red lines represent that of hadrons selected with and without the dep cut, respectively. The distributions are normalized with the maximum of them. Relative entry at $|DCA| > 1$ mm to the peak after applying de cut is larger than that without dep cut.

4.9.6 Fake Track Contribution

Fake tracks, which are reconstructed with hits created by another track, have a wider DCA distribution than true tracks, which are reconstructed with hits created by themselves. It creates a large background at a large DCA region. The fake tracks mainly created by decays of light neutral mesons such as π^0 and η. Decays from light mesons create hits very closely. For an example of a reconstruction of an electron from a π^0 decay, a fake hit is created by the positron from the same π^0 decay very close to a true hit created by the electron. Therefore, the fake hit is likely to be associated, especially when the true hit is not measured since it locates on a dead area. In such case, the fake track is not rejected by the isolation cut since a close hit, which corresponds to the true hit in this case, is not detected. From a study of the PISA simulation with π^0 single tracks with any fiducial cut, $\sim 1\%$ in total simulation tracks are the fake tracks, whereas $\sim 0.1\%$ in total of the single-track simulation of the charm or bottom electron. Since the yield ratios of the electrons from π^0 and η decays and the conversion electrons are less than 40% in the inclusive electrons, the
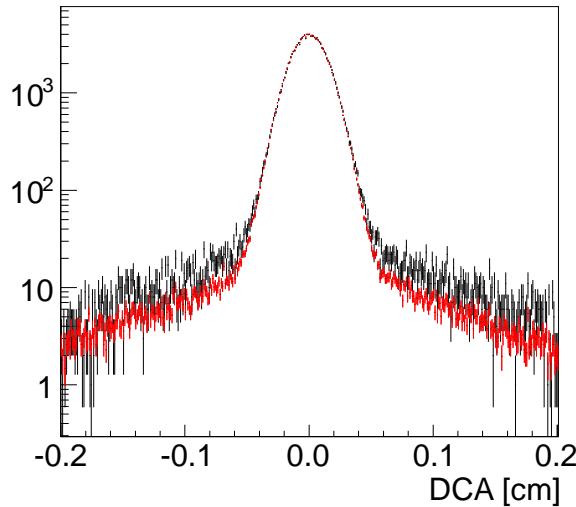
Figure 4.54: The DCA distributions of hadrons with $p_T > 1$ GeV/c. The black and red lines represent that of hadrons selected with and without the `dep` cut, respectively. The distributions were normalized with the maximum of them.

S/N ratio defined as the ratio of the numbers of the true and the fake tracks, is very large, $100 \sim 1000$. However, the background from the fake tracks is important since it can be comparable to bottom electrons at a low p_T region, and its DCA distribution is similar to that of bottom electrons.

The yield and shape of the DCA distribution of the fake tracks are evaluated independently. The yield is evaluated from the PISA simulation. The PISA simulations are performed with three fiducial cuts for Gr2, Gr3, and Gr7, and the fractions of the fake tracks in all electrons in the simulation are evaluated as a function of p_T. The simulations were performed for the electrons of π^0 and η decays and the conversion electrons. A error band is defined to cover $\pm 1\sigma$ of all the three fractions, and the center of the band is defined as the central point. Figure 4.55 shows the central points and error bands as a function of p_T. The top-left, top-right bottom panels shows those for the electrons from π^0, from η, and the conversion electrons, respectively. Since there is not a clear p_T dependence, it is assumed that the fractions are independent of p_T. The mean value of all the analysis p_T bins is assigned as the fraction for each of the sources and the unbiased variance is assigned as the error of the fraction. At last, the three fractions are combined with respect to the yield ratios of these sources, which are shown in Fig. 4.44, then, the fraction of fake tracks in the inclusive electrons is calculated. Figure 4.56 shows the fraction as a function of p_T. The fraction decreases as p_T increases since the yield ratios decrease.

In order to evaluate the shape of the DCA distribution, fake tracks are deliberately reconstructed by rotating CNTs 10 degrees. The rotation is performed for azimuthal or polar angle, randomly selected from them. These tracks are called rotated fake

130
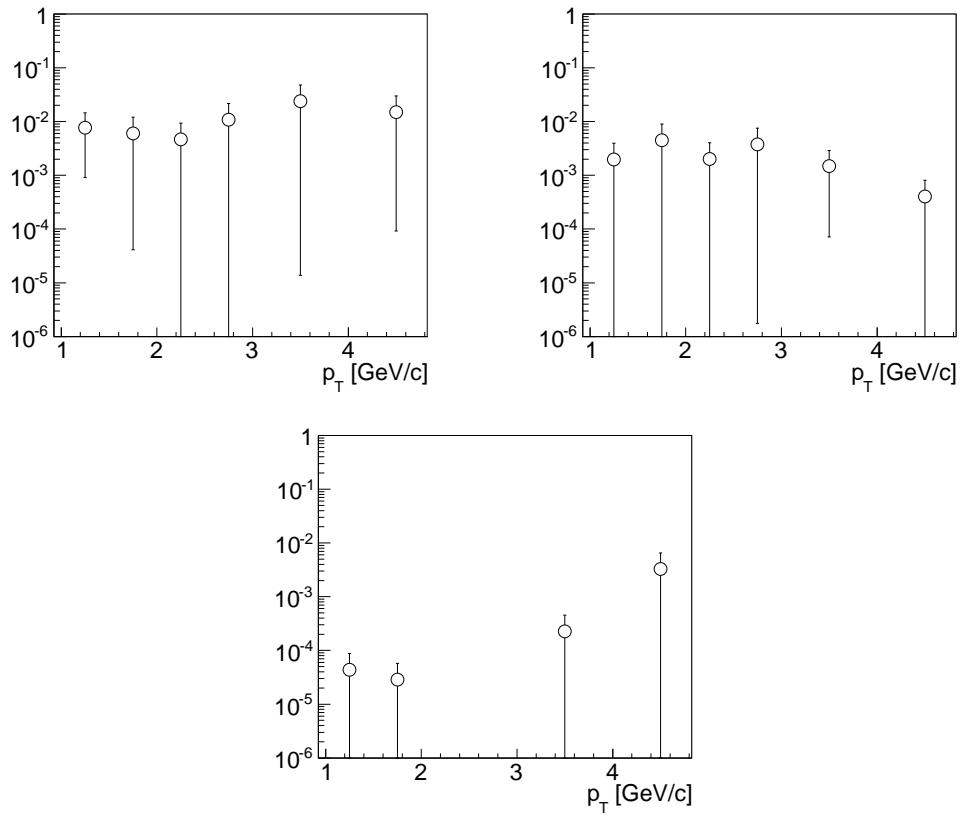
Figure 4.55: Fractions of fake tracks in all electrons in the PISA simulation as a function of p_T. The top-left, top-right bottom panels show those for the electrons from π^0, from η, and the conversion electrons, respectively.

131
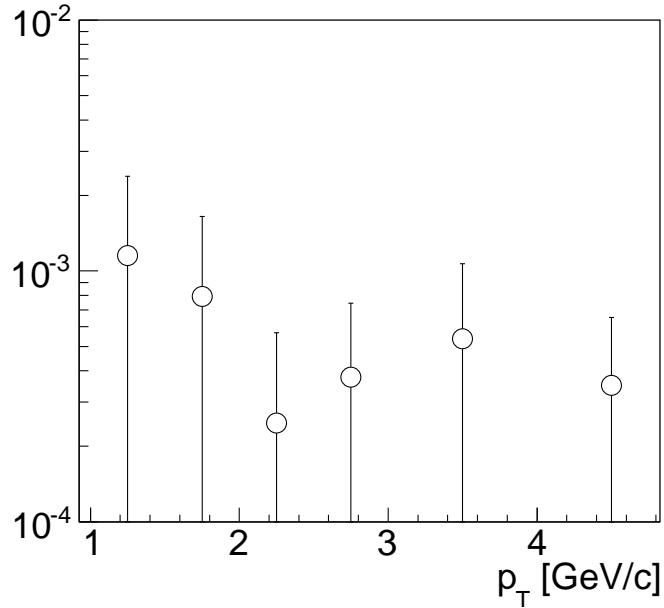
Figure 4.56: The fraction of fake tracks in the inclusive electrons as a function of p_T.

tracks in this thesis. The rotated fake tracks can not simulate the fake tracks completely. A large part of the fake tracks are created with a correlated hit such as a hit created by a particle with the same mother. On the other hand, the rotated fake tracks can not simulate these correlated fake tracks. Therefore, it can only provide a rough estimation. Figure 4.57 shows the DCA distribution of the rotated fake tracks of all charged particles with $p_T > 1$ GeV/c. The distribution is fitted by a Gaussian at $|\text{DCA}| < 0.15$ μm. The mean is $+81.6$ μm and RMS is 175 μm. Then, the Gaussian fittings are repeated by changing the fitting range and by fixing the mean of the Gaussian on $+81.6$ μm, which is the result of the fitting at $|\text{DCA}| < 0.15$ μm. The results are summarized in Table 4.10. When the mean of the Gaussian is changed to ± 100 μm, the changes of the fitting results are within the errors. The DCA distribution of the fake tracks is approximated by a Gaussian. The RMS of the Gaussian is set to 250 μm. In addition, the RMS is changed from 150 to 650 μm in systematic error evaluation, described in Sec. 4.10. The mean of the Gaussian is also changed to ± 100 μm.

4.10 Systematic Error Estimation

There are 8 items which derives the systematic errors, which are listed below. The systematic errors derived from the uncertainties of the yield and template of DCA distribution of each electron sources are evaluated by repeating the fitting procedure
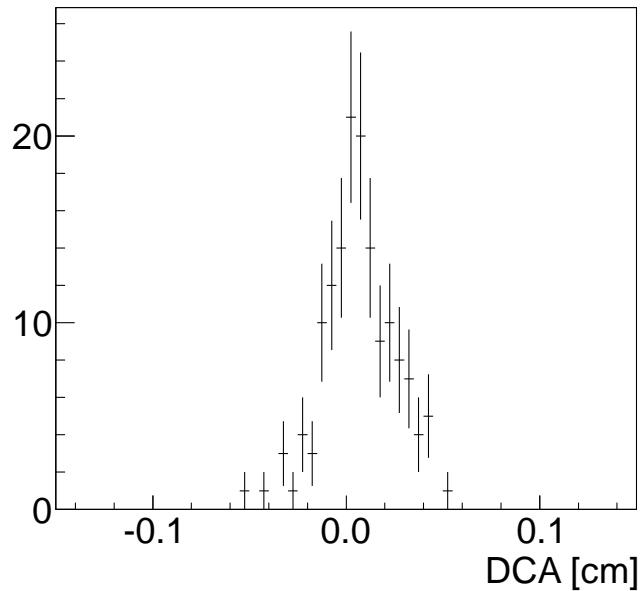
Figure 4.57: The DCA distribution of the rotated fake tracks with $p_T > 1$ GeV/c.

Table 4.10: The results of the Gaussian fitting of the DCA distribution of the rotated fake tracks.

fitting range	RMS of the Gaussian
-0.15 < DCA < 0.15 cm	175 ± 15 μm
-0.15 < DCA < -0.02 cm	381 ± 266 μm
0.02 < DCA < 0.15 cm	207 ± 34 μm

and the variations of f_b are evaluated, which correspond to the 1st to 7th items. The 8th item corresponds to the error for the efficiency of the isolation cut. The evaluations are performed about following items:

1. Yield of each electron sources: Yield ratios of all sources are shifted one by one. The shifts are performed for ± 1 σ in Fig. 4.44. The shift of the fake track contribution is in Fig. 4.56.

2. The mean of DCA distributions: The mean in simulations was shifted to reproduce the DCA distribution of the data, as is explained at Sec. 4.9.1. Figure 4.48 shows the mean values of the DCA distributions of the data and the simulation. The mean values in the simulation successfully reproduce that of the data, and is changed ± 10 μm in the study of the systematic error estimation. The mean values of all electrons are changed at the same time except for the hadron contamination, conversion electrons, and fake tracks, whose mean values are evaluated independently.

3. The DCA resolution: The starting point of tracks in simulations are smeared to reproduce the width of the data. As is shown in Fig. 4.47, the width of hadrons in the simulation well reproduces that of the data, and the difference is ~ 5 μm. Therefore, the width in the simulation is changed ± 5 μm. The widths of all electrons are changed at the same time except for the hadron contamination, conversion electrons, and fake tracks.

4. The DCA distribution of conversion electrons: The mean and width are changed. As is discussed at Sec. 4.9.4, the distribution is approximated by a Gaussian and its mean and width are calculated by the fitting functions of Eq. 4.64 and 4.65. The parameters at these equations are changed ± 1 σ in this study.

5. The DCA distribution of fake tracks: The total yield, mean, and width are changed.

   5-1. Mean: changed ± 100 μm.

   5-2. RMS: changed to 200, 300, 400, 500, 600, and 700 μm and calculated the standard deviation.

6. The DCA distribution of heavy-quark electrons :

   6-1. Particle ratios (D^+/D^0, D_s/D^0, Λ_c/D^0, B^+/B^0, B_s/B^0, Λ_b/B^0).

   6-2. p_T spectra of charm and bottom quarks.

   6-3. Charm and bottom masses.

   The amounts of the changes are listed in Sec. 4.7.2.

134

Table 4.11: Summary of systematic errors.

p_T range (GeV/c)	1.5-2.0	2.0-2.5	2.5-3.0	3.0-4.0	4.0-5.0
1	$< 1\%$	$< 1\%$	$< 1\%$	$< 1\%$	$< 1\%$
2	$\pm 1\%$	$\pm 3\%$	$\pm 7\%$	$\pm 3\%$	$\pm 6\%$
3	$\pm 39\%$	$\pm 20\%$	$\pm 18\%$	$\pm 24\%$	$\pm 14\%$
4 (mean)	$\pm 1\%$	$< 1\%$	$< 1\%$	$< 1\%$	$< 1\%$
4 (RMS)	$\pm 1\%$	$< 1\%$	$< 1\%$	$< 1\%$	$< 1\%$
5-1	$< 1\%$	$< 1\%$	$< 1\%$	$< 1\%$	$< 1\%$
5-2	$\pm 2\%$	$< 1\%$	$< 1\%$	$< 1\%$	$< 1\%$
6-1 (D^+/D^0)	$\pm 3\%$	$\pm 1\%$	$\pm 1\%$	$\pm 1\%$	$< 1\%$
6-1 (D_s/D^0)	$< 1\%$	$< 1\%$	$< 1\%$	$< 1\%$	$< 1\%$
6-1 (Λ_c/D^0)	$< 1\%$	$< 1\%$	$< 1\%$	$< 1\%$	$< 1\%$
6-1 (B^+/B^0)	$< 1\%$	$< 1\%$	$< 1\%$	$< 1\%$	$< 1\%$
6-1 (B_s/B^0)	$< 1\%$	$< 1\%$	$< 1\%$	$< 1\%$	$< 1\%$
6-1 (Λ_b/B^0)	$\pm 4\%$	$\pm 4\%$	$\pm 4\%$	$\pm 5\%$	$\pm 5\%$
6-2 (charm)	$\pm 8\%$	$\pm 7\%$	$\pm 8\%$	$\pm 10\%$	$\pm 1\%$
6-2 (bottom)	$\pm 36\%$	$\pm 38\%$	$\pm 40\%$	$\pm 43\%$	$\pm 41\%$
6-3 (charm)	$< 1\%$	$< 1\%$	$< 1\%$	$\pm 4\%$	$\pm 9\%$
6-3 (bottom)	$< 1\%$	$< 1\%$	$< 1\%$	$< 1\%$	$\pm 1\%$
7	$\pm 6\%$	$\pm 12\%$	$\pm 9\%$	$\pm 6\%$	$\pm 4\%$
8	$\pm 27\%$	$\pm 9\%$	$\pm 8\%$	$\pm 8\%$	$\pm 6\%$
total	66%	46%	48%	54%	48%

7. Fitting range: The default fitting range is |DCA| $<$ 1.0 mm. In addition, the fittings with the ranges of ± 0.75 mm and ± 1.25 mm are performed.

8. The error derived from the error of r^{iso} is also quadratically added in the systematic error.

The changes of the results by $+1\sigma$ and -1σ shifts about all items except for the RMS of the DCA distribution of the fake tracks and p_T spectra and masses of charm and bottom quarks, are averaged and the averages are assigned both positive and negative sides of the systematic error since the changes are symmetric. The averages are quadratically added in the systematic error. As for the RMS of the DCA distribution of the fake tracks, the changes are evaluated with 6 patterns and their standard deviation is added in the systematic error. As for p_T spectra of charm and bottom quarks, two spectra are utilized for both charm and bottom, and the changes by the spectra which shift p_T spectra of quarks larger are assigned. As for the quark masses, both of the changes are assigned. Since the variation of the p_T spectra and masses are limited, the same errors are assigned for both positive and negative sides.

Chapter 5

Result

In this chapter, the fraction of the bottom contribution in the heavy-quark electron, f_b, and the cross sections of charm and bottom electrons are described. As is described in the beginning of chapter 4, differential cross sections of charm and bottom electrons are evaluated by multiplying the differential cross section of the heavy-quark electrons and f_b. f_b is evaluated in this thesis by the DCA approach, and previously measured result of the differential cross section of the heavy-quark electrons is used [15]. Results of DCA fitting and f_b is described in Sec. 5.1. The differential cross section of the charm and the bottom electrons are calculated in Sec. 5.2. The total cross section of bottoms is measured from the differential cross section of bottom electrons, which is described in Sec. 5.3.

5.1   Fraction of Bottom Contribution

f_b is calculated as a function of p_T by using the DCA distribution of the inclusive electrons. It is calculated by fitting the DCA distribution of the inclusive electrons of the data using the distributions of electrons from all sources described at Sec. 4.9. The overview of the DCA fitting is provided at Sec. 4.1.

Figure 5.1 shows f_b in the heavy quark electrons as a function of electron p_T with a FONLL calculation [26]. The black points represents the fractions and the bars and the boxes associated to the points represents the statistical and the systematic errors, respectively. The statistical error corresponds to a fitting error. Evaluation of the systematic error is described in Sec. 4.10. The red line represents the central value in FONLL prediction and magenta dotted line represents the uncertainty of the FONLL calculation. The results are also summarized in Table 5.1. The results of the fitting of the DCA distributions are shown in Fig. 5.2 to 5.6. The black points represent the DCA distribution of the data. The magenta, blue, green, cyan, gray, purple, and brown lines represent the distributions of charm electrons, bottom electrons, conversion electrons, electrons from short-life hadrons, from K_{e3}, fake tracks, and hadron contamination, respectively. The red line represents sum of these components.

χ^2/NDF values are summarized in Table 5.2. Lower-right panels show ratios between data and the fitting result. The fitting results successfully reproduced the DCA distributions in the data.
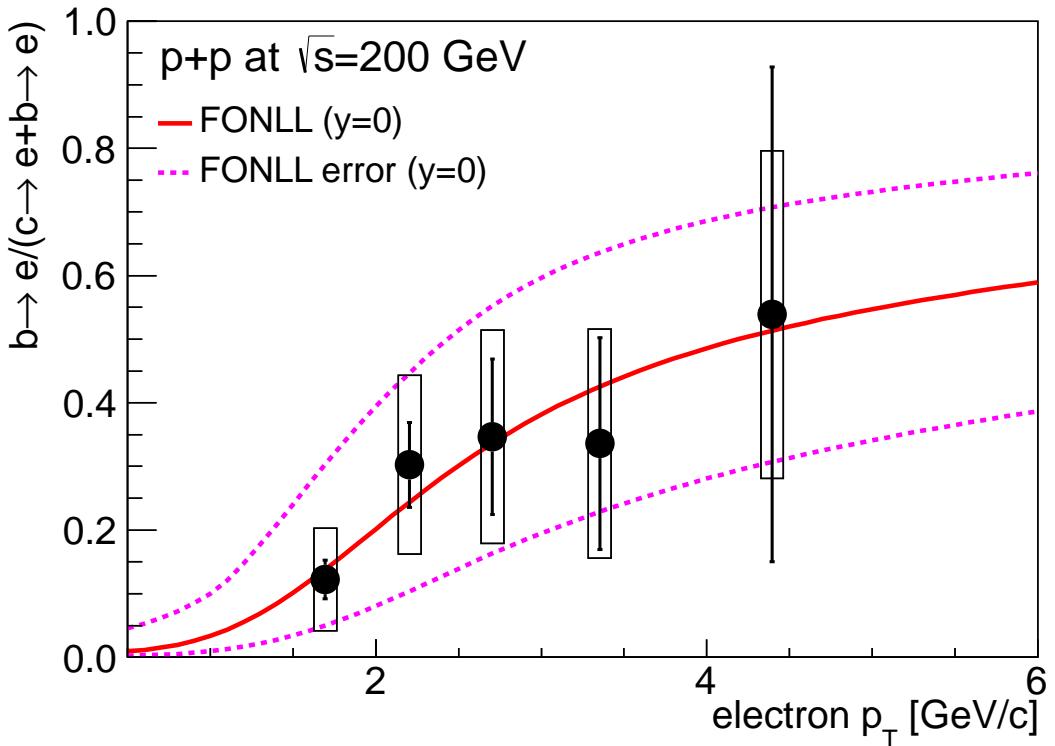

Figure 5.1: The fraction of the bottom contribution in the heavy quark electrons as a function of electron p_T with FONLL calculation. The black points represent the fractions and the bars and the boxes associated to the points represent the statistical and the systematic errors, respectively. The red line represents the central value in the FONLL calculation and the magenta dotted line represents the uncertainty of the calculation.

5.2 Cross Section of Electrons from Charm and Bottom

The cross section of the charm and the bottom electrons are calculated by using f_b and the cross section of the heavy quark electrons. The cross section of the heavy quark electrons reported in Ref. [15] is used. Figure 5.7 shows the differential invariant cross sections of the charm and bottom electrons with FONLL calculations [26]. The magenta and blue points represent the cross sections of the charm and bottom electrons, respectively. The bars and boxes associated to the points represent the statistical and the systematic errors, respectively. The magenta and blue lines represent
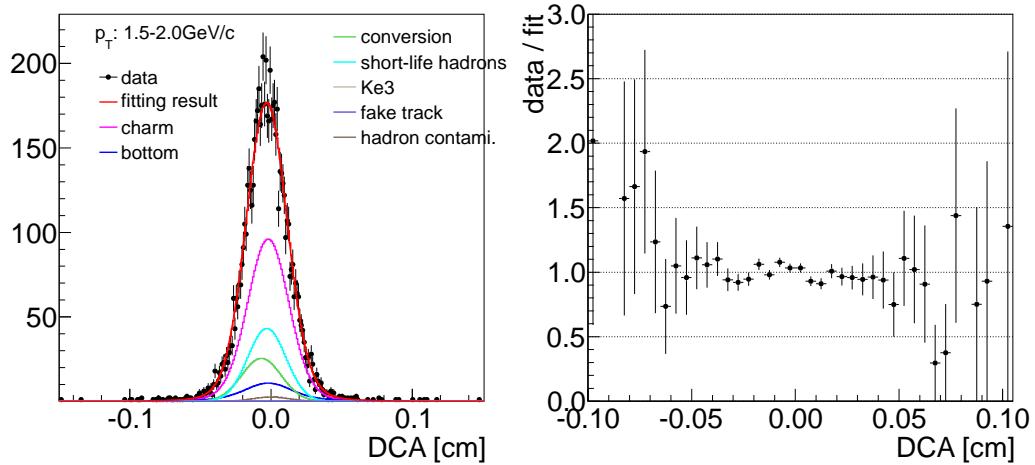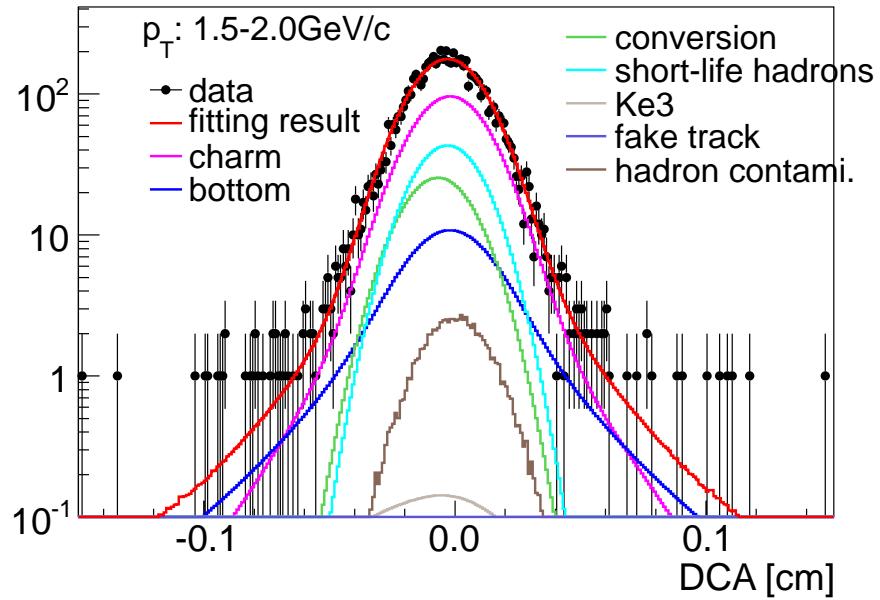
Figure 5.2: Upper and lower-left panels shows a fitting result of the DCA distribution of electrons with $1.5 < p_T < 2.0$ GeV/c. The black points represents the DCA distribution of the data. The red line represents the fitting result. The magenta, blue, green, cyan, gray, purple, and brown lines represent the distributions of charm electrons, bottom electrons, conversion electrons, electrons from short-life hadrons, from K_{e3}, fake tracks, and hadron contamination, respectively. Lower-right panel shows a ratio between data and the fitting result.
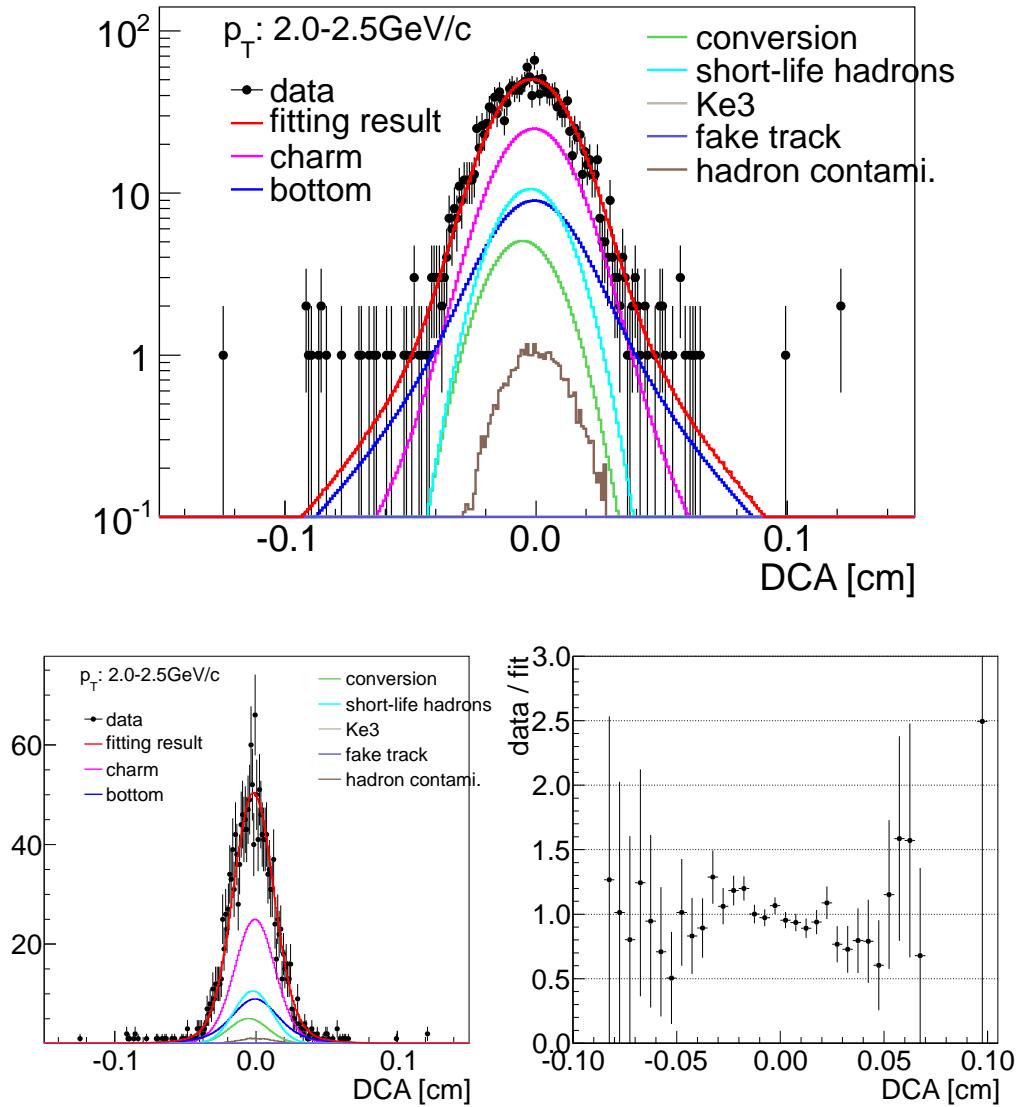
Figure 5.3: Upper and lower-left panels shows a fitting result of the DCA distribution of electrons with $2.0 < p_T < 2.5$ GeV/c. The black points represents the DCA distribution of the data. The red line represents the fitting result. The magenta, blue, green, cyan, gray, purple, and brown lines represent the distributions of charm electrons, bottom electrons, conversion electrons, electrons from short-life hadrons, from K_{e3}, fake tracks, and hadron contamination, respectively. Lower-right panel shows a ratio between data and the fitting result.
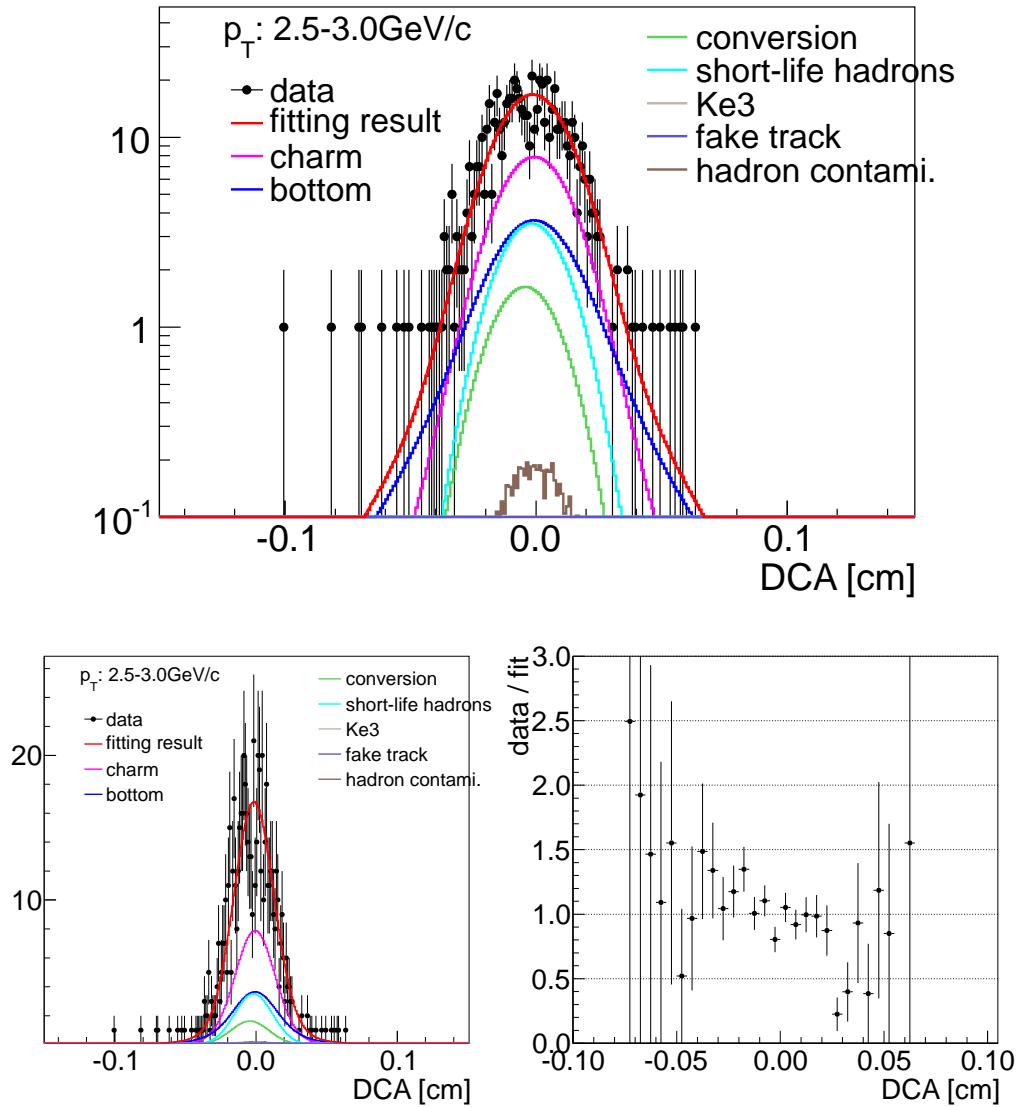
Figure 5.4: Upper and lower-left panels shows a fitting result of the DCA distribution of electrons with $2.5 < p_T < 3.0$ GeV/c. The black points represents the DCA distribution of the data. The red line represents the fitting result. The magenta, blue, green, cyan, gray, purple, and brown lines represent the distributions of charm electrons, bottom electrons, conversion electrons, electrons from short-life hadrons, from K_{e3}, fake tracks, and hadron contamination, respectively. Lower-right panel shows a ratio between data and the fitting result.
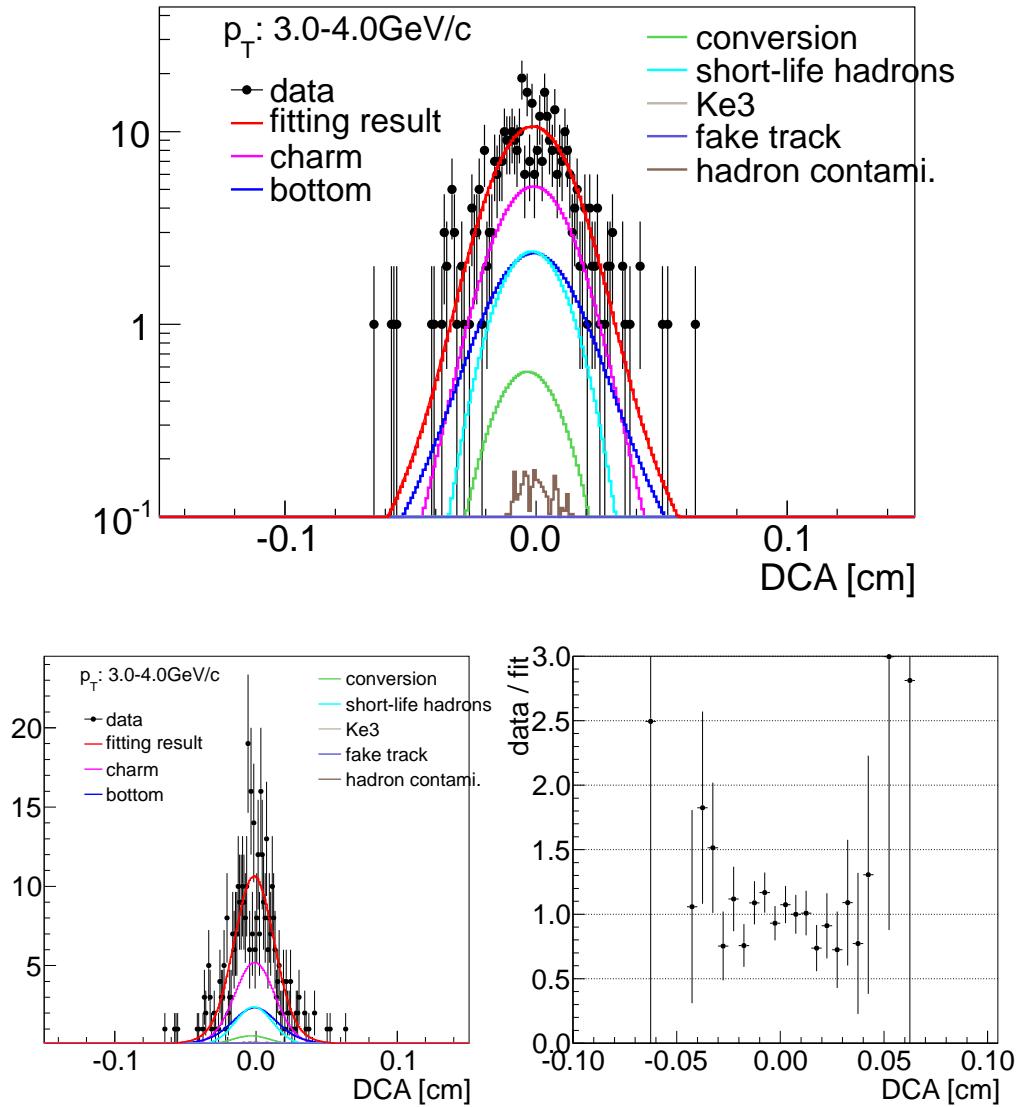
Figure 5.5: Upper and lower-left panels shows a fitting result of the DCA distribution of electrons with $3.0 < p_T < 4.0$ GeV/c. The black points represents the DCA distribution of the data. The red line represents the fitting result. The magenta, blue, green, cyan, gray, purple, and brown lines represent the distributions of charm electrons, bottom electrons, conversion electrons, electrons from short-life hadrons, from K_{e3}, fake tracks, and hadron contamination, respectively. Lower-right panel shows a ratio between data and the fitting result.
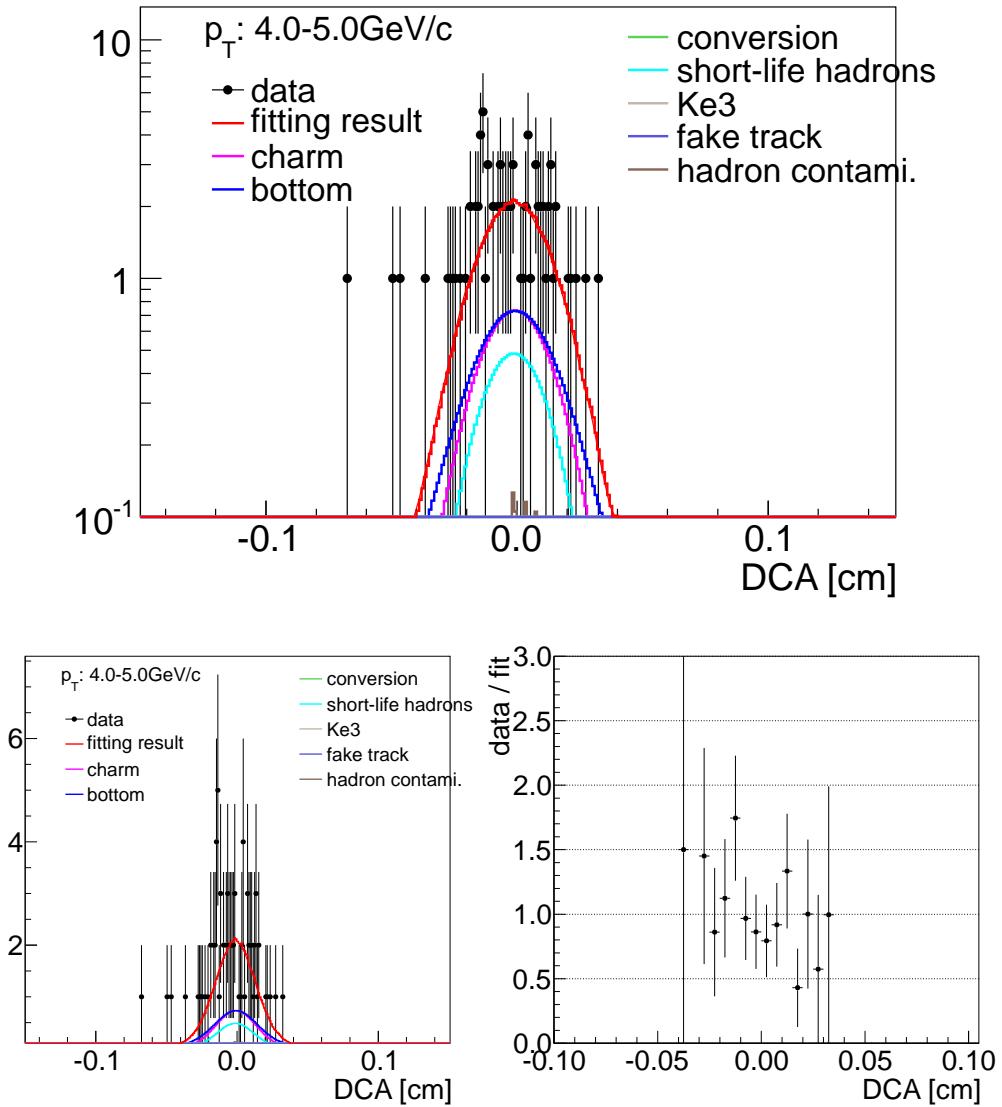
Figure 5.6: Upper and lower-left panels shows a fitting result of the DCA distribution of electrons with $4.0 < p_T < 5.0$ GeV/c. The black points represents the DCA distribution of the data. The red line represents the fitting result. The magenta, blue, green, cyan, gray, purple, and brown lines represent the distributions of charm electrons, bottom electrons, conversion electrons, electrons from short-life hadrons, from K_{e3}, fake tracks, and hadron contamination, respectively. Lower-right panel shows a ratio between data and the fitting result.

143

Table 5.1: The result of the bottom fraction as a function of p_T.

p_T	bottom fraction
1.69 GeV/c	0.122 ± 0.031 (stat) ±0.0849437 (sys)
2.20 GeV/c	0.303 ± 0.066 (stat) ±0.155334 (sys)
2.71 GeV/c	0.347 ± 0.122 (stat) ±0.195511 (sys)
3.35 GeV/c	0.336 ± 0.167 (stat) ±0.195655 (sys)
4.40 GeV/c	0.539 ± 0.389 (stat) ±0.277709 (sys)

Table 5.2: χ^2/NDF of the DCA fitting.

p_T	χ^2/NDF
1.69 GeV/c	0.92
2.20 GeV/c	0.52
2.71 GeV/c	0.52
3.35 GeV/c	0.49
4.40 GeV/c	0.23

the FONLL calculations for the cross sections of the charm and bottom electrons, respectively. The green and cyan lines represent the calculations for b → e and b → c → e, respectively.

The integration of the cross section of the bottom electrons are 48.7 ± 7.5 (stat) ± 27.9 (syst) nb. The cross section of the bottom electrons of the FONLL calculation for the corresponding region, 1.5< p_T <5 GeV/c and $|y|$ <0.5, is $25.8^{+12.4}_{-8.8}$ nb, which is consistent with our result.

A consistency check between the cross sections of the heavy quark electrons of the result and the simulation to create heavy quarks was performed. This check is important since the DCA distributions of the charm and bottom electrons depend on the p_T slopes of charm and bottom quarks in the simulation. The upper and lower panels of Fig. 5.8 show the cross sections of the charm and bottom electrons, respectively. The magenta and blue points represent our results for the charm and bottom electrons, respectively. In this analysis, three different spectra are used to estimate the systematic error derived from uncertainties of the p_T spectra of charm and bottom quarks, as is written in Sec. 4.7.2. The red, green, and cyan lines represent the spectra of the PYTHIA simulation, the single-weighted, and the double-weighted spectra. These spectra are scaled independently in order for the following χ^2 to be minimum.

$$\chi^2 = \sum_i \left(\frac{E\frac{d^3\sigma}{dp^3}(\text{data})|_{\text{PT=PT,i}} - E\frac{d^3\sigma}{dp^3}(\text{sim})|_{\text{PT=PT,i}}}{\sigma_{\text{data}}|_{p_T=p_{T,i}}} \right)^2. \tag{5.1}$$

Here, σ_{data} is the square root of the statistical and systematic error of the result. The χ^2/NDF values for each of the p_T spectra are summarized in Table 5.3. The results are matched to the p_T spectrum created by the PYTHIA simulation (red line), which
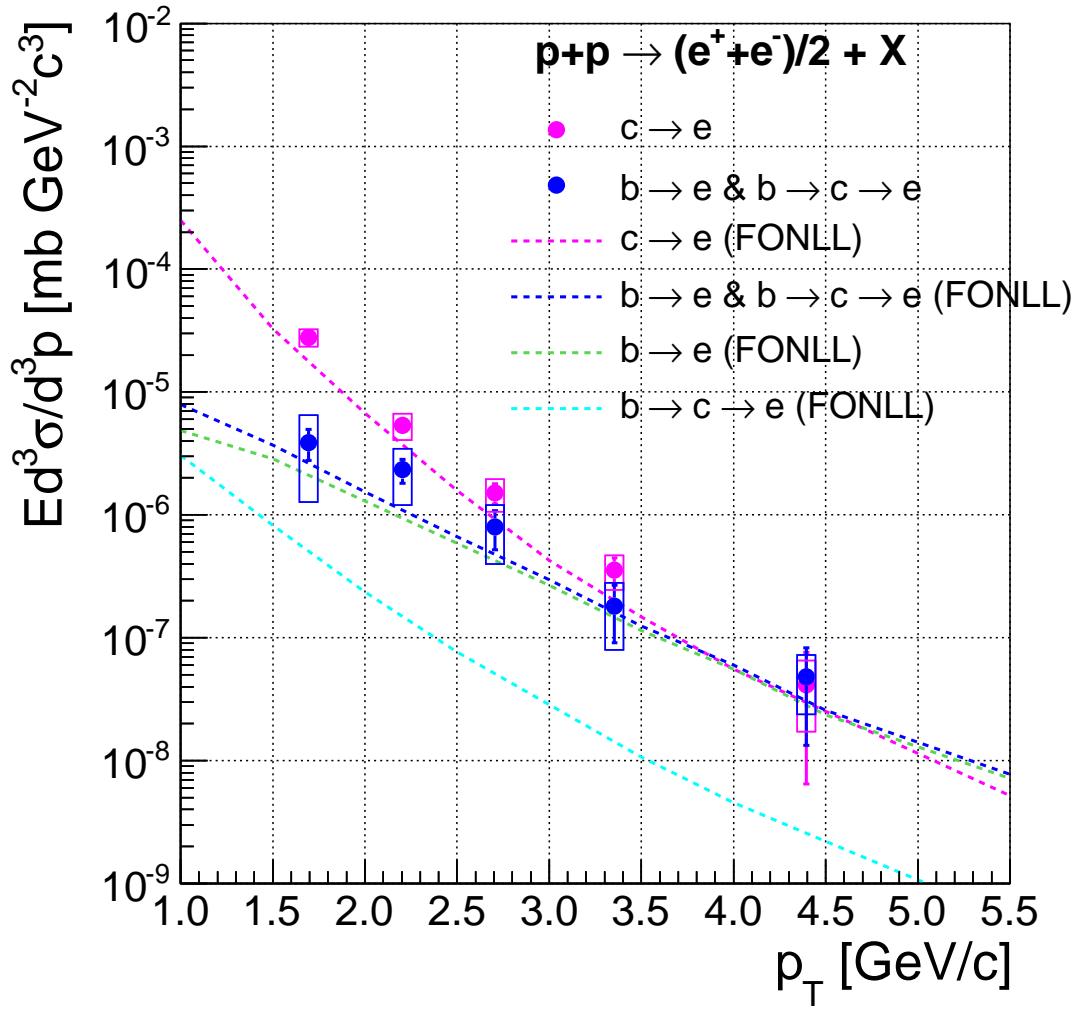
Figure 5.7: The differential invariant cross sections of the charm and bottom electrons with FONLL calculations. The magenta and blue points represent the cross sections of the charm and bottom electrons, respectively. The bars and boxes associated to the points represent the statistical and the systematic errors, respectively. The magenta and blue lines represent the FONLL calculations for the cross sections of the charm and bottom electrons, respectively. The green and cyan lines represent the calculations for b → e and b → c → e, respectively.

is used to evaluate the central point.

Table 5.3: χ^2/NDF of the DCA fitting.

p_T	charm	bottom
PYTHIA	0.36	0.29
single-weighted	0.14	0.56
double-weighted	0.03	0.96

5.3 Total Cross Section of Bottom Production

Total cross section of bottom is calculated from that of the bottom electrons. The calculation is performed as follows:

$$
\sigma_{b\bar{b}} = \int \int \frac{1}{2\pi p_T} \frac{d\sigma_{b\bar{b}}}{dp_T dy} dp_T dy
$$
$$
= C_{b\rightarrow e} \cdot C_{BR} \cdot C_{p_T} \cdot C_y \left(\left. \frac{d\sigma_{b\rightarrow e+b\rightarrow c\rightarrow e}}{dy} \right|_{y=0} (1.5 < p_T < 5\text{GeV/c}) \right). \tag{5.2}
$$

In order to calculate the total cross section from the cross section measured in a limited phase space, following corrections are necessary.

1. Subtraction of the contribution of $b \rightarrow c \rightarrow e$.

2. Correction by the branching ratio.

3. Extrapolation of p_T range.

4. Extrapolation of rapidity range.

$C_{b\rightarrow e}$, C_{BR}, C_{p_T}, and C_y correspond to correction factors for these corrections. These correction factors are evaluated by using FONLL calculations with two sets of PDFs, CTEQ6.6 [79] and MSTW2004nlo [80] as follows:

$$
C_{b\rightarrow e} \cdot C_{BR} \cdot C_{p_T} \cdot C_y = \frac{\sigma_{b\bar{b}}}{\left. \frac{d\sigma_{b\rightarrow e+b\rightarrow c\rightarrow e}}{dy} \right|_{y=0} (1.5 < p_T < 5\text{GeV/c})}. \tag{5.3}
$$

The results of the calculations are as follows:

$$
\text{CTEQ6.6} : C_{b\rightarrow e} \cdot C_{BR} \cdot C_{p_T} \cdot C_y = 69.96^{+1.43}_{-2.04} \tag{5.4}
$$
$$
\text{MSTW2004nlo} : C_{b\rightarrow e} \cdot C_{BR} \cdot C_{p_T} \cdot C_y = 70.27^{+1.96}_{-2.28} \tag{5.5}
$$

Uncertainties of the branching ratios are not included in above result. The uncertainties are evaluated from the branching ratio of each bottom hadron and production

146
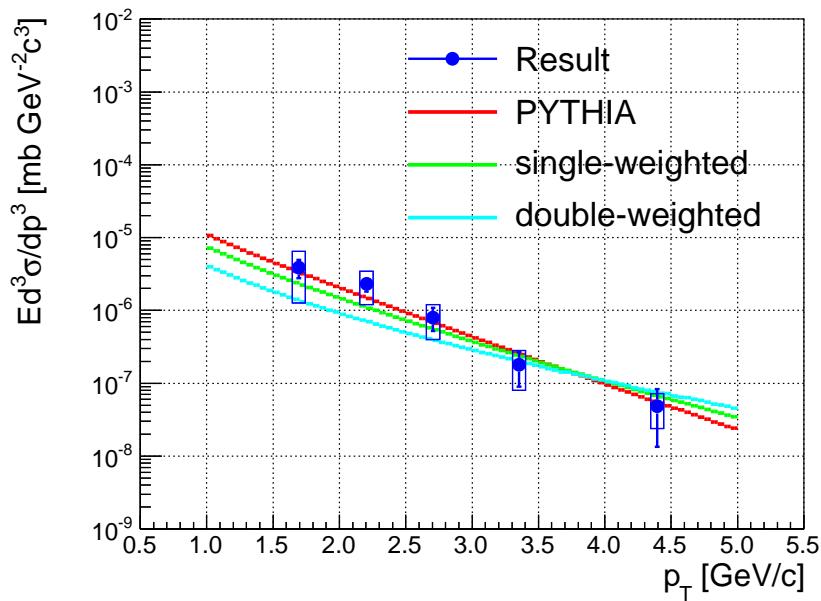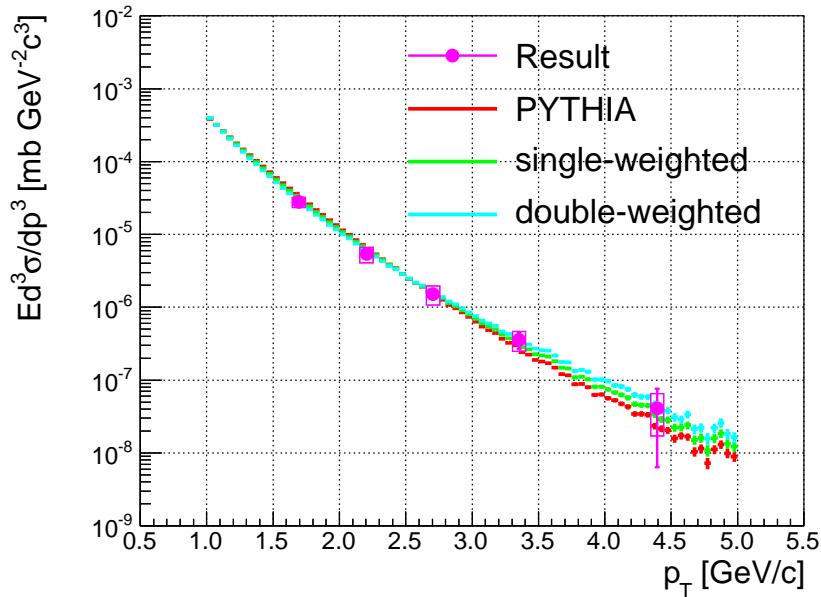
Figure 5.8: The cross sections of the heavy quark electrons of the result and the simulation to create heavy quarks. The upper and lower panels show the cross sections of the charm and bottom electrons, respectively. The red, green, and cyan lines represent the slope of the PYTHIA simulation, the single-weighted, and the double-weighted slopes. These slopes were scaled independently in order for the χ^2 in Eq. 5.1 to be minimum.

147

Table 5.4: Branching ratios of bottom hadrons decaying into electrons.

hadron	branching ratio
$B^{\pm}$	10.8 ± 0.4
B^0	10.1 ± 0.4
B_s	7.9 ± 2.4
B baryons	8.6 ± 2.5

ratios, which are summarized in Table 4.7. The branching ratios and their uncertainties are summarized in Table 5.4. As a result, inclusive $BR(b \to e)$ is determined to be $(10.0\pm1)\%$, and additional 10% of error is added to the correction factor. Finally, 70.08 ± 7.33 is used as the correction factor.

The integral of the differential cross section of the bottom electrons at $1.5 < p_T < 5\,\mathrm{GeV}/c$ is 48.7 ± 7.5 (stat) ± 27.9 (syst) nb. After the correction, the total cross section is

$$\sigma_{b\bar{b}} = 3.41 \pm 0.53(\mathrm{stat}) \pm 2.14(\mathrm{syst})\ \mu\mathrm{b}. \tag{5.6}$$

The result is consistent with the previous result reported by the PHENIX experiment, $3.2\ ^{+1.2}_{-1.1}$ (stat) $^{+1.4}_{-1.3}$ (syst) μb [15] and the FONLL prediction, $1.92^{+1.21}_{-0.78}\ \mu$b, is also consistent with our result.

Chapter 6

Discussion

In this chapter, discussions about the result presented at the previous chapter are described. Our result is compared with other results in Sec. 6.1. A comparison with a perturbative QCD (pQCD) calculation, and the reproducibility of the calculation for the heavy quark production is discussed in Sec. 6.2. The comparison is also performed including results of different collision energies with the total cross section of bottom quarks in Sec. 6.3. At last, future prospectives about A+A collisions are provided in Sec. 6.4.

6.1 Bottom Contribution in Heavy Quark Electron

The fraction of bottom contribution in the heavy-quark electrons, f_b, in $p+p$ collisions has been evaluated by other approaches by using correlations between the electrons and hadrons from the heavy-quark decays, as are reviewed in Sec. 2.4.1. The problem of these approach is that they can not be utilized in A+A collisions due to a large combinatorial background of uncorrelated hadrons. However, they can be utilized in $p+p$ collisions since the multiplicity of hadron is small in $p+p$ collisions, and thus, they can provide good references for our result. Figure 6.1 shows f_b as a function of p_T in $p+p$ collisions with $\sqrt{s} = 200$ GeV. The black points represent our result. The blue and green points represent the results reported from PHENIX and STAR experiments, respectively [15, 16]. The associated bars and boxes represent the statistical and systematic errors, respectively. The red line represents the prediction of the FONLL calculation and the magenta dotted line represents its uncertainty [26]. CTEQ6M is used as the parton distribution function (PDF) in this calculation. f_b measured by this work is consistent with other results. It demonstrates the DCA approach works in $p+p$ collision. The errors associated to our result are larger than others since the statistics is much smaller than others. The statistics for our work is $\sim 1/6$ and $\sim 1/50$ of the results from PHENIX and STAR experiments, respectively. The smaller

statistics is due to smaller integrated luminosity and a low reconstruction efficiency due to dead area of the VTX. The dead area of the VTX will be improved in a future A+A collision run.
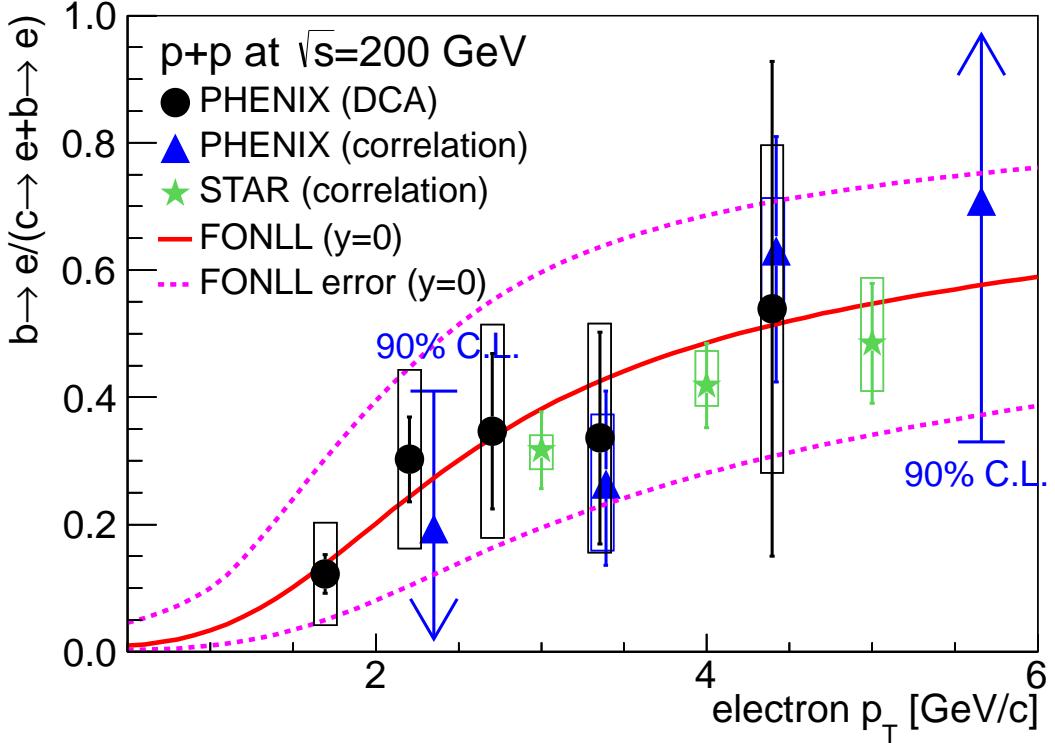
Figure 6.1: The fraction of the bottom contribution in the heavy quark electrons as a function of p_T in $p+p$ collisions with $\sqrt{s}$ =200 GeV. The black points represents the result measured by this work. The blue and green points represent the results reported from PHENIX and STAR experiments, respectively [15, 16], by using the correlation between the electrons and hadrons from the heavy quark decays. The associated bars and boxes represent the statistical and systematical errors, respectively. The red line represents the prediction of the FONLL calculation and the magenta dotted line represents its uncertainty.

In addition to the confirmation of the DCA approach, our result achieves to measure the fraction at lower p_T region, $1.5 < p_T < 2.5$ GeV/c, than others. A large azimuthal anisotropy of the heavy quark electrons has been observed at the region, which is shown in the lower panel of Fig. 2.9. It indicates that the heavy quark is affected by the dynamical expansion of the matter. Therefore, the evaluation of charm and bottom contributions at the region is important to study the behavior of heavy quarks in the matter. The result at the p_T region provides a reference to the result of A+A collisions for the corresponding region.

6.2   Comparison with Theoretical Prediction

The measured yield of heavy quarks in $p+p$ collisions provides a good test of pQCD calculations. The ratios of measured yield over the FONLL calculations are studied [26]. Figure 6.2 shows ratios of our results and the FONLL calculations of the charm and bottom electrons as a function of electron p_T. The upper and lower panels represent the ratios for the charm and bottom electrons, respectively. CTEQ6M is used as the PDF for the FONLL calculation. The dotted lines represent the error band of the FONLL calculations. The cross section of the FONLL calculations is consistent with that of the charm and bottom electron. When the ratios are fitted by a constant, the fitting results for charm and bottom are 1.40±0.18 and 1.44±0.41, respectively. Therefore, the FONLL calculations reproduce the results with the same level.

The similar tendency can be found in $p+\bar{p}$ collisions at $\sqrt{s} = 1.96$ GeV at Tevatron at low p_T. Figure 6.3 and 6.4 show the ratios of measured results at CDF and FONLL calculations of D and B hadrons, respectively, as a function of p_T of heavy-quark hadrons [28]. Both charm and bottom signal predicted by FONLL calculation is slightly smaller than the measured results.

6.3   Cross Section of Bottom Production

The total cross section of bottom evaluated based on our result is compared with other results measured in different collision energies. The comparison can provide another test of the pQCD calculation. Figure 6.5 shows the total cross sections of the bottom production from our result and other experiments in hadron collider as a function of the collision energy, $\sqrt{s}$ [81, 82, 83, 84, 28]. The results from CDF experiment is for the limited rapidity range, $|y| <0.6$. It was extrapolated assuming the rapidity distributions calculated by FONLL calculations. The solid line in Fig.6.5 represents cross section of the bottom production predicted by NLO pQCD calculation and dotted lines represent its uncertainty [85]. There is not a significant difference between the prediction and our result as well as other results.

6.4   Future Perspectives of Heavy Quark Measurement

The bottom fractions in d+A and A+A collisions are necessary to understand the behaviors of charm and bottom in the QGP. They will be evaluated by the DCA approach in near future. In order to achieve the approach, a precise tracking around the beam collision vertex is necessary to measure the DCA. The precise tracking is enabled by the VTX in our work, and our work is the first result measured with the VTX. A silicon tracking system is installed in ALICE experiment and will be installed
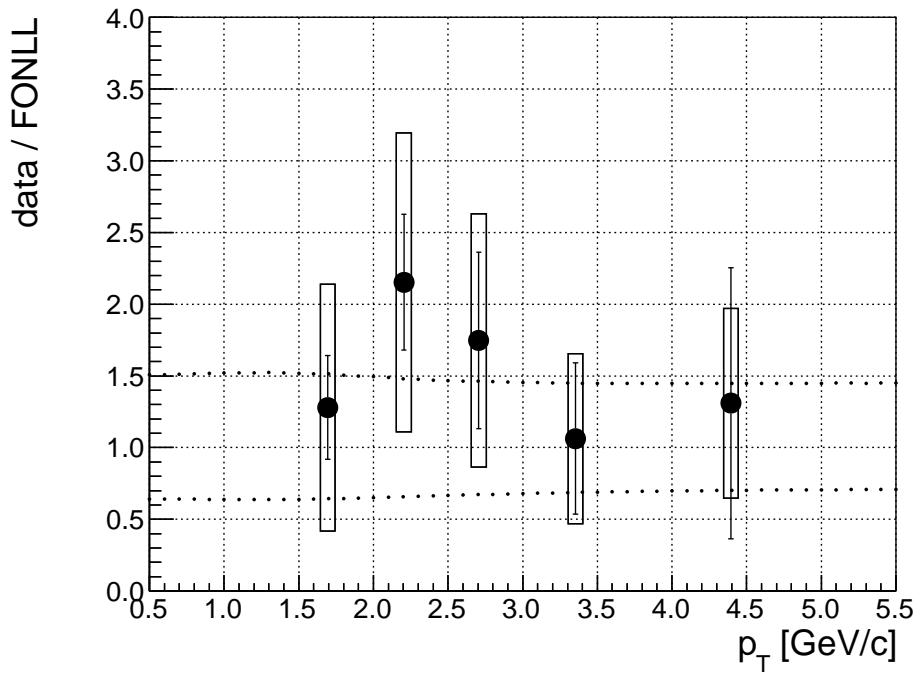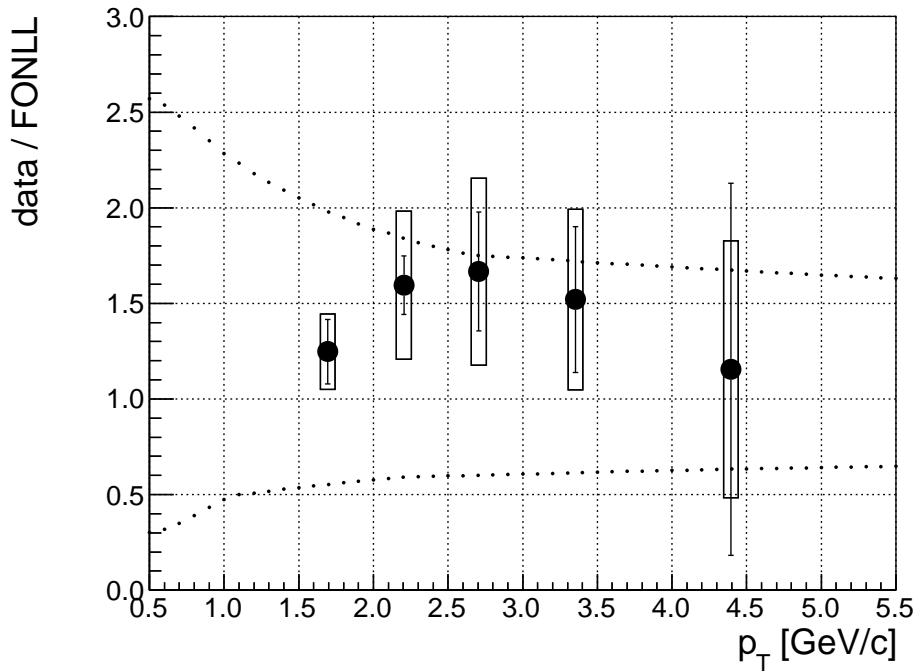
Figure 6.2: The ratios of measured result and the FONLL calculation of charm (upper) and bottom (lower) electrons as a function of electron p_T. The dotted lines represent the error band of the FONLL calculation.

152
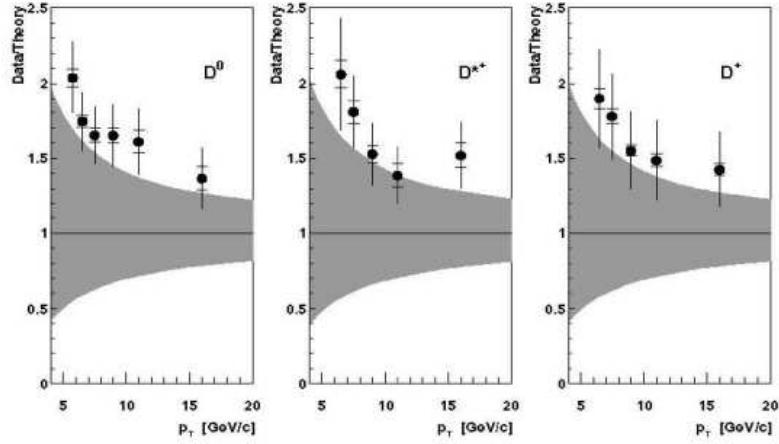
Figure 6.3: The ratio of measured result at CDF and FONLL calculations of D mesons as a function of p_T of the mesons. The left, middle, right panels show the ratios of D^0, D^{*+}, and D^+, respectively. The gray bands represent the uncertainties of the FONLL calculations.
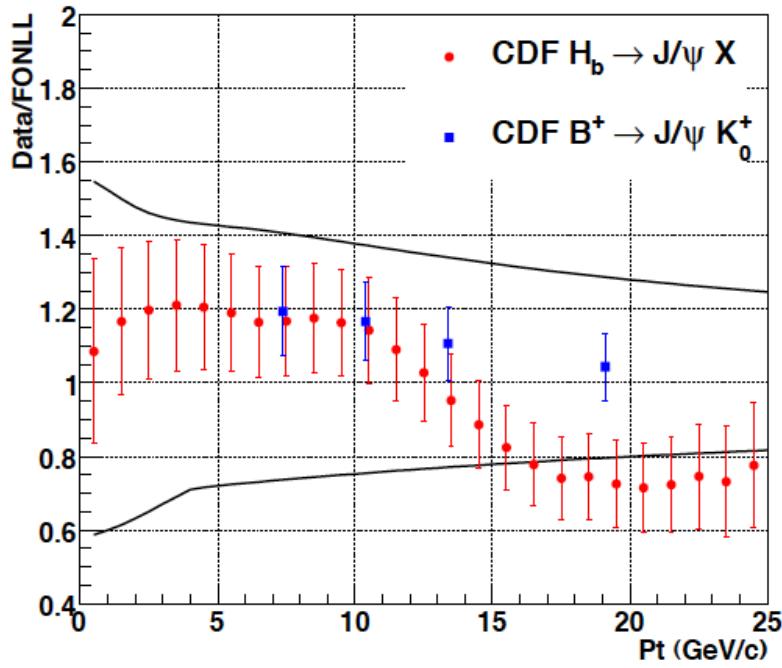
Figure 6.4: The ratio of measured result at CDF and FONLL calculations of bottom hadrons as a function of p_T of the hadrons [28].
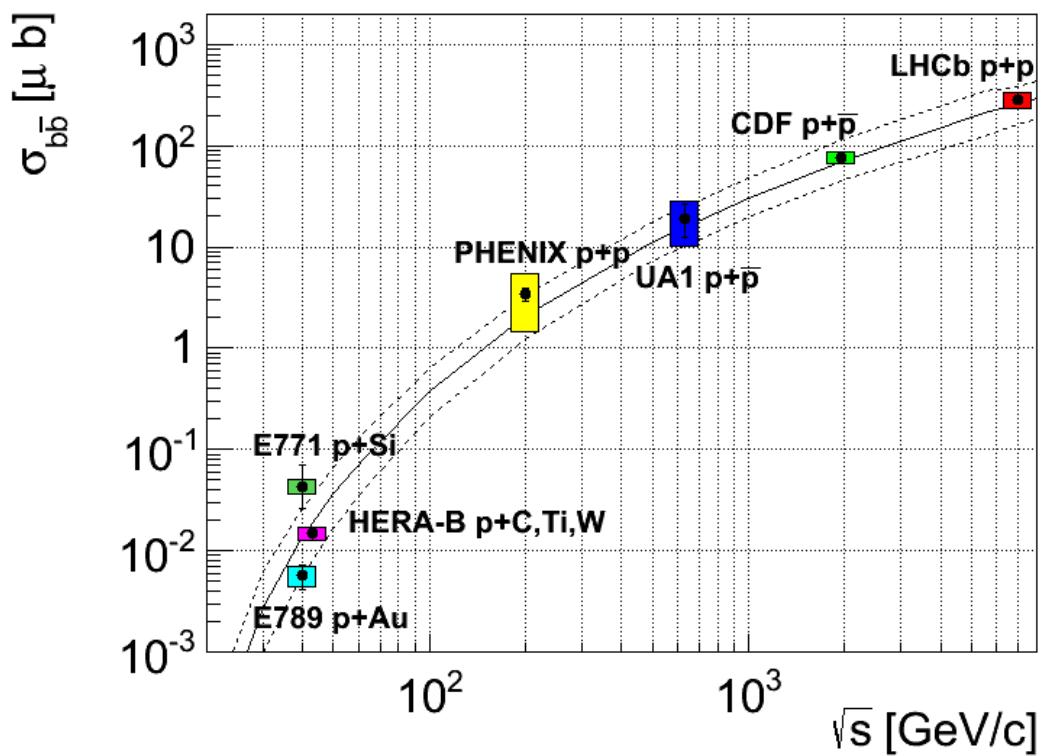
Figure 6.5: The cross section of bottom production measured with several collision energies with a pQCD prediction. The solid line represents the prediction by NLO pQCD and dotted lines represent its uncertainty.

154

in STAR experiment at 2014. At RHIC, Au+Au and d+Au collision experiments are planed to be carried out for Year-2014 and Year-2015 RUNs, respectively. The bottom fractions in Au+Au and d+Au collisions will be reported in future.

Here, expected performances in Au+Au collisions are discussed. Since multiplicity increases in Au+Au collision from p+p collisions ($\sim$100 (340) times increase at Au+Au collisions with 0-70% (0-5%) centrality [46, 45]), following differences between p+p and Au+Au collisions are expected:

- DCA resolution is improved since the beam collision point reconstructed for each collision can be used in Au+Au collision.

- S/N ratio which is the ratio of the heavy-quark electrons and other electrons changes.

Impacts of uncertainties of DCA resolution and the S/N ratio on the evaluation of f_b are described in following sub-sections. The contribution of fake tracks is also expected to increase in Au+Au collisions. However, an impact of the contribution is not estimated since it is hard to estimate the impact from studies with p+p collision data.

6.4.1 DCA resolution

The beam center, which is measured run-by-run described in Sec. 4.4.4, is used to measure the DCA in p+p collision due to low multiplicity ($dN_{ch}/d\eta|_{\eta=0} = d(N_{\pi^\pm} + N_{K^\pm} + N_{p^\pm})/d\eta|_{\eta=0} = 2.16 \pm 0.15$ [45]). DCA resolution of hadrons in p+p collisions is $(63.8 \pm 0.07)/p_T \oplus (128.3 \pm 0.02)$ μm, as is shown in Sec. 4.9.1. The constant term, 128.3 ± 0.02 μm, is mainly determined by the beam size, $115 \sim 129$ μm (Sec. 3.1). On the other hands, the beam collision point, which is measured collision-by-collision described in Sec. 4.4.4, can be used to measure the DCA in Au+Au collisions. The resolution of the beam collision point in Au+Au collisions is much better than the beam size, and thus, DCA resolution is improved. The resolution of the beam collision point in p+p collisions can be estimated from the width of the distribution of the beam collision point. The RMS of the Gaussian used to fit the peak of the distribution is $\sim$200 μm, thus, the resolution is about $\sqrt{200^2 + 125^2} = 156$ μm. When the resolution is assumed to be proportional to $(dN_{ch}/d\eta)^{-1/2}$ due to the central limit theorem, the resolution is estimated to be $\sim$15 (8) μm in Au+Au collisions with 0-70% (0-5%) centrality. The DCA resolution of electron shown in Fig. 4.10 does not contain a contribution of the uncertainty of the beam collision point. From the resolution, the DCA resolution which contains the uncertainty of the beam collision point in Au+Au collision is estimated and shown in Fig. 6.6. The DCA resolution in Au+Au collision is expected to be a half as good as that in p+p collisions at $p_T = 1.5$ GeV/c.

By subtracting background components from the inclusive electrons, the DCA distribution of the heavy-quark electrons can be obtained. The procedure to evaluate f_b
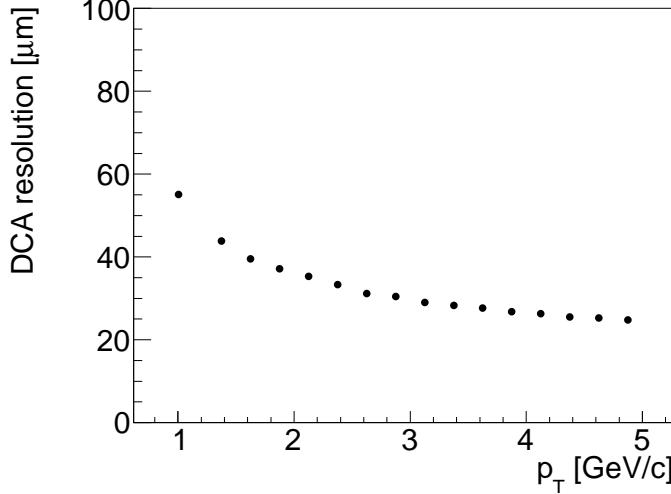
Figure 6.6: An expected DCA resolution of electrons as a function of p_T in Au+Au collisions with 0-70% centrality evaluated with expected resolution of beam collision vertex and DCA resolution shown in Fig. 4.10.

is simplified to evaluate with widths of DCA distribution of the heavy-quark ($\sigma(HQ)$), charm ($\sigma(c)$), and bottom electrons ($\sigma(b)$) as follows:

$$\sigma(HQ)^2 = (1 - f_b) \cdot \sigma(c)^2 + f_b \cdot \sigma(b)^2$$
$$= (1 - f_b) \cdot (\sigma_0(c)^2 + \sigma_{DCA}^2) + f_b \cdot (\sigma_0(b)^2 + \sigma_{DCA}^2), \quad (6.1)$$
$$f_b = \frac{\sigma(HQ)^2 - \sigma_{DCA}^2 - \sigma_0(c)^2}{\sigma_0(b)^2 - \sigma_0(c)^2}, \quad (6.2)$$

where σ_{DCA} is the DCA resolution. The uncertainty of the resolution, $\delta\sigma_{DCA}$, is transferred in f_b as $2\sigma_{DCA} \cdot \delta\sigma_{DCA}/(\sigma_0(b)^2 - \sigma_0(c)^2)$, and thus, it is proportional to σ_{DCA}. If an uncertainty of σ_{DCA} in Au+Au collisions is the same level as an effect of $\delta\sigma_{DCA}$ in f_b in Au+Au collision is expected to be a half as small as that in $p+p$ collisions.

6.4.2   S/N ratio

Conversion electrons and electrons from π^0 decay, which are the main background at low p_T, is suppressed owing to a small R_{AA} of π^0, ~0.3 in 0-93% centrality [86, 87]. Since π^0 and other light hadrons are mainly produced by the soft process, as is described, and thus, their yield is proportional to N_{part}, in Sec. 2.1.2. Since N_{part} is smaller than N_{coll}, as is described in Sec. 2.1.2, their R_{AA} is less than 1. On the other hands, the yield of the heavy-quark electrons is proportional to N_{coll} [18]. Therefore, the S/N ratio increases. However, if the same cut parameters about the isolation cut in Au+Au collisions as those used in $p+p$ collisions, which is summarized in Tab. 4.5, a

156

larger part of the heavy-quark electrons is rejected in Au+Au collision by the isolation cut due to a random association, i.e. ϵ^r in Eq. 4.49 is larger, than in $p+p$ collisions. Therefore, smaller rejection areas are necessary to be used in Au+Au collisions, and as a consequence, the S/N ratio decreases. When the rejection areas listed in Tab. 6.1 are used, which is $\sim 1/30$ of the rejection areas used for $p+p$ collisions, the survival fraction of the photonic electrons after the isolation cut increases to $\sim 40\%$ from $\sim 20\%$ in $p+p$ collisions. Figure 6.7 shows the survival fraction of the conversion electrons and electrons from π^0 decay [88]. Figure 6.8 shows the S/N ratio evaluated without the contribution of heavy quarkonia. From the figure, the S/N ratio is achieved to be larger than 1 at $p_T > 1.5$ GeV/c in Au+Au collisions, which is the same level as in $p+p$ collisions.

Table 6.1: Requirements of rejection by the isolation cut.

barrel	requirement
B0	-0.02<**cdphi**<0.04 ∩ |**dz**| <0.05
B1	-0.02<**cdphi**<0.06 ∩ |**dz**| <0.05
B2	-0.04<**cdphi**<0.08 ∩ |**dz**| <0.1
B3	-0.02<**cdphi**<0.08 ∩ |**dz**| <0.1
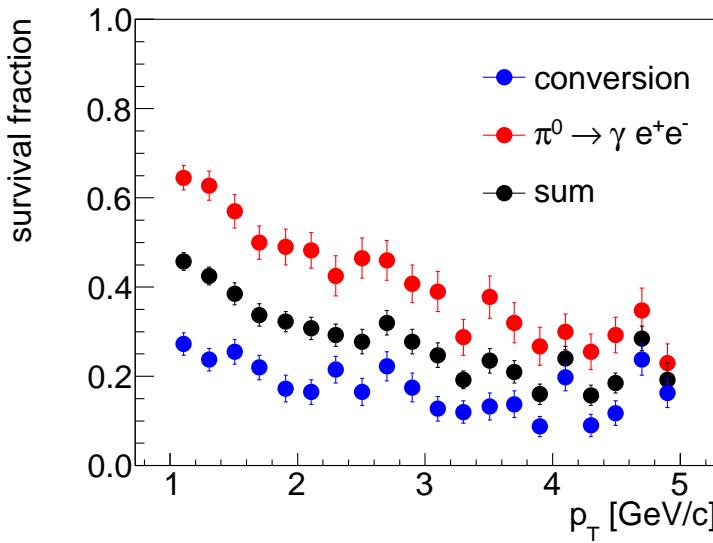
Figure 6.7: Survival fractions of conversion electrons (blue), electrons from π^0 decays (red), and average of them (black). The average is calculated with respect to their yields.
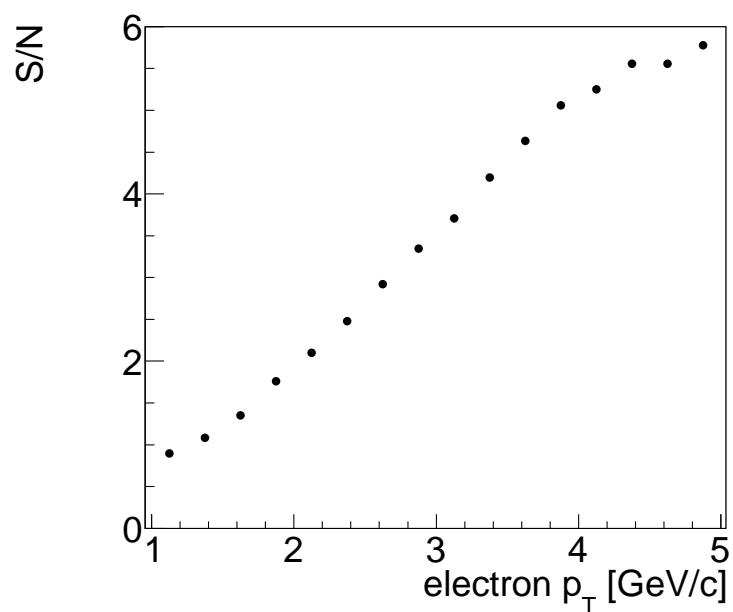
Figure 6.8: An expected S/N ratio in Au+Au collisions. The S/N ratio is defined as the ratio of the heavy-quark electrons and other electrons.

Chapter 7

Conclusion

A heavy quark is an interesting probe to understand a parton behavior in the extremely hot and dense matter created by the relativistic heavy-ion collision. The heavy quarks are only produced in initial parton scattering in heavy-ion collisions due to their large masses. It means that the properties of the heavy quarks at the initial stage of the heavy-ion collisions can be well described by those of $p+p$ collisions. Therefore, the difference of the final states of the heavy quarks between the heavy-ion collisions and $p+p$ collisions represents modifications during passing through the matter. The heavy quarks are expected to take longer time to equilibrate with the matter than light quarks since the energy loss of the heavy quarks is smaller than that of light quarks due to dead cone effect [13]. Due to the long relaxation time, a history of interactions between the matter and the heavy quarks, which are strongly related to the properties of the matter, can be preserved in their diffusion during passing through the matter.

Since the energy loss depends on quark mass, the comparison of modifications during traveling in the matter between charm and bottom can test descriptions of the interaction. There are results about charm and bottom measurement in $p+p$ collisions [15, 16]. However, the results are only for high-p_T region and the approaches employed to extract the results are hard to be employed for heavy-ion collisions due to a large background derived from the high multiplicity condition of heavy-ion collision. A new approach has been developed to evaluate the fraction of the bottom contribution in the heavy-quark electrons. The fraction is evaluated by using the distances of the closest approach to the beam collision vertex, called DCA. DCA distributions of the electrons from charm and bottom decays have significantly different widths due to the difference of their life-times. The fraction can be evaluated by using the difference of their widths. Tracking with a good position resolution is necessary around a beam collision point to achieve the measurement. A silicon tracking system called VTX has been installed in PHENIX experiment in 2011 to achieve the precise tracking.

The bottom fraction has been evaluated by the new approach in $p+p$ collisions

with $\sqrt{s} = 200$ GeV at $1.5 < p_T < 5$ GeV/c. The bottom fraction at $p_T < 2.5$ GeV/c is succeeded to be measured for the first time. A large azimuthal anisotropy of the heavy quark electrons has been observed at the region, thus modifications of p_T spectra of electrons from charm and bottom decays at the p_T region is interesting since affects of charm and bottom from the matter is expected to appear at the region. The fraction at $p_T > 2.5$ GeV/c is consistent with other results, and thus it is confirmed that the evaluation by the new approach has been succeeded. The result can also provide a good test of perturbative QCD (pQCD) calculations. There is not a significant difference in differential cross sections of the electrons from charm and bottom decays between the predictions and measured results though center values of the predictions are ~50% smaller than the measured results. The integral of the differential cross section of the bottom electrons at $1.5 < p_T < 5$ GeV/c and $|y| < 0.5$ is 48.7 ± 7.5 (stat) ± 27.9 (syst) nb. The total cross section of the bottom production is also determined by extrapolating with FONLL calculations, and it is 3.41 ± 0.53 (stat) ± 2.14 (sys) μb. There is not a significant difference between the prediction and our result.

The bottom fractions in d+A and A+A collisions, where A denotes nucleus, are necessary to understand the behaviors of charm and bottom in the extremely hot and dense matter. They are expected to be evaluated in near future. Au+Au and d+Au collision experiments are planed to be carried out for Year-2014 and Year-2015 RUNs at RHIC, respectively. These results combining with our result can clarify the behaviors of charm and bottom in the QGP, which leads to understand the parton energy loss and the space-time evolution of the QGP.

Acknowledgments

First of all, I would like to express my gratitude to my supervisor, Prof. H. Hamagaki. He has been encouraged me and his abundant knowledge has always stimulated and guided me. His valuable advice is helpful to complete this thesis. I wish to thank Dr. T. Gunji for his valuable advice about physics and data analysis. His comments and discussions with him are essential for this thesis. I am deeply grateful to Dr. Y. Akiba. He have led the VTX project, which is essential for this work. In addition, his insightful advice and rich knowledge about physics are essential to complete this work.

I would like to thank to all PHENIX collaborators. I am obliged to Prof. B. Jacak, who was the spokesperson until 2012, and Prof. J.L. Nagle and Dr. D.P. Morrison, who are the co-spokespersons since 2012, for their excellent leadership. I'm also obliged to Dr. A. Taketani, Dr. M. Kurosawa, Dr. R. Nouicer, Mr. H. Asano, Prof. S. Bathe, Dr. M. Bobrek, Dr. K. Boyle, Mr. J. Bryslawskyj, Dr. V. Cianciolo, Dr. C.-H. Chen, Dr. L. Ding, Dr. A. Dion, Dr. A. Enokizono, Mr. J. Kanaya, Dr. J. Koster, Mr. T. Koblesky, Dr. T. Hachiya, Dr. A. Lebedev, Dr. E.J. Mannel, Dr. M. McCumber, Dr. D.P. Morrison, Prof. J.L. Nagle, Mr. H. Nakagomi, Prof. C. Ogilvie, Dr. R. Pak, Dr. C. Pancake, Prof. M. Rosati, Dr. H. Sako, Dr. S. Sato, Mr. A. Shaver, Dr. M. Shimomura, Dr. P. Stankus, Dr. M. Stepanov, Dr. M. Wysocki, and other people who work for VTX development and operation, and data analysis with VTX. I thank for their dedications for the VTX and giving me meaningful comments and advice for the analysis. Especially, I would like to express my thanks to Dr. A. Taketani, who is the leader of development of the pixel detector, Dr. M. Kurosawa, who is the main person of operation of the pixel detector, and Dr. R. Nouicer, who is the leader of development and operation of the stripixel detector. In addition, I am also obliged to Dr. E.J. Desmond, Dr. J.S. Haggerty, Dr. C. Pinkenburg, and Dr. M.L. Purschke for helping for installation and data taking of VTX. Dr. C. Pinkenburg also helped for the development of VTX software.

I would like to express my appreciation to Dr. H. En'yo, Prof. K. Ozawa, and Prof. S. Esumi for their support for my research. Thanks to their support, I could concentrate on my research. I would also like to acknowledgement for support from Japan Society for the Promotion of Science (JSPS). I would like to express my thanks to secretaries of Radiation Laboratory at RIKEN, Ms. N. Kiyama, Ms. K. Sakuma, Ms. K. Suzuki, and Ms. M. Yamamoto, and RBRC, Ms. E. Adachi, Ms. T. Ito,

Bibliography

[1] V. Schoefer, *et al.*, 2012.

[2] J.C. Collins and M.J. Perry, Phys. Rev. Lett. **34**, 1353 (1975).

[3] H. Satz, Nucl. Phys. **A418**, 447 (1984).

[4] F. Karsch, E. Laermann and A. Peikert, Phys. Lett. B**478**, 447 (2000).

[5] F. Karsch, Nucl. Phys. **A698**, 199 (2002).

[6] F. Karsch, PosCPOD **07**, 026 (2007).

[7] T. D. Lee, Nucl. Phys. **A538**, 3 (1992).

[8] L. McLerran, Rev. Mod. Phys. **58**, 1021 (1986).

[9] J. James, *et al.*, Phys. Rev. Lett. **93**, 252301 (2004).

[10] S. S. Adler, *et al.*, Phys. Rev. Lett. **91**, 072301 (2003).

[11] K. Adcox, *et al.*, Phys. Rev. Lett. **89**, 212302 (2002).

[12] K. H. Ackermann, *et al.*, Phys. Rev. Lett. **86**, 402 (2001).

[13] Y. L. Dokshitzer and D. E. Kharzeev, Phys. Lett. B**519**, 199 (2001).

[14] G. D. Moore and D. Teaney, Phys. Rev. C**71**, 034907 (2005).

[15] A. Adare, *et al.*, Phys. Rev. Lett. **102**, 082002 (2009).

[16] M. M. Aggarwal, *et al.*, Phys. Rev. Lett. **105**, 202301 (2010).

[17] M. Kasai, *et al.*, RIKEN Accel. Prog. Rep. **42**, 212 (2009).

[18] A. Adare, *et al.*, Phys. Rev. C**84**, 044905 (2011).

[19] J.D. Bjorken, Phys. Rev. D**27**, 140 (1983).

[20] P.F. Kolb, Heavy Ion Phys. **21**, 243 (2004).

[21] R.J. Glauber and G. Matthiae, Nucl. Phys. **B21**, 135 (1970).

[22] R.J. Glauber. Lectures in theoretical physics, 1959.

[23] A.K. Chaudhuri, arxiv:1112.3757 (2012).

[24] B.B. Back, *et al.*, Phys. Rev. C**74**, 021902(R) (2006).

[25] M. Cacciari, *et al.*, JHEP.**9805**, 007 (1998).

[26] M. Cacciari, *et al.*, Phys. Rev. Lett. **95**, 122001 (2005).

[27] M. Cacciari, *et al.*, Phys. Rev. Lett. **89**, 122003 (2002).

[28] D. Accosta, *et al.*, Phys. Rev. D**71**, 032001 (2005).

[29] H. Agakishiev, *et al.*, Phys. Rev. D**83**, 52006 (2011).

[30] A. Adare, *et al.*, Phys. Rev. Lett. **109**, 242301 (2012).

[31] B. Abelev, *et al.*, Phys. Rev. D**86**, 112007 (2012).

[32] A. Adare, *et al.*, Phys. Rev. Lett. **96**, 032302 (2006).

[33] J.W. Cronin, *et al.*, Nucl. Phys. **D11**, 3105 (1975).

[34] K.J. Eskola, V.J. Kolhinen and C.A. Salgado, Eur. Phys. J. **C9**, 61 (1999).

[35] H. Wohri and C. Lourence, J. Phys **G30**, S315 (2004).

[36] R. Rapp and H.v. Hees, arxiv:0803.0901 (2008).

[37] P. Danielewicz and M. Gyulassy, Phys. Rev. D**31**, 53 (1985).

[38] K. Adcox, *et al.*, Nucl. Phys. **A757**, 184 (2005).

[39] S. Caron-Huot and G. D. Moore, Phys. Rev. Lett. **100**, 052301 (2008).

[40] W.M. Alberico, *et al.*, Eur. Phys. J. **C71**, 1666 (2011).

[41] Y. Akamatsu, *et al.*, Phys. Rev. C**79**, 054907 (2009).

[42] M. He, R.J. Fries and R. Rapp, Phys. Rev. C**86**, 014903 (2012).

[43] S.K. Das, *et al.*, Phys. Rev. C**80**, 054916 (2009).

[44] P.K. Kovtun, D.T. Son and A.O. Starinets, Phys. Rev. Lett. **94**, 111601 (2005).

[45] A. Adare, *et al.*, Phys. Rev. C**83**, 064903 (2011).

164

[46] S.S. Adler, *et al.*, Phys. Rev. C**71**, 034908 (2005).

[47] J. Beringer, *et al.*(Particle Data Group), Phys. Rev. D**86**, 010001 (2012).

[48] H. Hahn, *et al.*, Nucl. Instrum. Meth. **A499**, 245 (2003).

[49] Y. Akiba, *et al.*, Nucl. Instrum. Meth. **A433**, 143 (1999).

[50] L. Aphecetche, *et al.*, Nucl. Instrum. Meth. **A499**, 521 (2003).

[51] K. Adcox, *et al.*, Nucl. Instrum. Meth. **A499**, 489 (2003).

[52] S.H. Aronson, *et al.*, Nucl. Instrum. Meth. **A499**, 480 (2003).

[53] T. Sakaguchi, *et al.*, Nucl. Instrum. Meth. **A453**, 382 (2000).

[54] W. Snoeys, *et al.*, Nucl. Instrum. Meth. **A465**, 176 (2001).

[55] M. Garcia-Sciveres, *et al.*, Nucl. Instrum. Meth. **A511**, 171 (2003).

[56] Z. Li, *et al.*, Nucl. Instrum. Meth. **A518**, 300 (2004).

[57] J. Tojo, *et al.*, IEEE Trans. Nucl. Sci. **51**, 2337 (2004).

[58] S.S. Adler, *et al.*, Nucl. Instrum. Meth. **A499**, 560 (2003).

[59] J.T. Mitchell, *et al.*, Nucl. Instrum. Meth. **A482**, 491 (2002).

[60] J. Myrhiem and L. Bugge, Nucl. Instrum. Meth.**160**, 43 (1979).

[61] GEANT Detector description and simulation tool. CERN Program Library Long Write-up W5013, CERN, Geneve.

[62] T. Sjöstrand, S. Mrenna and P. Skands. Pythia manual. `http://home.thep.lu.se/~torbjorn/pythia/lutp0613man2.pdf`.

[63] T. Affolder, *et al.*, Phys. Rev. D**65**, 092002 (2006).

[64] E. Lohrmann, arxiv:1112.3757 (2011).

[65] R. Aaij, *et al.*, Phys. Lett. B**694**, 209 (2010).

[66] D. Buskulic, *et al.*, Phys. Lett. B**361**, 221 (1995).

[67] T. Aaltonen, *et al.*, Phys. Rev. D**77**, 072003 (2008).

[68] P. D. Acton, *et al.*, Phys. Lett. B**295**, 357 (1992).

[69] A. Adare, *et al.*, Phys. Rev. D**76**, 051106 (2007).

[70] A. Adare, *et al.*, Phys. Rev. D**83**, 032001 (2011).

[71] A. Adare, *et al.*, Phys. Rev. D**83**, 052004 (2011).

[72] R. Averbeck, *et al.*, PHENIX Internal Analysis Note **89** (2001).

[73] A. Adare, *et al.*, Phys. Rev. C**84**, 044902 (2011).

[74] S. S. Adler, *et al.*, Phys. Rev. Lett. **98**, 012002 (2007).

[75] A. Adare, *et al.*, Phys. Rev. C**81**, 034911 (2010).

[76] A. Adare, *et al.*, Phys. Rev. D**82**, 012001 (2010).

[77] A. Adare, *et al.*, Phys. Rev. D**85**, 092004 (2012).

[78] A. Adare, *et al.*, arxiv:1211.4017 (2012).

[79] P. M. Nadolsky, *et al.*, Phys. Rev. D**78**, 013004 (2008).

[80] A.D. Martin, *et al.*, arxiv:0901.0002 (2009).

[81] I. Abt, *et al.*, Phys. Rev. D**73**, 052005 (2006).

[82] D. M. Jansen, *et al.*, Phys. Rev. Lett. **74**, 3118 (1995).

[83] T. Alexopoulos, *et al.*, Phys. Rev. Lett. **82**, 41 (1999).

[84] C. Albajar, *et al.*, Phys. Lett. B**256**, 121 (1991).

[85] R. Vogt. private comunication.

[86] A. Adare, *et al.*, Phys. Rev. Lett. **101**, 232301 (2008).

[87] A. Adare, *et al.*, Phys. Rev. C**87**, 034911 (2013).

[88] Y. Akiba, *et al.*, PHENIX Internal Analysis Note **1064** (2012).